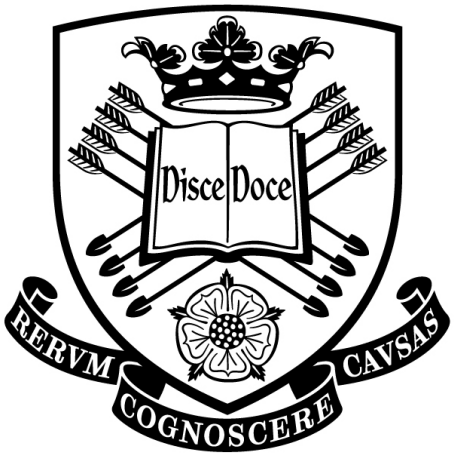

The University Of Sheffield.

The University Of Sheffield.

2D Patterning and 3D Printing of Novel PGSm for Peripheral Nerve Repair and Soft Tissue Engineering

August 2017

Thesis submitted to The University of Sheffield, Materials Science and Engineering, for the degree of Doctor of Philosophy

Dharaminder Singh

Dharaminder.co.uk

Dharaminder.Singh@gmail.com

ABSTRACT

A lack of appropriate, structurable, biomaterials has limited the development of research into soft tissue engineering. Often the biomaterials currently in use have inappropriate materials properties for soft tissue engineering, and cannot be structured into complex three dimensional scaffold designs. The aim of this study was to develop the novel formulation biomaterial PGSm (Polyglycerol sebacate methacylate), which can be photocured into complex 2D/3D structures for peripheral nerve repair and soft tissue engineering.

PGSm was synthesized, and characterized chemically and mechanically. High internal phase emulsions of PGSm (polyHIPEs) were photocured into 3D foams. PGSm was printed via microstereolithography into nerve guidance conduits and tested for use in peripheral nerve repair *in vitro, ex vivo* and *in vivo.* Porous PGSm conduits were developed and tested *ex vivo,* with an intended use for larger gap injuries. Porous polyHIPE PGSm was developed into tunable microparticles and explored for use as a cartilage tissue-engineering scaffold. The polyHIPE was also developed as an *in vitro* neuronal model and a scaffold for ESCs. Results show the material was developed into a photocurable polymer, capable of being 3D printed into highly accurate NGCs. PGSm conduits performed well overall and regeneration into the distal stump was witnessed *in vivo.* Techniques were developed to photocure reproducible porous polyHIPE conduits, with promising initial *in vitro/ex vivo* results. Porous microparticles were seen to allow for the development of cartilage like tissue *in vitro.* PolyHIPE PGSm was used for neuronal models and stem cell scaffolds. In summary the developed PGSm is useful for simple and complex scaffolds for soft tissue engineering.

ACKNOWLEDGEMENTS

"Those who think they can and those who think they can't are both usually right"

Completing a PhD has been a far greater challenge than I would ever have imagined. There were many enjoyable moments, and just as many testing ones. However I would not have made it this far without help.

Firstly this would not have been possible without my parents. Getting through a PhD was so much easier knowing both of you were by my side. Also thanks to the rest of my family for your support throughout: special thanks to my sister, brother in-law, grandparents, niece Tara and nephew Gurman.

I would also like to thank those I have worked with: my supervisors Dr Frederik Claeyssens who always had interesting ideas and conversation, Professor John Haycock for providing me with helpful guidance and advice throughout. Thanks to Professor Harry Moore and Andy Wood for providing me with embryonic stem cells and supporting me with cell culture advice. Thanks to Dr Helen Bryant and Dr David King for providing me with neuroblastoma cell lines. I would also like to thank Dr Adam Harding, Dr Emad Albadawi and their supervisor Professor Fiona Boissoinaide who performed the *in vivo* implantations and took confocal images of the dissected nerves, which were then analysed by both Adam and myself. Chondrocytes used in experiments were donated by Sarah Lindsay, and Aileen Crawford, thank you both for the cells and for helping teach my masters student. Thanks also to Shruti Gurbaxani, a masters student I taught,

who helped with microparticle studies. A big thanks also to the EPSRC for sponsoring my PhD throughout.

Last but surely not least, thanks to my colleagues and friends for keeping me on track throughout. Ric Plenderleith for help throughout my masters and Jim Duggan who was an invaluable help in giving my PhD a real focus. I would like to thank: Leyla Zilic for helping to develop my caffeine addiction, Ahssad Fiaz for being a good friend throughout (and that unmentionable favour), Tom Paterson for being my travel buddy in at least 7 different countries, Lindsey Dew for the jokes in the amazing Poland, Colin Sherbone in showing me the ropes (mainly in CoD zombies), Chris Tse for teaching me all I know in Mandarin, Alexandra Beneng for those endless conversations, Sarina Chand for bringing me luck (and making the office fun) and Shalmali Deshpande for teaching me what tapenade is (and making me recycle).

This thesis is dedicated to my late brother Gurvinder Singh

- I hope to keep you proud -

OUTPUTS

Presentations

BiTeg (2014, Sheffield, UK) - **Poster** Presentation

"PGSm for use as a peripheral nerve guide"

Eurpoean society of biomaterials (2015, Poland) - **Poster** Presentation

"PGSm as a peripheral nerve guide"

Termis World Congress (2015 Boston, USA) - **Poster** Presentation

"Poly glycerol sebecate for use as a peripheral nerve biomaterial"

USES (2015, Sheffield, UK) - **Oral** Presentation

"Photocurable PGS for peripheral nerve repair"

BiTeg (2015, York, UK) - **Oral** Presentation

"Exploring tunable and porous PGSm for peripheral nerve repair in vivo"

World Biomaterial Congress (2016, Canada) - **Oral** Presentation

"3D printed novel PGSm nerve guidance conduits for in vivo analysis"

Imagine Life Symposium (2016 Sheffield, UK) - **Poster** Presentation

"PGSm a neuronal biomaterial"

Termis EU (2016 Uppsala, Sweden) - **Poster** Presentation

"In vivo implantation of novel photocurable PGSm 3D printed nerve guidance conduits for nerve repair"

TCES (2016 London UK) - **Oral** Presentation

"3D printed novel PGSm nerve guidance conduits in vivo"

TERMIS EU (2017 Davos, Switzerland) – **Oral and Poster** presentation

"*In vitro, ex vivo and in vivo analysis of novel 3D printed PGSm nerve guidance conduits for peripheral nerve repair*"

Awards

1st Researchers night photo competition	- 2013
BiTeg 2nd Place Poster Award	- 2014
Discovery night Image competition	- 2014
USES poster 2nd place Award	- 2014
Materials image competition winner	- 2014
Imaging life Image competition winner	- 2015
Biomaterials image competition winner	- 2016
Imaging life 3rd place poster Award	- 2016
TERMIS EU Oral Presentation RF 3rd Prize	- 2017

Funding obtained

Uni of Sheffield, Learned Society (2015)	- £450
Armourers and brasiers gauntlet trust (2015)	- £900
Institute of Physics travel fund (2015)	- £300
IOP, C R Barber trust (2015)	- £175
Uni of Sheffield, Learned Society (2015)	- £450
University of Sheffield travel award (2016)	- £400
Armourers and brasiers gauntlet trust (2016)	- £800
Macro Group, D.H.Richards bursary (2016)	- £500
Uni of Sheffield, Learned Society (2016)	- £450
TCES travel bursary (2016)	- £150
Engineering department travel fund (2017)	- £230
Learned society (2017)	- £450

TABLE OF CONTENTS

GLOSSARY

ACI	– Autologous chondrocyte implantation
AFM	– Atomic force microscopy
ANOVA	– Analysis of variance
ATR-FTIR	– Attenuated total reflectance FTIR
BSA	– Bovine Serum Albumin
CNS	– Central nervous system
DAPI	– 4′,6-diamidino-2-phenylindole
DMA	– Degree of methacrylation
DMB	– Dimethylene blue assay
DMD	– Digital micromirror device
DMEM	– Dulbecco's modified Eagle's medium
DRG	– Dorsal root ganglion
DSC	– Differential scanning calirometry
E	– Young's modulus
E_r	– Reduced modulus
ECM	– Extra cellular matrix
EDTA	– Ethylenediaminetetraacetic acid
ESC	– Embryonic stem cells
EtOH	– Alcohol
FCS	– Fetal calf serum
FDA	– Food and Drug administration
FTIR	– Fourier transform infared spectroscopy
GaG	– Glycoamino glycans
GPC	– Gel permeation chromotography
H&E	– Haemotoxylin and Eosin
HCL	– Hydrochloric acid
hESC	– Human embryonic stem cell
HIPE	– High internal phase emulsion
HMDS	– Hexamethyldisilazane
ICC	– Immunocytochemistry
ICM	– Inner cell mass

IHC	– Immunohistochemistry
IPSC	– Induced pluripotent stem cell
MACI	– Matric induced autologous chondrocyte implantation
MAPTMS	– 2-(trimethoxysilyl) propyl methacrylate
MEHQ	– Mono methyl ether of hydroquinone
MicroCT	– Micro computer tomography
MSC	– Mesenchymal stem cell
MTT	–(3-(4,5-Dimethylthiazol-2-yl)-2,5-Diphenyltetrazolium Bromide)
M_w	– Molecular weight
NB	– Neuroblastoma
NGC	– Nerve guidance conduit
NMR	– Nuclear magnetic resonance
NTF	– Neurotrophic factors
PBS	– Phosphate buffer saline
PCL	– Polycaprolactone
PDI	– Poly Dispersity Index
PDMS	– Polydimethylsiloxane
PEGda	– Polyethylene glycol diacrylate
PGS	– Poly(glycerol sebacate)
PGSm	– Poly(glycerol sebacate methacrylate)
PGSa	– Poly(glycerol sebacate acrylate)
PI	– Photoinitiator
PMMA	– Polymethyl methacrylate
PNI	– Peripheral nerve injury
PNS	– Peripheral nervous system
RBF	– Round bottom flask
SD	– Standard deviation
SEM	– Scanning electron microscopy
T_g	– Glass transition temperature
TE	– Trophectoderm
THF	– Tetrahydrofuran
TRITC	– Tetramethylrhodamine
UV	– Ultraviolet
YFP	– Yellow fluorescent protein

LIST OF FIGURES

1. INTRODUCTION

This PhD research project is multidisciplinary by nature and covers a broad range of topics. I began my research by investigating polymers for peripheral nerve repair and then expanded this research into other areas for soft tissue engineering. For that reason, this thesis starts with a general introduction (1), which gives an overview of tissue engineering and polymers. There is then a general methods section (2), followed by seven individual chapters containing experimental work and results (3.1-3.7). Each chapter containting experimental work and results are a separate chapter of their own and comprises of a brief introduction/literature review, specific methods, results, discussion and conclusion. The first chapter (3.1) introduces the polymer PGSm, chapter (3.2) then explores the polymer as a porous polyHIPE. My research then investigated the use of PGSm in peripheral nerve repair with chapter (3.3) related to the production and efficacy of PGSm nerve guidance conduits and (3.4) related to the production of porous polyHIPE conduits. I then explored other uses of PGSm for soft tissue engineering with chapters (3.5, 3.6, and 3.7) related to cartilage repair, neuroblastoma models and stem cell scaffolds respectively. The thesis then closes with an overall conclusion (4).

1. Tissue Engineering

Tissue engineering developed as a field of research based fundamentally around the idea of using biocompatible materials, often seeded with cells, to

replace tissue and organs within the body. Replacing tissues within the body dates at least as far back as the 16th century[1]. However it wasn't until the 1970's and 1980's that the field of "Tissue Engineering" began to form, with Robert Langer and Joseph Vacanti at the forefront of tissue engineering research[2,3]. Initially tissue engineering explored the use of biocompatible scaffolds (biomaterials), cells, growth factors and bioreactors to create an engineered-tissue to be implanted within the body. After decades, tissue-engineering research has matured developing exciting and effective methods of novel clinical applications. Technological and scientific advances have driven the research into new and exciting areas including the development of tissue-engineered models for *in vitro* analysis and drugs testing.

2. Regenerative Medicine

Regenerative medicine is a research area closely linked with tissue engineering. The two terms are often used interchangeably and the differences can be vague, however regenerative medicine can be characterized as the study of regenerating a loss of function to overcome medical problems, often through the use of stem cells[4,5]. Both tissue engineering and regenerative medicine often involve the use of biomaterials.

3. Biomaterials

The term biomaterial is used to address any materials used within the body. Although biomaterials have been extensively researched throughout history, they didn't become widely used until the 1860's when the introduction of aseptic techniques minimalised the risk of infection[6]. Initial implants were metallic biomaterials focused on the skeletal system throughout the 1900s. By the Second World War research turned toward polymers. Polymers were introduced to the field when pilots became injured with fragments of

polymethyl methacrylate (PMMA) from aeroplane canopies. The pilots did not suffer an adverse reaction when the PMMA remained within the body, leading to the use of PMMA and then other polymers as biomaterials[6].

Biomaterials used within the body can be separated into metallic biomaterials, polymeric biomaterials, ceramic biomaterials, composite biomaterials and natural materials. Metals are often used for their conductivity and strength, ceramics boast inertness and high compressive strength, composite materials are often used for their specific materials properties and natural materials have the benefit of being highly biocompatible by nature. Polymers are extensively used as biomaterials in tissue engineering and are explained in further detail in paragraphs below.

Ideal biomaterials for use in tissue engineering scaffolds would be biocompatible, as they would not cause an adverse reaction within the body. The material would have similar mechanical properties to that of the tissue, rigid materials for bone and flexible materials for softer tissues. The biomaterial would often need to be porous, for cell infiltration and to allow for nutrient exchange. In most tissue engineering applications degradability is advantageous, as prolonged exposure within the body increases the risk of an adverse reaction; the degradation products should also be non-toxic and resorbable within the body. A final requirement for an ideal biomaterial scaffold would be the ease of production and structurability[2].

4. Polymers

The word polymer is derived from the Greek, “poly” which translates to many and “mer” which translates to units. This breakdown of the word provides a useful basic definition of polymers, which consist of many smaller sub units to

create a larger network[7]. Polymers can occur naturally, such as silk and proteins, or can be synthesized synthetically such as polystyrene and nylon[8]. Whilst natural polymers are also widely explored in tissue engineering, the research in this study is based around synthetic polymers and therefore synthetic polymers remain the focus of the following paragraphs.

Polymeric networks can be built up from many of a single type of structural unit (monomer) or many of different types of structural units. The process by which these monomers combine to form a polymer is known as a polymerization reaction. The polymer networks are built from a large number of high molecular weight (M_w) polymer chain molecules of differing lengths. Although the exact M_w required for the material to be called a polymer isn't well defined, it is thought from literature to be approximately 25,000 g/mol[9]. If the length of polymer chains within a network are closely related, then the polymer is understood to have a low poly dispersity index (PDI). If the polymer chains are regular then dense packing and crystallization can occur, however if the polymer chains are irregular then amorphous polymers can be formed. Within amorphous polymers a temperature change can allow individual polymer chains to slide across each other when a force is applied, without structural changes in the polymer. The ability of chains to slide across each other can change a polymers material properties from a brittle, "glassy," plastic state into a more flexible "rubbery" state. The temperature at which this occurs is known as the glass transition temperature (T_g)[9]. Polymer networks can contain both crystalline and amorphous domains.

5. Polymers in Tissue Engineering

Synthetic polymers have many medical applications and are widely used in tissue engineering. Polymers are used in implants, surgical tools, dressings,

sutures, prosthetics, dental materials, drug delivery systems and tissue engineering scaffolds. The popularity of these synthetic polymers in tissue engineering stemmed from their reproducibility, ability to be structured, affordability, adaptable materials properties and mechanical properties. One of the major limitations of synthetic polymers however is their lack of biocompatibility. Often tissue engineering scaffolds are required to not only be inert, demonstrating no adverse response, but to also contain cell adhesion sites and actively promote regeneration. Whilst natural materials contain these adhesion sites aiding cell growth, they are often limited in their reproducibility, tunability, accessibility and produceability (ease of structuring). Often to make polymers more biocompatible, natural materials are incorporated within synthetic polymers. This can however complicate scaffold production and affect affordability.

6. Polymerization

Synthetic polymers are synthesized through two types of polymerization reaction, chain polymerization and step polymerization. One important chain polymerization method, known as free radical polymerization, occurs in three steps, initiation, propagation and termination. Initiation involves the appearance of a free radical, which initiates the addition of the first monomer to the polymer chain. Propagation then occurs rapidly, whereby many monomers are added in an instant, this propagation is terminated at the termination step whereby two free radicals react with each other. Polycondensation reactions are one important example of the other type of polymerization, step polymerization. Polyesters are often formed through the polycondensation reaction of an acid and an alcohol[9]. Addition (polyaddition) is another example of polymerization that utilises the step growth

polymerization mechanism, it differs from polycondensation reactions as the polymer is produced with no additional small molecules (water)[10].

7. Photosensitive polymers and photoinitiators

Photosensitive polymers (also known as photopolymers) are materials that are modified physically or chemically as a result of exposure to light. Photosensitive materials are not a new technology, with examples of sunlight induced, crosslinked Judean asphalt being used in the mummification process in ancient Eygpt[11]. Photosensitive materials are now however developed into advanced materials with many capabilities and applications. The modification often occurs in the presence of a photoinitiator, a molecule that releases reactive species (often free radicals or cations/anions) as a result of exposure to light. There are five main mechanisms by which photosensitive polymers change. Photosensitive polymers can undergo photoinduced chain growth polymerization, they can undergo step growth polymerization, functional group modification can occur, the polymer can be broken down through photoinduced cleavage reactions and finally the polymer can undergo photoinduced crosslinking[12].

8. Photocrosslinking

Crosslinking defines the process of joining several polymer chain molecules together, creating a single giant molecule. This crosslinking can be photoinduced (stimulated by light), through a process known as photocrosslinking (also known as photocuring.) A material must be photosenstive for photocrosslinking to occur. Photocrosslinking of polymers occurs when light initiates a reaction between polymer chains through the excitation of a reactive functional group, often in the presence of a photointiator (PI)[12]. Some photosensitive polymers are able to rapidly

photocrosslink from a liquid to a solid in the presence of ultra-violet (UV) light, a process known as UV curing. The speed of this crosslinking has led UV curing to be used in many applications including coatings, adhesives, printing inks for 3D printing and stereolithography purposes[12]. Because of technological and computing advances, UV curing techniques are now used to create rapidly producible, high-resolution 3D structures through stereolithography techniques.

9. Glycerol

Glycerol ($C_3H_8O_3$) is a common alcohol with three hydroxyl groups (Glycerol ≥99%, Sigma-Aldrich, UK). The compound was first identified by Carl W Scheele in 1779. The glycerol backbone is found in all lipids known as triglycerides. At room temperature glycerol is a viscous liquid, which is non-toxic and colourless. The etymology of the word glycerol is derived from the greek "*glykys*", meaning sweet and the sweet tasting glycerol is often used in the food industry as a sweetener[13]. The versatile organic compound has distinctive properties, including its hygroscopic nature, leading to over a thousand further applications of the compound, including personal care products, toiletries, cosmetics and pharmaceuticals[14]. The three hydroxyl groups contained in glycerol are hydrophilic in nature and are responsible for the hygroscopic nature (ability to draw water molecules from environment.)

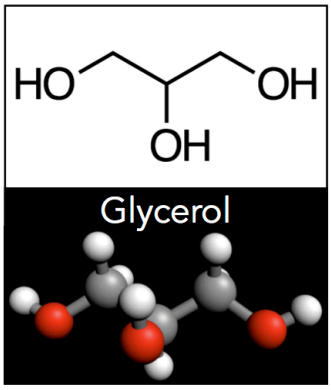

Figure 1: Chemical diagram of glycerol, (Chemdraw, PerkinElmer, US)

10. Sebacic acid

Sebacic acid ($C_{10}H_{18}O_4$) is a dicarboxylic acid (Purity 99%, Sigma-Aldrich, UK), consisting of eight backbone carbons capped with two carboxylic acid groups (COOH). At room temperature the compound appears as white flakes or powdered crystals. The etymology of the word sebacic is derived from the latin "sebaceous", meaning tallow candle, this is used as sebacic acid derivatives are used in the production of candles. Other applications of sebacic acid derivatives include plasticizers, lubricants, hydraulic fluids and cosmetics[15]. Sebacic acid has also been used in the synthesis of polymers such as polyesters, poly-urethanes, polyamides and more[16–18].

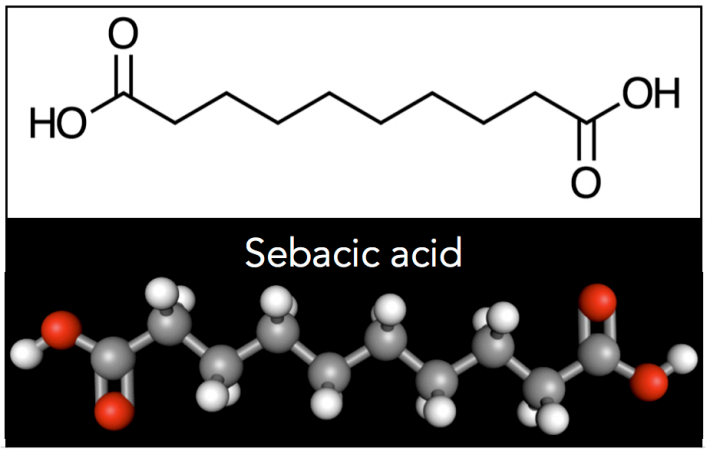

Figure 2: Chemical diagram of Sebacic acid

11. PGS – Poly(glycerol sebacate)

Initial research by Nagata *et al.* between the years 1996-1999 explored the use of glycerol and various dicarboxylic acids, including sebacic acid, for the synthesis of biodegradable polymers[19,20]. Sebacic acid based polymers were produced with a 2:3 ratio of glycerol to sebacic acid, completely crosslinking the polymer creating a stiff, rigid material, unfavourable for use in biomaterials. In the year 2002, Wang *et al.* built upon this initial work by Nagata *et al.* instead opting to use a 1:1 ratio of glycerol to sebacic acid. This

resulted in a polyester not completely crosslinked, with hydroxyl groups attached to the polymer backbone[18]. This polymer became known as poly(glycerol sebacate) (PGS.) The equimolar monomer ratio of PGS created a more flexible, softer material, ideal for a range of different biomaterial applications. All further PGS studies have focused on this 1:1 ratio of glycerol to sebacic acid. PGS synthesis creates a soft colourless material with many advantageous features. The monomers are inexpensive, the material is biodegradable through surface degradation, it has mechanical properties similar to that of the native tissue and Wang *et al.* found it to be biocompatible both *in vitro* and *in vivo*. PGS is a bioresorbable polymer, degradation products glycerol (essential for lipids) and sebacic acid (metabolic intermediate in fatty acids) are both metabolized within the body[21]. Also whilst PGS is not currently FDA approved, sebacic acid copolymers have been FDA approved, as shown in a study by Legnani *et al.*, whereby they use sebacic acid copolymers for drug delivery[22].

PGS has become a widely researched biomaterial. The extensively reported synthesis involves a two-step reaction. The first step involves the polycondensation reaction of glycerol and sebacic acid in an equimolar reaction. The second step is to thermally crosslink the prepolymer using high temperatures and vacuum, over several days. This secondary step highlights some of the known disadvantages of PGS; thermal curing can add expense, is time consuming and dramatically impedes the structuring capabilities of the polymer.

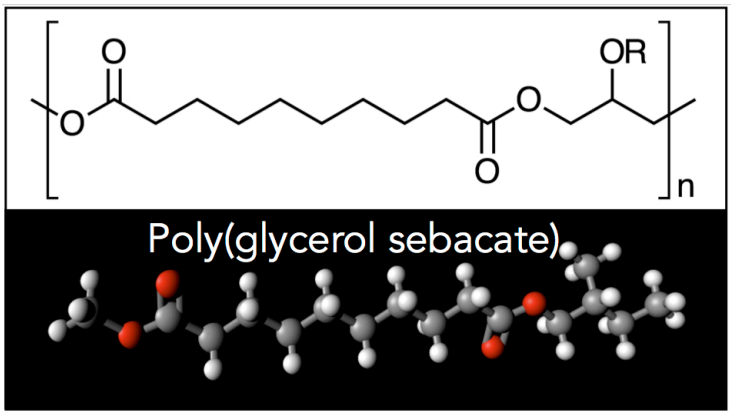

Figure 3: Chemical diagram of Poly(glycerol sebacate)

12. PGSa – Poly(glycerol sebacate acrylate)

The need for high temperatures, vacuum and the time taken at this secondary step can make the use of PGS unfavourable, particularly regarding the structurability of PGS. This was however addressed when Nijst *et al.* [23] chemically modified the PGS prepolymer by introducing acrylate moieties, thus creating PGSa (poly (glycerol sebacate acrylate)). The introduction of these acrylate moieties made curing the polymer via ultra violet radiation possible (for photocrosslinking see page 6). This eradicated the need for high temperatures, vacuum and was cured in a matter of seconds. Also by varying the levels of acrylate moieties introduced to the prepolymer Nijst *et al.*. had some control over mechanical properties[23]. The method outlined by Nijst uses acryloyl chloride to introduce the acrylate moieties, acryloyl chloride is acutely toxic and can be fatal via inhalation. The chemical can also be prone to spontaneous reactions/polymerization, therefore the chemical requires delicate care.

13. Porous PGS

Porosity can be very important in tissue-engineered scaffolds. It can be used to create sites for cell encapsulation and can be used to allow for nutrient exchange via diffusion.

There is currently limited research on the use of porous PGS scaffolds as biomaterials. One of the major factors limiting the development of research in this area, is the structural strength of the polymer to withstand being made into a porous network, with soft porous polymer networks known to be susceptible to collapse[24]. There have been a few examples of porous PGS scaffolds in literature; these were produced by either particle leaching[25,26], lyophilization[27,28] or glycerol leaching[24]. These leaching and freeze drying techniques often used PGS mixed with other polymers, or PGSa, to increase the scaffolds structural stability. These porous scaffolds often lacked definition of the pores and had limited controllability over pore size.

14. Applications of PGS

PGS is a versatile biomaterial with similar mechanical properties to soft tissues, this has lead to many uses in tissue engineering research. The use of PGS in tissue engineering has been explored for many different applications including its uses in; cardiovascular applications including cardiac patches[29,30], blood vessels[31], micro fluidics[32], tympanic perforations[33], drug delivery[22], retinal transplantation[34], neural repair[35] and many more. Much of the current research has focused around simple PGS scaffolds, either 2-dimensional, or simple 3-dimensional scaffolds casted of PGS. This is largely due to the secondary thermal curing step impeding the structurability of the polymer.

Applications of PGS related to individual research chapters can be found in the introductions within the relevant chapters (3.1-3.7). The below sections provide some background information on uses of PGS in tissue engineering. One study, by Georfe Engelmayr *et al.*, explored the use of PGS as a scaffold for cardiac tissue engineering[36]. The study microablated sheets of PGS into a

honeycomb structures to be used for neonatal rat heart cell seeding and the development of cardiac grafts. Results showed that the polymer and honeycomb structure was able to overcome some of the scaffold mechanical limitations previously observed and allowed for the formation of aligned, electrically excitable heart cells. This research is very promising and highlights the usefulness of the soft elastic PGS however, due to the synthesis method of ablation, the scaffold designs were limited in their complexity and 3D depth.

Wang *et al.* explored the use of PGS as part of a dual polymer scaffold for the production of a cell free synthetic neo artery graft[37]. Synthetic grafts were produced using a porous salt leached PGS inner core and an electrospun polycaprolactone (PCL) outer wall, with the PCL providing stability to the scaffold. Results shows the scaffolds degraded rapidly and 3 months after surgery, were able to yield neo-arteries that resembled the native blood vessels. This study however was performed using a small animal model (rat) and results from larger animal model studies are still pending.

Chronic ear infections are often treated surgically via drainage with tympanostomy drainage tubes. These tubes perforate the tympanic membrane and often following removal of the tubes the membrane struggles to restore/close the holes created. Decellularised tissues and alginate materials have been shown to speed the closure of the perforations when implanted surgically, however, the restored tympanic membrane tissue lacks the native architecture. PGS plugs have been developed, by Masiakos PT *et al.*, to be implanted surgically in order to enhance the speed of closure of tympanic membrane perforations[33]. Six weeks after surgical implantation of PGS scaffolds within the tympanic membrane perforations of a chinchilla,

results showed that more than 90% of perforations had closed. However after 16 weeks following surgery the scaffold had unfavorably remained and future studies would focus on speeding the degradation rates of the PGS scaffolds.

Across the world retinal degeneration exists as a pressing problem. Stem cell and retinal progenitor therapies have, however, been shown to help slow and reverse the degeneration. Cells within these therapies are often injected intravitreously towards the affected area of the retina. To ensure cells efficiently reach the affected area of the retina in a localized manner, polymer scaffolds are often used. PGS was explored, by Redenti *et al.* as a scrollable and injectable polymer scaffold[38]. *In vivo* studies performed using mice, show that retinal progenitor cells survived long term and expressed mature markers, suggesting the potential use of PGS in advancing retinal tissue engineering therapy techniques. This study shows a great deal of promise, but we still await the outcomes from larger animal model studies.

15. Project aims and objectives

The overall aim of this project was to develop PGSm, a novel methacrylated photocurable formulation of the well-known biomaterial PGS and to explore some of the potential uses in soft tissue engineering, with a focus on peripheral nerve repair. Below is a breakdown of the overall aims:

i. *To synthesise the PGSm polymer, characterize it chemically, mechanically and assess its photosensitive capabilities*

ii. *Modify PGSm to create porous polymer polyHIPE scaffolds, ideal for tissue engineering*

iii. *Assess PGSm for its capabilities in peripheral nerve repair, testing the biomaterial in vitro, ex vivo and in vivo*

iv. *Create porous PGSm nerve guidance conduits using reproducible techniques and asses for peripheral nerve repair*

v. *Analyse porous PGSm polyHIPE microparticles for use as a biomaterial for cartilage repair*

vi. *Explore the potential of PGSm scaffolds as a neuronal model*

vii. *Explore the material capabilities as embryonic stem cell scaffolds*

2. METHODS

The below Materials and Methods section covers the general methods and techniques used throughout the PhD. Methods relating to specific Chapters (3.1-3.7) are found therein.

1. Scaffold preparation and production

1.1 - Functionalization of glass cover slips

Glass cover slips were used as a substrate to photocrosslink PGSm onto for 3D printed stamps and for cell culture purposes, allowing for easier handling of scaffolds and ensuring PGSm disks to sink to the bottom of well plates filled with medium. Functionalization of the glass coverslips was performed using 3-(trimethoxysilyl) propyl methacrylate (MAPTMS, Sigma-Aldrich), 10wt% in tolurene (C_7H_8, Sigma-Aldrich); this allowed PGSm to better adhere to the glass. Glass cover slips were first introduced to piranha solution (80:20 sulfuric acid, hydrogen peroxide, Sigma-Aldrich) for an hour to clean the surface and expose the hydroxyl groups. They were then placed into a solution of MAPTMS for a minimum of 24 hrs, and washed before use.

1.2 - PDMS mould production

A 1:10 ratio of Silicon Elastomer curing agent (Sylgard) to Silicon Elastomer (Sylgard) was vigorously mixed; the resulting solution was centrifuged at 10,000 RPM to remove the air trapped within the polydimethylsiloxane (PDMS). The liquid PDMS was poured, carefully to not create air bubbles, over a flat glass surface and cured at 80°C, for 2 hours. The PDMS was then cut/punched into the moulds required.

1.3 - PGSm flat disk production

Flat PGSm disks were crosslinked using PDMS, (a low surface energy low fouling silicone polymer). Once the PDMS was cured, circular sections were punched out. The circular sections were 20 mm in diameter, slightly larger than the 13mm glass coverslips. A drop of polymer (15-30 μL) with 2wt% photointitator (2-hydroxy-2-methylpropiophenone, Sigma) was then added to a functionalized 13 mm glass coverslip. The flat bottomed, PDMS circle is then gently placed on top, allowing the drop of polymer to spread across the surface of the coverslip evenly. The coverslip-polymer-PDMS construct is then placed underneath a UV lamp and cured. Once the polymer is cured the PDMS circle is peeled off and the flat surfaced PGSm disk remains adhered to the coverslip. The PDMS circle was reused several times.

2. Printed 3D scaffold production

2.1 - Direct write UV printing

Direct write UV printing utilizes a liquid polymer well on a moving translation stage with a focused laser beam scanning across the surface of the polymer, crosslinking the polymer into computer designed structures. Models were written in g-code and input into the Aerotech software. The direct write setup was designed in-house. A well was made by punching a hole into several layers of adhesive tape and attaching it to a microscope slide. The well was filled with PGSm and placed onto the Aerotech high-precision xyz translational stage. UV light was focused from a passively Q-switched DPSS microchip laser (Alphalas), it was collimated and focused through a Gaussian lens setup and onto the liquid polymer well.

2.2 - 2-photon polymerization

Polyethylene glycol diacrylate (PEGda 700 M_w) was used for 2-photon polymerization as this polymer has been well characterized with this technique. The initial PEGda template structure was cured by 2-photon polymerization using an in-house designed setup. A glass slide containing a 10 mm diameter hole, with a glass coverslip (13 mm diameter) adhered to the base by adhesive tape, was used to create a well for the photocurable prepolymer PEGda. This was then placed upon an Aerotech xyz translation stage (Aerotech), capable of 100 nm accuracy. The translation stage was able to move the polymer well relative to the focal point of a 20x objective. A laser (ALPHALAS gmbh, Germany) provided a pulsed light through the 20x objective lens, to cure a voxel at the focal point within the well, as the translational stage moved a 3D structure was printed. The laser set up and lenses used are described in figure 4. The Aerotech stage was controlled using the default computer programme N-view, this was useful for homing the device to default positions and moving it using simple commands. For the patterning of the scaffold template, SCA software was used. The SCA software was able to define parameters and sketch out 3D images with adequate spacing, and fill density relative to the objective. STL files of the scaffold were input into the software and it was possible to slice the 3D image into patternable slices. The scaffolds were sliced into 5 layers. The PEG template was then printed into the boundary between the prepolymer and the glass, this ensured firm attachment of the first layer of the polymer to the glass coverslip. Scaffolds took between 7-10 hours to print, approximately 2 hours per layer with 2 μm hatching (filling of solid space between lines). Print times were dependent upon the intricacy of the structure.

A Q-switched diode pumped solid state 532 nm laser was used (P-1064 from ALPHALAS Gmbh); this had a maximum peak power of 1 MW and sub nanosecond pulses. An external second harmonic generation (SHG) unit was used by the laser to modify the beam to a 532 nm wavelength, from the 1064 nm source. A shutter was used to control the emission of the beam. A series of lenses were used to expand the laser beam, focus the beam, remove the unwanted 1064 nm wavelengths still emitted and pass through a neutral density filter.

Figure 4: 2 photon polymerization laser set up. Labels describing lenses and components are available in Table 1

Label in Figure 5	Device	Description
A	Laser	P1064, Alphalas gmbh, Germany
B	Shutter	LS6ZM, Uniblitz Electronics
C	Piano Concave Lens	LC4 252 25.4mm F=-30, Thor Labs
D	Hot mirror	FM01 Thor Labs, Germany
E	Focusing lens	LA4236, F=125, UV fused silica,
F	Neutral density filter	Attenuator, Throats, Germany

Table 1: Lenses/components used in Figure 2, the 2 photon polymerization laser setup

2.3 – Stereolithography

Scaffolds were produced by microsterolitography using PGSm (2wt% photointitator, 2-hydroxy-2-methylpropiophenone, Sigma-Aldrich, UK). A 405 nm laser (Vortran Stradus 405 nm) was directed through a series of lenses, focusing and collimating the beam onto a DMD (digital micromirror device), (DLP7000, Texas instruments). A computer-designed image was uploaded to the DMD, (Software ALP-4.1, basic Controller Suite). A cross sectional tube image was reflected off the DMD onto a mirror and down onto the liquid PGSm polymer. PGSm was cured at the surface, crosslinking and hardening into the cross-sectional tube design. The Z-stage (Thorlabs), was slowly lowered into the liquid polymer (0.3 mm/s), allowing the cross-linked material to lower and be replaced with unpolymerised PGSm on top, which in turn was polymerised, creating a 3D printed structure. Once the desired height was reached the structure was carefully removed from the Z-stage and placed in methanol to allow any uncured polymer to be washed away.

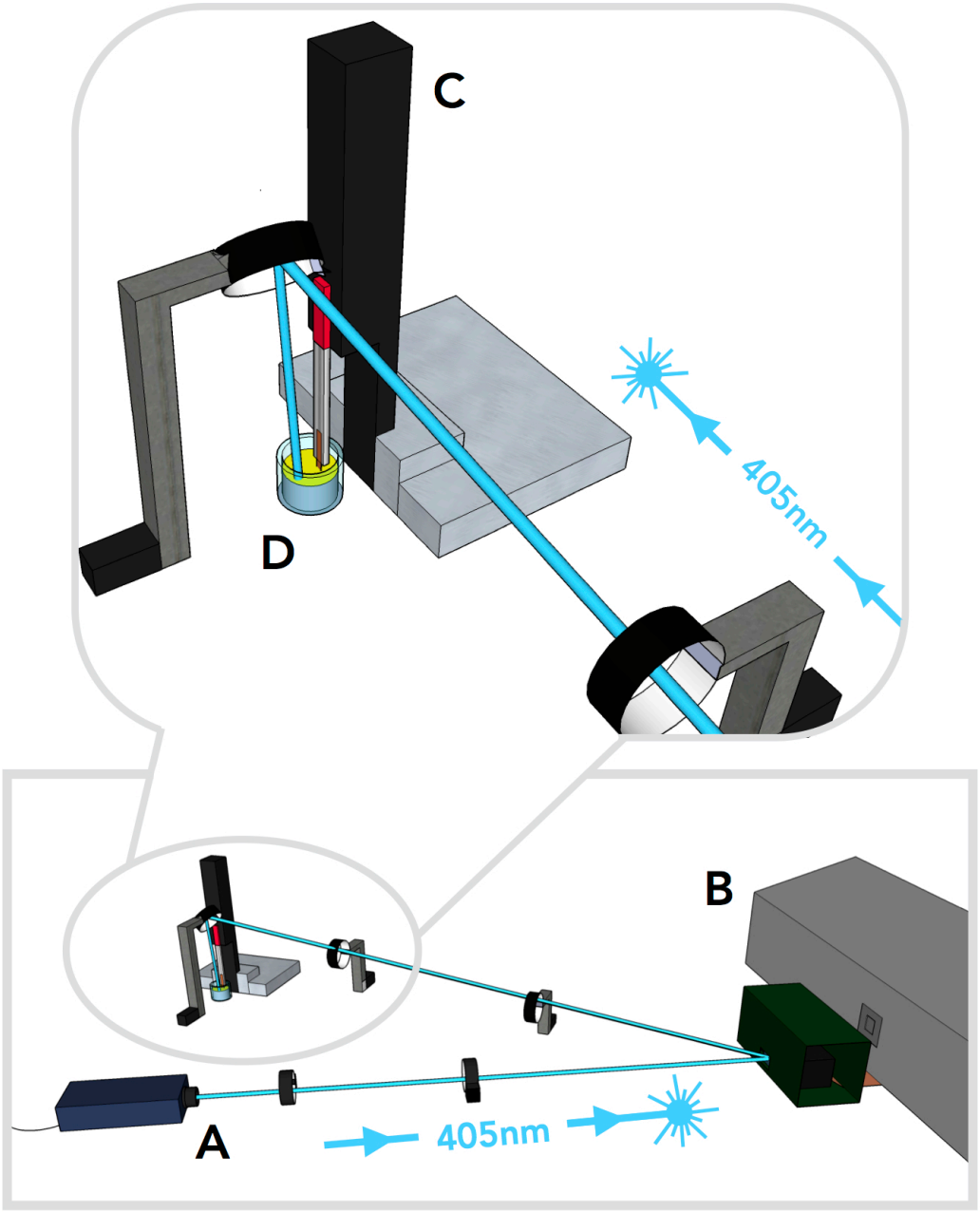

Figure 5: Computer designed model (Google Sketchup) of the micro stereolithography setup used to produce nerve guidance conduits (NGC's). A 405nm laser (A) emits light through a series of lenses focusing the beam onto the surface of a digital micromirror device (DMD) (B), the DMD reflects a computer designed image down onto the surface of a motorized Z-stage (C), which lowers into a container of liquid polymer (D). As the UV light hits the surface of the polymer a Z-stage lowers, carrying the crosslinked polymer down and fresh uncrosslinked PGSm onto the surface. As the stage is lowered, the polymer crosslinks and 3D structures are formed.

3. Cell Culture

3.1 - Sample sterilization for cell culture

All sterilization techniques were performed in sterile conditions within a class-II biological safety cabinet. Polymer scaffolds and glass coverslip controls were sterilized prior to cell seeding (TCP is sterile packaged). Scaffolds and coverslips were submerged in 70% ethanol for up to 7 days, with fresh ethanol supplied every day. After ethanol sterilization the scaffolds and coverslips were washed three times, in PBS, for a minimum period of fifteen minutes each time. Scaffolds were then introduced to a medium wash prior to cell seeding experiments.

3.2 - Cell culture - freezing and thawing

All cell culture techniques were performed in sterile conditions within a class-II biological safety cabinet. Cell techniques may differ slightly for individual cell lines/cells (see individual chapters 3.1-3.7). Cells were either stored in liquid nitrogen or were used from primary animals. Cells stored in liquid nitrogen were frozen at a restricted rate of 1°C per minute (Mr. Frosty, Thermofisher), in fetal calf serum (FCS) containing dimethyl sulfoxide (DMSO, 10%). Cells stored in liquid nitrogen were thawed by immediately being warmed to 37°C. The cells were then introduced to cell specific medium and centrifuged at approximately 200 g for 5 minutes. A cell pellet was visible and the supernatant above was removed. The cell pellet was then resuspended in fresh medium and transferred to a tissue culture dish (T75), 10 mL of medium was added and the T75 was incubated at 37°C in 5% CO_2.

The centrifugation step allows for the removal of DMSO which can be harmful to cells during culture, however it is added prior to freezing to limit the likelihood of ice crystal formation which could damage cells.

3.3 - Cell passage

Cells were generally passaged when nearing full confluency of the culture dish, around 70-80% confluency.

Cell passage techniques are often specific to individual cells. Generally medium was removed from cell culture dishes and three PBS washes performed gently across cells. A trypsin-EDTA (Sigma) solution was then added (5 mL in a T75) to detatch cells from the surface. The solution was left for a short period of time, often 5 minutes, however dependent on the cells used; or until detachment was visible under a light microscope. Once detached the cell solution was mixed with an equal amount of cell medium to inhibit the trypsin and the sample was transferred to a centrifuge tube. The solution was centrifuged at approximately 200 g for 5 minutes, the resultant cell pellet remained at the bottom and the supernatant removed. The cell pellet was resuspended in fresh medium and split into the required number for passage (often 4), this allows for more space for the cells to grow. The split of cell suspension was then added to a fresh T75, 10 mL of medium added and incubated at 37°C with 5% CO_2.

Some cells require a more gentle technique to detach from the culture dish and some require more forceful techniques. Trypsin is known to proteolytically damage cells and although it is used for a minimum period of time, there are other detachment methods that can be adopted. Other gentle detachment solutions are available and mechanical passaging can also be effective. Mechanical passaging can be done by gently tapping the culture dish repeatedly on the side, instead of using trypsin-EDTA solution, this disturbs the attachment of cells leading to their detachment. This method of mechanical passaging can be useful, however it can also leave cells in clusters

rather than a single cell solution. Cells can also be detached from the surface using a cell scraper, this can be particularly useful in strongly adherent cells and in creating sheets of cells. Mechanical passaging was performed when passaging neuronal (NG108-15) cells, however trypsin was used prior to experimentation to allow for a better single cell suspension. Cell scrapers were explored for use with stem cells and allowed for cell sheets to be removed, however EDTA solutions were used to enable single cell suspensions.

3.4 - Cell counting

Cells were counted using a Neubauer haemocytometer. The haemocytometer and the coverslip were cleaned with 70% IMS and air-dried. The cover slip was slightly moistened and placed on top of the haemocytometer, the moisture allowed it to attach to the haemocytometer via suction. When the haemocytometer is raised up to the light Newton Rings should be visible, indicating that the coverslip was successfully attached to the haemocytometer. Newton rings are an interference pattern caused by the reflection of light between two surfaces, like a rainbow ring. Cells were resuspended in a small amount of medium (often 1 mL). 15 µL of cell suspension was then transferred to the haemocytometer. The tip of the pipette was placed at the edge of the coverslip, between the coverslip and the haemocytometer; and the cell suspension was allowed to run underneath the coverslip. This was repeated for the opposite side of the haemocytometer also. The haemocytometer was then placed under the microscope and cells were counted within the centre square on the grid. Cells, which lay on the top and left borders were included and cells on the bottom and right borders excluded. The mean average of cells counted was taken from both sides of the haemocytometer and the number multiplied by 10^4 to estimate the total number of cells per mL.

3.5 - MTT assay

Scaffolds and coverslips were prepared by removing all medium from wells and gently washing samples three times. An MTT solution (3-(4,5-dimethyiazol- 2-yl)-2,5-diphenyl tetrazolium bromide, yellow tetrazole, 0.5 mg/mL in PBS) was added to the wells and the well plate was placed in the incubator at 37°C for 40minutes. The MTT solution was then removed from the wells and 600 µL cellusolve solution (2-ethoxy ethanol) was added to each well. Three 200 µL samples of this solution in each well was then transferred to a 96 well plate. The 96 well plate was placed into a plate reader that reads the optical density of the samples. The plate reader (Bio-Tek ELx800) was set at wavelengths of 540nm and referenced at 630nm.

3.6 - Alamar blue

Alamar blue/Reazurin is blue coloured, which when reduced turns into the fluorescent red resofurin. A stock solution of Alamar blue was made for all experiments from 12.6 mg of resazurin dissolved in 50 mL of PBS. Medium was removed from the cell culture well and replaced with Alamar blue medium solution (1:10, alamar blue stock solution to cell medium.) The well plate returned to the incubator, after 4 hours 3x 200 µL samples were taken from each well and placed into a 96 well plate. The well plate was read using either an absorbance plate reader or a fluorescent plate reader ($\lambda_{Ex}/\lambda_{Em}$, 560 nm/590 nm). Fresh medium is added to the well plate of cells and returned to the incubator.

3.7 - Immunohistochemistry and fixing

Cells scaffolds were washed in PBS 3 times. Extra time was taken for three-dimensional tissue or cell constructs to allow adequate rinsing (specific times stated in relevant chapters (3.1-3.7). The cells and/or cell scaffold constructs are then fixed in 10% formalin or 3.7% formaldehyde in PBS for 15 minutes,

porous scaffolds seeded with cells are fixed for 20 minutes per mm depth. If the fixation period was too long over crosslinking of antigens can occur, adversely affecting antibody binding. The samples were then washed twice in PBS. Immunocytochemistry buffer (ICC buffer, 1% bovine serum albumin, 0.1% Triton X-100 in PBS) buffer was then added to each well at room temperature for 20 minutes to both block and permeabilize the samples.

Blocking prevents non-specific antibody binding by introducing a non-specific protein (bovine serum albumin). Permeabilization (Triton X-100) allows penetration within the cell membrane and is required when internal cell components are being examined. Antibody binding for cell surface antigens does not require permeabilization. ICC buffer was removed and primary antibodies diluted in ICC buffer were added (for specific primary antibody concentrations please see the individual methods sections in the relevant chapters) and incubated at 4°C for 18 hours overnight (ideally), or at room temperature for 2 hours.

The primary antibody was removed and the samples washed twice in PBS. The secondary antibody (dissolved in ICC buffer) was then added for 2 hours at room temperature. The secondary antibody was removed and the samples washed (3x 5 mins in PBS). Samples were submerged in PBS, and imaged by confocal microscopy imaging using a water-dipping objective.

4. Imaging

4.1 - Confocal image acquisition

For all confocal image acquisition an upright Zeiss LSM 510 confocal microscope, with water/oil dipping lenses was used. Multi channel images

and z-stack images were taken; individual chapters discuss specific image acquisition techniques used in further detail.

4.2 – Scanning electron microscopy

Scaffolds were imaged using a Phillips Xl-20 SEM scanning electron microscope. The polymer scaffolds were dried and placed onto adhesive carbon pads. The pads were then adhered to a metal SEM stub for image acquisition. The stubs, pad and scaffold were gold coated to increase conductivity, allowing for optimum SEM conditions. The stub containing the gold-coated scaffold was then transferred to the SEM machine and imaged.

Scaffolds containing cells underwent a different preparation procedure drying technique. The cells were fixed in glutaraldehyde for ten minutes at room temperature. The samples were then washed in distilled water for 5 mins. The samples were then periodically washed in distilled water and ethanol solutions of ratios of 40:60, 30:70, 20:80, 10:90, 0:100, for 15 minutes each, to dehydrate the samples. After the final ethanol wash the samples were placed in a 1:1 solution of hexamethyldisilizane (HMDS) and ethanol and left and room temperature for an hour. After the hour the solution was removed and a final solution of pure HMDS was added. The samples were then left to air dry and are gold coated, attached to stubs and imaged.

4.3 - MicroCT

Samples to be analysed with Micro-CT were rinsed in PBS and fixed in glutaraldehyde as above. The samples were rinsed in PBS and underwent a second fix in an aqueous solution of 2% osmium tetroxide for 2 hours. The samples were then analysed using a Skyscan 1272 high resolution microCT.

3.1 PGSM SYNTHESIS AND CHARACTERIZATION

Aim: The aims of this chapter are to successfully synthesise the novel photocurable PGSm and to characterize it chemically, mechanically and via structuring of the polymer.

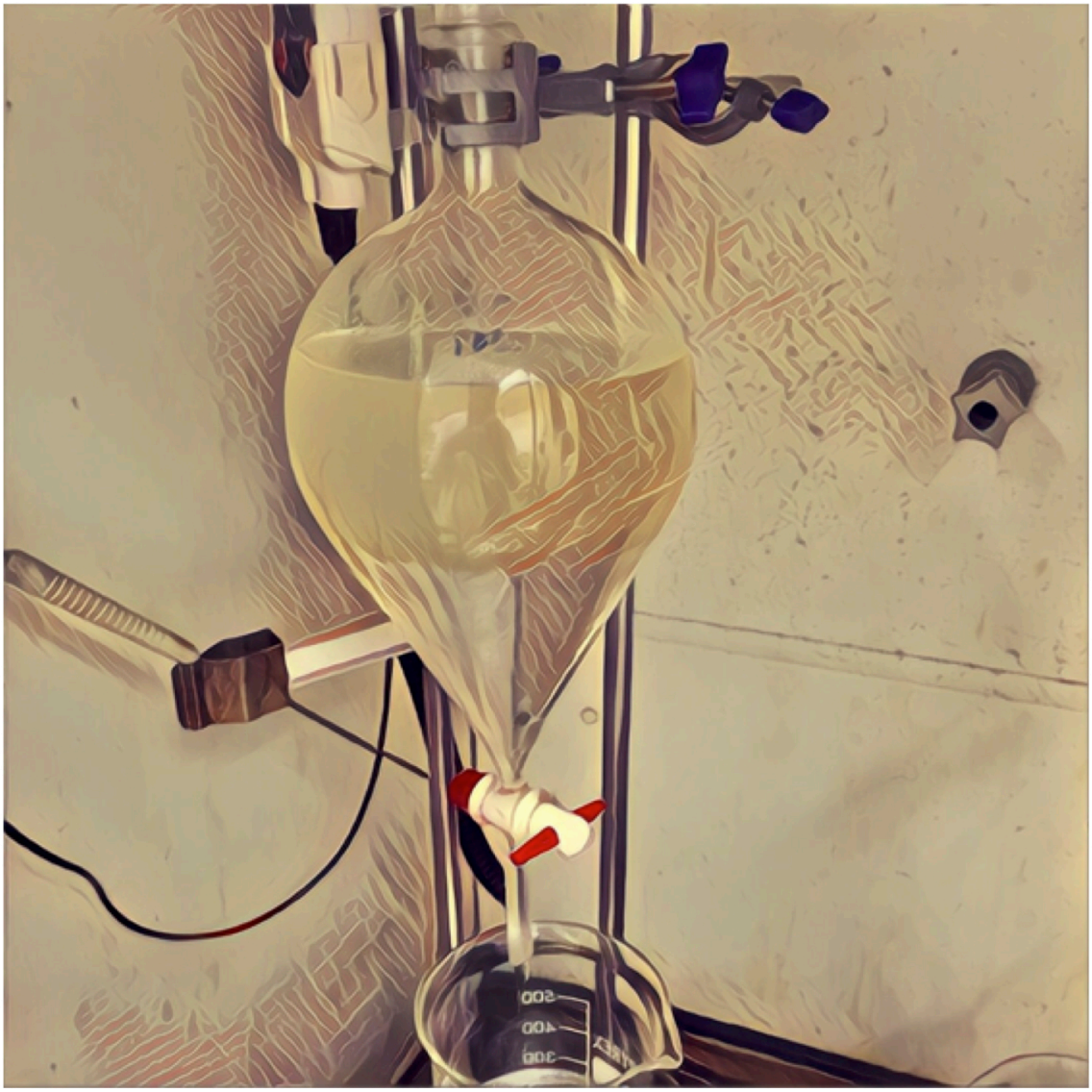

Solvent wash of PGSm. Image taken from Figure 10, page 35

1. Methods

1.1 PGS Prepolymer Synthesis

The synthesis of PGSm was divided into two steps: i) polycondensation (PGS prepolymer synthesis) and ii) methacrylation (PGS methacrylation). Methacrylate moieties were added using methacrylic anhydride to create a photocurable polymer. Triethylamine was used as a neutralising base for hydrochloric acid (HCL) production when used for PGSa synthesis, with acryloyl chloride (Nijst et al)[23]; it was used similarly here. All chemicals were purchased from Sigma-Aldrich (Poole, Dorset, U.K.) unless otherwise stated and reactions were performed inside a fume cupboard. PGS prepolymer synthesis is well described in literature[18]. Briefly, equimolar sebacic acid and glycerol was added to a 500 mL three neck round bottom flask (RBF) at 120 °C in a nitrogen environment for 24 h. The reaction vessel was then placed under vacuum for a further 24 h. After 48 h, completion of the polycondensation reaction was confirmed using ATR-FTIR.

1.2 PGS methacrylation

The RBF containing the PGS prepolymer was cooled to 0°C, dichloromethane (DCM) was added to dissolve the PGS prepolymer. Mono methyl ether of hydroquinone (MEHQ, 0.01 wt%) was added as a photoinhibitor to make the reaction less susceptible to spontaneous photopolymerization. PGS prepolymer contains 78 mMol of hydroxyl groups per 20 g (790 mMol in 202.56 g)[23]. Methacrylic anhydride was slowly added at different quantities (0.25-1.00 mol/mol of hydroxyl groups on PGS) to allow for a varied degree of methacrylation. Equimolar amounts of triethylamine (Sigma-Aldrich, UK) was added alongside the methacrylic anhydride. The prepolymer was allowed to return to room temperature and was left stirring for 24h. The prepolymer was

removed from the RBF and purified using methanol distillation and solvent washes. Methanol distillation involved dissolving the polymer in methanol at -80°C for the polymer to precipitate. The polymer was solvent washed in excess hydrochloric acid and ethyl acetate to remove impurities. The polymer was then dried using magnesium sulphate and the remaining solvents were removed using a rotary evaporator.

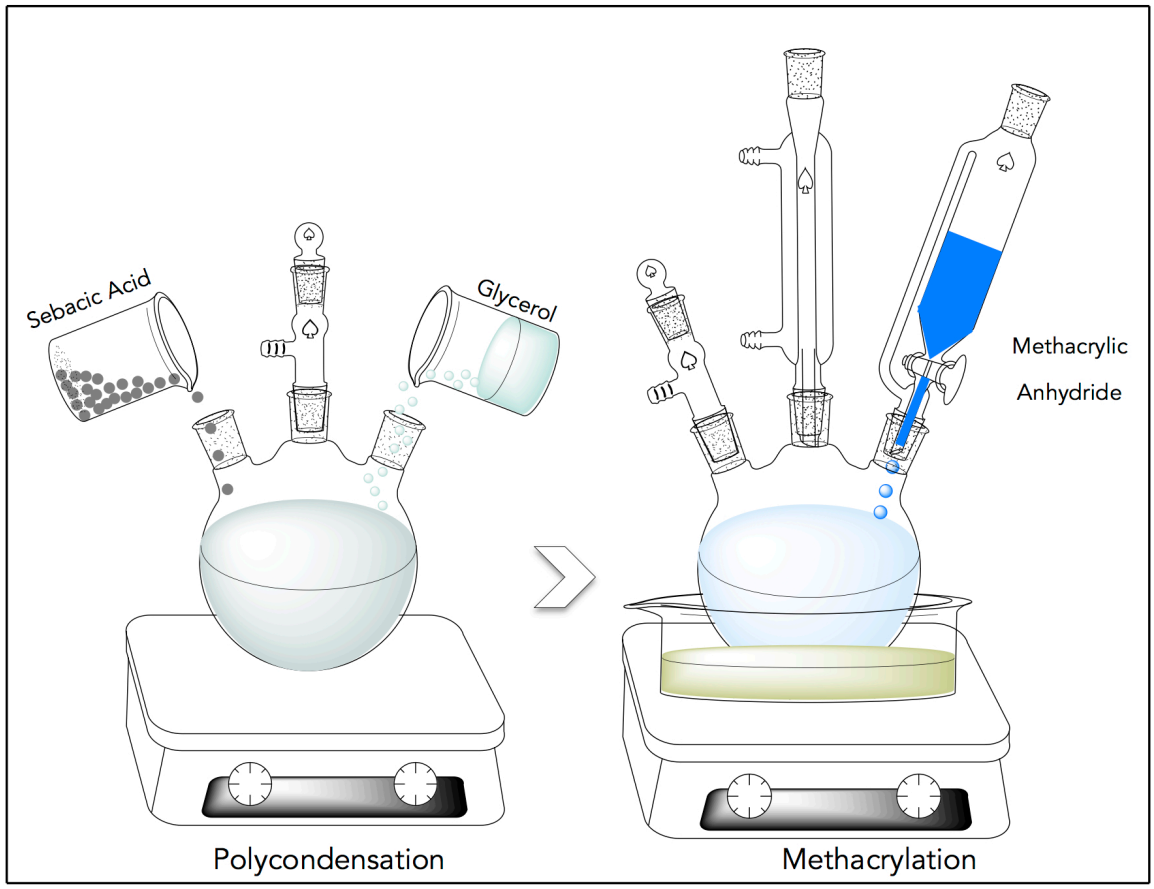

Figure 6: Diagram describing the PGS polycondensation and methacrylation steps. (Diagram drawn using ChemDraw)

1.3 FTIR-ATR

Traditional infa-red spectrometers transmit infa-red light through the body of a material analysing absorption, whereas the ATR-FTIR (attenuated total reflectance - fourier transform infa-red) analyses the change in the total internal reflectance of the infa-red beam caused by the polymer. During the polycondensation reaction attenuated total reflectance-Fourier Transform Infa

Red spectroscopy (ATR-FTIR) was performed on the prepolymer (Nicolet iS50 spectrophotometer, ThermoFisher Science). Spectra were obtained at intervals within the polycondensation reaction.

1.4 NMR

PGSm samples of different degrees of methacrylation were dissolved in deuterated chloroform ($CDCl_3$), filtered through glass fibre wool and 700µl added to a nuclear magnetic resonance (NMR) tube (Norell 507HP). Hydrogen atoms were replaced with deuterium in the deuterated chloroform, allowing for the accurate reading of the polymer in the H-NMR. The NMR tube was analysed by H-NMR 400MHz (AV-400, Bruker).

1.5 GPC

The purpose of the GPC was to analyse PGSm in order to understand the hydrodynamic volume, relative molecular weight and polydispersity index of the polymer (PDI). The polymer was dissolved in chloroform and gel permeation chromatography (GPC) performed (Viscotek GPCmax chromatograph with Waters 410 differential refractive index (DRI) detector); using tetrahydrofuran (THF), and Polymer Labs PLgel 5 µm mixed C columns. Both sets of columns consist of two columns measuring 300 mm x 7.5 mm, with a flow rate of 1 mL/min. The data was obtained and analysed using Polymer Labs, Cirrus software (Cirrus, Agilent).

1.6 Differential Scanning Calorimetry (DSC)

The polymer was cut into small sections (approximately 3 × 3 mm), weighed and placed in a titanium DSC pan. The pan was covered and pressed shut, sealing the polymer. Empty titanium pans were placed into two furnaces

individually. Baseline tests were performed and deducted from the polymer results. The pan containing the polymer was placed alongside an empty tray into individual furnaces and the DSC analysis (DSC6, Perkin Elmer) was performed between -70°C and 250°C using both single-cycle and dual-cycle methods.

1.7 Shape memory

A strip of PGSm was cured, shaped into a coil and cooled quickly below the glass transition (T_g) by being dropped into liquid nitrogen (-196°C). It was noted whether the material kept its structure and how long it took to return to its original structure when allowed to return to room temperature. The structure was photographed at regular intervals as it returned to room temperature.

1.8 Nanoindentation

A Hysitron triboscope TS70 nanoindenter, attached to a Veeco dimension 3100 AFM was used for nanoindentation studies. A matrix of 6 indentations was used, spaced 8μm apart (see below). A minimum of 3 indentation tests were undertaken and results averaged. The polymer sample was loaded for 5 seconds, held for 10 seconds, and unloaded for 5 seconds. The hold period was added to allow any affects from creep in the polymer to be minimized.

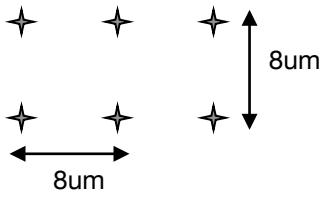

The equation below was used to calculate the Young's modulus of the polymer samples. The Oliver Pharr method was used to analyze each of the unloading segments of the polymer indentation. This provided a modulus value calculated from the unloading (reduced modulus E_r). The modulus value for the indenter was known. For mathematical modeling, polymer scaffolds

such as PGS are known to have approximate Poisons ratios between 0 - 0.5. A Poisons ratio of 0.25 (v) was chosen as an intermediary value for modeling[39].

$$\frac{1}{E_r} = \left(\frac{1 - v^2}{E_{sample}}\right) + \left(\frac{1 - v^2}{E_{indenter}}\right)$$

Equation 1: Equation used to calculate the reduced modulus of the material

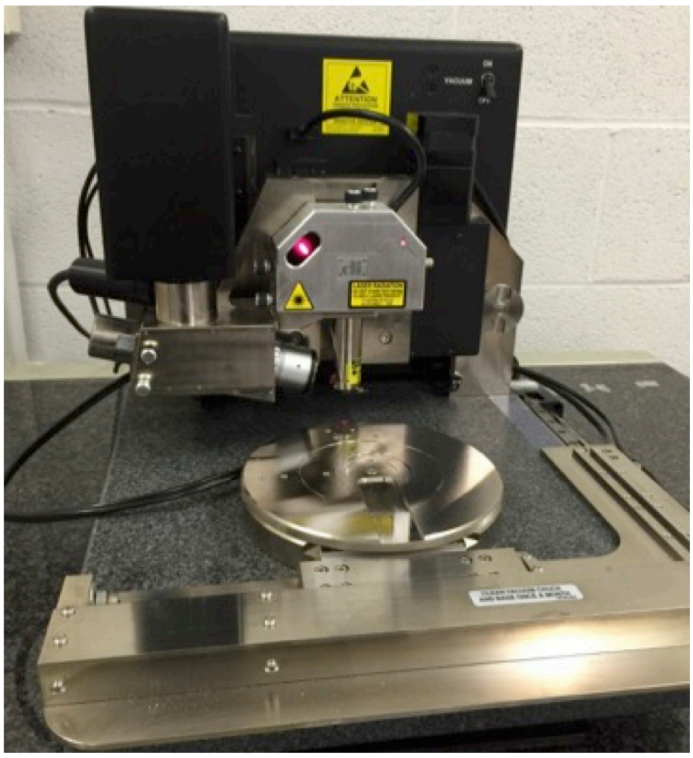

Figure 7: Digital photograph of Hysitron triboscope TS70 nanoindenter used for experimentation

1.9 Contact Angle – surface properties

Water contact angle measurements were taken with a goniometer to understand the physical surface properties of the different methacrylations of the polymer. A 3µL droplet of deionized water was placed onto a flat surface of PGSm of varying degrees of methacrylation. The goniometer lens incorporates gradations to enable the measurement of the contact angle

between the water droplet and the polymer surface accurately. A minimum of three sample replicates was taken.

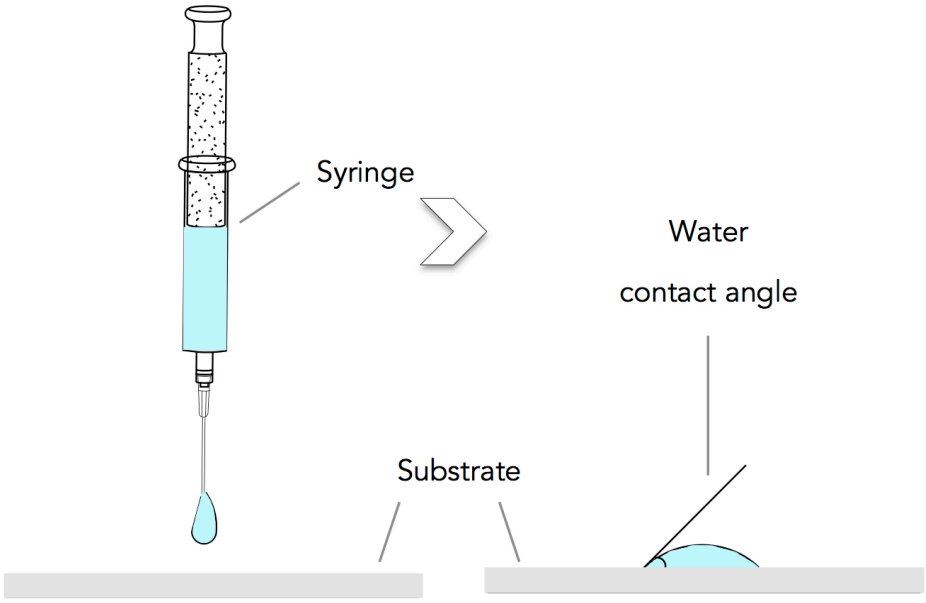

Figure 8: Computer designed image (ChemDraw) describing the water contact angle method.

1.10 Degradation

Initial degradation studies were performed on the polymer PGSm to determine whether the material would degrade outside the body. PGSm polymer samples were created 1 cm × 1 cm × 0.3 cm and placed in phosphate buffer saline (PBS) with a physiological pH of 7.4. The samples were either static, on a rocker or continuously stirred using a magnetic stirrer. All samples were kept at room temperature. Samples were weighed dry (before being placed in PBS), weighed whilst wet at several intervals (excess water shaken) and dried at the end of the experiment and weighed again. The experiment ran for 40 days.

1.11 Enzymatic degradation

PGS degradation rates are reported to be unaffected by changes in pH[40]. Therefore enzymatic degradation studies were performed in PBS with a physiological pH of 7.4.

Enzymatic degradation studies were performed in PBS with a physiological pH. PGSm disks of varying degrees of methacrylation were prepared with a diameter of 11 mm and a depth of 1 mm. The disks were placed in a 6-well plate. Lipase from *Thermomyces lanuginosus* (100,000 U/g Sigma-Aldrich, UK) at a concentration of 2000 U/mL in PBS was added to each well. The well plate was placed on an orbital shaker and incubated at 37°C for the duration of the experiment (72 h). The PGSm disks were weighed before the lipase solution was added, at regular intervals throughout the experiment with excess solution shaken off and at the end of the experiment once dry. The size of the samples, and the change in weight over three days was used to calculate the rate of degradation of the PGSm disks.

1.12 PGSm optical properties

Part of the characterization process for PGSm involved researching the optical properties of the polymer, optical properties weren't a requirement of any of the projects worked on in this thesis, but may be useful for further projects. PGSm (0.75 methacrylation) when fully crosslinked became a transparent polymer. A 200 µL drop of PGSm was placed onto a PDMS surface, treated with hydrophobic silanizing agent. The droplet remained on the surface with a visibly high contact angle to the PDMS (expected with a hydrophobic surface), the PGSm was then fully crosslinked under a UV lamp. Once cured the PGSm droplet was removed and placed onto a glass microscope slide, here it was used as a magnifying lens. The glass slide/lens setup was attached to an

iPhone 6 plus using adhesive tape and images taken of a neubauer hemocytometer with and without the PGSm lens.

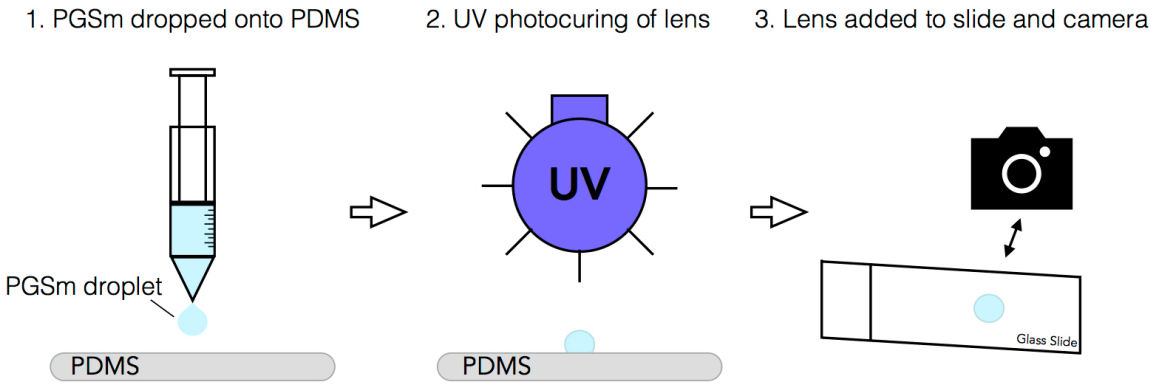

Figure 9: Diagram showing a PGSm droplet being placed on PDMS (1), being UV photocured (2) and being removed, placed onto a glass slide and attached to a camera (3). Iphone 6 plus camera used for experimentation (Keynote, Apple).

1.13 PGSm patterned scaffolds

To confirm PGSm had photocurable capabilities it was structured into patterned scaffolds. Direct write UV patterning (see methods page 15) was used to produce printed PGSm scaffolds. Designs were sketched and then converted manually into g-code and input into the Aerotech software. This enabled the translational stage to move, and when working alongside the shutter, allowed for the polymer to be cured according to the coded design. The design was cured in PGSm onto functionalized glass coverslips/microscope slides, creating patterned scaffolds.

2. Results

PGSm was synthesised and methodologies adapted to ensure reproducible PGSm synthesis. Prior to photocuring, the polymer was a viscous liquid with a consistency similar to honey. PGSm was almost colourless, transparent, with just a small yellow hue. The figure below shows digital images of the polycondensation of PGS, the methacrylation of PGSm, the solvent washing of the final polymer and a skeletal chemical diagram of the polymer synthesis (Fig 10).

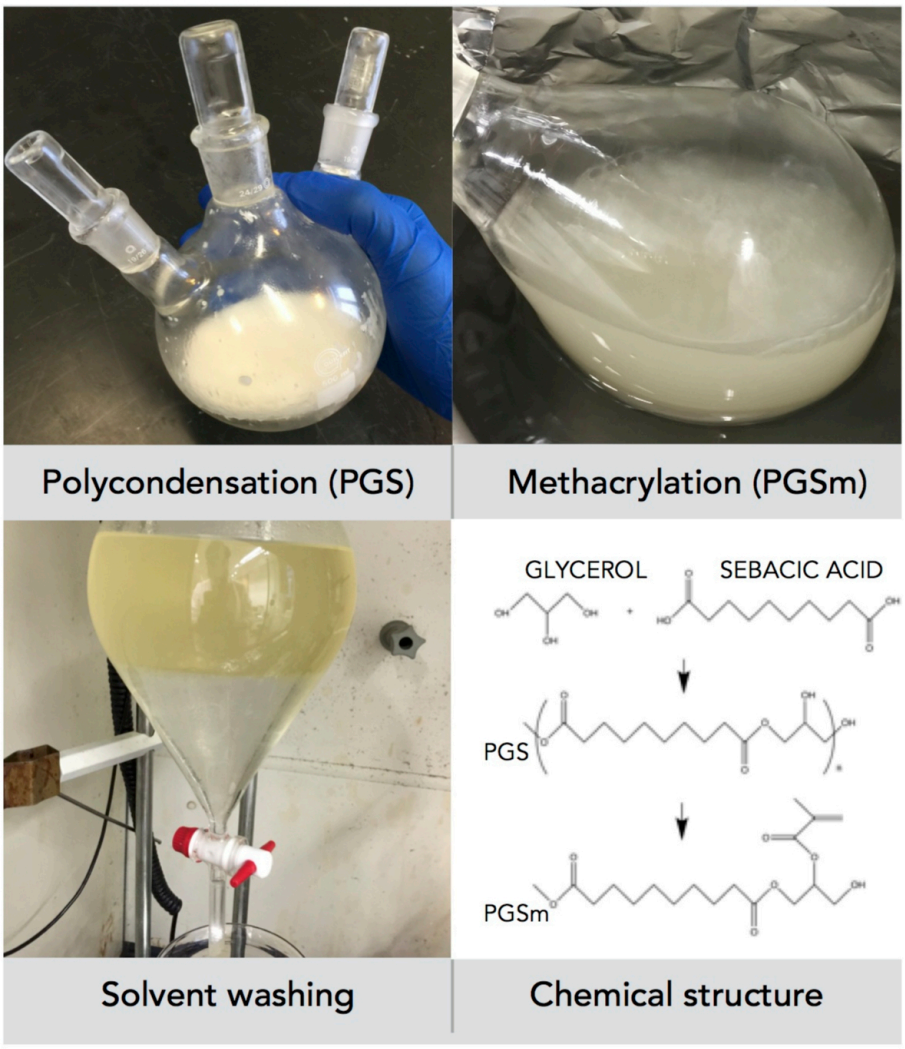

Figure 10: Diagram showing the polycondensation of PGS, methacrylation and solvent evaporation in rotary evaporator, solvent wash and a chemical synthesis diagram

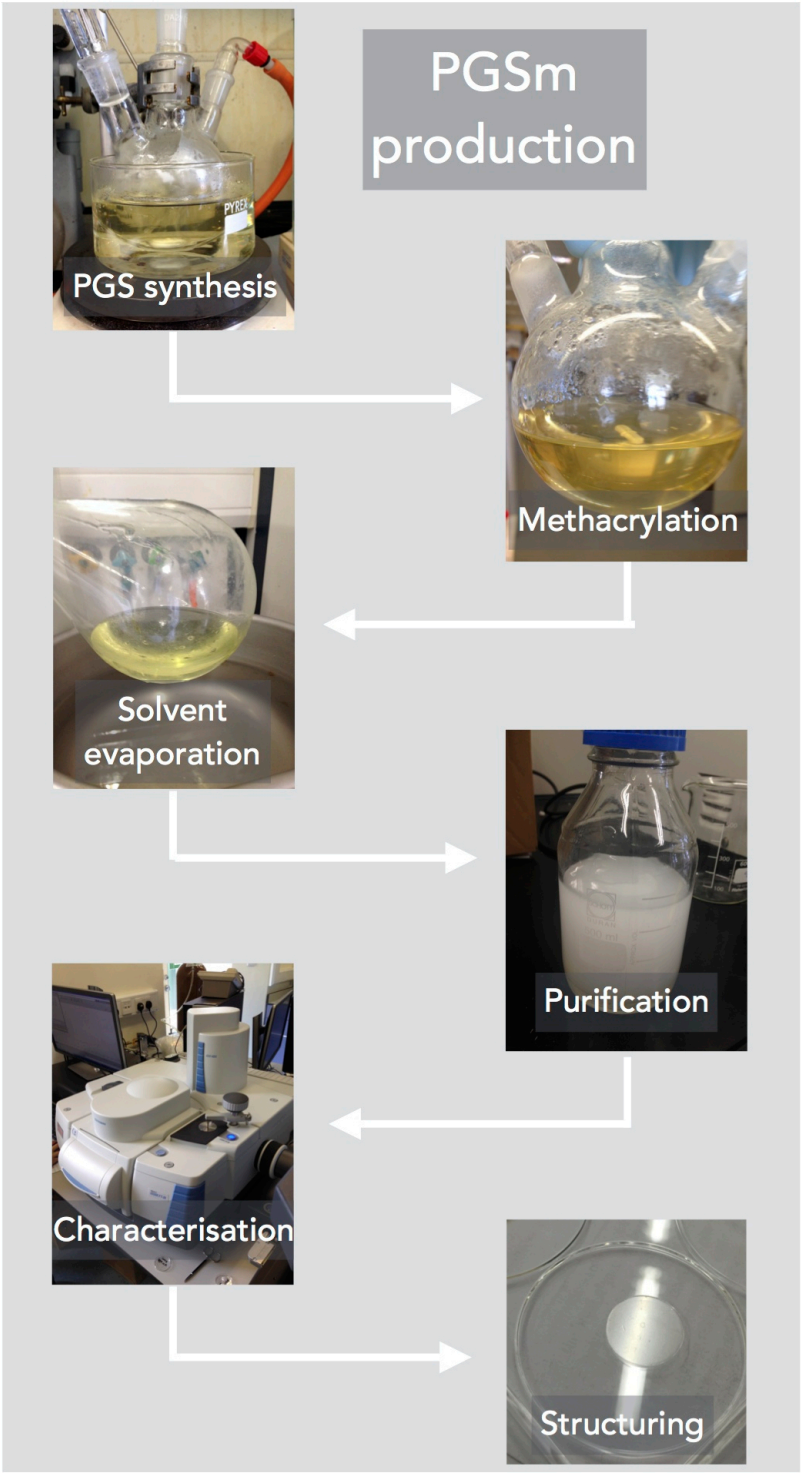

Figure 11: Diagram showing synthesis methods of PGSm. Showing the synthesis of PGSm, methacrylation in RBF, solvent evaporation, methanol purification, chemical and mechanical characterisation (FTIR image) and structuring into the solid PGSm.

ATR-FTIR spectra from 24 h, 44 h and 48 h of the polycondensation reaction showed a peak shift from 1693 cm^{-1} to 1733 cm^{-1}. FTIR analysis confirmed the polycondensation reaction and the formation of the polymer. From the spectra it was clear that there was a significant change to the 24 h spectrum versus that of the 44/48 h spectra. The 44/48 h spectra showed a lower hydroxyl stretch at 3470 cm^{-1}, an ester peak at 1740 cm^{-1} and a carbonyl to ester peak shift from 1693 cm^{-1} to 1733 cm^{-1} between the 24 h and the 44 h or 48 h spectra. These were signs of ester formation and confirmation of the PGS prepolymer synthesis.

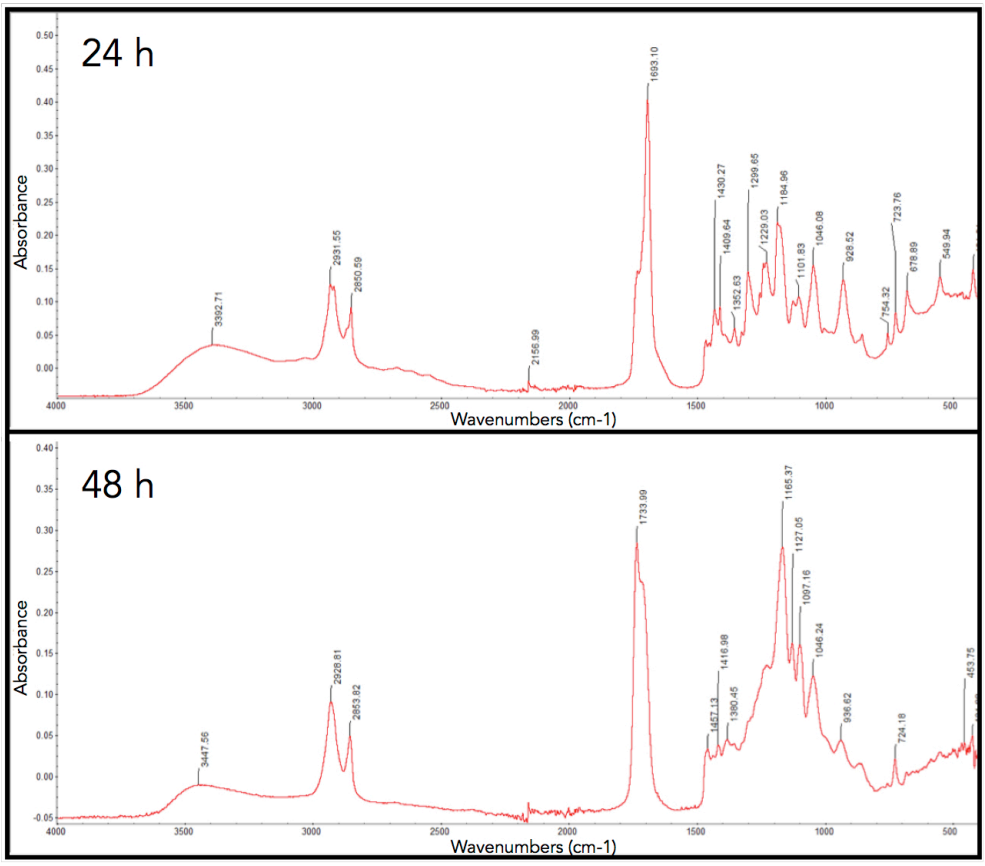

Figure 12: Example FTIR-ATR (Nicolet iS50 spectophotometer) spectra results, obtained during PGS polycondensation at times 24 h & 48 h. Results show shifts from carbonyl to ester peaks (1693 cm^{-1} to 1733 cm^{-1}) confirming polycondensation.

GPC results showed M_n = 1361 g/mol, M_w=3609 g/mol and a dispersity index of 2.65. Nuclear magnetic resonance was used to analyse the polymer ^{1}H NMR (400 MHz, $CDCl_3$). Chemical shifts were referenced relative to $CDCl_3$ peak at 7.27 ppm. The chemical composition was confirmed of sebacic acid $-COCH_2CH_2CH_2-$ with peaks at 2.2, 1.5 and 1.2 ppm; and of glycerol $-CH_2CH-$ with peaks at 5.2, 4.2, 3.7 ppm. The degree of methacrylation was calculated using the signal intensity of the methylene groups on the backbone of the sebacic acid (1.2 ppm) and comparing it to the signal intensities of the methacrylate groups (6.25, 5.8, 5.3 ppm). Available hydroxyl groups were methacrylated between 25-100%, (degree of methacrylation, 0.25, 0.50, 0.75, 1.00). DSC results revealed the glass transition temperature to be -30°C.

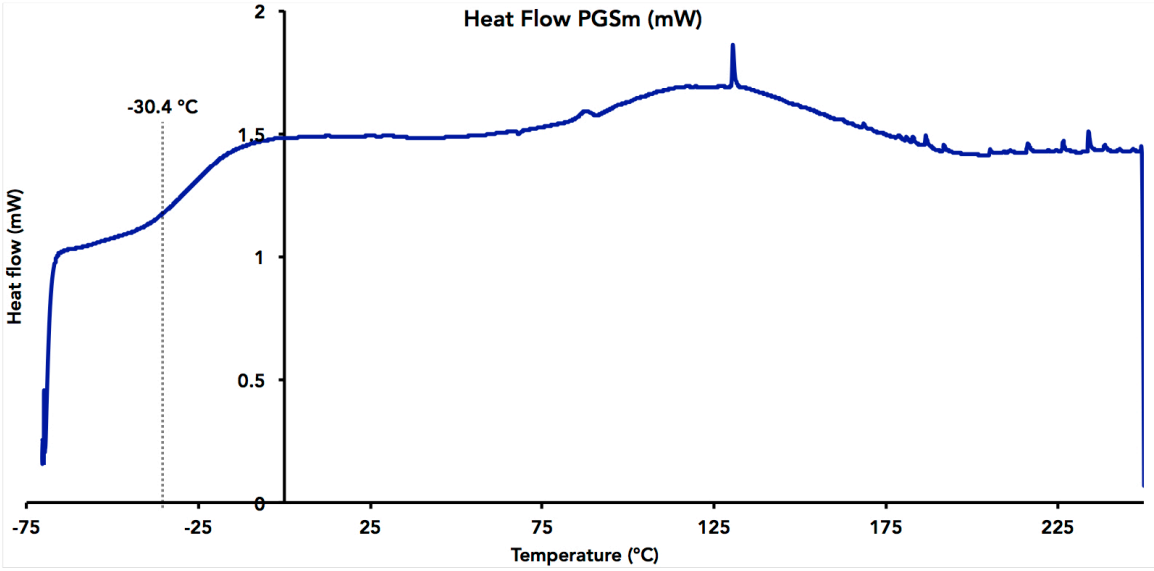

Figure 13: Example graph showing DSC results of heat flow vs temperature on PGSm between -75 °C and 250 °C. Glass transition region highlighted at -30°C.

A strip of PGSm was deformed into a coil and cooled below the T_g, where the coil shape was fixed. When the material returned to room temperature the strip returned to its original shape, indicating the shape memory properties of PGSm.

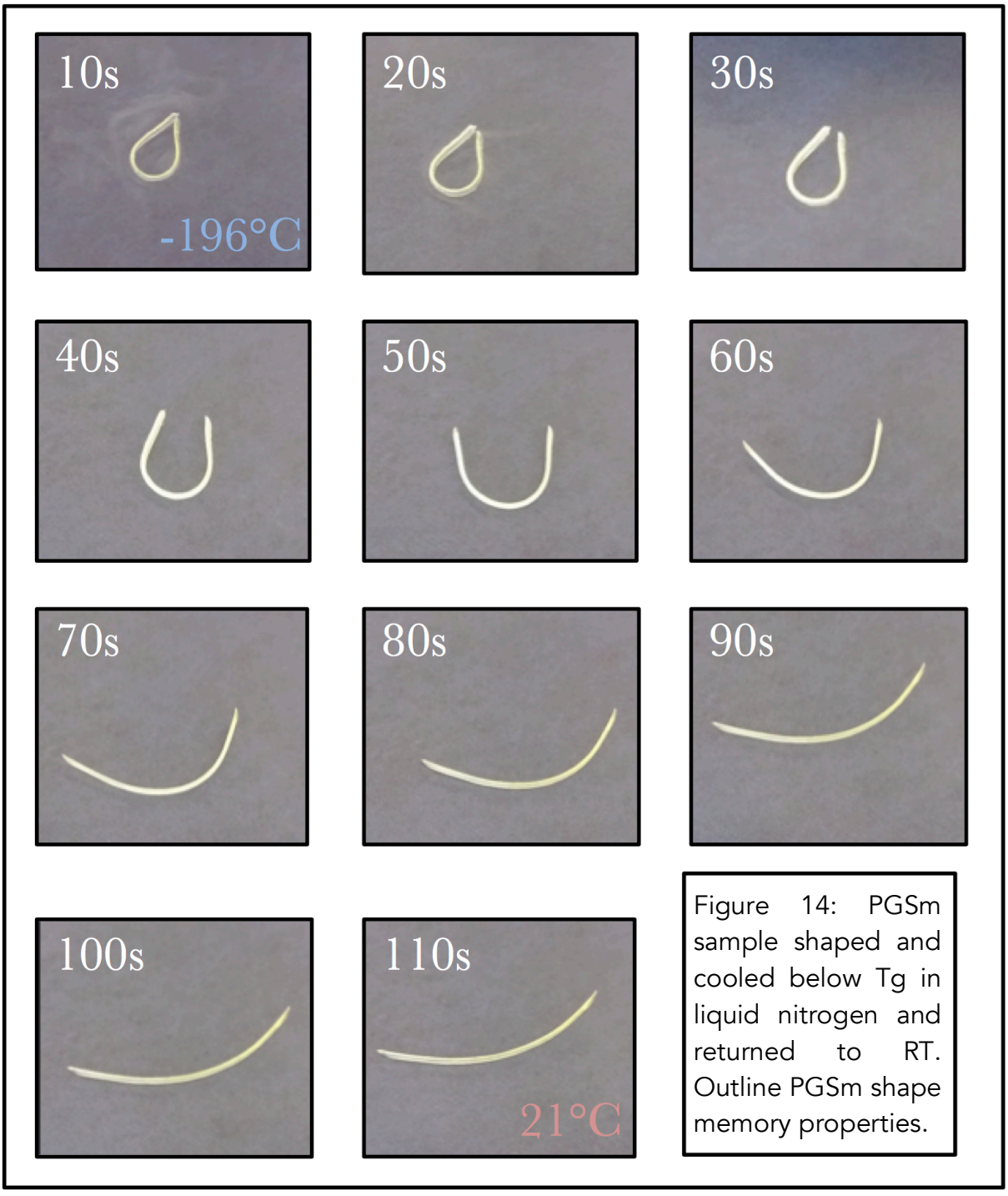

Figure 14: PGSm sample shaped and cooled below Tg in liquid nitrogen and returned to RT. Outline PGSm shape memory properties.

Nanoindentation was performed to understand the Young's modulus of the material (Fig 15). Results showed a clear relationship between the increase in the degree of methacrylation and an increase in stiffness. Nanoindentation was used to calculate the compressive modulus values. These modulus values are representative on a very small scale and may affect the biocompatibility on a cellular level.

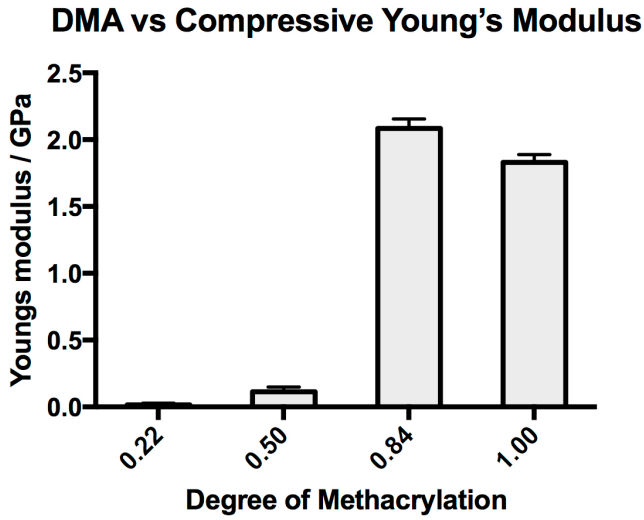

Figure 15: Compressive modulus values obtained from nanoindentation for varying degrees of methacrylation (DMA) of PGSm (n=18). *Standard deviation error bars.*

Goniometry water contact angle results (Fig 16) showed an increase in the hydrophobic surface property of the polymer with an increase in the degree of methacrylation.

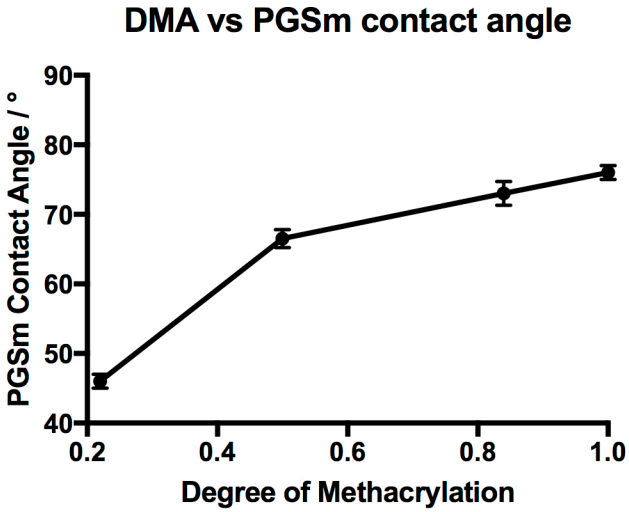

Figure 16: Results showing the surface properties/water contact angle at varying degrees of PGSm methacrylation (degree of methacrylation, DMA) (n=3). *Standard deviation error bars.*

Degradation studies in PBS after 40 days showed no change in mass of the polymer samples in static, rocker or under stirring conditions. Enzymatic degradation results (Fig 17), showed that with an increased degree of methacrylation the degradation rate of the polymer decreased.

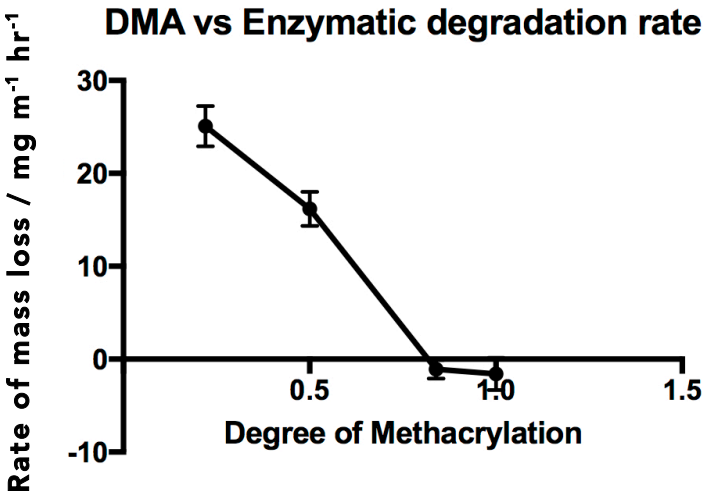

Figure 17: Enzymatic rate of degradation of the polymer PGSm decreases with an increase in methacrylation (0.75 methacrylation) (n=5). *Standard deviation error bars.*

Crosslinked PGSm droplets were used as magnifying lenses to highlight the transparency and potential optical capabilities of the polymer PGSm. The inclusion of the PGSm lens magnified the image approximately 12x.

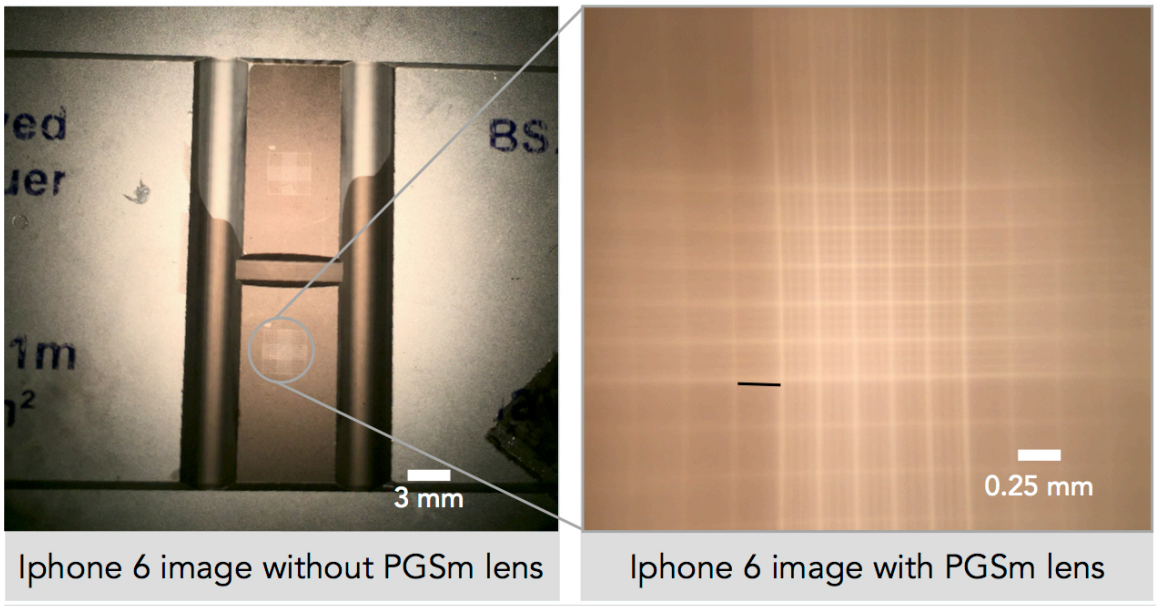

Figure 18: Iphone 6 plus digital image of Neubauer hemocytometer with and without PGSm lens. Approximate magnification 12x.

PGSm was structured via direct write UV printing, demonstrating the polymers photocurable abilities. The polymer was printed into high resolution computer designed scaffolds

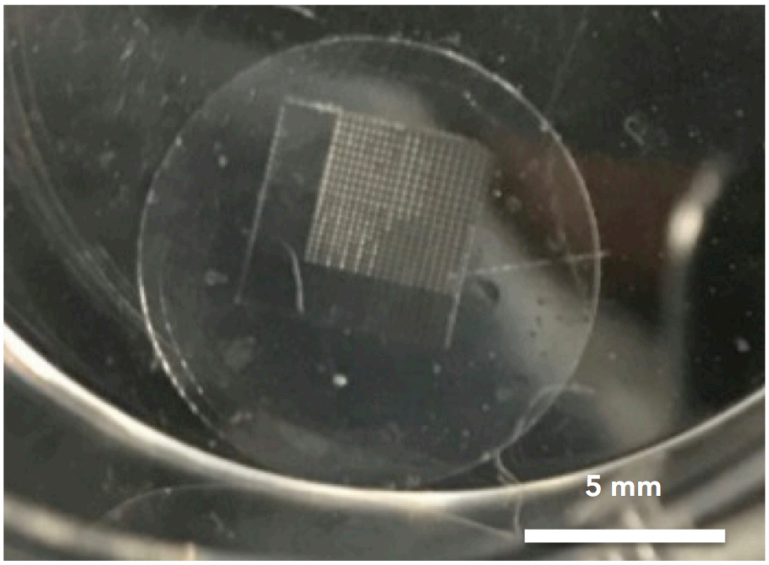

Figure 19: Digital image of patterned PGSm, printed onto a glass coverslip by direct write printing

3. Discussion

It is reported in the literature that that whilst PGS exhibits excellent biomaterial properties for soft tissue engineering applications, an inability to structure the material continues to limit its use. Synthesizing a photocurable form of PGS enables structuring of the material. There are a small amount of studies in the literature available regarding the use of a photocurable PGS, and all of these publications use PGSa, a formulation introduced by Nijst et al[23]. One of the drawbacks to the methodology outlined by Nijst et al. is the use of the acryloyl chloride, which is acutely toxic via inhalation. Acryloyl chloride is also highly reactive and can be prone to spontaneous reactions. In my PhD I investigated the use of a novel formulation of photocurable PGS, PGSm, which instead uses the less harmful and reactive methacrylic

anhydride. Results show that a methodology was developed, synthesising the reproducible polymer PGSm.

Methacrylate groups were added to synthesized PGS prepolymer to allow the photocurable PGSm to be additive manufactured via stereolithography techniques. PGSm was then chemically and mechanically characterized. Results showed that with an increasing degree of methacrylation: PGSm became stiffer, the surface became more hydrophobic and the degradation rate decreased. This highlights the potential tunability of the PGSm material properties, similar outcomes were observed by Nijst et al. when exploring PGSa[23]. The ability to tune PGSm material properties makes it a favorable biomaterial for a range of potential uses. Material stiffness and surface properties (hydrophobic nature) are known to effect cell interactions and viability on scaffolds, with stiff hydrophobic materials often presenting a less favorable substrate for cell attachment. It is therefore necessary to initially perform *in vitro* analysis of cells on flat disks of PGSm to understand whether the degree of methacrylation affects cell cultures.

The propensity of PGSm to degrade is important for some uses in tissue engineering, as non-degradable materials have been shown to increase the likelihood of inflammation and long-term problems. It is important that the material degrades at an acceptable rate depending upon the application, which is why tunable degradation rates are useful for biomaterials. PGSm samples degraded in enzymatic lipase solutions, however samples in PBS showed no significant difference in mass loss over a 40-day period, demonstrating the potential ability of PGSm to be stored prior to surgery in an "off-the-shelf" approach. Macrophage cells are a known component of an acute inflammatory response, which would occur immediately after the implantation of a medical device in the body. Lipase is an enzyme secreted by

macrophages[41] and is known to catalyze the cleavage of ester groups from polyesters by hydrolysis[40,42]. It is postulated therefore that if PGSm was implanted *in vivo*, the material would degrade through the hydrolysis of ester bonds via lipase digestion[40]. Enzymatic degradation studies with lipase are therefore considered a good *in vitro* model to closely mimic degradation in the physiological environment.

The PGSm polymer synthesized possessed many qualities admirable in choosing a biomaterial; the material had variable mechanical properties, degradation rates, and surface properties; the material was also photosensitive, allowing for it to be readily structured. Structuring of traditional PGS is one of the current disadvantages in the use for medical devices and biomaterials. Results from the direct write UV patterning show that PGSm can be structured into intricate scaffolds and printed using stereolithography techniques. When fully crosslinked PGSm is a soft, flexible, elastomeric material with results also indicating the polymer has shape memory capabilities. PGSm showed a high level of transparency when crosslinked, with minimal light scattering witnessed. This transparency and ability to photocure, allowed the production of a simple PGSm magnification lens, capable of up to 12x magnification.

The polymer was however susceptible to rapid photopolymerization in the presence of UV light and therefore needed to be kept away from light prior to being polymerized. Also at lower degrees of methacrylation the polymer became very viscous and difficult to handle, this could be overcome by dissolving the polmer in a solvent before use.

4. Conclusion

To conclude this chapter it is understood that a reproducible photocurable form of PGSm has been successfully synthesized. It has been chemically analysed, mechanically tested and structured three dimensionally: with properties ideal for use as a biomaterial. The material is a biodegradable, soft, tunable, elastomeric biomaterial with many properties ideal for tissue engineering.

3.2 PGSM POLYHIPE

Aim: The aims of this chapter were to create a high internal phase emulsion from PGSm, with interconnected pores, useful for tissue engineering and to characterize the resultant porous foam mechanically and assess its biodegradability.

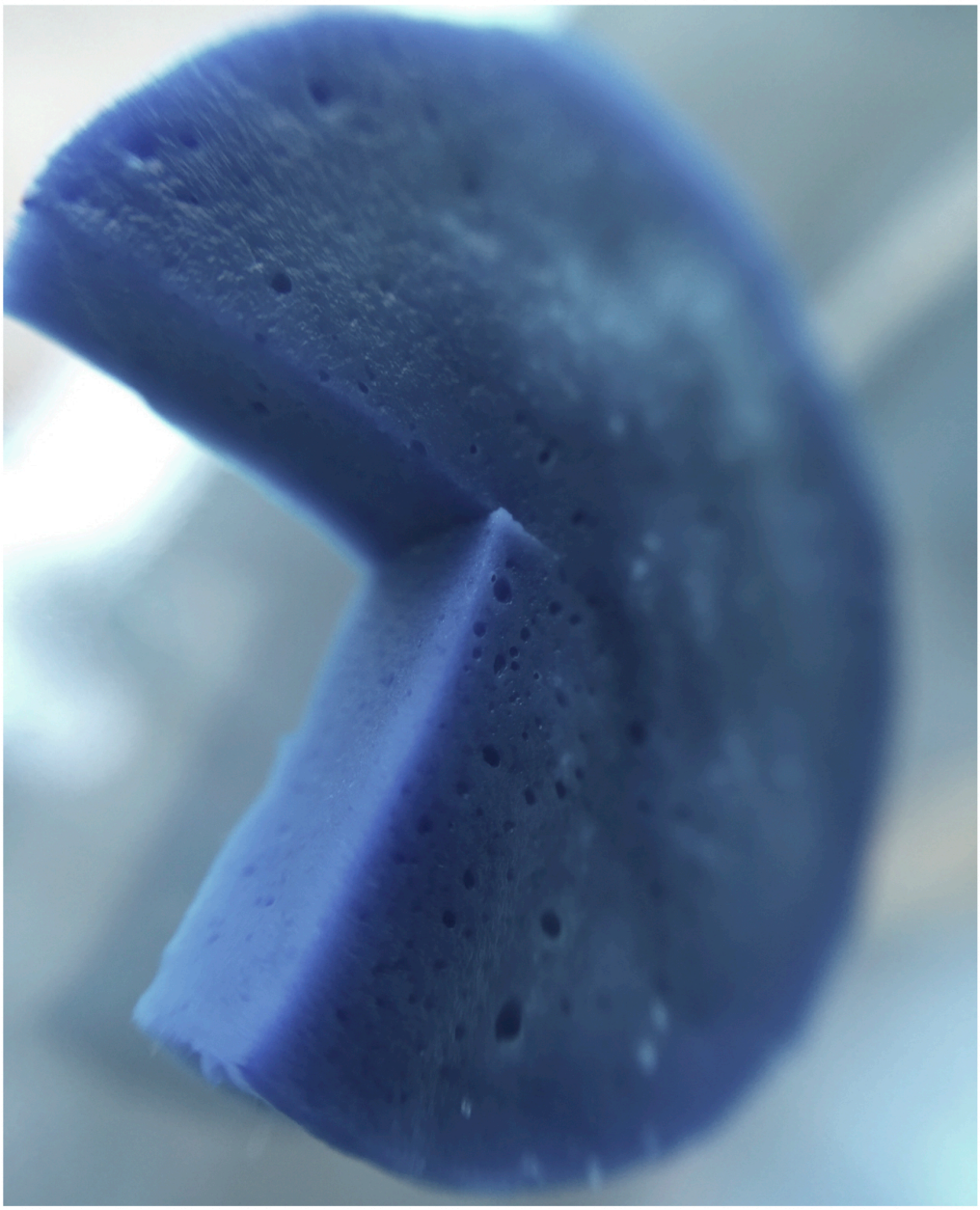

Image of PGSm poly-HIPE foam, (dyed blue for visualization)

1. Introduction

1.1 Porous PGS techniques

The literature reveals an interest in developing porous tissue engineering scaffolds from PGS. However, this has been impeded due to a lack of mechanical strength related to porous PGS scaffolds, making clinical applications difficult[43]. There are a few examples of porous PGS scaffolds produced by particle leaching[25,26], lyophilization[27,28], electrospinning using carrier polymers[44] or glycerol leaching[24]. A common technique used is porogen leaching, whereby a material/gas is mixed within the polymer. The polymer is cured and the porogen leached out, leaving behind a porous material. This can be useful as it is a quick method of introducing pores into the polymer, however there is a poor level of controllability of the pore sizes, density, distribution and interconnectivity. It has also been reported that porogen leached PGS is often too soft as a tissue-engineered scaffold, and further polymers are linked within the PGS to increase the strength of the scaffold[37,43]. Another common technique is to mix PGS with a carrier polymer, enabling the material to be electrospun. This offers an increased strength and a small level of controllability of pore sizes, density and distribution, however the introduction of another polymer may change the material properties of the scaffold. Also with this technique pore sizes are still difficult to control and the morphology of the pores can often be irregular. Both techniques limit the structurability of the polymer into complex scaffold designs and this is why alternative methods of introducing porosity into PGS scaffolds must be explored, such as the production of porous PGSm poly-HIPES.

1.2 Emulsions

An emulsion can be defined as droplets of one liquid (internal phase) dispersed within another immiscible liquid. Examples of emulsions can be seen in everyday items such as emulsion paint, milk and mayonnaise.

High Internal Phase Emulsions (HIPE), were originally defined by Lissant as materials with more than 70% internal phase[45]. This definition has since been updated with a HIPE now identified as a material with an internal phase volume greater than 74.05% (as this is the maximum packing density of homogenous spheres within a volume[46]).

1.3 HIPEs

A HIPE is an emulsion synthesized through the mixing of two immiscible liquids, often oil and water. One phase is dispersed into droplets (dispersed phase), which is dispersed within the other phase (continuous phase), creating either a Water-in-Oil (w/o) or an Oil-in-Water (o/w) emulsion. The dispersed phase is often added to the continuous phase whilst being stirred mechanically, the agitation allows for the dispersed phase liquid to be broken into droplets. When the emulsion contains a volume of over 74.05% of the dispersed phase then the emulsion is classed a HIPE. If too much of the dispersed phase is added the emulsion can invert, with the dispersed phase becoming the continuous phase and the continuous phase becoming the dispersed. Also the droplets in the dispersed phase can often merge in a process known as Ostwald ripening and the two phases can separate out from each other. The addition of a surfactant however can help facilitate the stabilisation of the emulsion[47]. A surfactant works by decreasing the interfacial tension between the oil and the water allowing for the formation of a more stable emulsion. Choosing the correct surfactant, one which is insoluble in the dispersed phase, helps prevent the emulsion from inverting[46,48].

1.4 HIPE history and nomenclature

The research of HIPEs is not a new field of research, with examples being studied in the 1960s and the term "HIPE", first being used in 1966[49]. The term polyHIPE is used to define the polymerized HIPE foam, however it is often used interchangeably with the emulsion HIPE. Medium internal phase emulsions (MIPE) and low internal phase emulsions (LIPE) are now used to describe emulsions with 30-74% and below 30% of internal phase respectively[50]. The term voids, or pores refers to the space once occupied by the dispersed droplets when removed/dried. Research into HIPEs has grown, along with technological and polymer advances[51]. Biodegradable HIPEs are of great interest, particularly for use in tissue engineering where porous polymers are ideal for tissue-engineered scaffolds.

1.5 Poly-HIPES, thermal and photocrosslinking

HIPEs can be formed from a polymer and another immiscible liquid. Often the polymer makes up the continuous phase, which stretches around droplets of water (the dispersed phase). This is an example of a water-in-oil HIPE.

The HIPE phases will begin to separate over time. Stable emulsions are more resistant to this separation and take longer to separate. Once the high internal phase emulsion is produced the polymer surrounding the droplets of water can be fully crosslinked. This allows the material to turn into a solid, the droplets of water to be removed and it leaves behind a porous poly-HIPE scaffold. The poly-HIPE can be crosslinked in several ways, with the most common methodology being thermal crosslinking. Crosslinking the polymer thermally often takes time, this can be problematic as the stability of the emulsion is time dependent. Another method of crosslinking the polymer within the emulsion is via photocrosslinking using UV light, this however requires a photosensitive polymer. The crosslinking of photosensitive

polymers using UV light happens rapidly and almost instantaneously, however photocrosslinking the polymer within a HIPE can often take slightly longer due to light scattering and the presence of water particles.

1.6 Poly-HIPE pore morphology and interconnectivity

HIPEs can be synthesized with a dispersion phase volume higher than the minimum 74.05%. As 74.05% is the maximum packing density for uniform spheres, emulsions with a higher volume than 74.05% must have either polydisperse droplets (droplets of different sizes) or non-spherical polyhedral droplets. Once dried it is the shape of the dispersion phase droplets (now removed) that contributed to the pore morphology.

Interconnectivity within HIPE pores are important in tissue engineering, to allow nutrient exchange and flow within the scaffold. Closed pore scaffolds (scaffolds with pores not interconnected) have limited use in tissue engineering, with open pored scaffolds allowing for better diffusion and providing sites for cell migration and seeding. There are many things that affect the interconnectivity of HIPEs, the quantity of dispersed phase and the amount of surfactant are two variables that directly affects the interconnectivity. During polymerization of HIPEs smaller pores/holes are created in the wall between two closed pores, this smaller hole is known as a throat and it is a series of these throats that ensures the HIPE remains interconnected[52].

The level of porosity, size of the pores and shape can be controlled by varying the parameters in the production of poly-HIPEs. Smaller droplets of the dispersed phase, leads to smaller pore sizes in the scaffold. There are many parameters that can change pore size, one of which is changes in the rotational speed of mixing to agitate the dispersed phase.

1.7 Biodegradable poly-HIPEs

Biodegradable poly-HIPEs are of particular interest to the field of tissue engineering. The ability to have a soft, biodegradable, porous material, with interconnected pores available for cells to be seeded into and protection for the cells during any implantation; makes poly-HIPEs ideal for many tissue engineering applications. As scaffolds in tissue engineering are often used as carriers for cells, once the cells and scaffold has been implanted back into the body, the scaffold has served its purpose and would ideally degrade to minimize the risk of any adverse reactions. It is also important that the degradation products are not toxic[51,53].

1.8 PGS poly-HIPE

There are currently no publications available in literature related to the production of PGS emulsions, or any PGS derivatives into emulsions. This may be due to the lengthy times required for thermal curing of PGS and the instability of the polymer in emulsions, causing the emulsion to separate through Ostwald ripening, prior to thermal crosslinking. One way to overcome this would be to use PGSm, as it has been seen in previous PGSm chapters (chapter 3.1) to crosslink instantly in the presence of UV light. PGSm has also been mechanically analysed and is understood to be stiffer than that of PGS (PGSm has a tunable stiffness), this would help with providing strength to the porous scaffold.

1.9 Summary

In summary, it is understood from chapter 3.1 that PGSm has many excellent properties for a biomaterial. By introducing porosity into PGSm it would make the polymer an even more versatile material for tissue-engineering applications. Current techniques to introduce porosity into PGS lack controllability and structurability of the scaffold, furthermore porous PGS

scaffolds often lack the structural strength required for a scaffold. By varying the production of HIPEs it is possible create materials with controllable porosity. Additionally by using a stiffer PGSm, it can be possible to introduce more strength into the structure of PGSm porous scaffolds. For these reasons this chapter focuses on the production of PGSm poly-HIPEs.

2. Methods

2.1 Emulsion synthesis and PGSm HIPE production

The surfactant, hypermer B246, 0.2g (SIGMA) was added to a 25 mL glass universal and gently warmed to liquefy the waxy substance. A small magnetic stirrer was added, alongside photoinitiator 0.2 g (2-hydroxy-2-methylpropiophenone, Sigma), and PGSm, 1 g. solvents chloroform and tolurene were added at 1 g, and 0.5 g respectively. A Universal container was set in a water bath on a magnetic stirring hot plate at 55°C, and 450 revolutions per minute. Distilled water was then added at a rate of 1 g per 90 seconds, the total volume of water added was dependent upon the ratio of HIPE required. As the magnetic stirrer agitated the solution, droplets of the water were formed and the oil phase (polymer) was stretched around these droplets. As the emulsion was synthesized the solution turned from a thin transparent liquid, to a more viscous brilliant white solution. The rotational speed (400 rpm – 600 rpm) of the hot plate and the volume ratio of water (0.67 – 0.85) was varied during experimentation.

The emulsion was then poured into molds and the polymer fully crosslinked in the presence of UV light. Crosslinked HIPE scaffolds were then introduced to methanol, cycled within a Soxhlet extractor overnight, to remove any uncrosslinked polymer and to allow for the removal of water from within the pores. Any methanol remaining within the pores was evaporated away at

room temperature or under vacuum. Samples were freeze-dried before imaging via SEM to maintain the internal structure.

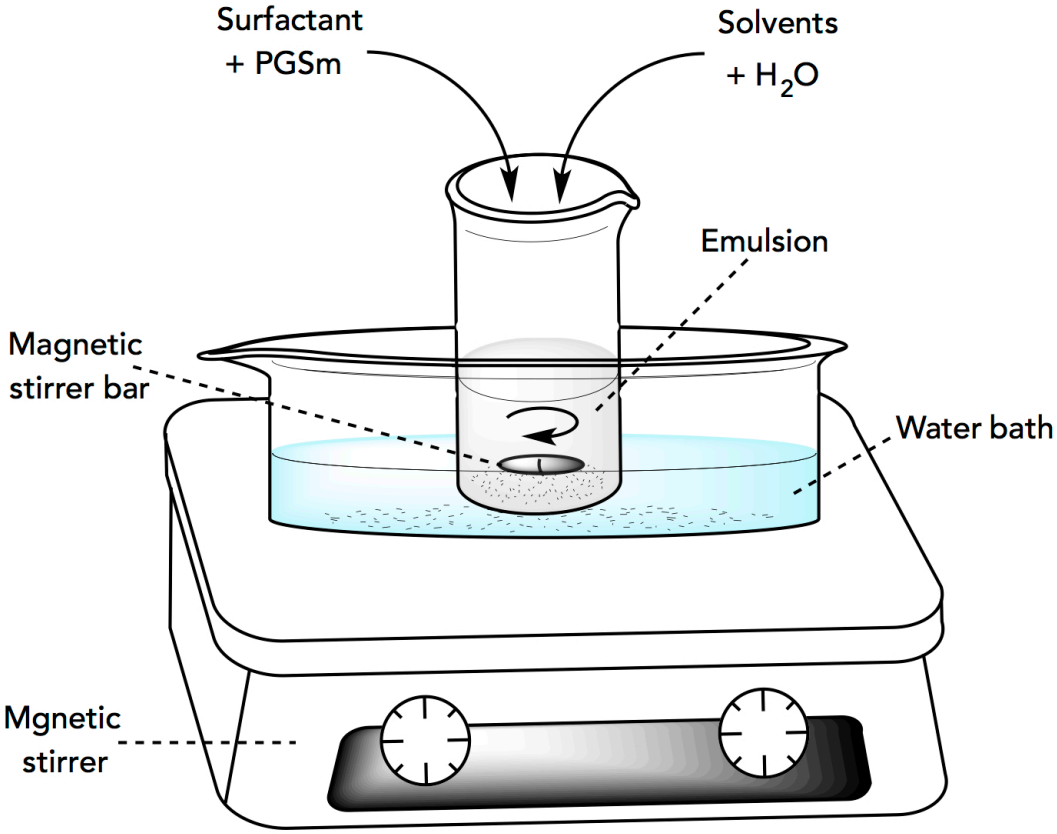

Figure 20: Diagram of emulsion synthesis methodology. (ChemDraw).

2.2 Mechanical compression test of PGSm polyHIPE

Emulsions were synthesized as above and a flat sheet of PGSm HIPE was photocrosslinked at approximately 5 mm thick. Circular constructs 6 mm in diameter were cut from the sheet using a biopsy punch. The HIPE samples were soaked in methanol and allowed to dry, to ensure the removal of water from within the pores. The area and depth of the HIPE disks was recorded. The HIPE disks were then transferred to the mechanical testing machine for analysis. Compressive mechanical properties were assessed using a Hounsfield mechanical tensometer (H100ks, Hounsfield, UK) and 10 N load cell (HTE1-10N). The compression test was set at a rate of 0.25 mm/min with

a max load of 10 N in the QMAT software (ProLabMas). The area and depth of the HIPE disks was used to calculate the compressive modulus value of the samples.

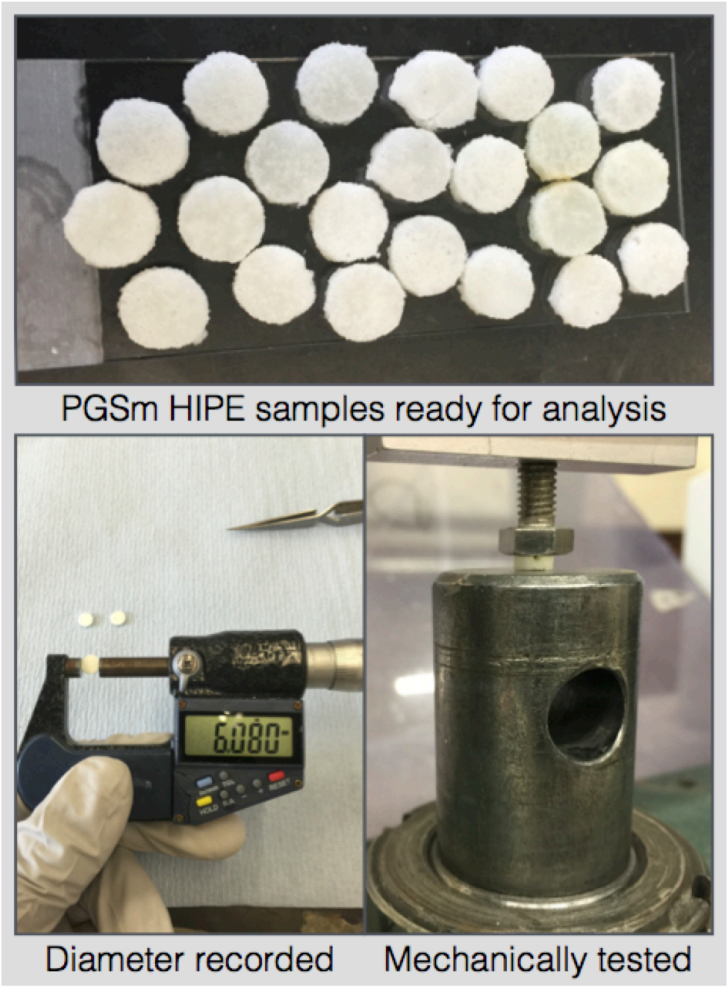

Figure 21: Digital photographs of HIPE samples ready for mechanical testing after crosslinking and drying. Sample size was accurately measured using digital calipers and a digital image was taken during mechanical testing.

2.3 Enzymatic degradation of PGSm HIPE

Samples were punched from a flat sheet of polyHIPE, alongside solid PGSm samples, ready for the degradation studies. Enzymatic degradation studies were performed in PBS with a physiological pH. Samples were prepared with

a diameter of 6 mm and a depth of 3 mm. The disks were placed in a 24-well plate. Lipase from *Thermomyces lanuginosus* (100,000 U/g Sigma-Aldrich, UK) at a concentration of 2000 U/mL in PBS was added to each well. The well plate was placed on an orbital shaker and incubated at 37°C for the duration of the experiment. The PGSm disks were weighed before the lipase solution was added, at regular intervals throughout the experiment with excess solution shaken off and at the end of the experiment once dry. The size of the samples, and the change in weight over three days was used to calculate the rate of degradation of the PGSm disks.

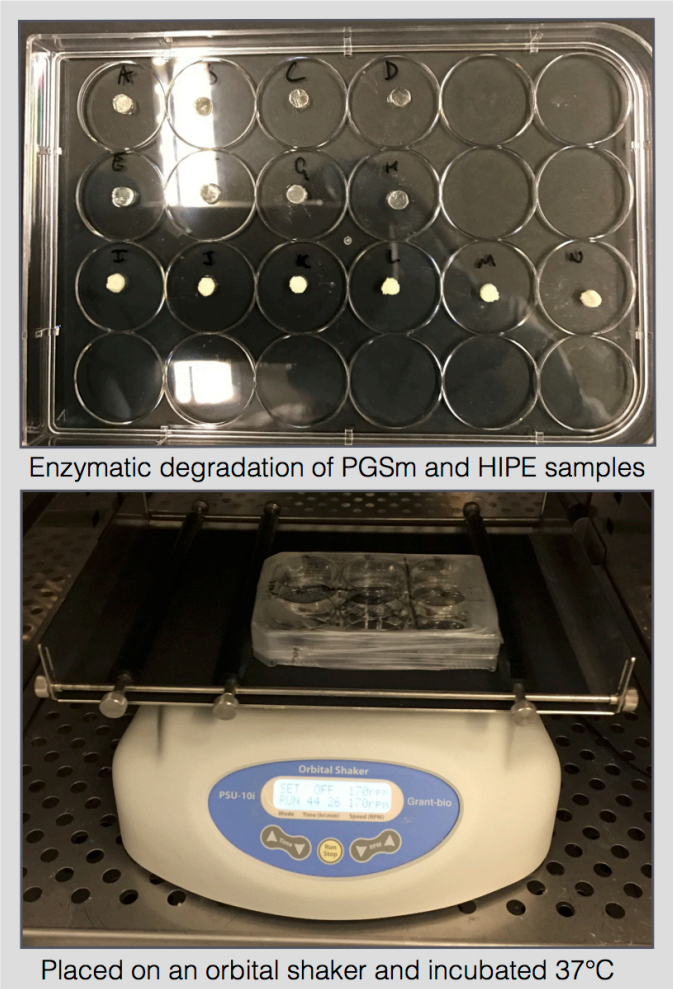

Figure 22: Digital photographs showing PGSm and PGSm HIPE samples ready for degradation studies and samples on an orbital shaker incubated at 37°C.

3. Results

Initial results confirmed that PGSm high internal phase emulsions could be produced successfully. The emulsions varied in stability depending upon how they were produced. The rotational speed and water content was varied to determine the ideal conditions for the production of PGSm poly-HIPE for tissue engineering. A rotational speed (stir rate) of 450 rpm was used for experimentation whilst the water content was adjusted and a water content ratio of 0.82 was used whilst rotational speeds were varied. SEM micrographs (Fig 23) were taken of the resulting PGSm polyHIPE materials and the porosity assessed. With low water content ratios (0.67) MIPEs were produced and with excessively high water content ratios (0.85) pores began to collapse (Fig 23). SEM images also show that rotational speeds of 450 rpm produced the most uniform pores. There was a clear trend between the increase rotational speed during PGSm HIPE production and a decrease in the average pore diameter (Fig 24). Also there was less variability between the pore diameters with an increased rotational speed, as can be seen from the smaller SD error bars. This shows that rotational speed could be used to help tune the pore diameters within PGSm poly-HIPE scaffolds. Results of the compressive mechanical property tests indicate that the compressive modulus of the PGSm poly-HIPE increases with an increase in rotational speed (Fig 24).

Further results from mechanical testing, on PGSm HIPEs of varied water content, suggest that with an increase in water content (volume ratio of HIPE) there was a increase in the compressive modulus. The increase in compressive modulus seems fairly linear up until the volume ratio of 0.85 for water content, whereby it increased dramatically (Fig 24). As the value for 0.85 was dramatically higher, graphs below are represented both with and

without this 0.85 value omitted, allowing for a clearer visualization of the rest of the data (Fig 24).

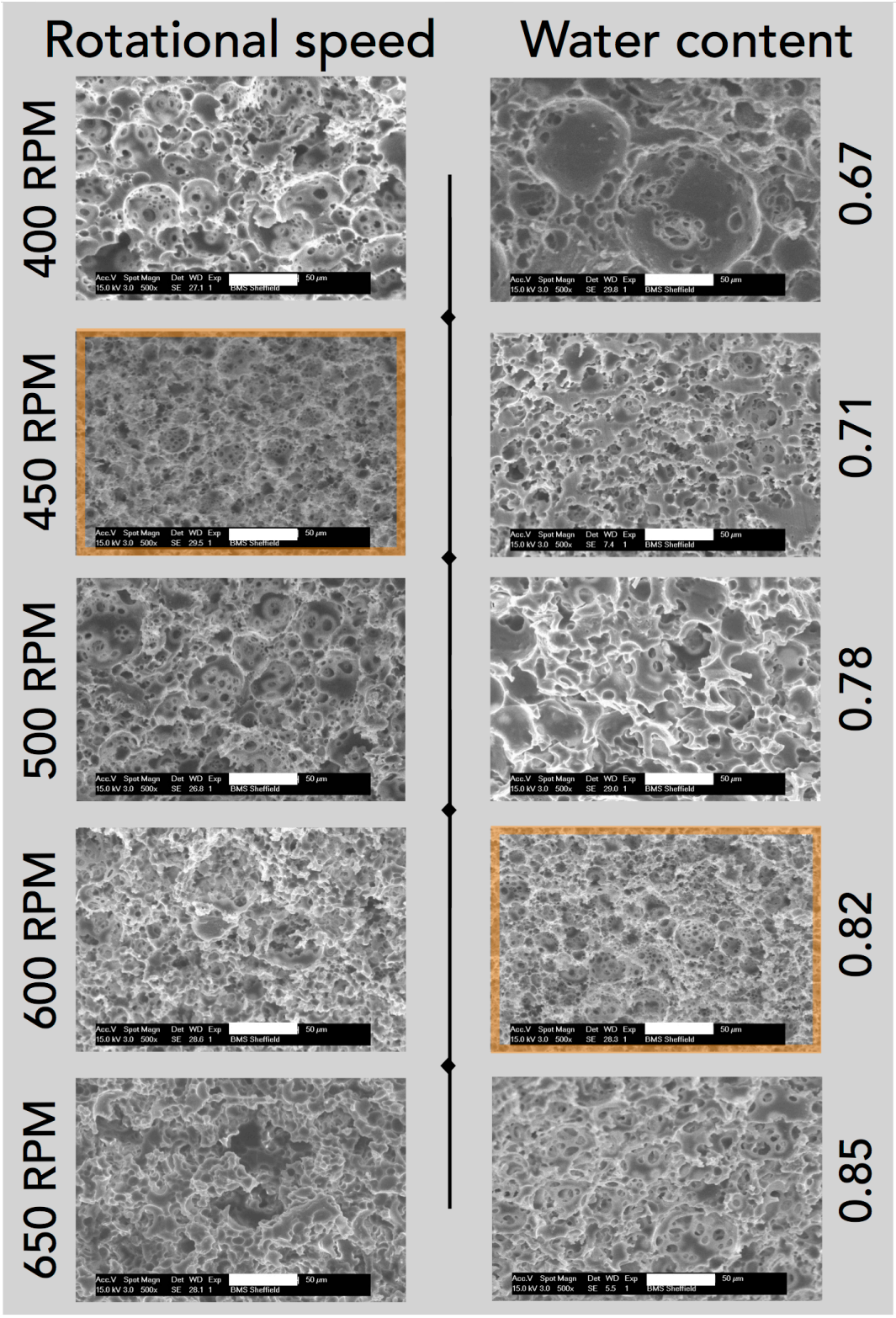

Figure 23: SEM images of PGSm HIPE with varied rotational speed and water content. 450 RPM and 0.82 water ratio chosen for further experiments, 50μm scale bar (white).

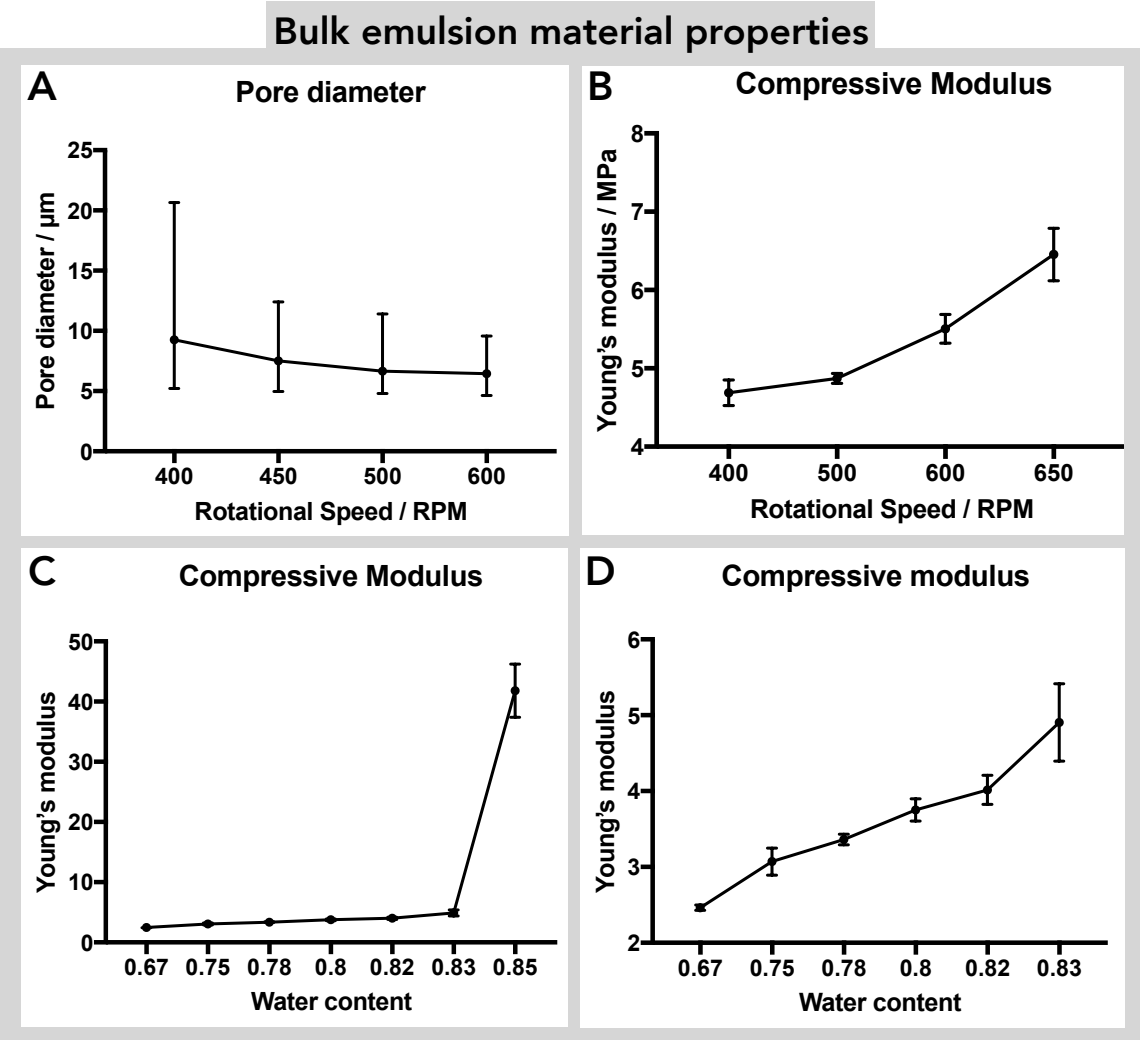

Figure 24: The relationship between the change in rotational speed during PGSm HIPE production and pore diameter (A) and compressive modulus (B). The relationship between the water content ratio of PGSm HIPE and the compressive modulus (C and D). Graph D uses data from the first six points in graph C, omitting only the final modulus value from the PGSm HIPE water ratio (0.85). Results show a reduction in pore diameter and an increase in stiffness with increasing rotational speed (A+B). Results show an increase in stiffness with an increase in the PGSm HIPE water content (C+D) (standard deviation error bars, n=3).

There was no significant difference in the enzymatic degradation results across nine days between the two solid PGSm variables of 0.75 and 0.5 degree of methacrylation (Fig 25). There was however, a difference between the solid 0.5 methacrylation PGSm and the PGSm HIPE. Results indicate that

the PGSm HIPE initially has similar percentage mass loss to that of the solid polymers, however by day nine the percentage mass loss of the HIPE increases at a faster rate than the solid PGSm.

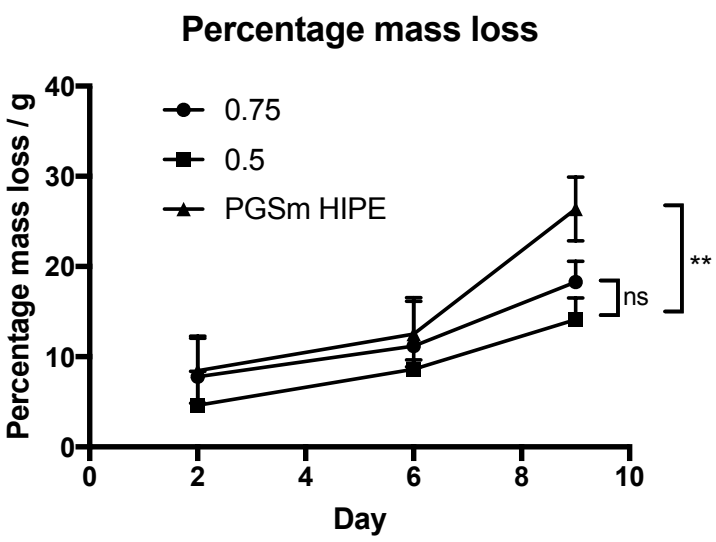

Figure 25: Graph showing the percentage mass loss of solid PGSm polymers of 0.75 and 0.5 methacrylation, and PGSm HIPE, across nine days. 2-way Tukey ANOVA tests, with multiple comparisons show a significant difference between 0.5 and PGSm HIPE, no significant difference between 0.5 and 0.75 (standard deviation error bars, n=3).

Results from the overall percentage mass lost show that the PGSm HIPE lost a significantly higher percentage of its mass than both the solid PGSm polymer groups. There was no significant difference in the mass loss of the two solid PGSm groups.

Figure 26: Graph showing the overall percentage mass lost over nine days from two solid PGSm variables and a PGSm HIPE. One way ANOVA with multiple comparisons show there was a significant difference between the PGSm HIPE and both solid PGSm groups, and no significant difference between the two solid PGSm groups (standard deviation error bars, n=3).

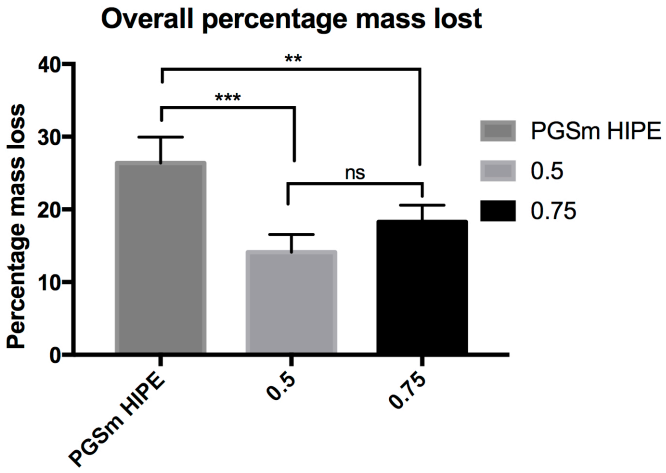

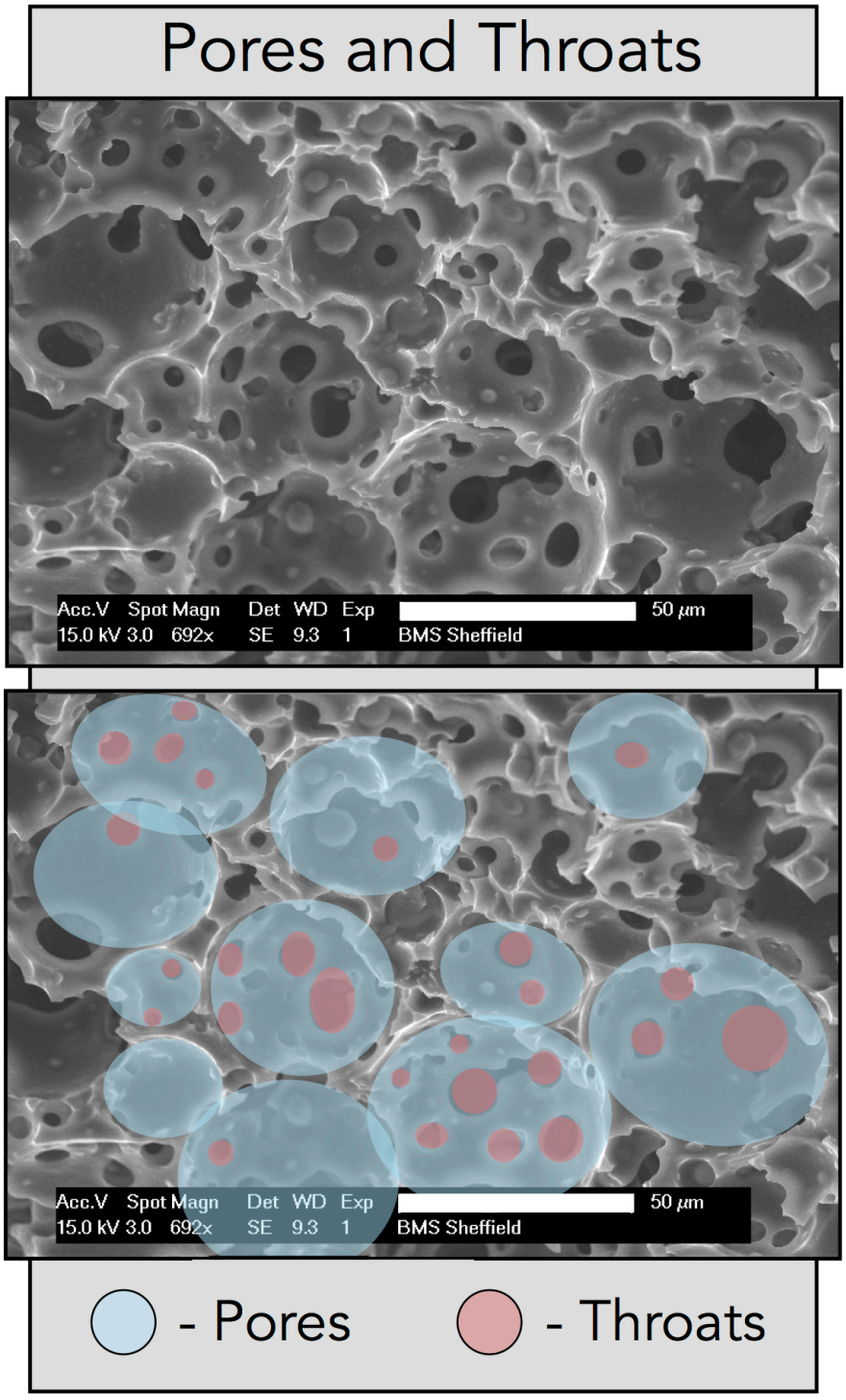

Figure 27: SEM images with a computer overlay, highlighting the presence of pores and throats within the PGSm polyHIPE.

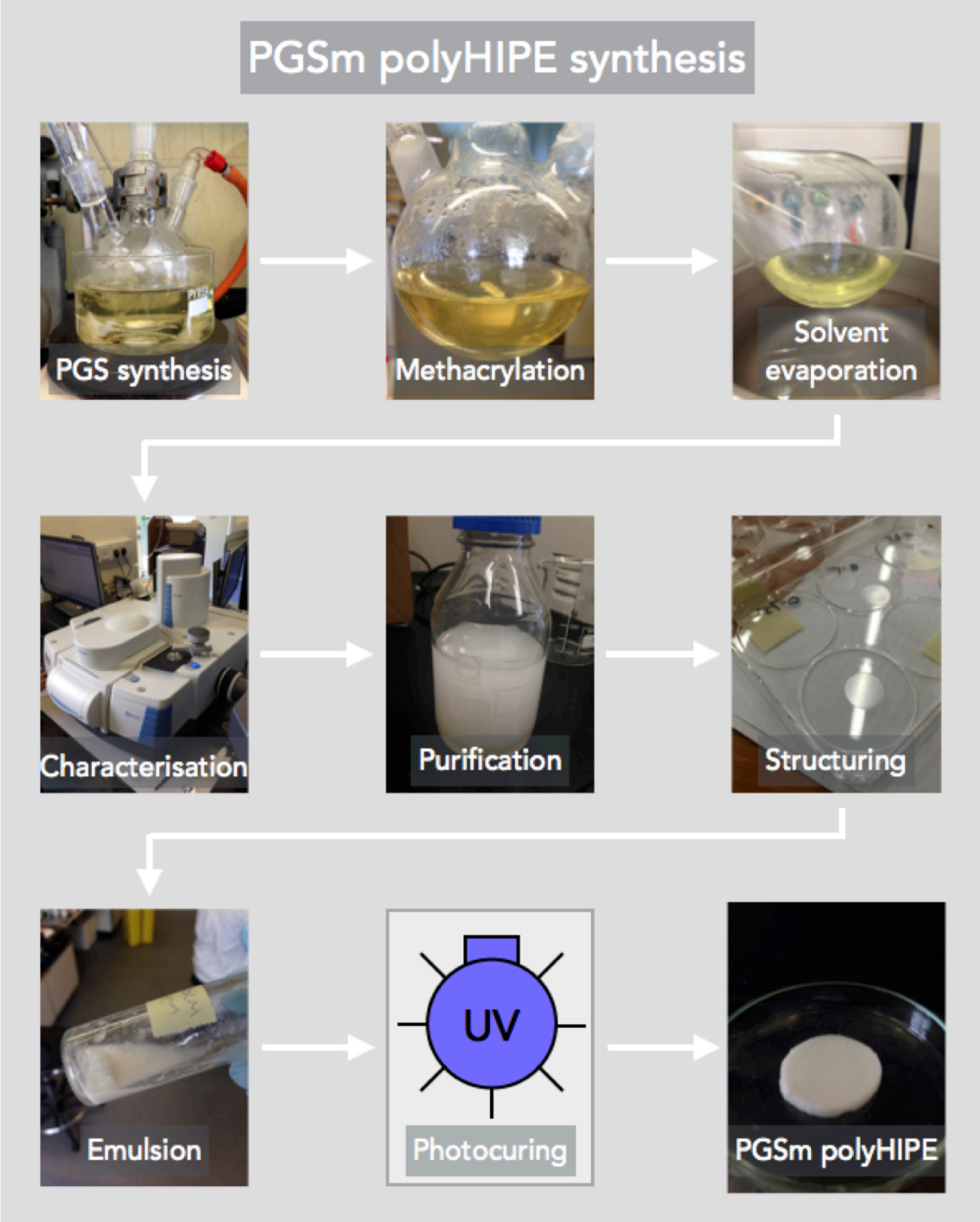

Figure 28: Diagram outlining the synthesis process from PGS synthesis to PGSm polyHIPE production.

4. Discussion

There are currently no examples of PGSm emulsions or HIPEs in literature. There are a few examples of porous PGS biomaterials, however these often have limited controllability and insufficient structural strength as a tissue-engineering scaffold. As PGSm is known to be slightly stiffer than PGS, with a tunable modulus, it was postulated that porous PGSm, produced by creating high internal phase emulsions, would make useful scaffolds for tissue engineering. In this chapter the novel formulation PGSm, was produced intio PGSm HIPEs, capable of being structured into complex scaffolds due to their ability to be photocrosslinked.

Creating an emulsion from a polymer can be a difficult process, with many parameters and variables involved. One of the biggest challenges is finding the correct surfactant that would help the polymer form an emulsion. A methodology was developed in this study whereby stable emulsions could be formed from PGSm. Production parameters were tweaked to understand the effect on the porosity and SEM micrographs were taken of the resultant HIPEs. Results show (Figs 23 and 24) that increasing the rotational speed whilst mixing the emulsion, produces pores with a smaller mean diameter, and of a smaller range of sizes (more homogenous pore size). The compressive modulus of PGSm HIPE scaffolds also increases with both an increase in the rotational speed and an increase in the water content ratio. This indicates an increased level of controllability, related to both the porosity and mechanical strength of PGSm HIPE scaffolds. At a water content ratio of 0.85, the compressive modulus is dramatically higher (more stiff), this can be attributed to the fact that there is less polymer within the HIPE supporting the scaffold, and therefore many of the pores have collapsed, leaving a far stiffer material. This was also seen during handling and in SEM imaging (Fig 23).

Due to the homogeneity of the pores and the additional structural stiffness of the scaffolds, samples were made using a 450 rpm rotational speed and 0.82 water content ratio for all further experimentation, including degradation studies. This produced scaffolds with an average compressive modulus of 4.02 MPa and an average pore diameter of 8 μm. Although the PGSm poly-HIPE scaffold included pores slightly larger and smaller, the average of 8 μm pores may be ideal for some tissue engineered scaffolds, with Corning reporting that porous materials with 8 μm pores are suited for a range of cancer invasion cell studies[54]. It was difficult to determine the area of a HIPE surface, due to the large number of open pores therefore the rate of degradation was problematic to study. Instead, the percentage mass loss was used which provides a more representative measure of degradation.

The initial rate of mass loss was observed as being similar between the PGSm HIPE and the two solid PGSm samples. However, by day nine the PGSm HIPE degraded at a faster rate. PGS is known to undergo surface degradation, particularly as it is understood that within the body the biomaterial degrades enzymatically via the hydrolysis of ester bonds[40]. The graph (Fig 25) begins to illustrate that the solid PGSm degrades at a linear rate, which may indicate surface degradation of the polymer, however with only 3 time points this cannot be confidently concluded. Initially the PGSm polyHIPE samples followed this linear degradation trend, however by day nine there was an increase in mass loss. This may be because of the surface morphology of the PGSm polyHIPE. As the PGSm polyHIPE was very porous, there was a very high surface area related to the amount of PGSm. The walls of the PGSm polyHIPE were also very thin and this may preclude the material to undergo a very short period of surface degradation before the surface is so thin it mimics

bulk degradation. This may explain why there is a sudden loss in mass at day nine. Total percentage mass loss across the nine days was plotted to compare PGSm HIPE with the two solid polymer groups (Fig 26). It was clear from the enzymatic degradation study that the PGSm HIPE scaffolds degraded at a faster rate than that of similarly sized solid PGSm scaffolds.

5. Conclusion

To conclude PGSm was successfully produced as a high internal phase emulsion for the first time. The emulsions could be quickly crosslinked into complex biomaterial scaffolds through UV photocrosslinking, including casting and 3D printing via direct UV writing and stereolithography (further evidence can be found in chapters 3.4 and 3.5). The PGSm HIPEs are tunable, with a controllable porosity, size and density of pores, as well as varied mechanical strength. The scaffolds synthesized are able to maintain their structure without collapse, a problem often attributed to other porous PGS scaffolds. The PGSm polyHIPE scaffolds had high levels of interconnectivity and porosity, making them favourable materials for tissue engineering. *In vitro* studies can now be performed to determine the biocompatibility of the scaffolds, and whether the porosity will aid cell survival by providing domains or a surface for cell attachment and by allowing nutrient/waste product exchange.

3.3 PGSM NERVE GUIDANCE CONDUITS FOR PERIPHERAL NERVE REPAIR

Aim: The main aims of this chapter were to assess the use of the novel PGSm as a material for the peripheral nerve repair of large injury gaps.

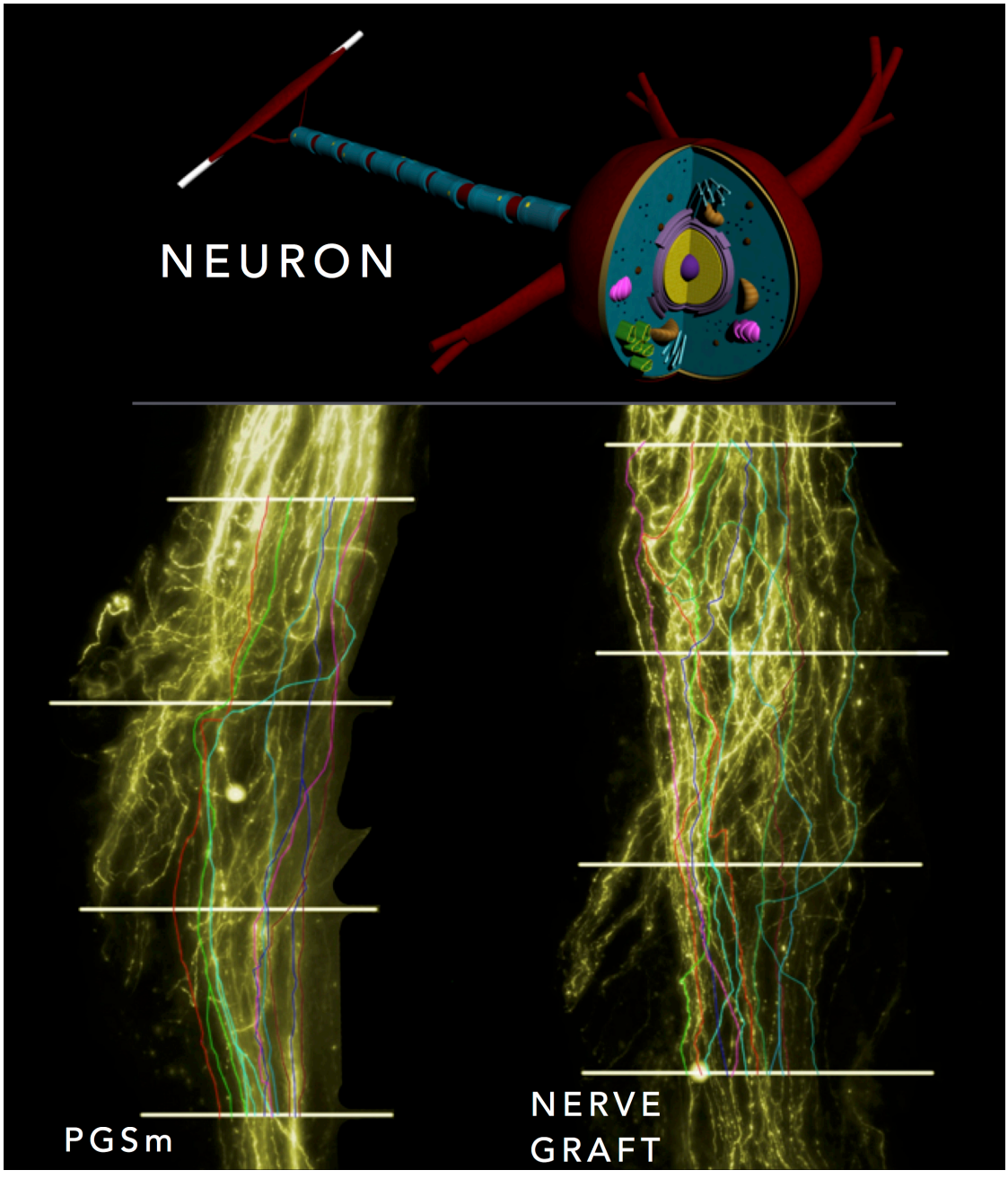

Computer designed model of neuron (Maya, Autodesk) and axon tracing images from in vivo study. Images taken from, Fig 31 and 43.

1. Introduction

Studies have found that 2.8% of trauma injuries are related to peripheral nerve injury [55]. Peripheral nerve injury is known to affect over 300,000 people across Europe annually [56]. These injuries can have a variety of causes, such as traumatic wounds, thermal and chemical damage, myelin or axonal degeneration and acute compression[57]. The peripheral nervous system does demonstrate the ability to regenerate after injury and self-regeneration from re-extension of the peripheral nerve can happen naturally, however, if the nerve is severely damaged, or the trauma gap too large; regeneration may be encouraged surgically.

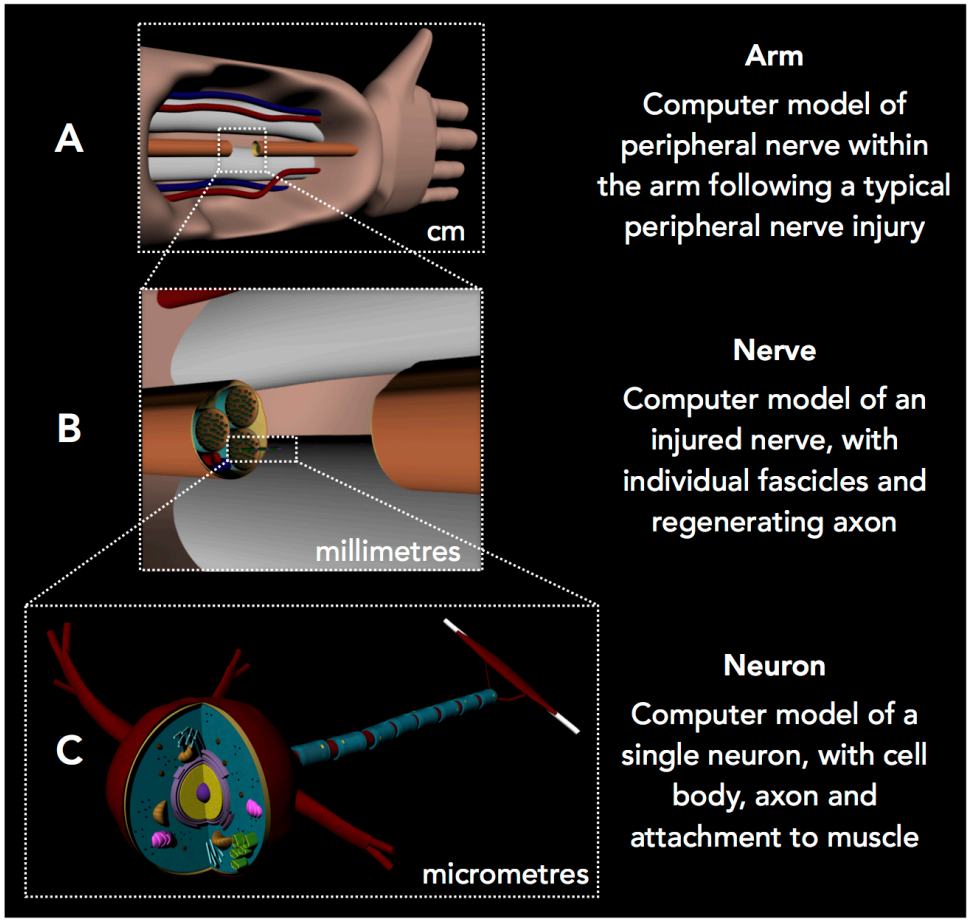

Figure 29: Computer model of (A) the peripheral nerve injury within the arm, (B) a higher magnification detailed model of the peripheral nerve and (C) a very high magnification model of an individual neuron with cell body and extended axon (Maya, Autodesk). All scales are approximate.

1.1 Peripheral nervous system – anatomy

The Peripheral Nervous System (PNS) is distinct from the Central nervous system (CNS), and doesn't offer the same level of protection; leading to the peripheral nervous system being susceptible to injury[58,59]. The CNS is confined within the skull and vertebral column, whereas the PNS is spread across the extremities of the body making peripheral nerve injuries more common.

The Peripheral Nervous System (PNS) can be broadly split into three sub categories: the cranial nerves – distributed across the head and attached to the brain; the spinal nerves – distributed throughout the somatic area of the body and attached to the spinal cord; and the autonomic nervous system, subdivided into the parasympathetic and sympathetic systems. The peripheral nervous system has a complex physiology with two main duties; the first is to carry signals from the central nervous system, to the target tissues. The second is to receive information at body's peripherals and to interpret it into nerve signals carried to the central nervous system[60]. Peripheral nerves are extended from neuronal cells. The cell bodies are located in the spinal chord, dorsal root ganglia and the brain. In contrast the axons traverse to the peripherals of the body (outside brain and spinal cord), (see Fig 29 and 30). A dense fatty substance called myelin, produced by Schwann cells, often surrounds the axons. The myelin wraps insulated axons in to segments, separated by gaps known as nodes of Ranvier. When signals pass along the axon, they cannot pass through the myelinated internodal regions that make up 95% of the length of the axon, due to the high resistance in the myelin sheath[61]. Instead when the myelin membrane at a node is excited the local circuit flows outside and depolarizes the membrane at the next node, essentially jumping from node to node. Impulses therefore jump more

efficiently from node to node, known as saltatory conduction. Due to the low capacitance of the myelin sheath and low energy required to depolarize, this efficient jumping process (saltatory conduction) makes conducting signals faster[62].

The extra cellular matrix of the nerve fibril, basal lamina, is produced by Schwann cells and consists primarily of laminin, collagen, fibronectin and agrin. Axons are grouped together into bundles, supported by several layers of connective tissue, which is collectively known as the peripheral nerve. Figure 30 outlines the anatomy of the nerve fibril and the peripheral nerve. The epineurium, made primarily of collagen and elastin, covers the nerve and can form between 30-75% of the cross sectional area of the nerve. It's physiology allows for the nerve to be stretched in response to everyday bodily movements[61]. The perineurium is the cellular layer that is formed by the perineurial cells and is far less accommodating to movements/stretches than the epineurium. The endoneurium lies within the perneurium and is a matrix of collagen that surrounds the individual axons[61].

It has been well documented that peripheral nerves possess the ability to regenerate following injury. Axons are able to spontaneously regenerate from the proximal stump (closest to cell body), past the injury site and into the distal stump (stump furthest from cell body). The nerve then reinnervates along the damaged nerve, to the peripherals, restoring function. Three main factors determine whether a nerve will spontaneously regenerate, the first is whether the nerve survives from injury. Survival can be affected by factors such as the type of neuron, age, degree of injury and distance of injury from the cell body. The nerve must also be able to switch from signaling to growth mode, enabling protein synthesis for axon regeneration. The second is

whether the environment the axon is growing through into the distal stump is adequate to provide enough support for nerve regeneration. And the third is whether the axons are able to reinnervate to the target distal stump with the stump accepting reinnervation[63 64].

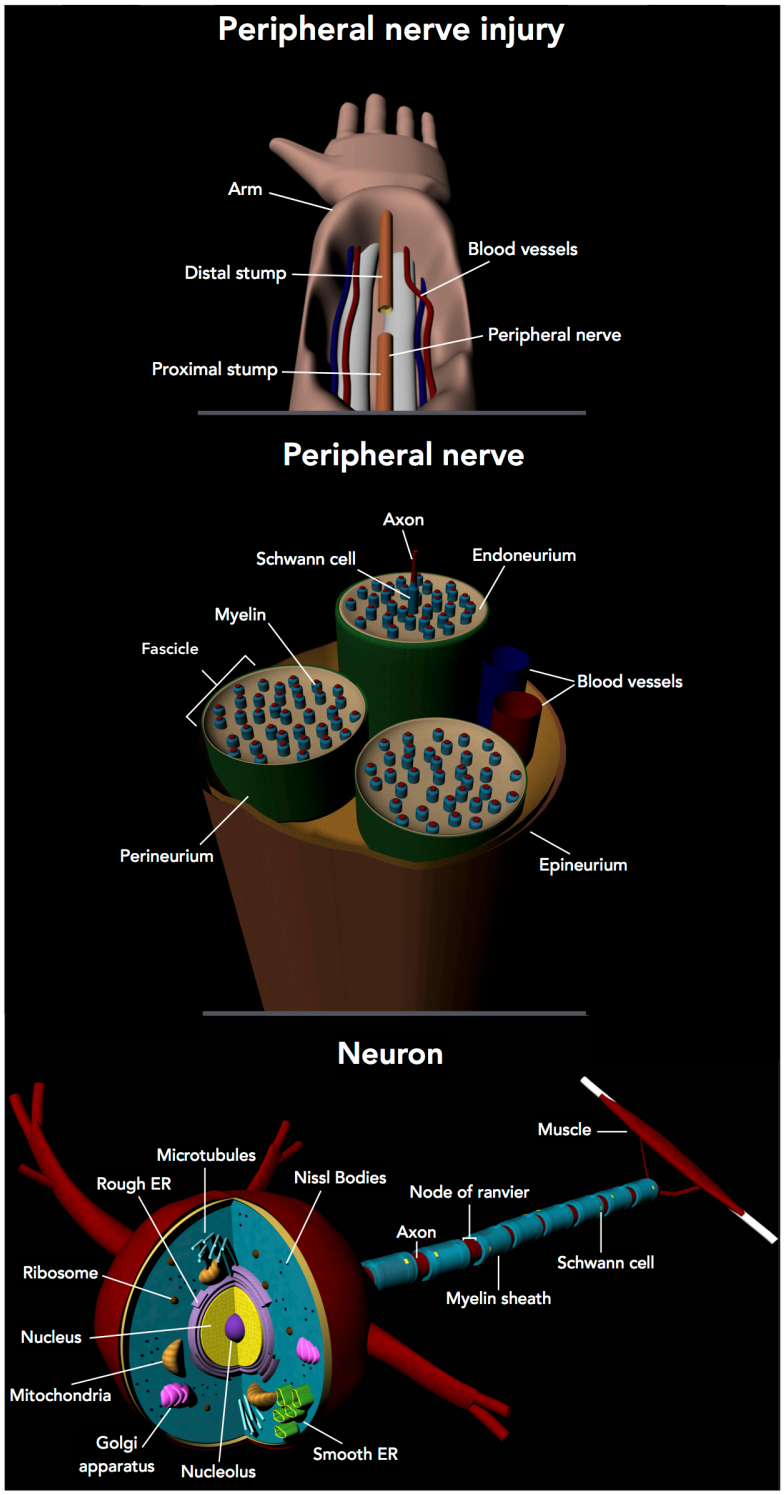

Figure 30: Models of PNI, Peripheral nerve and neuron, not to scale (Maya, Autodesk).

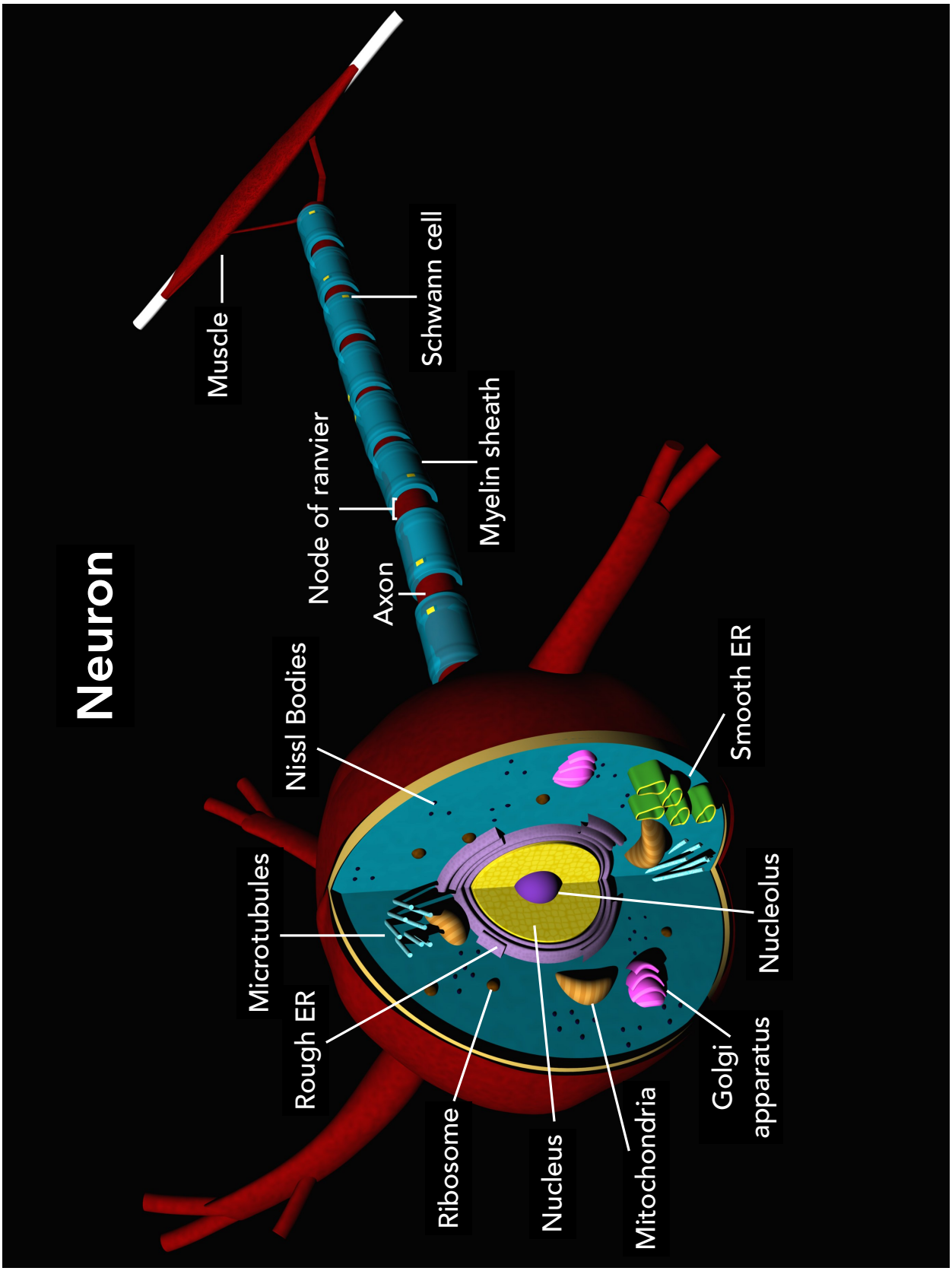

Figure 31: Magnified, annotated computer model of a neuron, not to scale (Maya, Autodesk).

1.2 Peripheral nerve injury

It is understood that peripheral nerve injuries are caused by a variety of different mechanisms, such as traumatic wounds, thermal or chemical damage, myelin or axonal degeneration and acute compression[57]. Following peripheral nerve injury, axons act quickly to seal the ends of the transected nerves to minimize the loss of axoplasm, the cytoplasm within the axon[65]. If the cell body survives the injury, then the proximal stump swells and undergoes retrograde degeneration up to the first node of ranvier[63]. The severed axons retract several millimetres and the proximal part of the axon begins to sprout vigorously for several days after injury. Growth cones are created at the nodes of Ranvier in the proximal axon, with filopodia extending from them in all directions. As soon as filopodia reaches a suitable microenvironment, the distal target, it then becomes the sole survivor and the rest of the filopodia die. Whilst this is occurring on the proximal end of the axon, the distal stump undergoes cytoskeleton and membrane breakdown, leading to Wallerian degeneration[66]. This is where the Schwann cells shed myelin immediately after injury; this myelin attracts phagocytes and other macrophages to the area to remove the bits of myelin and axonal debris. The Schwann cells then appear to undergo dedifferentiation, changing phenotype from myelinating to repair cells[67]. This is where they revert to a state similar to stem cells and are able to proliferate[68]. This proliferation and subsequent redifferentiation allows organized columns of Schwann cells to be created with tubes of basal lamina, these are known as a Schwann cell column, or bands of Bügner [64,67]. The bands of Bügner help create optimal conditions for neuronal growth and cone adhesion. The columns of Schwann cells are able to upregulate the synthesis and secretion of neurotrophic factors (NTF's); these help keep the nerve alive after injury. The basal lamina (specialized extra cellular matrix), creates a scaffold for neural cells to grow on, these cells

grow readily on the basal lamina as it contains good adhesion molecules such as laminin and fibronectin[64]. Through this method the body can effectively regenerate its nerves at approximately 1-3 mm per day, with good rates of success. The main problem however, is that the body only has the ability to do so over very short injury gaps[65]. This is why an alternative method is needed which mimics the microenvironment created by the body, but allows regeneration to be effective over greater distances.

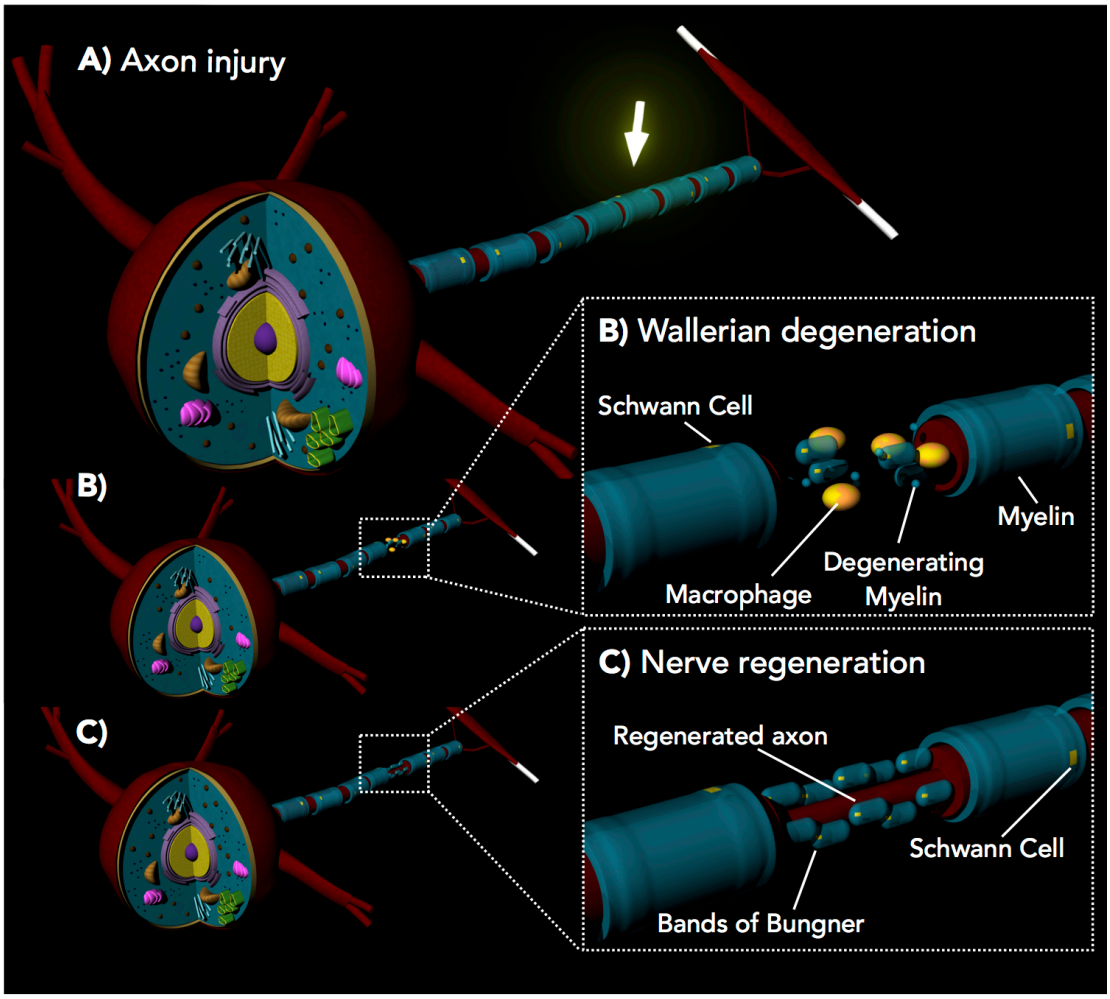

Figure 32: Computer model of a neuron with axon nerve injury (A), Wallerian degeneration (B) and axon regeneration (C). Arrow indicates the area of injury in (A). (B) Describes Wallerian degeneration with the presence of macrophages, a break down in myelin and fewer Nissl bodies in the cell body. (C) Shows axonal regeneration through Schwann cell bands of Bügner. Image for illustration purposes only, not to scale (Maya, Autodesk).

1.3 Prevalence and cause of peripheral nerve injury

The prevalence and cause of peripheral nerve injury is not a topic that is widely researched, with studies often using small populations of patients or having other limitations. One study, by J Noble et al[55], is of particular interest with a relatively large patient population (5,777), and performed over a good length of time (10 years). These trauma patients were admitted to Sunnybrook Health Science Centre in Ontario Canada between the years 1986-1996. It was found that 2.8% of the patients admitted were identified as having an injury to at least one of the peripheral nerves of interest. Of this 2.8% of patients, with peripheral nerve injuries, it was found that motor vehicle accidents were responsible for 46% of these. If the data for motorcycle accidents is included then the figure rises to 55.9% of peripheral nerve injuries in this study was caused by motor vehicle and motorcycle related accidents. The most common nerve to be injured in this study was the radial nerve in the upper arm; it was also found that there was a higher incidence of peripheral injuries in the upper extremities compared with the lower. 54% of patients with peripheral nerve injuries required surgery. Of this 54% requiring surgical help for peripheral repair, only 62.5% of patients were found to have good accuracy with functional outcome and 34% of these were deemed to have had poor or no function after surgery, highlighting the need for alternative approaches/increased efficiency in peripheral nerve repair.

The study found that 55.9% of peripheral nerve injuries were caused by motor vehicle or motorcycle accidents. The worldwide vehicle population is increasing and reached over 1 billion vehicles in 2011, this may be an indicator that peripheral nerve injuries may also increase in numbers over the coming years – further highlighting the need to address the current repair techniques[69].

1.4 Peripheral nerve repair techniques

Following both World Wars, peripheral nerve repair became a greater issue of importance due to the vast amount of peripheral nerve injuries[70]. This led to a great deal of development in treatment methods for peripheral nerve repair. Presently there are three main clinical solutions practised to treat peripheral nerve injuries, these are suturing, auto-grafting and the use of a nerve guidance conduit.

1.5 Microsurgical repair (suturing)

Nerve regeneration generally only occurs if the severed nerve is separated by a short gap of 1-2 mm; any injuries with a larger gap in the severed nerve would require surgical intervention. If the injury creates a gap in the nerve larger than approximately 2mm but less than approximately 5mm, then the two nerve ends can be reconnected surgically without putting too much tension on the nerve cable. This technique is known as direct repair or end-to-end suturing. This would allow regeneration of the nerve, which should lead to functional recovery[57]. In this technique the entire nerve trunks are moved toward each other and reconnected together through sutures. The sutures are placed through the epineurium (outer most layer of peripheral nerve fibre.) As the epineurium contains elastic fibres, it can be stretched slightly to help facilitate the nerve reconnection and suture placement[71]. Microsurgical nerve repair can show impressive results, with success rates reported of up to 70% of patients exhibiting the return of motor and sensory functions[72]. Stretching of the nerve stumps excessively creates tension and can hinder the regeneration of the nerve. Therefore when there is a case of severe tissue loss, or a gap separating the nerve ends larger than approximately 5 mm, then the nerve is thought to be not suitable for simple reconnective surgery

and an alternative means for the management of nerve regeneration must be considered[73].

1.6 Autograft repair

Currently the most common treatment method for large gap peripheral nerve injuries (up to approximately 20mm) is autografting; this has become a "gold standard" therapy for nerve regeneration[74]. Autografting requires the removal of a nerve from the patient's own body and using it to bridge the gap at the injury site. The donor nerve used is usually the sural nerve[57]. The sural nerve runs along the foot, up the calf and is commonly used because it is deemed less important than the injured nerve and is almost entirely a sensory nerve[75]. The sural nerve is also used because it is a sensory nerve thought to cause the least trauma on the body. However, recent studies (2012) by Roberto S Martins *et al.* has shown that patients who have harvested their sural nerve tend to lose between 20-25% of sensitivity and between 5-7.5% of patients suffered from shock like pain, stabbing pain and numbness in the foot[76]. It is therefore understood that despite this treatment method showing the most effective large gap nerve regeneration results, it also has major disadvantages to the patient; including donor site morbidity, scarring, painful neuroma formation (growth of nerve tissue at donor site) and the requirement of multiple surgeries [77,78]. This increased number of surgeries could expose the patient to increased amounts of pain, excess trauma through surgery and an increased risk of infection. There are also a limited number of autologous donor nerves available. These are the problems motivating neuroscientists and surgeons to create better alternatives to autologous nerve grafts[72]. Nerve allografts from donor patients have been considered, however this method is particularly undesirable as the patient would require immunosuppressants to reduce the immune response witnessed from surgery[57].

1.7 Nerve guidance conduit repair

The third method currently used to aid nerve regeneration is to use a nerve guide conduit, generally this is a biocompatible tube of either natural materials or synthetic polymers, used to minimize axonal dispersion and create an appropriate microenvironment for nerve repair[57]. For many years the use of a nerve guides was seen as an alternative solution to the problem. As early as 1880 experiments were carried out by Gluck, exploring the possibilities of using a resorbable decalcified bone tube as a guided conduit for the regeneration of nerves[79,80]. Unfortunately it wasn't until 1882 that Vanlair was able to overcome the problem of scar formation and successfully apply the bone tube for the regeneration of the sciatic nerve within a dog[81]. Modern nerve guide conduits are typically tubular conduits made from natural materials or synthetic polymers. The main function of these conduits is to bridge the gap between the proximal and distal nerve stump, direct axonal growth, direct Schwann cell migration and prevent scar formation[57]. Currently natural materials such as, chitosan, laminin, fibronectin and collagen have been used with some success. Although, natural materials possess good cell binding domains for aiding neuronal and glial attachment and migration, and show good biocompatibility (desirable properties for nerve regeneration); they often lack the mechanical material properties to create an adequate 3D structure for nerve conduit guides. Further control and better success rates for nerve regeneration has motivated experimentation with synthetic materials. Using synthetic polymers allows control over reproducibility and degradation rates of nerve guides, however there may be a lack of cell control. The effectiveness of current clinical examples of NGCs is limited in the regeneration of the nerve at larger injury gaps. It is believed that this effectiveness can be increased with the use of appropriate materials, by

adding support cells, neurotrophins and by creating a suitable microenvironment design inside the tube[82,83].

1.8 Materials selection

Selecting the appropriate material for use with nerve guide conduits can prove to be crucial for the success of the nerve guide. When choosing a material for use as a nerve guide conduit it is important to consider many material properties, such as the Young's modulus, biocompatibility, degradation properties and the ability to be structured. By choosing a material with ideal properties, or by controlling the properties, it is believed that a more effective nerve guidance conduit can be designed.

The ideal material must have a similarly low Young's modulus to that of the native tissue (approximately 0.45 MPa) to ensure the surrounding tissue is not damaged, but must be stiff enough to allow it to be surgically manipulable[84]. The material must also be flexible, as if the material is too stiff tension would be created with the movements of the body. The material must be biocompatible, limiting any rejection by the body through an immune/inflammatory response. As with any non-biodegradable material in the body, the extended time it remains implanted increases the risk of complications; literature has shown these complications with non-biodegradable silicon nerve conduits[85]. It is therefore assumed that the ideal material should be biodegradable, however, the material must degrade in a suitable time frame following both the regeneration and maturation of the nerve. Conduit designs have also become more complex to enhance the regeneration of the nerve, it is therefore very important that the material can be structured easily into these complex designs[86].

Natural materials have been considered for use, as they have the added advantage of being naturally more biocompatible. The high success rates of regeneration and nerve function when using autografts, has led to research taking place looking at the use of allografts for nerve repair. The main risks with this are the risk of disease and an immune response. In order to use a fresh allograft it is necessary to use immunosuppressants, and even then an unwanted immune response can still be observed, as was shown in a study performed by Mackinnon (2001) *et al*.[87]. Decellularization of allografts would maintain the physical and structural cues of the natural tissue, whilst removing cellular material that would trigger an immune response. Thermal, radiation and chemical decellularization techniques have been studied on allograft nerves, each producing slightly different results. Thermal decellularization is the most common, however not all the cell fragments are removed and the extra cellular matrix is often destroyed. It is believed, however, that a combination of decellularization techniques could provide more useful results and research is still being conducted into the use of decellularized nerves[88]. Natural materials such as chitosan, collagen, silk and many more have been studied for use in peripheral nerve repair. These highly biocompatible materials contain extracellular matrix molecules such as Laminin, Collagen and Fibronectin which have been shown to play a role in axonal growth[89–92]. The natural materials can possess good cell binding domains for aiding neuronal and glial attachment and migration, showing good biocompatibility; however they often lack the mechanical material properties to create adequate 3D structures for nerve guidance conduits.

Synthetic materials provide a more attractive choice for conduit material as they possess higher levels of adaptability. Degradation rates, mechanical properties and the structurability of the conduits can all be adapted

depending on the material chosen. Synthetic conduit materials are often soft biocompatible polymers made from lactic, glycolic acid and caprolactone[86]. Biocompatibility of the polymer is also very important to minimize the foreign body response.

1.9 NGC design

Whilst there has been much research into complex conduit designs, most clinical examples still use the simple single lumen, hollow tube. Research has explored alternative designs including the use of growth factors, supporting cells, collagen and laminin containing gels, incorporating a microenvironment within the tube, creating a permeable conduit and the use of an electrically conductive conduit[93].

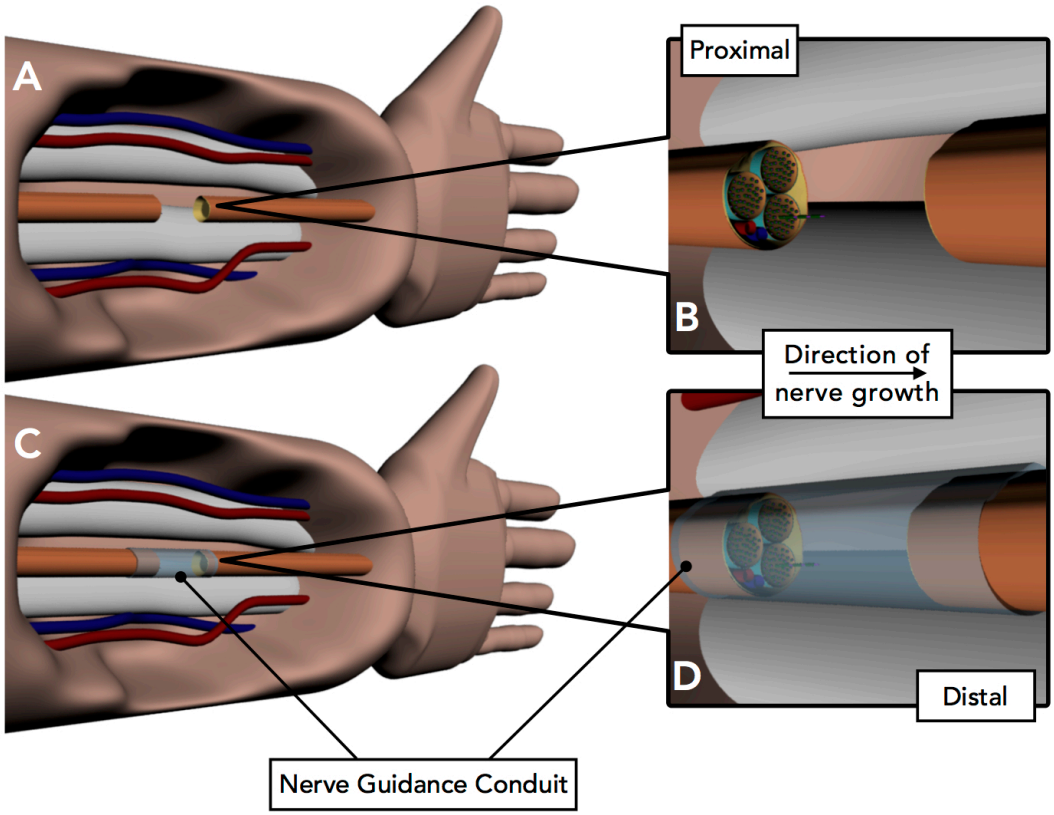

Figure 33: Computer model of PNI (A) and surgical repair using a conduit (B). Magnified images (B,D), showing the axonal growth following injury. Nerve in greater detail (B), blood vessels, fassicles and extending axons are present. (D) describes in detail the operation of a simple nerve guidance conduit, aligning axonal growth across the injury site (Maya, Autodesk)

1.10 NGC design - Collagen and laminin gels

Collagen and laminin containing gels have been explored by often simply filling the interior of a conduit/tube. Vitrogen (PureCol, Advanced BioMatrix) and Matrigel (Matrigel, Corning) are two common gels investigated[94]. The extracellular matrix components within the gel may aid regeneration by providing an attractive substrate for the infiltration of cells and the binding of neurotrophic factors. The source of the collagen and laminin can however be a disadvantage; with examples often sourced from tumour cells or bovine sources[86].

1.11 NGC design - Growth factors

Following injury, specific neurotrophic factors are released from the ends of the transected nerve to aid the support, survival, differentiation and regeneration of nerve tissue[95,96]. The inclusion of growth factors within the conduit has been seen to increase the efficacy of the conduit[97]. The growth factors can be added in solution to the inside of the tube, however, as the inclusion of growth factors is dose dependent they are often introduced using a delivery system such as microspheres or a porous mat[98]. This not only allows for the slow release of the growth factors but also provides an internal structure that may further aid regeneration. The most common growth factors explored are NGF, GDNF, neurotrophin-3 and FGF. The inclusion of growth factors may however over complicate the conduit, with extra care required during sterilization and also biological activity lowering over time[86].

1.12 NGC design - Supporting cells

Schwann cells are often incorporated to increase the efficacy of NGCs. Schwann cells are known to be actively involved in the regeneration of the

peripheral nerve and in forming the bands of Bügner. It is thought that the inclusion of these cells within the conduit would allow for easier formation of the bands of Bügner and the secretion of matrix molecules and neurotrophic factors stimulating regeneration. Whilst this seems like an attractive modification to the simple tube there are problems when translating to clinic. Cells must be harvested prior to implantation, using valuable time after injury. Also, as autologous cells are preferred, a donor nerve would still be required, triggering the disadvantages associated with autograft repair. Some research has, however, overcome some of these disadvantages by using bone marrow stem cells (BMSCs)[99].

1.13 NGC design - Internal microenvironments

Providing an internal microstructure would provide support for extending axons to adhere to. Many different designs and materials have been explored to create an internal microenvironment including the use of gels, the creation of microchannels, the use of denatured muscles and electrospun fibres. It is thought that whilst the inclusion of a microenvironment does considerably complicate the conduit design, it may also provide a considerable improvement on the effectiveness of the NGC. More complex conduit designs are often limited due to the small scale of the features required, however 3D printing and stereolithography techniques may offer an attractive method to produce the small scale complex internal microenvironment designs[100].

1.14 NGC design - Conductive conduits

It is believed that electrically conductive polymers may aid regeneration by accelerating axonal regeneration and can be used to align growth through

electrical stimulus. Research in this area has however been limited due to the non-biodegradable nature of conductive polymers[86,101].

1.15 NGC design – Permeable (porous) conduits

Permeability and porosity is an important consideration in the design of NGCs. To more closely mimic the native nerve, porosity is necessary to allow nutrient exchange. This is discussed in more detail in chapter 3.4.

1.16 Clinical nerve guidance conduits

In 2007 Axogen Inc, produced a commercially available decellularized cadaveric allograft called Avance and has since sold over 5000 units[88]. One study by Karabekmez *et al.* in 2009 looked at the early outcomes following the use of decellularized nerve allografts for peripheral nerve repair. The study concluded that there were no immune responses observed from the ten patients and that there was sensory improvement in all ten cases for allograft lengths between 0.5 to 3 cm[102]. The use of decellularized conduits is therefore an interesting one, however the conduits commercial success may be limited by the availability and ease of obtaining the allografts. Synthetic alternatives are being readily explored.

Initial synthetic options, involved the use of non-degradable silicon tubes. The main problem with these tubes was that over time chronic inflammatory responses would occur[103–105]. Biodegradable synthetic alternatives were then explored, many of which gained FDA (Food and Drug Administration) approved status. Many of these degradable conduits were made from FDA approved polymers and natural collagens. NeuraGen (Integra neurosciences) and Neuramatrix (Collagen matrix Inc)[106], were two of these FDA approved

biodegradable conduits that were made up of collagen type 1, degrading in 4 years and in 7 months respectively. Biodegradable synthetic polymer conduits have also been FDA approved, such as Neurotube (Synovis) and Neurolac (Polyganics BV). Neurotube is made of PGA poly glycolic acid, whereas Neurolac is made of Poly-DL-Lactide-Caprolactone, degrading over 3 months and over 16 months respectively. Whilst these biodegradable conduits essentially eliminated problems regarding chronic inflammation, both the synthetic and natural conduits' efficacy is limited when nerve gaps reach approximately 5 mm[105]. It is therefore thought that improved material selection, may vastly affect the efficacy of these nerve guide conduits. One material, which has been recently explored for peripheral nerve tissue engineering is poly glycerol sebacate.

1.17 Polyglycerol sebacate for peripheral nerve repair

Poly(glycerol sebacate) has been discussed previously (chapters 1 and 3.1). Briefly, the material is a soft, degradable, biocompatible polymer, ideal for soft tissue engineering. Whilst the material properties suggest the polymer would be useful for peripheral nerve repair, there has been little PGS research in this area. Sundback *et al.* has explored PGS for peripheral nerve repair, concluding that the material had no Schwann cell toxicity and deeming the material a good candidate for neuronal repair[35]. There was also minimal unwanted tissue response found from *in vivo* tests. Whilst the reports suggest PGS is an appropriate material for peripheral nerve repair, the study did not structure the material into nerve guidance conduits, or assess the ability of the polymer to aid nerve regeneration. Structuring PGS is known to be difficult due to the additional thermal curing requirements and as of yet structured PGS conduits for peripheral nerve repair have yet to be studied.

1.18 PGSm nerve guidance conduits

Poly(glycerol sebacate methacrylate) has been discussed in detail previously (chapter 3.1). Briefly methacrylate moieties have been added to the biomaterial PGS, making the material photosensitive, allowing it to be structured via stereolithography. PGSm is a novel formulation of the well-known biomaterial PGS and has yet to be explored for peripheral nerve repair. Whilst maintaining the advantages of using PGS for soft tissue engineering, PGSm also overcomes the tricky issue of structuring the polymer into simple and complex NGCs. This chapter will assess the use of PGSm as a material for peripheral nerve repair through the use of mechanical, *in-vitro, ex-vivo* and *in-vivo analysis.*

2. Methods

In-vitro analysis

For all *in-vitro* analysis experiments flat disks of PGSm were cured onto functionalized glass cover slips, full methodology can be found on page 14.

2.1 Neuronal cell culture

All polymer scaffolds and glass cover slip controls were sterilized in the same method prior to all cell seeding. Scaffolds and coverslips were submerged in 70% EtOH for up to 7 days, with fresh EtOH supplied every day. After EtOH sterilization the scaffolds and cover slips were washed three times in excess PBS for a period of fifteen minutes each time.

Neuronal (NG108-15 cells, Sigma-Aldrich, UK) passage 8/9, were cultured in a high glucose Dulbecco's modified Eagle's medium (DMEM), containing 10% (v/v) fetal calf serum (FCS), 0.25 μg/mL amphotericin B, 100 units/mL penicillin, 100 μg/mL streptomycin and 2 mM L-glutamine. Cells were

incubated at 37°C with 5% CO_2 and passaged when they reached 70-80% confluence, or every four days; whichever occurred first. Cells were detached from T75 culture flasks by removing medium, gentle washing and introducing 5 mL trypsin-EDTA solution (Sigma-Aldrich, UK) for approximately two minutes or until cell detachment was observed under the microscope. The trypsin was then immediately inactivated by the addition of FCS containing culture medium. The cell suspension was centrifuged at 200 g for 5 minutes, the supernatant was removed, the remaining cell pellet resuspended in 1 mL of medium and cells counted. Neuronal cells were seeded at a density of approximately 375 cells/mm^2 onto flat PGSm disks and glass coverslips. Cells were grown in medium containing FCS for 48 h to facilitate cell attachment and proliferation. After 48 h, the serum-containing medium was removed and serum free medium was introduced to encourage differentiation of the neuronal cells. Samples were incubated at 37°C, 5% (vol/vol) CO_2 and fresh medium changes were conducted every 3-4 days.

2.2 Schwann cell culture

Primary Schwann cells were isolated from 10-12 week old male Wistar rats, killed according to the regulation of Animals (Scientific Procedure) Act 1986, using a Schedule 1 method of cervical dislocation (Home Office, U.K.) The isolation, culture and purification methods followed were of those outlined by Kaewkhaw *et al.*[107] Briefly a 35 mm Petri dish coated with poly-l-lysine and laminin was initially used to culture the Schwann cells. The sciatic nerve was removed, epineurium stripped off and the nerve fascicles gently broken into smaller bundles. Collagenase was then used to dissociate the nerve tissue. The resulting cell suspension was filtered through a 40 μm cell strainer and then centrifuged at 400 G for 6 min. The cell pellet was washed in 10% FCS/DMEM and centrifuged again. The supernatant was removed and the pellet resuspended with Schwann cell culture medium.[107] The cell suspension

was then added to the Petri dishes and incubated at 37°C, 5% (vol/vol) CO_2. Fresh medium (MEM-D-valine containing 10% (v/v) FCS, 100U/mL penicillin, 100 µg/mL streptomycin, 0.25 µg/mL amphotericin, 5 µM forskolin and 2 mM L-glutamine) changes were conducted every 3-4 days and cells were passaged into tissue culture polystyrene T75 flasks once confluency was reached. Schwann cells were used for experimentation between passage 2-4.

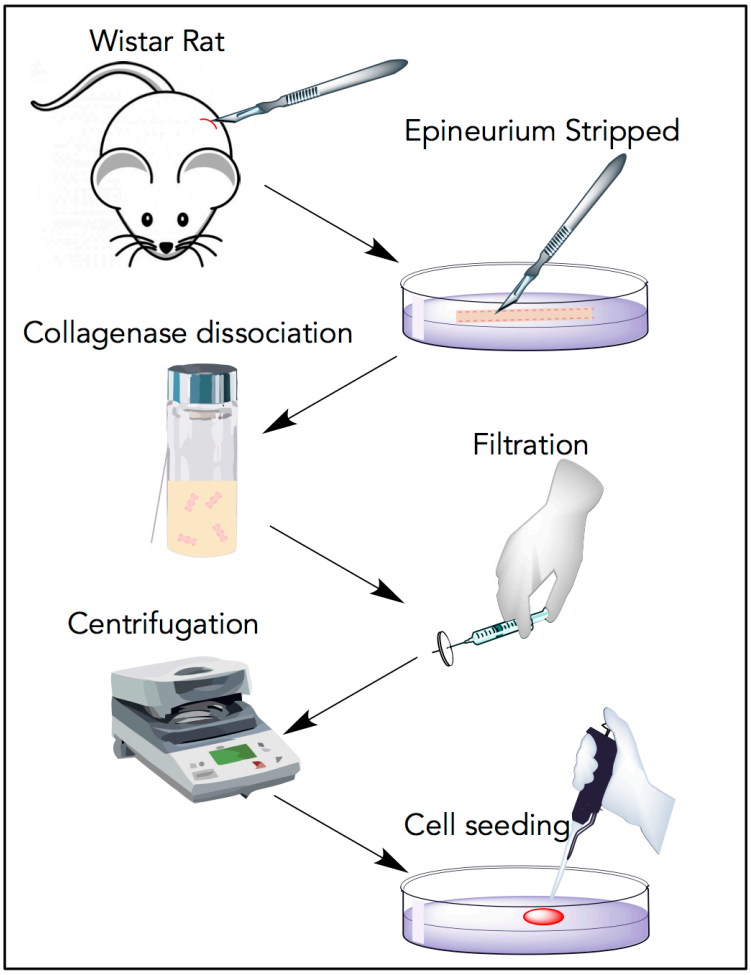

Figure 34: Computer designed image outlining Schwann cell isolation

2.3 Live/Dead analysis of neuronal and Schwann cells

Culture medium was removed from samples at experimental time points. Fresh culture medium was added containing 0.001% (v/v) Syto-9 (Invitrogen) and 0.0015% (v/v) propidium iodide (Invitrogen) and incubated at 37°C / 5% CO_2 for 15 minutes. The medium was then replaced with fresh medium and imaged using an upright Zeiss LSM 510 confocal microscope with an argon

ion laser (488 nm) for the Syto-9 label (λ_{Ex}/ λ_{Em} = 494 nm / 515 nm) and a helium-neon laser (543 nm) for the propidium iodide label (λ_{Ex}/ λ_{Em} = 536 nm / 617 nm). Resultant images, live cells labelled with syto-9 (green) and dead cells labelled with propidium iodide (red), were quantified using NIH Image J and a cell counter plugin. Three random field of view images were taken of each scaffold and the quantification of live versus dead cells was represented as a percentage. Neuronal live/dead studies were analysed on days 4 and 6. Schwann cell live/dead studies were analysed on days 2 and 4. A minimum of nine images from three separate experiments for each variable was analysed (minimum, *n=3)*. Standardized non-bias methodologies were used to sample all random images.

2.4 Neuronal neurite analysis

Neuronal cells were seeded onto scaffolds and cultured in DMEM with FCS (as above), after 48 h medium was removed and serum free medium introduced. On days 4 and 7 scaffolds were gently washed in PBS and neuronal cells fixed with 3.7% paraformaldehyde at room temperature for 15 minutes. Scaffolds were washed thrice in PBS and immersed in ICC buffer (immunocytochemistry buffer, 1% bovine serum albumin, 0.1% Triton X-100 in PBS) to block and permeabilise for 20 min at room temperature. Cells were incubated with a primary mouse anti-beta-III-tubulin antibody (ThermoFisher) at a 1:1000 titre in ICC buffer and refrigerated at 4°C overnight. The scaffolds were then washed in PBS and a secondary rabbit anti-mouse IgG Alexa Fluor 488 (λ_{Ex}/ λ_{Em} = 490 nm / 525 nm, ThermoFisher) was added at a 1:500 titre in ICC buffer for two hours at room temperature. Neuronal cells and scaffolds were washed in PBS and a 300 nM DAPI solution (λ_{Ex}/ λ_{Em} = 358 nm / 461 nm, ThermoFisher) in PBS (1 µg/mL) was added for ten minutes at room temperature. The scaffolds were placed in a 6 well plate, rinsed thrice for 5

min with PBS and three images were randomly sampled using an upright Zeiss LSM 510 confocal microscope with a water-dipping objective (Objective W N-Achroplan 10x/0.3, Zeiss, US). From each image 50 cells were sampled at random using an image grid and a computer random number generator. Results recorded for neurite population number, the number of neurites on each cell and the length of the neurites. Cells were counted using NIH Image J and the cell counter plugin.

NGC production and analysis

Conduits of different designs were produced experimentally with success, however, for the purposes of this initial PGSm study a simple single lumen tube was produced.

2.5 Micro-stereolithography NGC production

NGC tubes were produced by microstereolitography using PGSm (0.75 degree of methacrylation, 2wt% photoinitiator, 2-hydroxy-2-methylpropiophenone, Sigma-Aldrich, UK). A 405 nm laser (Vortran Stradus 405nm) was directed through a series of lenses, focusing and collimating the beam onto a DMD (digital micromirror device, DLP7000, Texas instruments). A computer-designed image was uploaded to the DMD, (Software ALP-4.1, basic Controller Suite). The cross sectional tube image was reflected off the DMD onto a mirror and down onto the liquid PGSm polymer. PGSm cured at the surface, crosslinking and hardening into the cross-sectional tube design. A Z-stage (Thorlabs) with platform was slowly lowered into the liquid polymer (0.3 mm/s), allowing the cross-linked material to lower and be replaced with unpolymerised PGSm on top, which in turn was polymersied, creating a 3D printed structure. Once the desired height was reached the NGC was carefully removed from the Z-stage and placed in methanol to allow any uncured polymer to be washed away. Post process laser cutting was used to

cut the ends of the tube (Mini 18 Laser, Epilog Laser, 40W). The Mini 18 Epilog laser was set to a power of 10% (4 W) and a vector write speed percentage of 20%. This created a 'clean' finish to the proximal and distal portions of the NGC tubes.

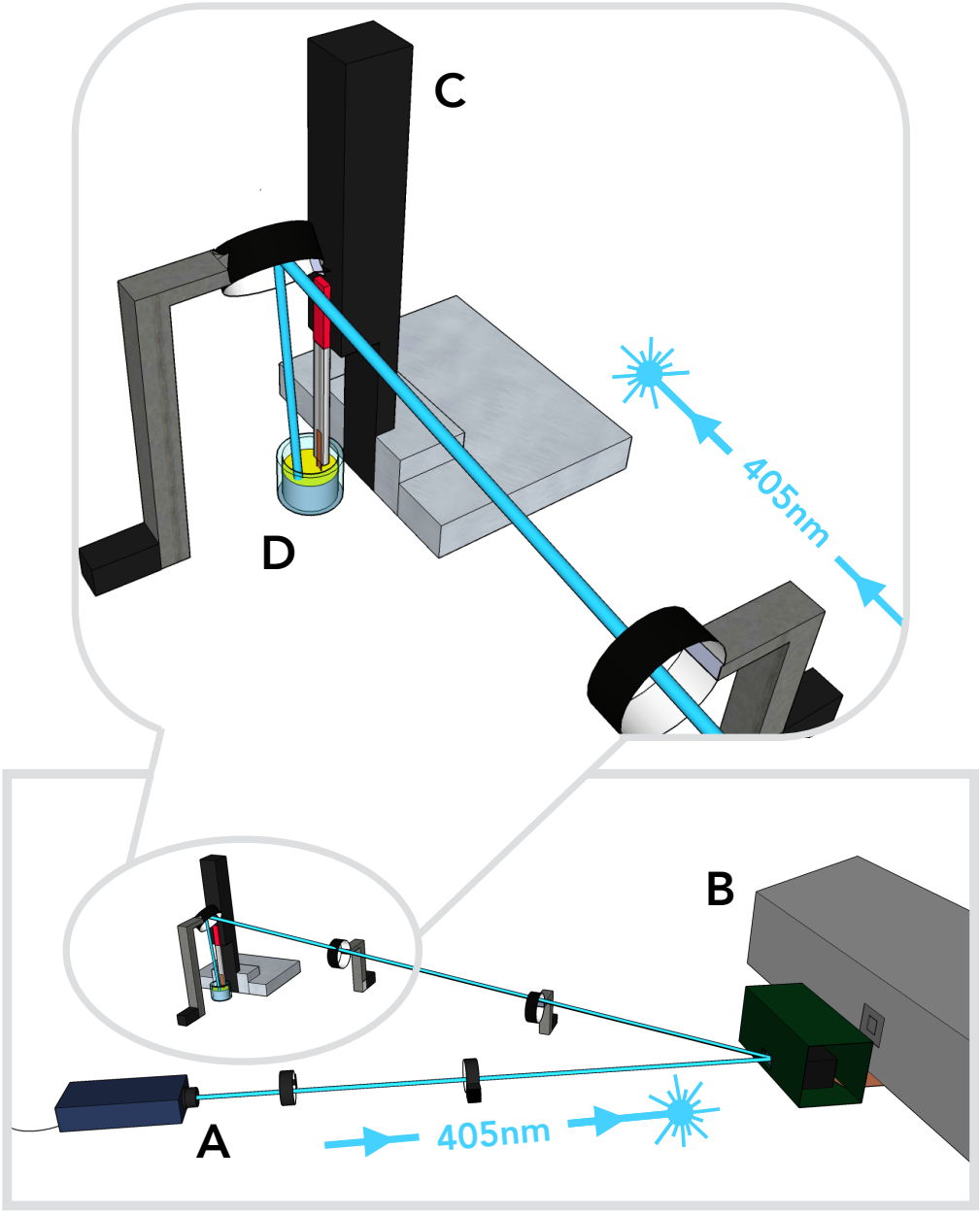

Figure 35: Computer designed model (Google Sketchup) of the micro stereolithography setup used to produce nerve guidance conduits (NGC's). A 405nm laser (A) emits light through a series of lenses focusing the beam onto the surface of a digital micromirror device (DMD) (B), the DMD reflects a computer designed image down onto the surface of a motorized Z-stage (C), which lowers into a container of liquid polymer (D). As the UV light hits the surface of the polymer a Z-stage lowers, carrying the crosslinked polymer down and fresh

uncrosslinked PGSm onto the surface. As the stage is lowered, the polymer crosslinks and 3D structures are formed.

2.6 NGC mechanical testing and Suture retention strength

NGC tubes were produced at 5 mm in length and 700 µm internal diameter, with a 350 µm wall thickness for *in vivo* implantation. Compressive mechanical properties were assessed using a Hounsfield mechanical tensometer and 10 N load cell. The compression test was set at a rate of 0.25 mm/min with a max load of 10 N. Modulus values were calculated, with example methods described below.

$$E = \frac{\sigma}{\varepsilon}, \qquad \sigma = \frac{F}{A_o}, \qquad \varepsilon = \frac{\Delta l}{l_o},$$

$$\therefore E = \frac{F l_o}{A_o \Delta L}, \qquad E = \frac{F}{\Delta l}\frac{l_o}{A_o},$$

$$A_o = \left(\pi\left(\frac{1.35mm}{2}\right)^2\right) - \left(\pi\left(\frac{1mm}{2}\right)^2\right) = 1.48mm^2,$$

$$l_o = 5mm, \qquad \frac{A_o}{l_o} = 3.378mm,$$

$$y = mx + c, \qquad F = m\Delta l + c, \qquad \frac{F}{\Delta_l} = m,$$

$$\therefore E = 3.378m$$

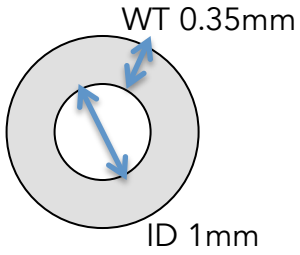

E = Youngs Modulus,
σ = Stress,
ε = Strain,
A_o= Cross Sectional Area
l = length
m = gradient of line

A suture was made in the NGC tube, 1 mm from the end of the tube using 9-0 Polyamide sutures. The conduit and suture was placed into the grips of the Hounslow testing machine and the machine tested the sample under tensile tension until failure at a rate of 0.25 mm/min. The suture retention strength of the material was calculated using techniques described in literature (load/suture diameter x wall thickness)[108].

Ex-vivo analysis

Conduits were produced as above and then bisected into a hemitube and attached to a glass cover slip for experimental and imaging purposes.

2.7 Dorsal Root Ganglion extraction and ex vivo seeding

A dorsal root ganglion body is unipolar, having a stem that extends towards the spinal chord and one that branches into the peripheral nervous system, making it a good model for both the PNS and the CNS. Complete isolation of rat DRGs can yield up to 40 DRG's and 100,000 neurons[109]. Rats were obtained and culled in accordance to all home office legislation and in accordance to the Animals (Scientific Procedures) Act 1986 (schedule I method).

Dorsal root ganglia were extracted from the spine of 8-12 week old male Wistar rats. The rat was placed on its stomach and an incision was made at the top of the neck, through the skin. A line was cut using sharp pointed scissors down the vertebral column and to the tail of the rat. The skin was peeled away and excess adipose tissue removed around the spine. The vertebral column was removed and excess tissue cut away. The spinal chord was cut in two for easier handling. A sagittal cut was made down the dorsal side of the vertebrae, exposing the spinal chord. The spinal chord was gently moved to one side, exposing the DRG connections to the spinal chord. These connections can be followed into the vertebrae laterally and using sharp tweezers the DRG bodies gently removed. DRGs were placed into culture medium (high glucose DMEM, containing 10% (v/v) fetal calf serum (FCS), 0.25 µg/mL amphotericin B, 100 units/mL penicillin, 100 µg/mL streptomycin and 2 mM L-glutamine) during dissection. The DRGs were then seeded onto PGSm NGCs for three weeks, with medium changes every 3 to 4 days.

2.8 DRG immunohistochemical staining and image acquisition

To facilitate *ex vivo* DRG analysis, hemitube NGCs were used (NGCs bisected longitudinally) to permit for confocal microscopy. DRG's were fixed as above for 30 minutes and then immunostained with primary rabbit anti-S100-beta polyclonal antibodies, at 1:250 titre (ThermoFisher) in ICC buffer and primary mouse polyclonal antibody beta-III-tubulin 1:1000 (ThermoFisher) in ICC buffer overnight at 4°C. Secondary antibodies Alexa Fluor 488 rabbit anti-mouse IgG (λ_{Ex}/ λ_{Em} = 490nm / 525nm, ThermoFisher) and Alexa Fluor 546 goat anti-rabbit (λ_{Ex}/ λ_{Em} = 556nm / 573nm, ThermoFisher) were added at a titre of 1:100 in ICC buffer for two hours at room temperature. Hemitubes seeded with DRGs were imaged using an upright Zeiss LSM 510 confocal microscope (EC Plan-Neofluar 40x/1.30). Images were taken across a z-stack (separation distance 25 µm, number of slices 12, total z-distance 300 µm, airy unit 1.5 AU) and compiled into a composite image, several composite images were stitched together (18 stitched composite images, Photoshop CS 2015, Adobe) to produce an image of the entire hemitube.

In-vivo analysis

PGSm NGCs (5 mm) were structured in the methods outlined above. Conduits were placed in methanol to remove any uncured polymer. NGCs were then sterilized in 70% EtOH, washed and stored in sterile PBS until implantation.

2.9 In vivo implantation of NGCs - common fibular injury model

In vivo implantation and image acquisition was performed by Adam Harding and Emad Albadawi (University of Sheffield, School of Dentistry). Raw data provided was analsed by both Adam Harding and myself. *In vivo* methodologies were performed in concordance with literature[110]. Briefly, from

a Home office approved supplier, Thy-1-YFP-H mice (YFP+) were obtained (JAX® mice, Maine, USA via Charles River UK Ltd, Margate, UK) and experiments were performed under UK Home Office project and personal licenses, in accordance with the Animals (Scientific Procedures) Act 1986 and with local ethical approval. Twelve YFP+ mice and 6 wild type C57B/6J (WT) mice were used for experimentation (18 total). For experimentation the PGSm NGC group consisted of 6 YFP+ mice (2 excluded from results due to technical failures) and the graft repair group consisted of 6 YFP+ and 6 WT mice. A 3 mm injury gap was created in the mouse and either a 5 mm conduit or nerve graft was fixed into place, bridging the gap from proximal to distal stump. After a period of three weeks the mice were anaesthetised and the common fibular nerve exposed, fixed and removed. Full methodologies for the model can be found in literature (Pateman et al).[110]

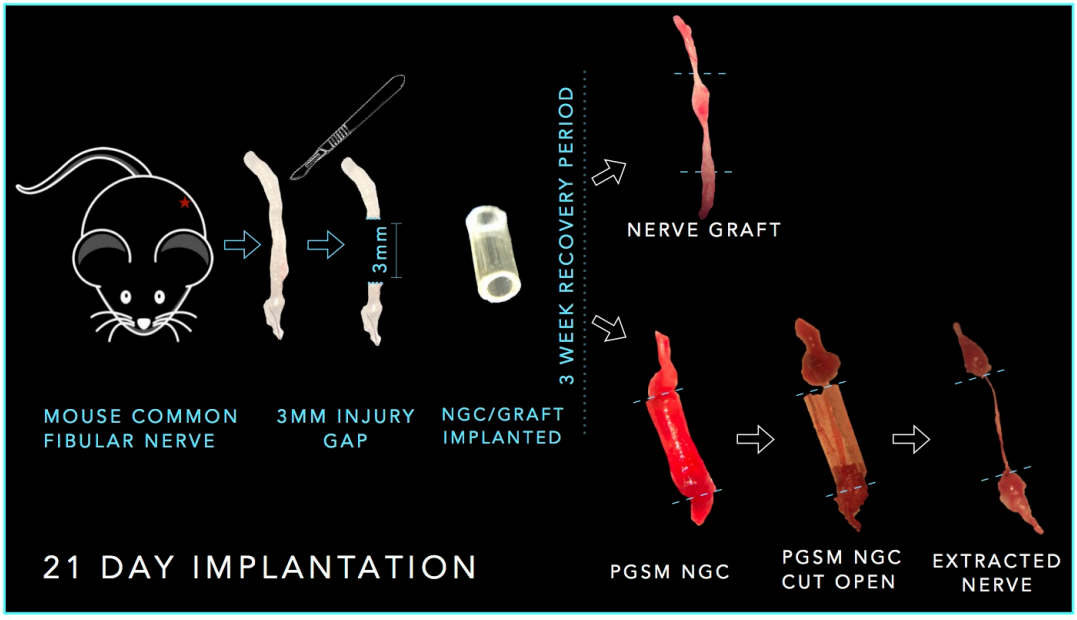

Fig 36: Annotated diagram outlining the basic methodology for peripheral nerve common fibular injury repair using a nerve graft and a PGSm conduit. (Digital images edited, Keynote, Apple)

2.10 In vivo image acquisition of nerves

Following *in* vivo expereimentation nerves were imaged in z-stacks using epi-fluorescence microscopy (Zeiss Axioplan2 Imaging microscope with QImaging QI Click camera) using Image Pro-Plus software (λ_{ex} = 467-498 nm / λ_{em} = 513-556 nm, 10x objective, 30 x 10 µm z-stack sections). These z-stacks were stiched together to obtain a composite image of the entire nerve (8-10 z-stacks, Adobe Photoshop). Full methodology can be found in literature (Pateman et al)[110].

2.11 In vivo nerve image analysis

Methodologies were used, in concordance with literature to determine the sprouting index (new axons at intervals), axon tracing (percentage axons remaining from proximal stump/start) and axon disruption (percentage increase in length of axons from the most direct route to regeneration) from the PGSm NGCs[110]. Full methodology in literature (Pateman et al)[110].

2.12 In vivo neuropathic pain analysis

Spinal cords were harvested (whilst within the vertebral column) immediately following the experimental cull and immersed in 4% (w/v) paraformaldehyde for 24 hours. Spinal cords were then dissected out of the vertebral column, immersed in a 30% (w/v) sucrose solution for 24 hours, frozen in OCT fluid and stored at -80°C.

2.13 IHC staining for neuropathic pain markers

IHC staining for neuropathic markers was performed by Emad Albadawi (University of Sheffield, School of Dentistry). The OCT embedded spinal cord tissues were mounted in a cryostat (Microm HM 560, Zeiss, UK) and transverse sections cut until reaching the L4 section. 10 µm thick sections were then collected (8-10 sections from each sample) and placed in separate wells of a 24 well plate containing Phosphate Buffer Saline (PBS). The sections were

washed twice in PBS to remove the sucrose solution and twice in Phosphate Buffer Saline-Triton (PBS-T; Fisons Scientific Equipment, Loughborough, UK) for 10 minutes. Sections were then incubated with PBS-T containing 10% Normal Donkey Serum (NDS; Jackson ImmunoResearch Inc, West Grove PA, USA) for 1 hour at room temperature. Sections were then incubated with PBS-T containing 5% normal donkey serum, NDS including the primary antibody Iba-1 goat polyclonal antibody (1:2500, Abcam, UK) for microglia, or GFAP rabbit polyclonal antibody (1:2000, Abcam, UK) for astrocytes. Following an overnight incubation at 4°C, the sections were washed twice in PBS for 10 minutes before secondary antibody incubation, Donkey anti-goat Cy3 antibody (1:500, Jackson, UK) for microglia, or Donkey ant-rabbit Cy3 antibody (1:500, Jackson, UK) for astrocytes, in PBS-T containing 2% NDS at room temperature for 2 hours in the dark. After a final PBS wash, the prepared sections were mounted onto glass slides (typically 3-5 sections on a slide) and coverslip attached with Vectashield® (Vector Lab, Burlingame, CA, US). Immunohistochemical controls were performed via omission of primary antibody.

2.14 IHC image acquisition and analysis of neuropathic pain markers

Immunohistochemical images were acquired using a fluorescent microscope (Axioplan2 Imaging; Zeiss, Welwyn Garden City, UK) fitted with Qimaging Retiga 1300R camera, and combination excitation filter Cy3 filter was used to examine the fluorescent markers. The microscope was linked to a PC running Image-Pro Plus v.7 software (Media Cybernetics, MD, USA). Five pictures from each section were taken; one for the whole section (using 5× magnification), two for a specific area (CFN projection) in the dorsal horn on both ipsilateral and contralateral sides (using 40× magnification), and two for a specific area (area of CFN project on) in the ventral horn on both ipsilateral and contralateral sides (using 40× magnification.)

Image-Pro Plus v.7 software (Media Cybernetics, MD, USA) was used to quantify the percentage area of Iba-1 and GFAP labeling. This system enables the percentage area of glial labeling to be calculated. The activation areas were highlighted by red, while the remaining areas were highlighted by yellow (Fig 37). Each reading was taken three times, and the mean average calculated.

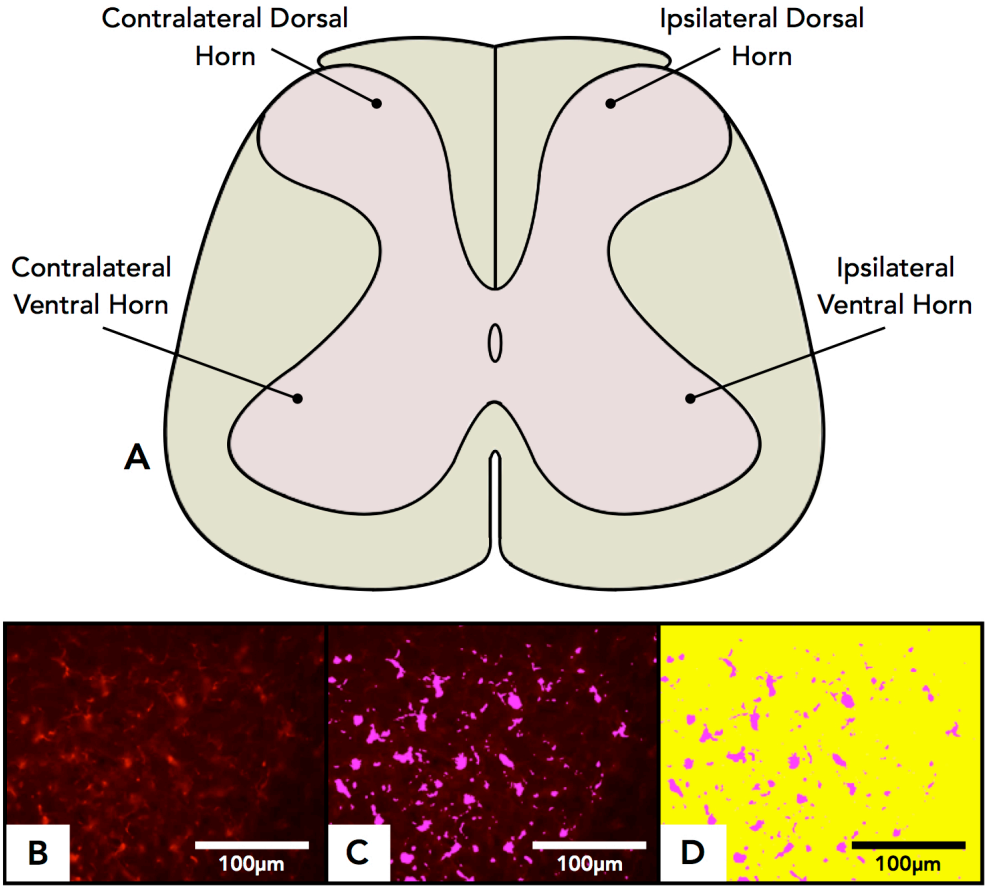

Figure 37: Computer designed annotated image of the L4 segment of spinal cord (A), this segment of spinal cord was analysed for neuropathic pain data. (B) a high magnification example image from an area of the L4 segment of spinal cord of the activation area (bright dots). The image underwent image analysis, (C) the process of highlighting the activation area (pink). (D) further analysis with the highlighted activation area (pink) and background (yellow). The contrast between pink and yellow allows for clear ratios of activation area to be obtained. Scale bar 100 µm.

2.15 Statistical analysis

Statistical comparisons between groups were made using GraphPad Prism (GraphPad Software, San Diego, CA). 2-way Tukey ANOVA tests with multiple comparisons were used to compare *in vitro* testing groups. For the sprouting index and axon tracing comparisons, a 2-way ANOVA with Bonferroni post-tests was performed and for axon disruption and glial comparisons a 2-tailed Student's t-test was used. Differences were considered significant when $p<0.05$.

3. Results

3.1 In vitro neuronal cell analysis

In vitro analysis experiments were performed on flat disks of PGSm with different degrees of methacrylation and a glass control. Live / dead neuronal cell results (Fig 38, A, B), show that all samples had a high percentage of live cells. There was a significant difference between live / dead results from the PGSm degrees of methacrylation and the glass control, with PGSm samples having a higher percentage of live cells than that of glass. Also there was a statistical increase in cell numbers between days 4 and 6, showing that cells were able to proliferate on the polymer surface *($p < 0.0001$).*

As neurite outgrowth is a marker for differentiation, the average neurite length was studied from confocal images to analyse the neuronal differentiation ability on PGSm (Fig 38, C). There was an overall statistical increase in neurite length from all of the degrees of methacrylation from day 4 to 6, which suggests that the neurites were able to extend with time and that neuronal differentiation is possible on PGSm.

Schwann cell live / dead results (Fig 38, E, F, G) showed that over days 4 and 6 there was a very high percentage of live cells on both the glass control and the PGSm scaffolds. There was no statistical difference between the Schwann cell growth on PGSm and glass scaffolds or between days 4 and 6; suggesting no increased Schwann cell toxicity of the PGSm disks compared with the glass control.

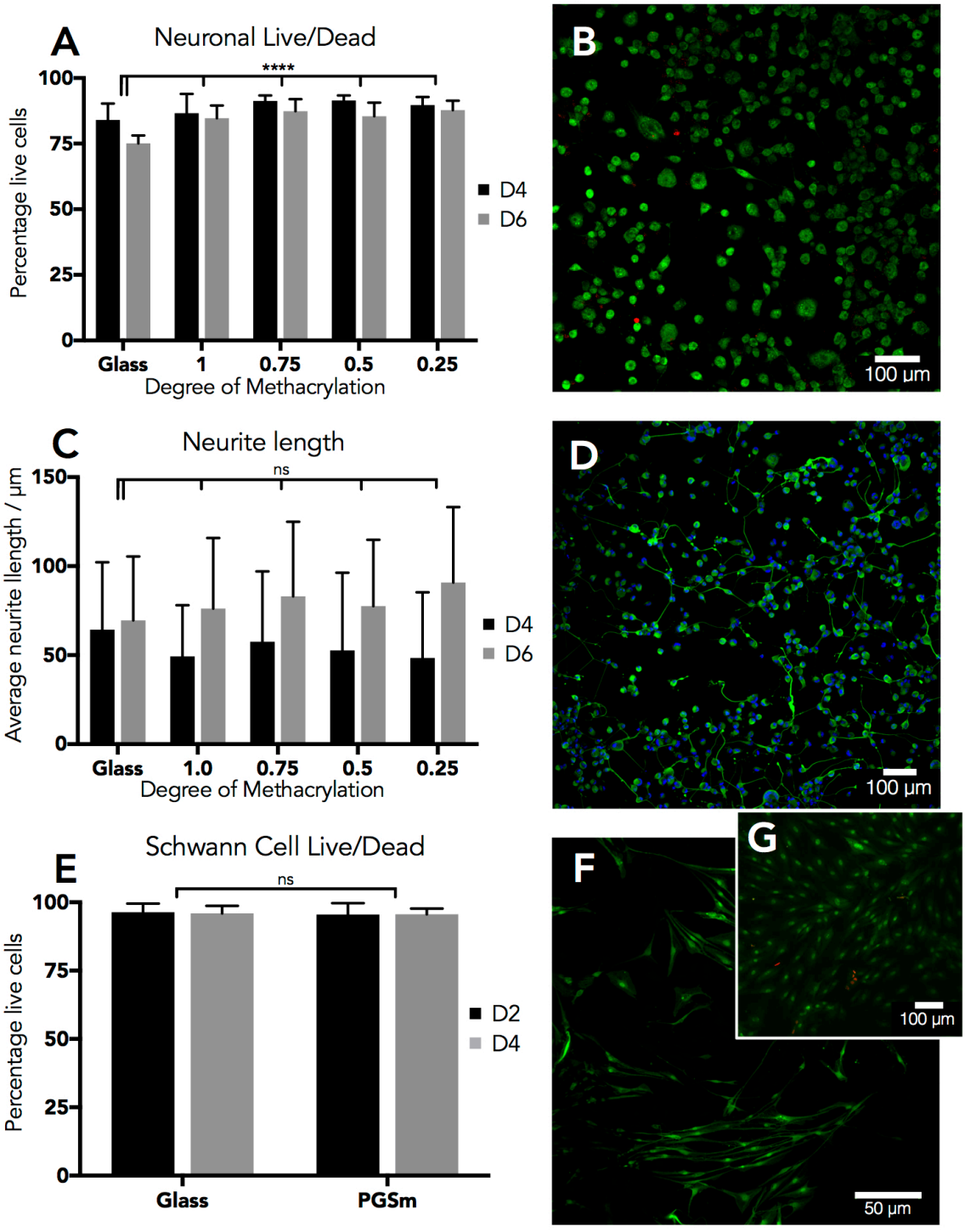

Figure 38: Neuronal cell live/dead graphs of the neuronal cell response when grown on different methacrylations of PGSm (n=6) (A). A corresponding example confocal micrograph, (B). Between the PGSm groups, 4 of the 6 comparisons showed no significant difference, only the highest methacrylation PGSm 1.0, showed a difference between the 0.75 and 0.25 methacrylation groups, ($p = 0.0102$, $p = 0.0456$). There is also a significant difference between days 4 and 6 ($p > 0.0001$). Statistical analysis showed a difference between the glass control and each of the PGSm groups (shown on graph) ($P < 0.0001$). Standard two way ANOVA with multiple comparisons (Tukey) was used to analyse all data.

Neurite length - (C) the average neurite length of differentiated neuronal cells on flat surfaces of PGSm of different degrees of methacrylation, on days 4 and 6 (n=6). Beta-III-tubulin and DAPI were used to show the neurite length in green and nucleus in blue (D). There was no statistical difference between the glass control and any of the degrees of methacrylation (shown on graph). Again, amongst the PGSm groups 4 of 6 comparisons showed no significant difference; only the highest degree of methacrylation 1.0 showed a difference between the 0.75 and 0.25 methacrylation groups ($p = 0.0127$, $p = 0.0303$).

Schwann cell live/dead - (E) Schwann cell live dead study. Schwann cells were seeded onto flat disks of PGSm and a glass control, live dead study performed on days 2 and 4 (n = 8). Live cells in green and dead cells in red (G). No statistical difference was seen between the time points ($p = 0.9018$). No significant difference was seen between the PGSm or glass groups ($p = 0.5799$) (shown on graph). The corresponding confocal image shows Schwann cells seeded onto the surface of PGSm, immunohistochemically labeled with S100-beta. The Schwann cells maintain a typical morphology and aspect ratio on the surface of the polymer.

3.2 3D printing NGC's

Conduits were synthesized using microstereolithography with a varied laser power, which showed signs of under and over curing (Fig. 39, Table 2). Overcuring can be seen (Fig 39, A and B) with an undulating wall surface. If the write speed became too quick then under curing could occur, with incorrectly formed, unstable NGCs (Fig 39, D). Table 2 outlines the parameters used to create the NGC's, with row C showing the optimum laser

and speed settings. Conduits were laser cut to an exact length. Fig. 40 shows SEM images of conduits before and after laser processing. Precise and reproducible PGSm NGCs were synthesised by this method.

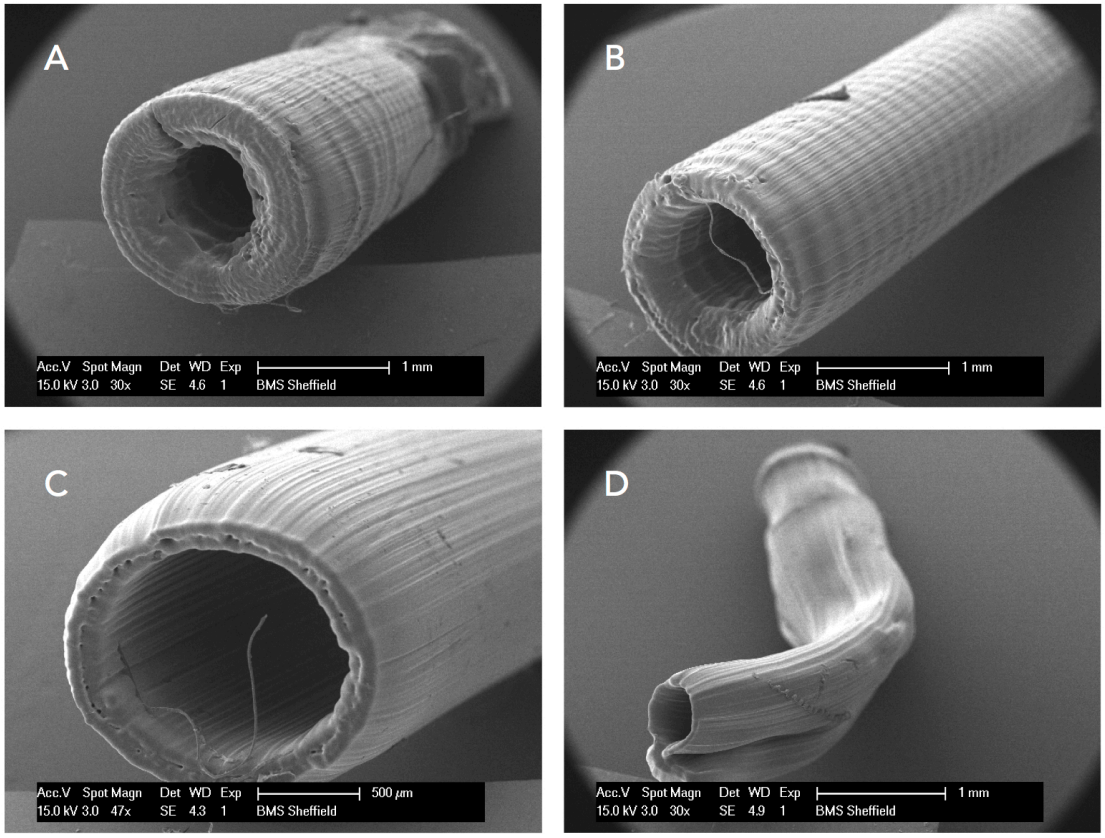

Figure 39: SEM images of NGCs produced at varying laser powers, overcured and undercured NGCs. (A) and (B) are examples of overcuring and undulating rings can be seen across the length of the NGC. NGC (D) is undercured and has therefore collapsed in on itself. (C) is the ideal laser power and write speed. Table 2 summarises conduit laser power and speed.

NGC Tube	Laser power, Mw	Write speed, mm $s^{=1}$	Length, mm
A	80	0.03	10
B	65	0.03	10
C*	30	0.03	10
D	10	0.03	10

Table 2: Outlines the laser process parameters (laser power and z-stage speed) to produce tubes presented in Figure 5. C signifies the ideal NGC synthesis parameters which were used for the implantable NGC.*

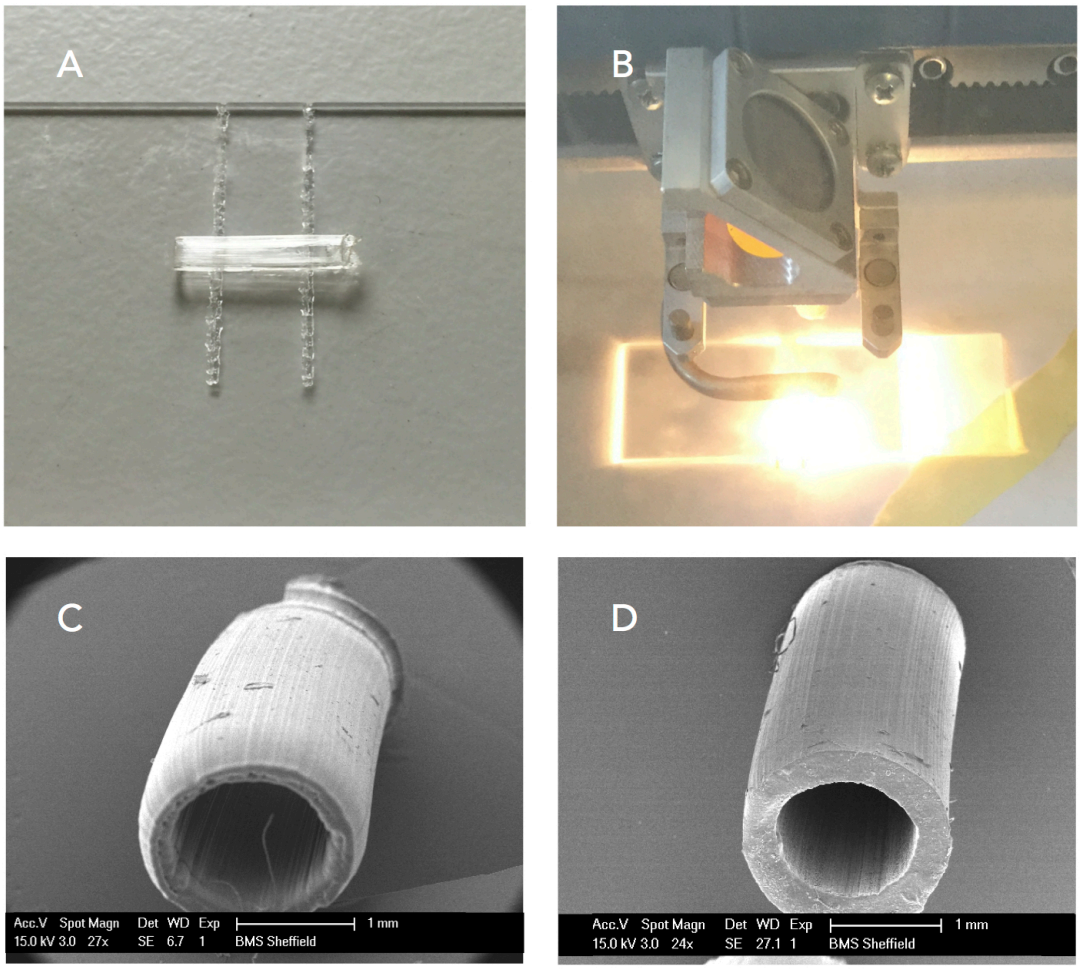

Figure 40: Post processing of NGCs before implantation. Digital photographs (A) and (B) a NGC prior to post processing and during the laser cutting. SEM images (C) and (D) a NGC before and after laser cutting.

3.3 NGC mechanical analysis

NGC's were produced for *in vivo* implantation. Images (Fig 41, A and B) highlight the elastic properties of the conduit when compressed between the fingers. Table 3 describes the mechanical properties of the conduits when compressed mechanically. Compression tests were performed on the conduits, which produced an average compressive Young's modulus of 3.2 MPa. Images (Fig 41, C and D) are a computer rendered image of the initial

conduit design and a digital camera image of a finished NGC ready for implantation. Longitudinal topographical grooves can be seen (Fig 41, D). SEM image (Fig 41, E), illustrates a PGSm NGC supporting several 9-0 Polyamide sutures through the conduit wall. Mechanical suture retention testing was performed also, (Table 3). The conduits were found to have an average suture retention strength of 12.3 MPa.

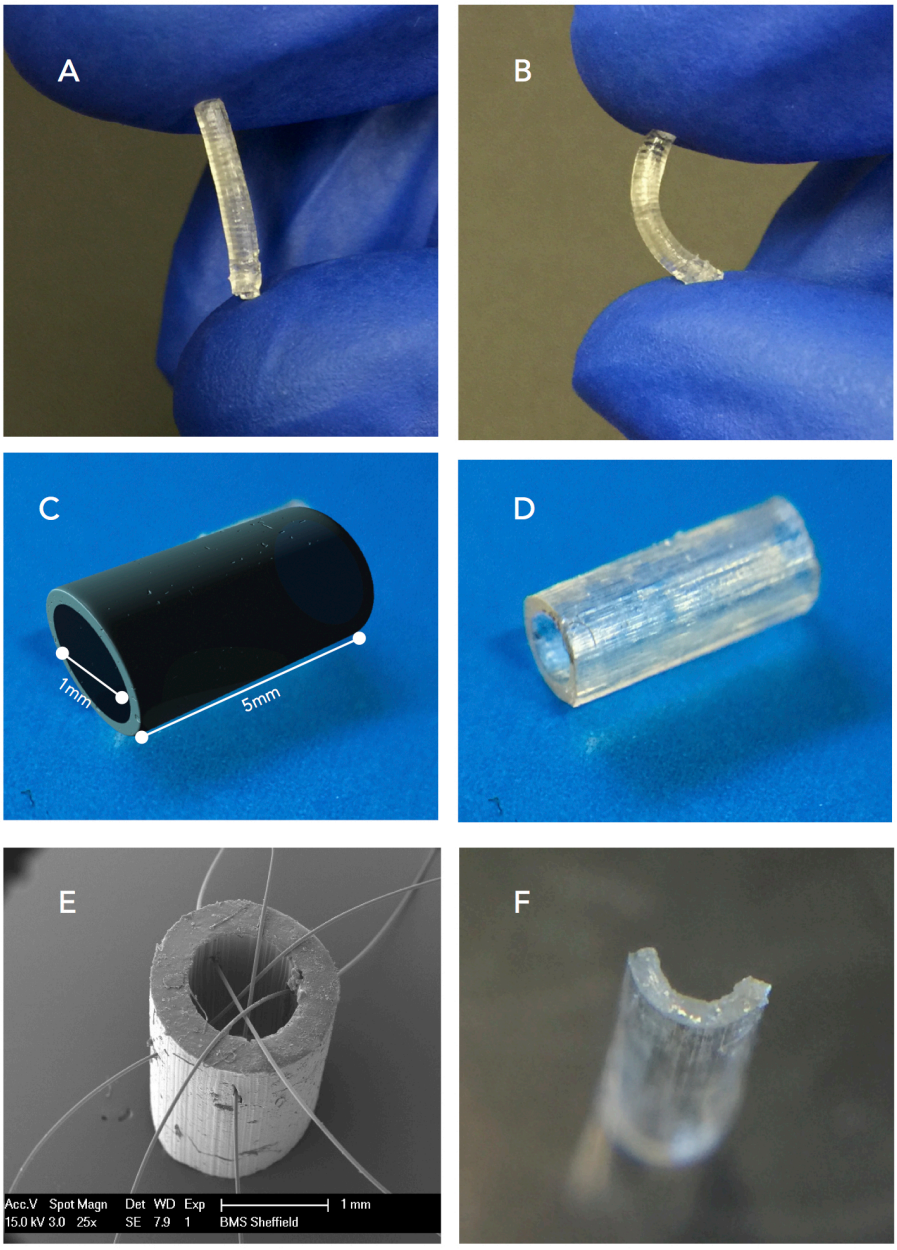

Figure 41: Digital photographs (A) and (B) the elastic properties of PGSm nerve guidance conduits when compressed. Image (C) a computer model (Maya, Autodesk) of the ideal 3D printed nerve with dimensions, (D) a photograph of the final 3D printed finished nerve ready

for implantation. (E) an SEM image, describing the PGSm conduits ability to withstand sutures. (F) a digital photograph of a NGC cut in half, creating a hemi-tube ready for ex vivo DRG analysis.

		Mechanical Compression Testing (n=7)			
NGC length (mm)	*Wall thickness (mm)*	*Max compression (mm)*	*Compression at break (%)*	*Young's Modulus (MPa)*	*Suture Retention Strength (MPa) (n=5)*
5	0.35	0.57 ± 0.27	11.4 ± 5.3	3.2 ± 1.2	12.3 ± 2.33

Table 3: NGCs were compressed in a Hounslow mechanical analysis machine. The average Young's modulus was calculated from the compression tests (n=7). Suture retention strength was also calculated, determining the strength of the conduits to hold sutures (n=5).

3.4 Ex vivo analysis by dorsal root ganglion culture

DRGs were seeded onto hemi-tube NGCs (Fig 41, F), and cultured for three weeks. The hemi-tubes were fixed and immunohistochemically labeled with anti-beta-III-tubulin antibody, anti-S100-beta polyclonal antibody and DAPI. Z-stack images were collected of the hemi-tubes and stitched together to give a complete image of the DRG within the hemi-tube (Fig 42). Image (Fig 42, A) higlights how neurites extended from, and Schwann cells migrated from, the DRG body and travelled across the entire length of the conduit. Neurite outgrowth and alignment along the topographical conduit cues was analysed. Neurites were split into three sections; Zone 1, which was closest to the DRG body; Zone 2, which was furthest from the DRG body and Zone 3/wall, which was identified as the conduit wall with no topographical grooves. Neurite alignment was poorest on the outer wall where there were no topographical cues. Zone 2 contained topographical cues and was furthest

away from the DRG body and showed a significant increase in neurite alignment ($p < 0.0001$)

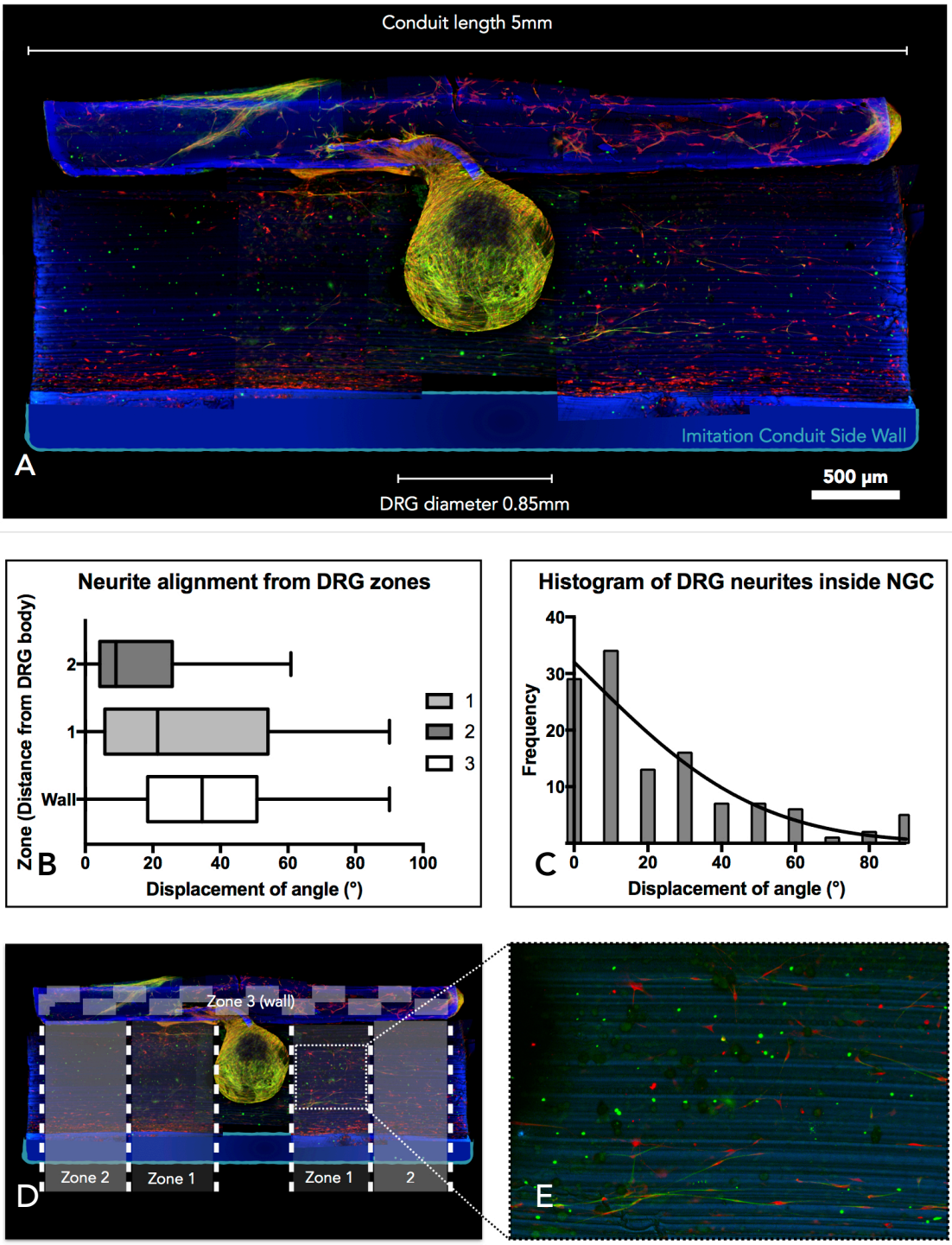

Figure 42: Ex vivo studies were performed whereby a DRG was seeded onto a PGSm hemi-tube NGC and cultured for 3 weeks. (A) the DRG body attached to the hemitube NGC with the neurite outgrowth and Schwann cell migration. Schwann cells were immunohistochemically labeled with S100-beta (Red), neurites with Beta-III-tubulin (Green) and nuclei with DAPI (Blue). The conduit auto-fluoresced in blue and it is difficult to discern

the DAPI cell nuclei, however this does allow visualization of the conduit and the topographical grooves. The side wall located toward the bottom of the image (A) is an annotated imitation side wall (extension of the real wall), added for visual effect. Z stacks were taken to image the entire hemi-tube, using a 10x objective. Several z-stacks were stitched together to create an image of the entire tube. The box and whisker plot (B), neurite alignment in different conduit zones (Zone 1, 2 and Wall can be seen in (D)). (E) a magnified image of an area of the NGC. The histogram (C) outlines the alignment of neurites in all zones within the conduit (population=120).

3.5 In vivo axon analysis

All animals recovered well from initial surgery, with no signs of autonomy or infection. Upon harvesting, the proximal nerve endings in two PGSm conduit repairs were found to be dislodged or otherwise obstructed with fibrin glue, preventing regeneration – these two were excluded from the final analysis. Graft-based repairs demonstrated a similar gross morphology to that observed in previous studies by this group, with slight bulging between graft and both proximal and distal nerve endings; whilst in the PGSm repairs the regenerated nerve tissue had an observably thinner diameter between nerve endings (Fig 43, C).

Transgenic YFP mice used had a subset of axons that were able to fluoresce, allowing for fluorescent imaging without immunolabeling. The mice were not immunocompromised. In terms of axon visualization, graft repair controls were comparable to previous studies, with areas of axon disruption located between the graft and nerve ends and fairly organised axons in the graft tissue itself [110]. PGSm repairs observably displayed fewer axons overall, with axons occupying a thin strip between nerve endings – correlating to the above observations of the harvested tissue.

Sprouting index analysis indicated a significant overall difference between the two repairs, with significantly fewer axons in PGSm repairs at each interval from 0.5mm to 4.0mm. Sprouting increased at the 0.0mm 'start' interval in both repair groups, to a similar level (126.75% [±8.85 SEM] and 135.67% [±5.09] in PGSm and graft repairs respectively), before declining at subsequent intervals. For PGSm repairs there was a large decline in sprouting index at the 0.5mm interval (75.00% [±14.46]) compared to that observed for grafts (124.83% [±13.63]) followed by a smaller decline across subsequent intervals. Further small declines were observed in PGSm repairs at subsequent intervals up to 3.0mm, where the lowest sprouting index value was observed (25.00% [±3.85]), the sprouting index values then remained at this level for all subsequent intervals. The sprouting index profile differed in graft repairs, with small declines observed up to the lowest value at the 2.0mm interval (79.67% [±7.45]), before values rose again towards the end of the graft (reaching 104.50% [8.27] at 3.5mm) before starting to decline at the distal nerve ending (86.33 [±7.53] at 4.0mm).

The proportion of unique axons from the 0.0mm interval reaching subsequent intervals was significantly different between groups only at the 1.0mm interval. Following initial declines in PGSm repairs, unique axon numbers remained steady at around 12-13% from 2.5mm onwards; while in graft repairs, a steady 2-3% decline in unique axons occurred at each interval from 2.0mm (29%) onwards.

The level of initial axon disruption was lower, though not to a significant level, in PGSm repairs (9.2% [±1.8]) compared to graft repairs (12.1% [±2.8]).

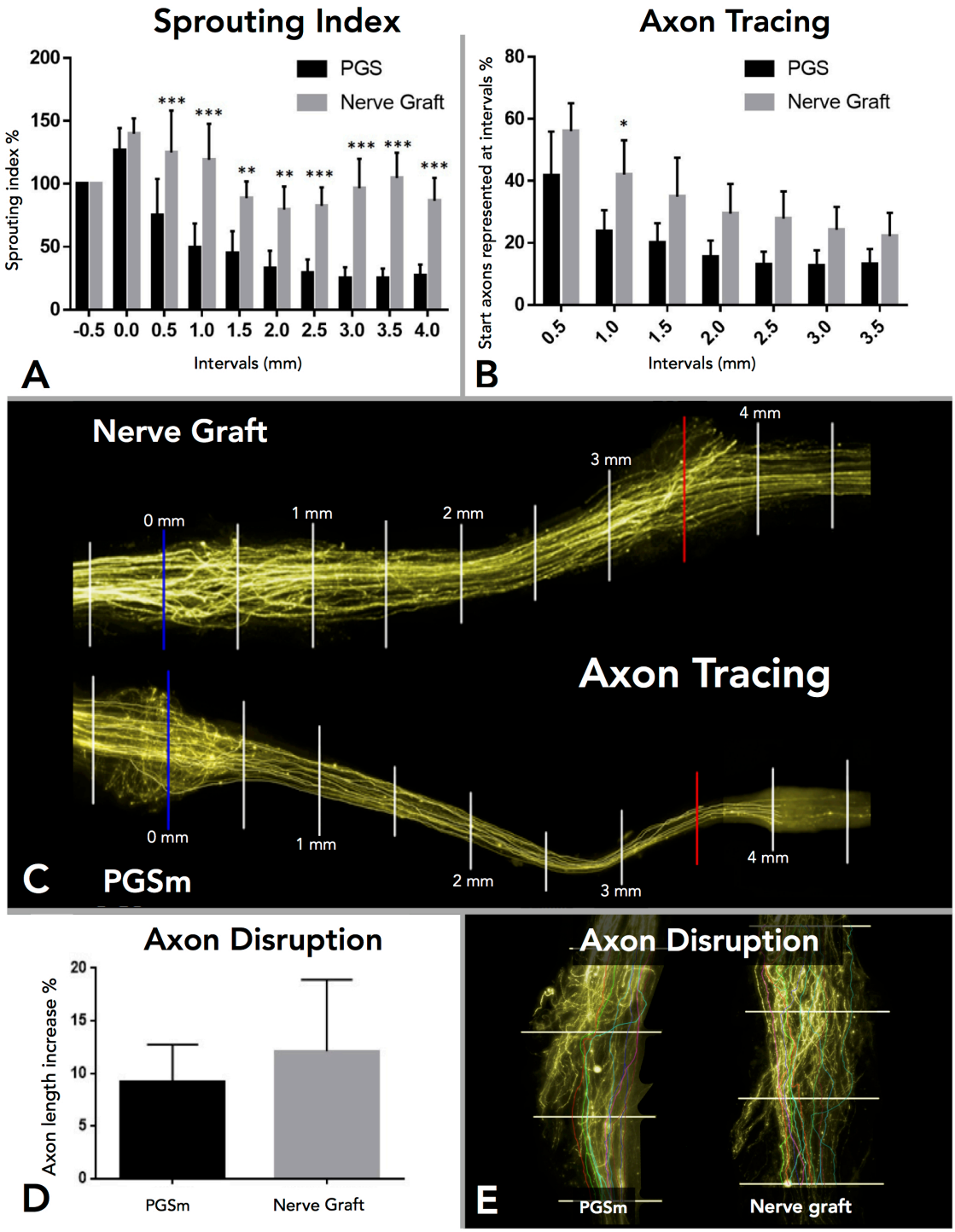

Figure 43: (A) Sprouting index values for each 0.5mm interval. (B) Unique axons from the repair start (0.0mm interval) represented at each subsequent interval within the repair. (C) Comparison axon tracing confocal images of conduit (bottom) and graft (top) image. 0.5mm segment lines. (D + E) Axon disruption across the initial 1.5mm of repairs.. (2-way ANOVA with Bonferroni post-tests). (n=6).

3.6 In vivo neuropathic pain analysis

No differences were observed in astrocyte or microglia activation in either dorsal or ventral horns of the spinal cord, with similar increases in glial activation for the injured side in all cases.

Astrocyte activation for the injury side of the dorsal horn was 129.25% [±5.14 SEM] and 124.75% [±4.28] of that for uninjured side in PGSm and graft respectively. In the ventral horn it was 132.15% [±4.22] and 127.88% [±4.42] in PGSm and graft respectively.

Microglia activation for the injury side of the dorsal horn was 130.25% [±6.36] and 127.68% [±4.21] of that for uninjured side in PGSm and graft respectively. In the ventral horn, it was 132.85% [±2.82] and 128.33% [±2.46] in PGSm and graft respectively.

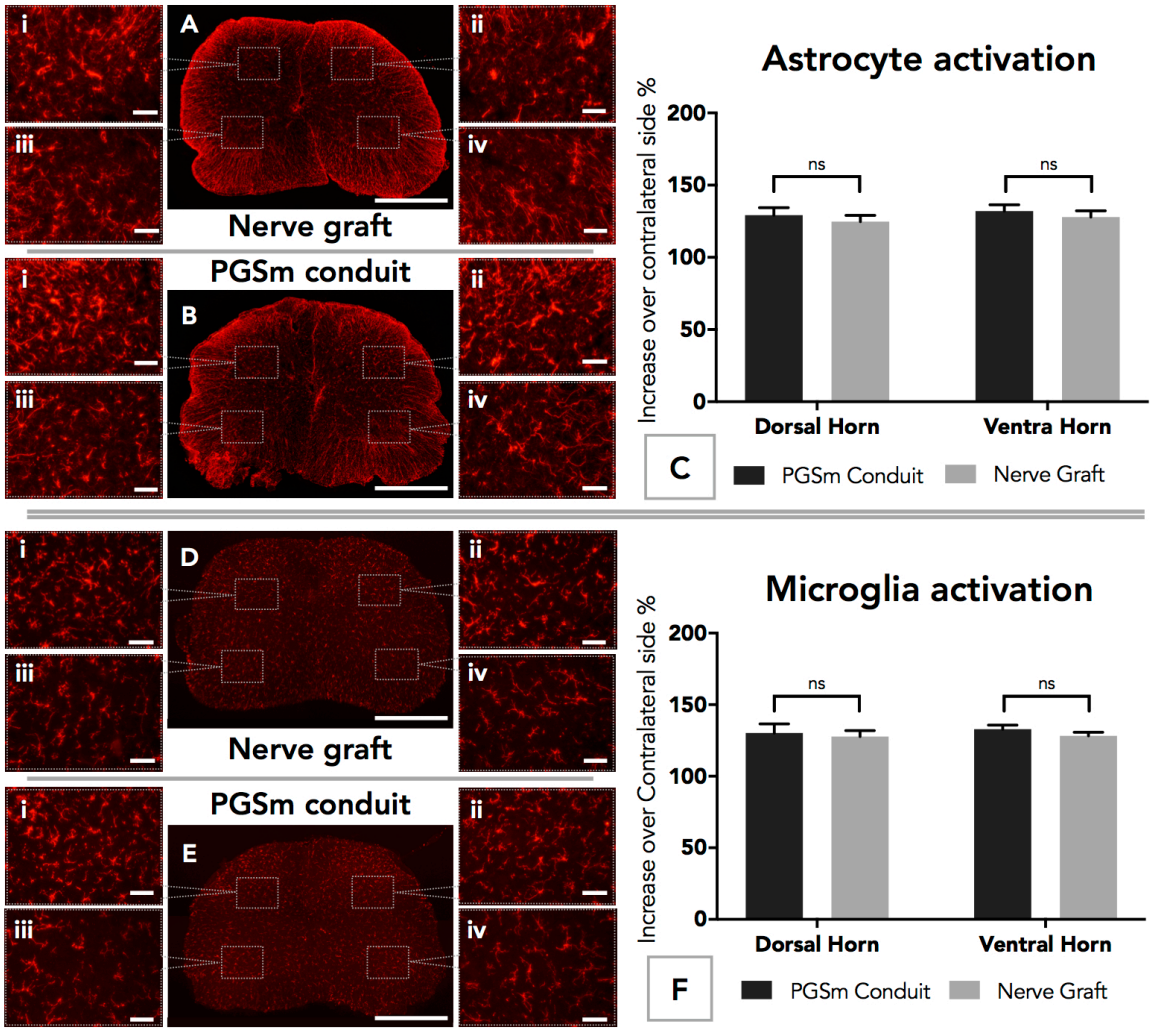

Figure 44: Figure 10 (A) (B) (C), astrocyte activation within L4 spinal cord sections. (A) illustrates a complete view of the nerve graft spinal section; (i-iv) represent higher magnification images of the corresponding spinal section ((i) ipsilateral dorsal horn, (ii) contralateral dorsal horn, (iii) ipsalateral ventral horn, (iv) contralateral ventral horn). (B) a complete view of the PGSm conduit spinal section with corresponding higher magnification images (i-iv). (C) a graph showing the increase in astrocyte activation (compared to contralateral side) in dorsal and ventral horns of the ipsilateral side of the spinal cord. No significant differences were detected between repair groups in either dorsal (129.3% [SEM = 5.1] for conduits; 124.8% [4.3] for grafts) or ventral (132.2% [4.2] for conduits; 127.9% [4.4] for grafts) horns (2-way ANOVA). (D) (E) (F), microglia activation within L4 spinal cord sections. No significant differences were detected between repair groups in either dorsal (130.3% [SEM = 6.4] for conduits; 126.7% [4.2] for grafts) or ventral (132.9% [2.8] for conduits; 128.3% [2.5] for grafts) horns (2-way ANOVA).

4. Discussion

A small number of studies have highlighted PGS as a potential material for peripheral nerve repair, however the structuring of the material and the implantation of PGS conduits *in-vivo* had not yet been explored. The main aim of this study was to assess the novel formulation of PGS, PGSm, for use in peripheral nerve repair and to identify whether it may be a suitable material to tackle the problem of larger peripheral nerve injury gaps. Experiments were designed in five key areas (1) assessing the biocompatibility of the material *in vitro*, (2) structuring the polymer into nerve guidance conduits, (3) testing the conduits mechanically and then analyzing the material through (4) *ex vivo* and (5) *in vivo* testing.

The material is already known to be a soft biomaterial with useful degradation rates (chapter 3.1). The first experimental area in this chapter assessed the materials biocompatibility. Materials stiffness, and surface properties (hydrophobic nature) are widely known to effect cell viability on scaffolds. It was therefore necessary to perform *in vitro* analysis of neuronal cells on flat disks of PGSm to understand whether the degree of methacrylation affected cell cultures. Live dead analysis of neuronal cells seeded onto disks of PGSm at varied methacrylations was performed (Fig 38, A). Results show that all samples had a high percentage of live cells. There was a significant difference between the degrees of methacrylation and glass control with PGSm samples having a higher percentage of live cells than that of glass. Also there was a statistical increase in cell numbers between days 4 and 6, showing that cells were able to proliferate on the polymer surface. As neurite outgrowth is a marker for differentiation, the average neurite length was studied from confocal images to analyse the ability of the material to permit neuronal differentiation (Fig 38, C). There was an overall statistical increase in neurite

length from all of the degrees of methacrylation from day 4 to 6 of neuronal cells when grown on PGSm. This suggests that the neurites were able to extend with time and that the material is permissive for use in neuronal differentiation. As there was no statistical difference between the cell culture results from any of the degrees of methacrylation, 0.75 degree of methacrylation was chosen for all further experiments. This degree of methacrylation was chosen, as it was a good compromise between being easy to structure while maintaining flexibility.

In vitro studies were then performed using primary Schwann cells (Fig 38, E). Both neuronal and glial cells play an important role during the regeneration of the peripheral nerve, deeming it important to study both types for peripheral nerve repair. Primary rat Schwann cells were seeded onto the polymer and live dead analysis performed after 4 and 6 days. Results showed that over both days 4 and 6 there was a very high percentage of live cells on both the glass control and the PGSm scaffolds. There was no statistical difference between Schwann cells grown on the PGSm and glass scaffolds or between days 4 and 6, suggesting no increased Schwann cell toxicity due to the PGSm disks compared with the glass control. Results from *in vitro* tests therefore indicate the material to be permissible for use as a NGC.

In vitro testing determined from neuronal and Schwann cell studies that the PGSm material was suitable for peripheral nerve repair and work began in the second key area of experimentation, structuring the PGSm into NGCs. During NGC production it was noted that by varying the laser power and the write speed (speed of the z-stage), the NGC's would undergo both over and under curing. If higher power laser emissions were used, then the write speed needed to be higher also to ensure over curing did not occur. Overcuring can

be seen (Fig 39, A and B) with an undulating wall surface. If the write speed became too quick then under curing could occur, with incorrectly formed, unstable NGC's (Fig 39, D). Table 2 outlines the parameters used to create the NGC's, with row C showing the optimum laser and speed settings. It was witnessed that there seemed to be persistent over curing at the base (start of structuring) of the NGC and under curing at the top (end of structuring). This issue was overcome through the use of post process laser cutting techniques. NGC's were produced and then laser cut to exact lengths allowing the unreliable ends of the printed conduits to be cut away (Fig 40). This created highly reproducible precisely designed conduits. The NGCs were elastic in nature, and when bent did not snap. This would make them easier to handle surgically. Also the NGC's were able to be bent a great distance before kinking occurred (Fig 41, A and B). Kinking of NGC's may hinder axonal regeneration, particularly with larger gap injuries. It is therefore advantageous to have a conduit, which can bend and move with the body before kinking occurs. The conduits produced also had topographical grooves, which ran along the internal wall of the conduit longitudinally. These grooves are visible (Fig 41, D and E), and were features created by the resolution of the DMD, a circumstance explained previously in literature[110]. The ability of the novel PGSm to be photocured allows for the polymer to be structured into reproducible conduits via micro stereolithography. This not only opens up PGSm for more complex nerve conduits; it also introduces the polymer to many other biomaterial and medical device applications with complex, bespoke and reproducible 3D structures possible.

The third area of experiments explored the mechanical properties of the NGCs. Compression tests were performed on the conduits, which produced an average compressive Young's modulus of 3.2 MPa (Table 3), a similar

modulus value to that of the native nerve[84] (modulus of nerve 0.45MPa). It is important to closely mimic the modulus of the native tissue in order to minimize any stress on the tissue, however compromises must also be made allowing for easy surgical manipulation of the conduit. It is thought that the conduits in this study address this compromise well. The NGC's were also tested for whether they can support and hold sutures, necessary for larger animal models. SEM image (Fig 41, E) shows a PGSm NGC supporting several 9-0 Polyamide sutures through the conduit wall. Mechanical testing was performed and the conduits were found to have an average suture retention strength of 12.3 MPa, similar to that of the clinically used poly(tetrafluoroethylene, 23 MPa)[111]. This information is particularly useful when translated to clinical applications, as materials too soft may tear and brittle materials may break when sutured.

Once the NGCs were structured and mechanically analysed the fourth area, *ex vivo* analysis, began. DRGs were seeded onto PGSm hemitubes and glass controls. DRGs were able to adhere and show neurite outgrowth along the length of the PGSm NGCs. Neurites extended from, and Schwann cells migrated from, the DRG body and travelled across the entire length of the conduit (Fig 8, A). This indicates the materials ability to support and promote the regeneration of the DRG. Another requirement of a useful NGC is to direct axonal growth towards the distal stump. Graphs (Fig 42, B and C) describe the conduits ability to align neurites along the longitudinal topographical grooves of the NGC, directing growth from the proximal to distal stump in an effective manner. As can be seen in (Fig 42, B) the angle of the neurites becomes more aligned the further it grows from the DRG body, suggesting the topographical features within the NGC is directing the growth. The hemitube wall has no topographical cues, and is seen to have the least

aligned neurites, whereas Zone 2 is the furthest from the DRG and the extended period of topographical cues results in a statistically significant increase in the alignment of neurites. Histogram (Fig 42, C) highlights the alignment of the neurites within the hemitube towards the topographic grooves. The *ex vivo* study indicated that the PGSm conduit is both a good material and structure for peripheral nerve repair. The material allowed for the attachment of the DRG body with the extension of neurites and migration of Schwann cells; and the topographical cues aligned the neurites, directing them towards the ends of the conduit.

The final area of experimentation explored the suitability of the PGSm conduits through *in vivo* analysis. Transgenic YFP mice were used for the *in vivo* studies, these mice had a subset of axons that were able to fluoresce. This was useful as the axon growth could be fluorescently imaged, without immunolabeling, also the mice were not immunocompromised. The implanted PGSm conduits stimulated and successfully directed axonal regeneration across the injury gap, this is visible in the confocal images of the graft whereby axon regeneration can be seen directed into the distal stump (Fig 43, C). From the sprouting index results it can however be seen that the nerve grafts performed better than the PGSm conduits. The largest decline in the sprouting index for the conduits occurred at the 0.5mm interval, the conduit results then decline at a slower rate up until 3.0mm, whereby the sprouting index percentage settles. This initial fall is witnessed in the nerve grafts also, however to a lesser extent. This suggests that the PGSm material does provide an appropriate substrate to stimulate and permit the regeneration of axons, this is inferred as the sprouting index percentage settles by 3.0mm and does not decline further. However the initial dramatic sprouting index decline may also suggest that there is an insufficient area of

substrate available for the axons to attach along and regenerate. Indicating either inappropriate sizing of the conduit or a lack of microenvironment within the conduit. Results from the axon tracing were only significantly lower in the conduit at 1 mm, conduit results then decline slowly up to 2.5 mm, after which the unique axon number remained constant. Again this shows an initial dramatic decline of the unique axon number, before remaining stable further into the conduit. The axons may be ill-fitting within the conduit and only some axons may reach the outer substrate wall, this idea is backed by the confocal images, whereby the axon grouping in the conduit appears to be thin and compact toward one side of the conduit. This problem could be addressed with the inclusion of more intricate microenvironments within the conduit tube. The overall result of the axon tracing does however show that beyond the one result at the 1 mm interval, there isn't any significant difference between the graft and conduit. Also the level of initial axon disruption was not significantly lower in the conduits than the nerve grafts. It is therefore clear that in terms of axonal regeneration, the PGSm material poses as a great candidate material in the use of nerve guidance conduits. Similar studies were performed within the group using PEG conduits. These PEG conduits allowed for regeneration to occur across the injury gap however they were stiff and created tension/stress in the surrounding tissue[110]. Furthermore it was noted that the stiffness of the PEG conduits made them difficult to implant.

For a conduit to be accepted over a longer time period it becomes essential that there is a limited negative biological response to the PGSm conduit. One method to assess this is by analyzing the level of neuropathic pain stimulated by the implanted conduit. Literature has shown a direct relationship between both spinal microglial and astrocyte activation with neuropathic pain[112,113]. Previous in-house studies with nylon conduits showed a far higher activation

of the spinal microglia and astrocytes compared with the nerve graft, suggesting high levels of neuropathic pain and inappropriate conduits long term. The results in this study show both the astrocyte and microglia activation in the conduits have no significant difference to that of the nerve grafts, indicating no significant increase in neuropathic pain. This suggests a high level of biocompatibility of the material and appropriateness for the material to be used in longer term, larger gap models.

There are some studies in literature that explore the use of stereolithography produced 3D scaffolds as a conduit, however these are often not implanted *in vivo* or are non degradable[110,114,115]. It is believed this is the first time in literature a degradable stereolithography printed scaffold has been implanted and explored for use in peripheral nerve repair.

5. Conclusion

This chapter set out to assess the use of PGSm for peripheral nerve repair. The material was taken from polymer synthesis through to *in vivo* testing, as a basis for potential use in the clinic. PGSm was developed to overcome the structuring issues of PGS. The material properties of the PGSm were found to be appropriate for peripheral nerve repair, furthermore the material was structured and 3D printed into reproducible NGC's. The material performed well with neuronal and glial *in vitro* cell studies. *Ex vivo* studies indicated the materials proficiency as a substrate for neuronal outgrowth, with surface topographical grooves advantageously directing neurites. *In vivo* results show that the PGSm conduits allow for the regeneration and support of axons, directing axonal growth, and exhibiting no increased negative neuropathic pain response compared with native nerve grafts. In some areas the nerve graft performed better than the conduit; suggesting that whilst the PGSm

conduits now provide a desirable option for peripheral nerve repair, further conduit designs could be explored to maximize the potential of the polymer. The stereolithography setup used allows for the production of conduits with more complex designs, such as the inclusion of a PGSm microenvironment. Also the conduits flexibility, resistance to kinking and ability to withstand suturing highlights its potential use in future larger gap models. In larger gap models nutrient exchange would become a greater struggle in a closed system conduit, studies were also conducted (chapter 3.4) to create porous conduits of this material to further enhance its credentials as an appropriate material for the large gap repair of the peripheral nerve. One of the limitations of this design of conduit was that it was necessary to accurately match the conduit size to allow for regeneration to occur, the inclusion of features inside the lumen may help to overcome some of these issues. In this model fibrin glue was used to attatch the conduit to the nerve, there were some complications witnessed with use of the glue and future studies in larger models should instead use sutures to fix the conduit in place.

3.4 POROUS POLYHIPE NGCS

Aim: The aim of this chapter was to explore and find an appropriate production methods to create reproducible and uniform, porous PGSm polyHIPE conduits to be analysed by in vitro *and* ex vivo *analysis.*

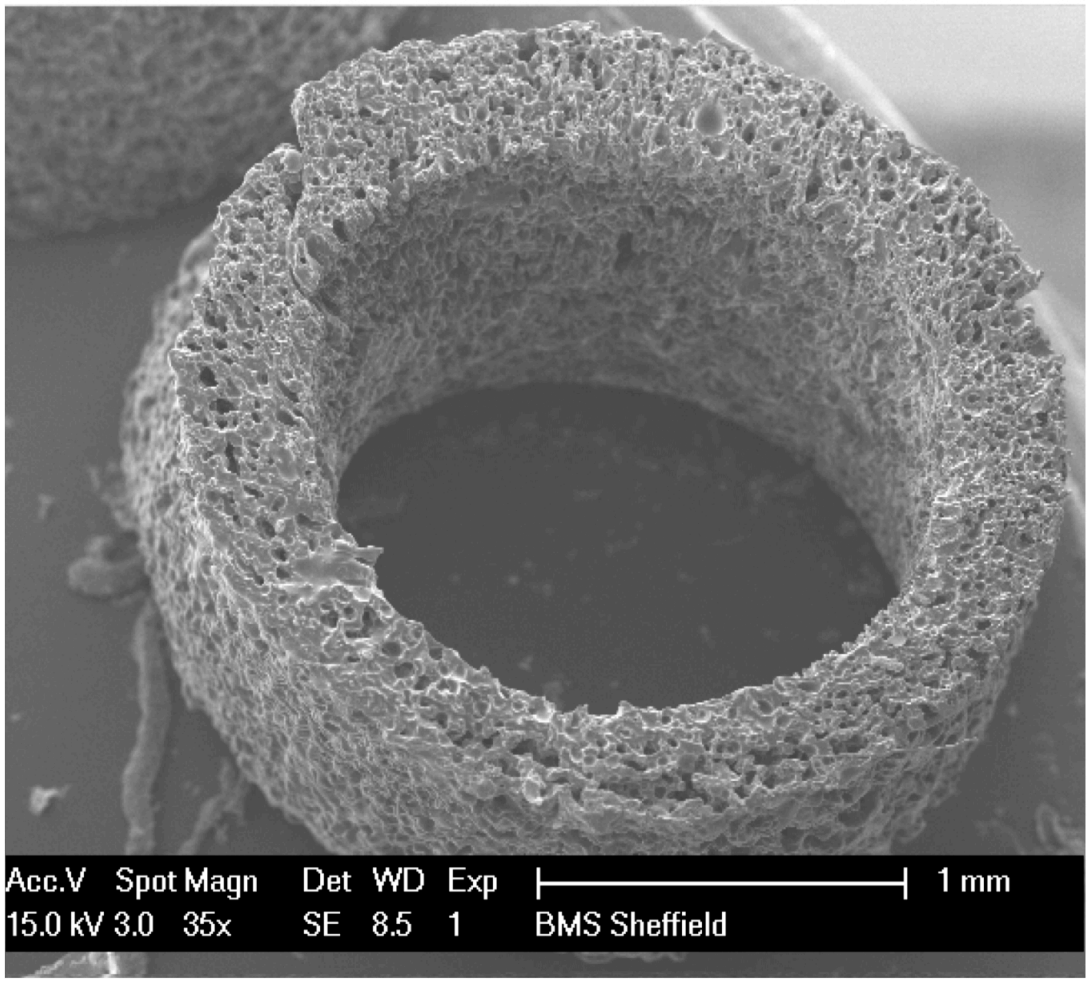

SEM image of a porous PGSm NGC. Image taken from Figure 52

1. Introduction

1.1 NGC design – Permeable (porous) conduits

Permeability is an important consideration with conduit design. Most of the conduits currently available are non-permeable. It is known, however, that permeability allows for nutrient exchange within the conduit and the surrounding tissue. This may be one of the limiting factors of the efficacy of conduits in large gaps[116]. It is understood that the nerve may have good levels of nutrient exchange at the ends of the conduit where the conduit meets the proximal/distal stumps, however in larger gap injuries nutrients may not travel the distance from the ends of the conduit and therefore a higher level of nutrient exchange is required. It is therefore suggested that permeable conduits would be more ideal for larger injury gaps and would better mimic the native tissue. It must also be noted that the level of porosity and size of the pores is important, with a too highly porous (or large) pore design potentially disrupting axonal growth. One 2009 study, researching the effects of porous PCL conduits, determined that a porosity of 80% provided the best results[117]. Conduits with porosity less than 80% were deemed inadequate as they provided insufficient nutrient and oxygen diffusion. The study also found conduits were most effective at pore sizes ~10-40 μm. It is also reasonable to understand that the actual level of porosity required may be different depending upon conduit design and materials selection.

Porosity is often introduced into polymer scaffolds via a techniques such as, particle leaching, gas foaming, freeze drying, or electrospinning techniques[118]. Another technique being explored in research is the use of polyHIPEs, these have the advantage of being able to control the size of pores and level of porosity.

1.2 PolyHIPE nerve guidance conduits

There are no current examples in literature of polyHIPE NGCs, this may be because of complex emulsion synthesis methods for biocompatible polymers. PolyHIPE conduits may however offer a useful approach in the synthesis of porous conduits, with control over level of porosity, pore size and structurability of the conduits.

Literature reports of effectiveness with 80% porosity and ~10-40 μm pores[117] is thought to be achievable through the use of polyHIPE conduits, as polyHIPEs have a minimum porosity of 74%, and controllable pore size.

1.3 PGSm polyHIPE NGCs

There are currently no examples of PGS/PGSm HIPE in literature. Chapter 3.2 describes the successful synthesis and analysis of PGSm HIPE. Structuring the HIPE into nerve guidance conduits proved to be a complicated process. This chapter aims to determine a reproducible method for the synthesis of PGSm polyHIPE NGCs and to evaluate conduits via *in vitro* and *ex vivo* analysis.

2. Methods

2.1 PGSm polyHIPE production

Chapter 3.2 discusses in detail the production of PGSm polyHIPEs. These high internal phase emulsions were used to create porous scaffolds via three production techniques: microstereolithography, needle tube casting and suture tube casting. The techniques are described below.

2.2 Micro-stereolithography: PolyHIPE NGC tubes

NGC production via stereolithography has been discussed previously (Chapter 3.3). Similar techniques were used to produce porous polyHIPE PGSm NGCs, for complete micro-stereolithography methodology see page 87. To produce the polyHIPE NGCs via this method, the laser was set to full power (100 W), and the z-stage speed lowered to 0.01 mm/s. This was necessary to overcome the scattering created by the water present within the emulsion and to enable the polymer to photocrosslink.

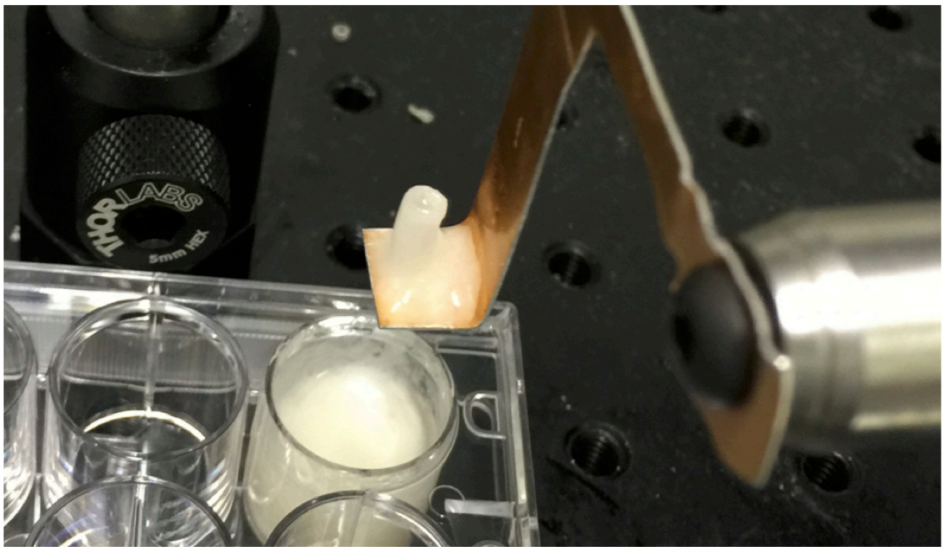

Figure 45: Digital photograph showing stereolithography polyHIPE PGSm setup.

2.3 Needle tube cast: PolyHIPE NGC tubes

A PDMS sheet was used as a substrate to hold the needle tube construct during photocuring, (Fig 46). A hole was made into the PDMS using a glass tube with an internal diameter of 1.5 mm (1), the tube was then inserted into the PDMS and filled with uncrosslinked PGSm emulsion (2). A metal needle was carefully inserted within the centre of the tube and pressed into the PDMS to hold it in place (3). The construct was then placed under a UV lamp for two minutes to ensure the emulsion was fully crosslinked (4). The needle was removed from the PDMS and glass tube (5) and the PGSm polyHIPE NGC was pushed off the needle and into methanol for any uncured polymer to be removed (6).

2.4 Suture tube cast: PolyHIPE NGC tubes

Two sections of PDMS sheet were used to hold a sutured tube construct during photocuring (Fig 47 illustrates the process). A hole was made into each PDMS section using a glass tube with an internal diameter of 1.5 mm. A USP size 4 suture was then carefully inserted up into one of the PDMS sections and through the centre of the hole made by the glass tube, with the end of the suture tied in a knot preventing it from pulling through. The suture was then threaded through the glass tube and loosely inserted into the centre of the hole made into the other PDMS section (1). The bottom of the glass tube was secured down into the PDMS, the tube filled with uncured PGSm emulsion and the suture pulled tight, securing the top PDMS section onto the tube (2). The construct was then placed under a UV lamp for two minutes to ensure the emulsion was fully crosslinked (3). The suture was cut at the top and the PDMS and glass tube was removed carefully (4). The whole length of PGSm polyHIPE NGC was then pushed off of the suture (5) and sectioned using a scalpel into the required size (6).

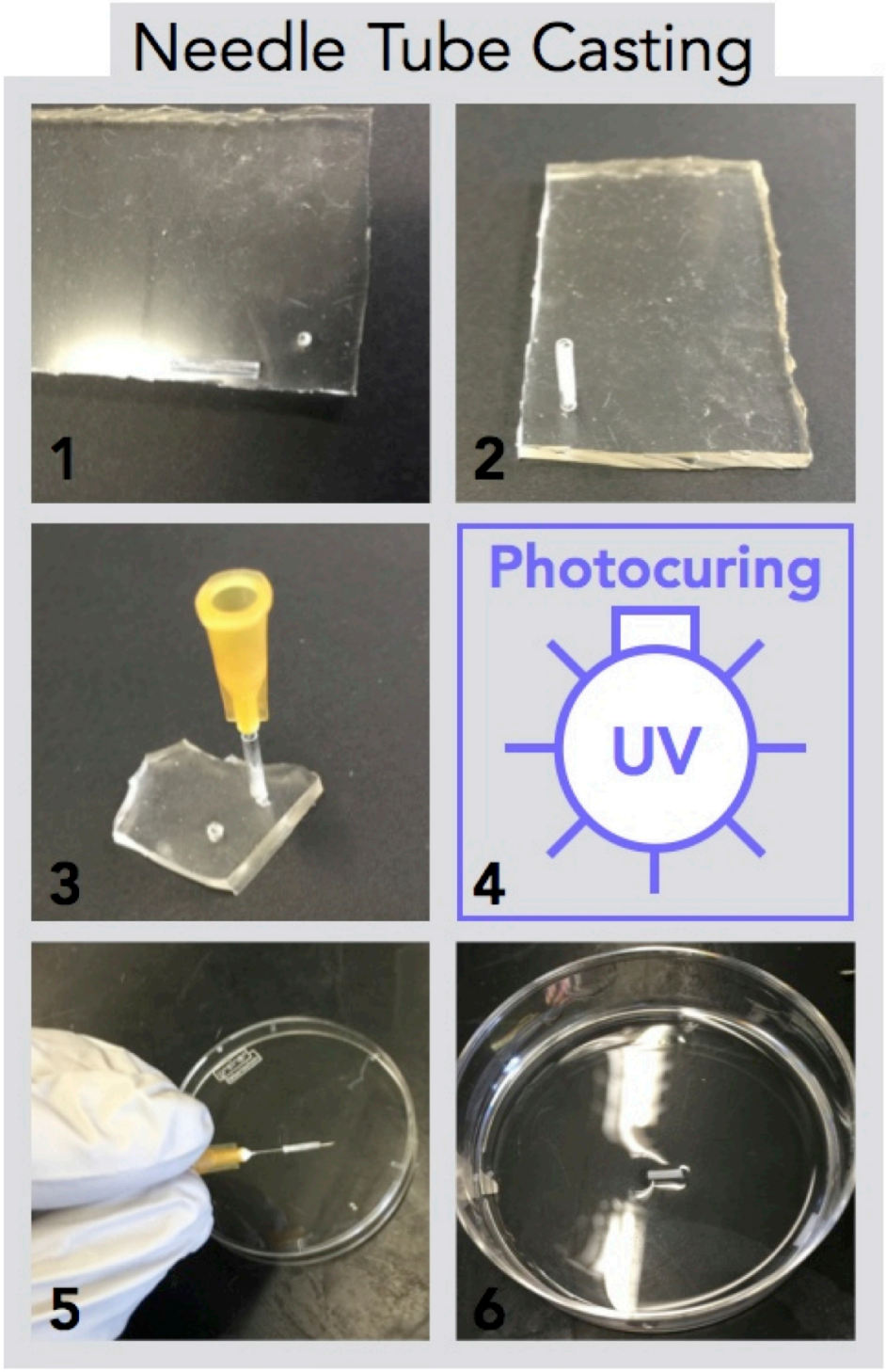

Figure 46: Process of producing porous NGCs via needle tube casting. Glass tube creates hole in PDMS (1), pushed into PDMS (2), filled with emulsion and needle added (3) UV photocured (4), removed from tube (5), and removed from needle (6).

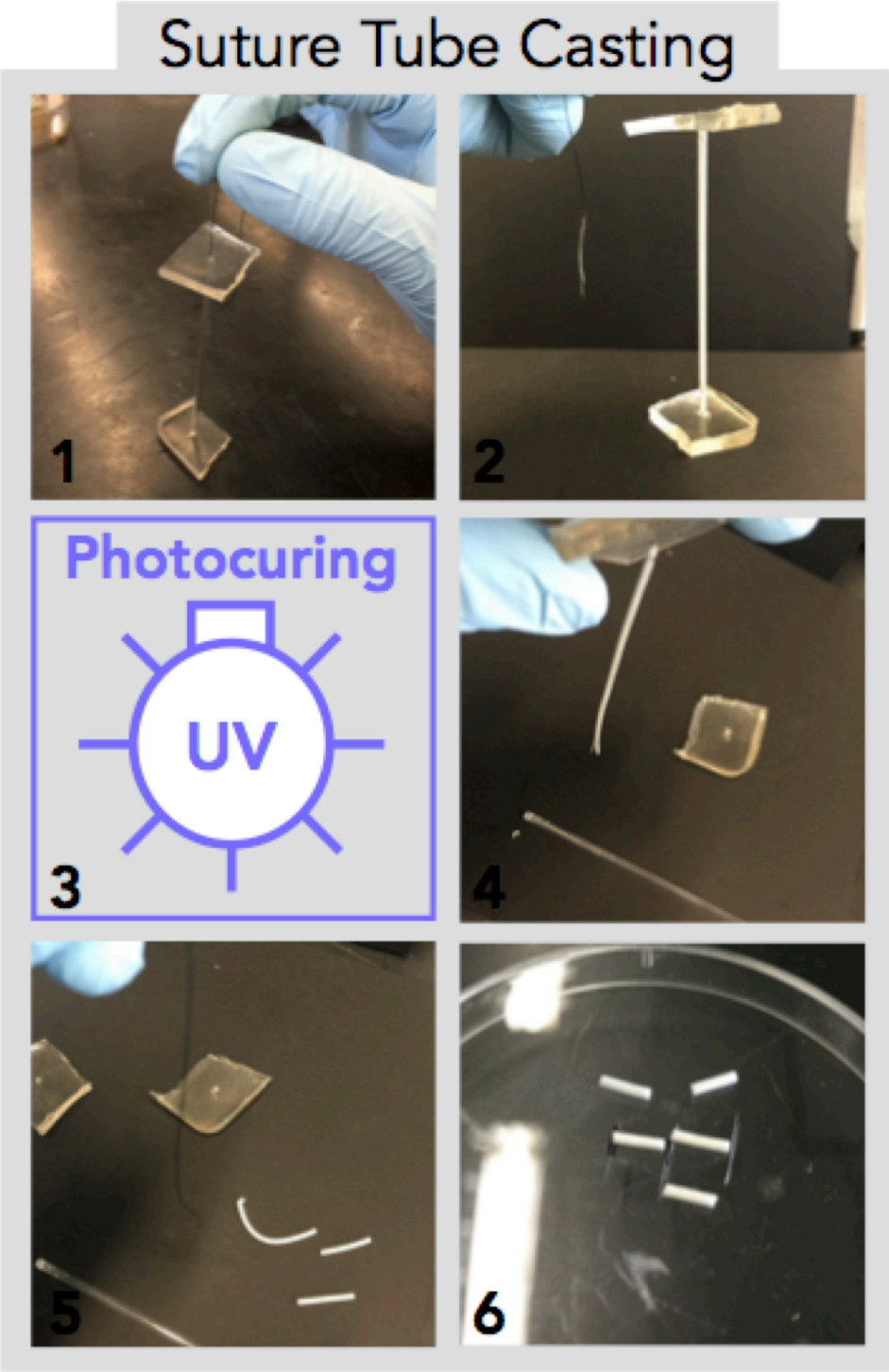

Figure 47 - Process of producing porous NGCs via suture tube casting. Tube inserted into PDMS and suture threaded (1), emulsion added (2), UV photocured (3), tube removed (4), suture removed (5), cut to size (6).

2.5 MicroCT scan

MicroCT scans were performed as outlined in the methods (chapter 2). Briefly, the conduit was secured in place using a polystyrene straw, which provided minimal interference with x-rays, allowing a complete scan of the porous conduits. The model was viewed and sectioned to understand the porosity throughout the whole conduit.

2.6 Schwann cell study

Primary Schwann cells were isolated from male Wistar rats as described previously (chapter 3.3). Briefly the Schwann cells were isolated and incubated at 37°C, 5% CO_2 in medium (MEM-D-valine containing 10% (v/v) FCS, 100U/mL penicillin, 100 µg/mL streptomycin, 0.25 µg/mL amphotericin, 5 µM forskolin and 2 mM L-glutamine). Cells were used between passages 2-4. Photocured PGSm polyHIPE disks, (13 mm diameter, 3 mm depth) were sterilized in 70% ethanol three times for a minimum of 24 hours. PBS was then introduced thrice and the polyHIPE disk centrifuged to force PBS into the pores. The disks were then placed into wells, fresh medium added, and incubated before experimentation. Prior to experimentation medium was removed and Schwann cells were seeded onto the surface of the disks in a 500 µL droplet containing 25,000 cells. Fresh medium was added and cells were cultured for 3 weeks, with medium changes every 3-4 days. The disk was then washed thrice in PBS, fixed in 3.7% paraformaldehyde for one hour and then washed in PBS twice further. The disk was then immunostained with primary rabbit anti-S100-beta polyclonal antibodies, at 1:250 titre (ThermoFisher) in ICC buffer and secondary antibody Alexa Fluor 546 goat anti-rabbit (λ_{Ex}/ λ_{Em} = 556nm / 573nm, ThermoFisher) was added at a titre of

1:100 in ICC buffer for two hours at room temperature. A Z-stack image was taken using an upright confocal microscope, over 308 μm, with 25 slices.

2.7 Dorsal Root Ganglion *ex vivo* seeding

DRGs were extracted and seeded as described previously in methods, chapter 3.3. Briefly, conduits were produced by suture tube casting, sterilized in ethanol as above, DRGs were then seeded into the end of the whole conduit and cultured for three weeks. The conduit was washed in PBS and immunostained with primary rabbit anti-S100-beta polyclonal antibodies, at 1:250 titre (ThermoFisher) in ICC buffer and primary mouse polyclonal antibody beta-III-tubulin 1:1000 (ThermoFisher) in ICC buffer overnight at 4°C. Secondary antibodies Alexa Fluor 488 rabbit anti-mouse IgG (λ_{Ex}/ λ_{Em} = 490nm / 525nm, ThermoFisher) and Alexa Fluor 546 goat anti-rabbit (λ_{Ex}/ λ_{Em} = 556nm / 573nm, ThermoFisher) were added at a titre of 1:100 in ICC buffer for two hours at room temperature. Fresh PBS was added then the conduits were imaged using an upright Zeiss LSM 510 confocal microscope (objective W N-Achroplan 10x/0.3, Zeiss, US), and a z-stack taken over 728 μm, with 25 slices. Several z-stacks were stitched together side by side for a more comprehensive PGSm polyHIPE conduit image.

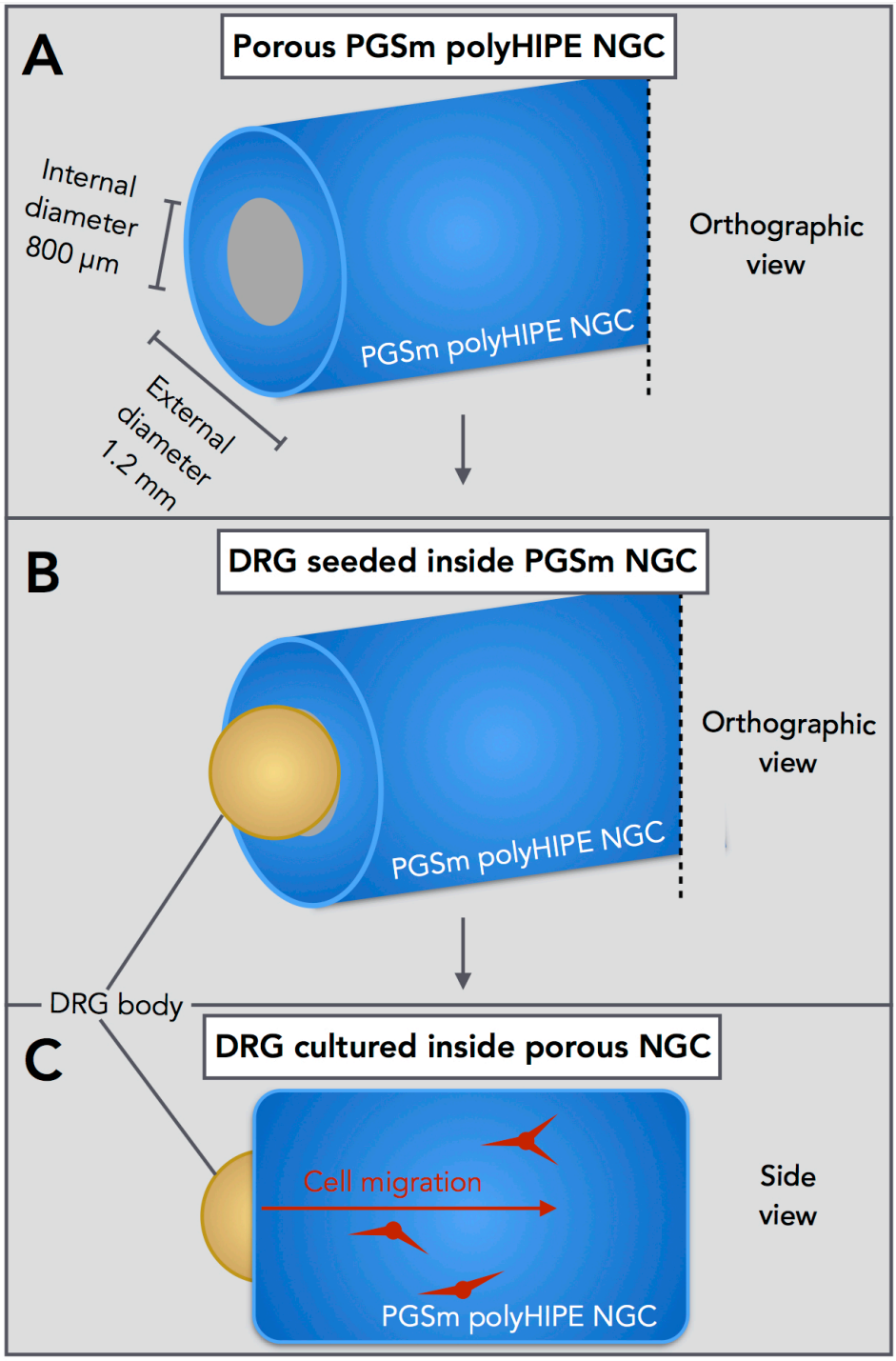

Figure 48: DRG seeding method into whole PGSm porous polyHIPE NGC. Porous PGSm conduit is produced (A), DRG seeded into the end of the conduit (B), and cultured for three weeks with cells migrating from DRG body (C).

3. Results

PGSm was synthesized into a polyHIPE emulsion, as described (chapter 3.2). SEM micrographs were taken of the bulk polyHIPE once photocured (Fig 49). Digital images (Fig 50), and SEM micrographs (Fig 51) illustrate conduits produced via stereolithography. The conduits appear non-uniform in shape. SEM micrographs of NGCs produced via stereolithography indicate a porous surface, however spherical pores seem stretched linearly (Fig 51, A, B, C).

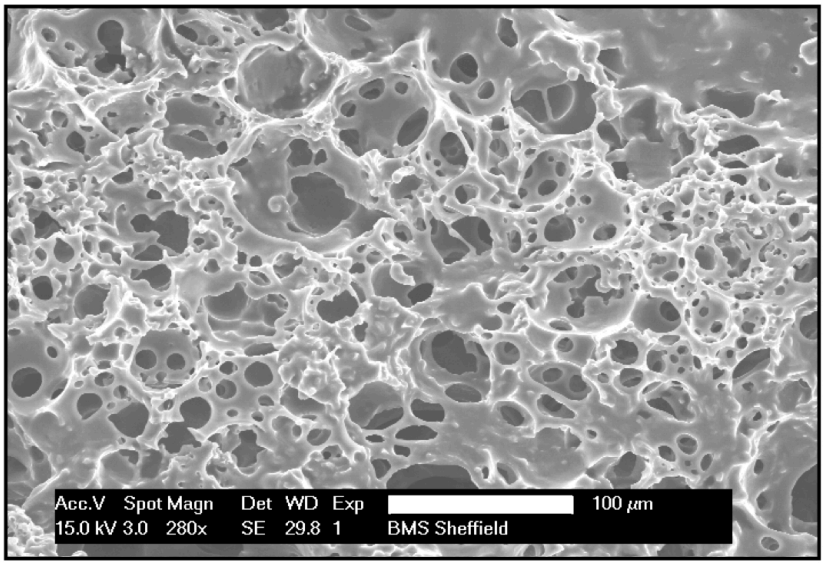

Figure 49: SEM image of highly interconnected, porous bulk PGSm PolyHIPE. 100 µm scale bar.

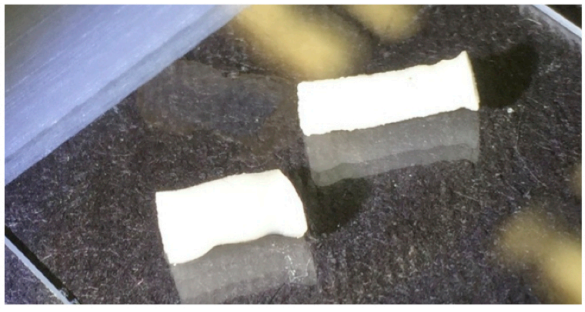

Figure 50: Digital photograph of irregular stereolithography produced polyHIPE NGCs.

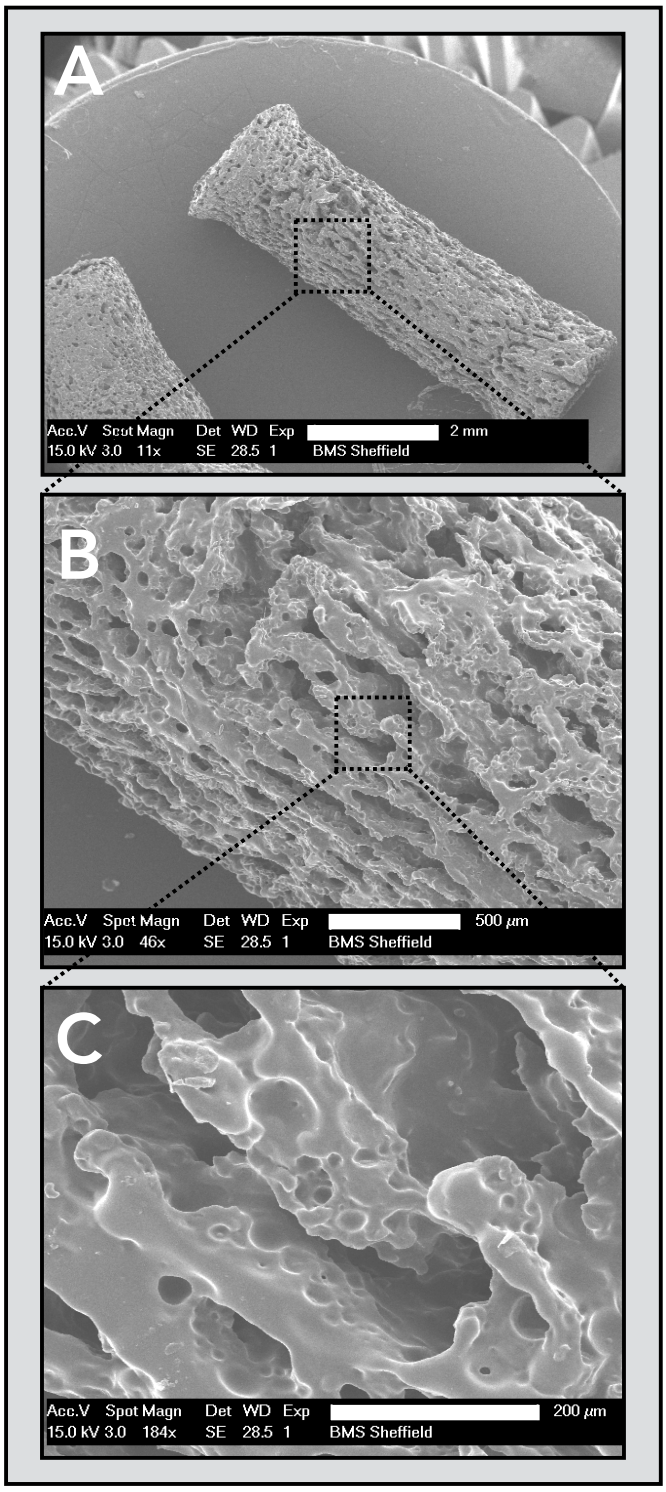

Figure 51: SEM micrographs of PGSm polyHIPE NGCs produced via stereolithography. HIPE pores became linear and stretched (B, C), however the conduit maintained a porous outer surface. A, B and C have scale bars 2 mm, 500 µm and 200 µm respectively.

Conduits were also successfully produced using a casting technique with a glass tube and a needle. SEM micrographs (Fig 52) indicate that the production method produced highly porous conduits, with surface porosity both internally and externally. The technique, however, produced one conduit at a time, which was time consuming and highly laborious.

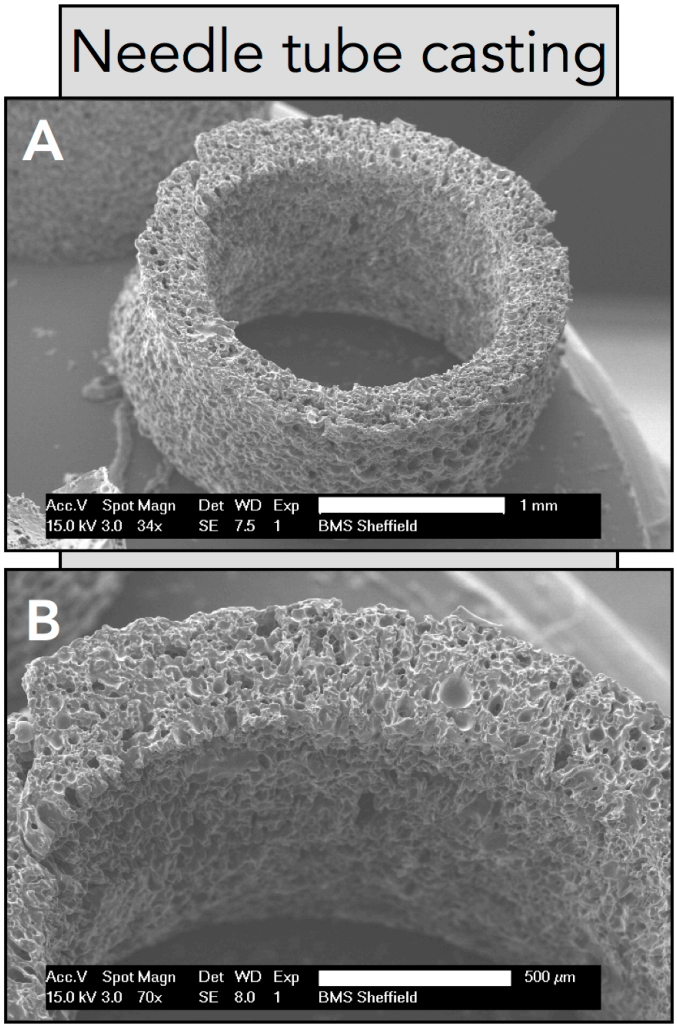

Figure 52: SEM micrograph of a highly porous conduit created via needle tube casting. A and B have scale bars 1 mm, and 500 µm respectively.

Casting techniques were then adjusted to create conduits capable of production in batches. Suture tube casting SEM micrographs (Fig 53), indicate successfully produced conduits, which are highly uniform, have outer and

inner porosity and was produced in a more timely batch process. Outer porosity is marginally less open and has lower porosity in this technique.

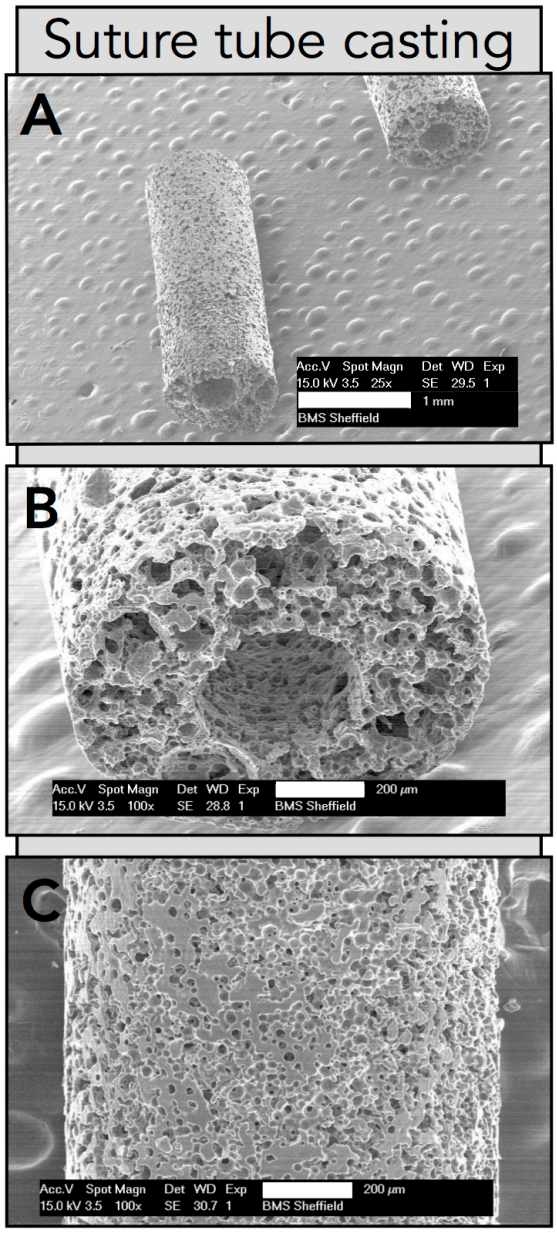

Figure 53: SEM micrographs of a uniform and porous PGSm polyHIPE conduits, created in a batch process suture tube casting technique. A, B, C have scale bars 1 mm, 200 µm, and 200 µm respectively.

Production techniques were adjusted and suture tube casting was chosen as the best method for PGSm polyHIPE NGC production. SEM micrographs (Fig 53) showed the outer porosity was lowered during production, however

microCT models indicated complete porosity throughout the conduit, as seen in screen captures of the 3D model (Fig 54). The conduits are highly uniform and have a clear internal lumen throughout.

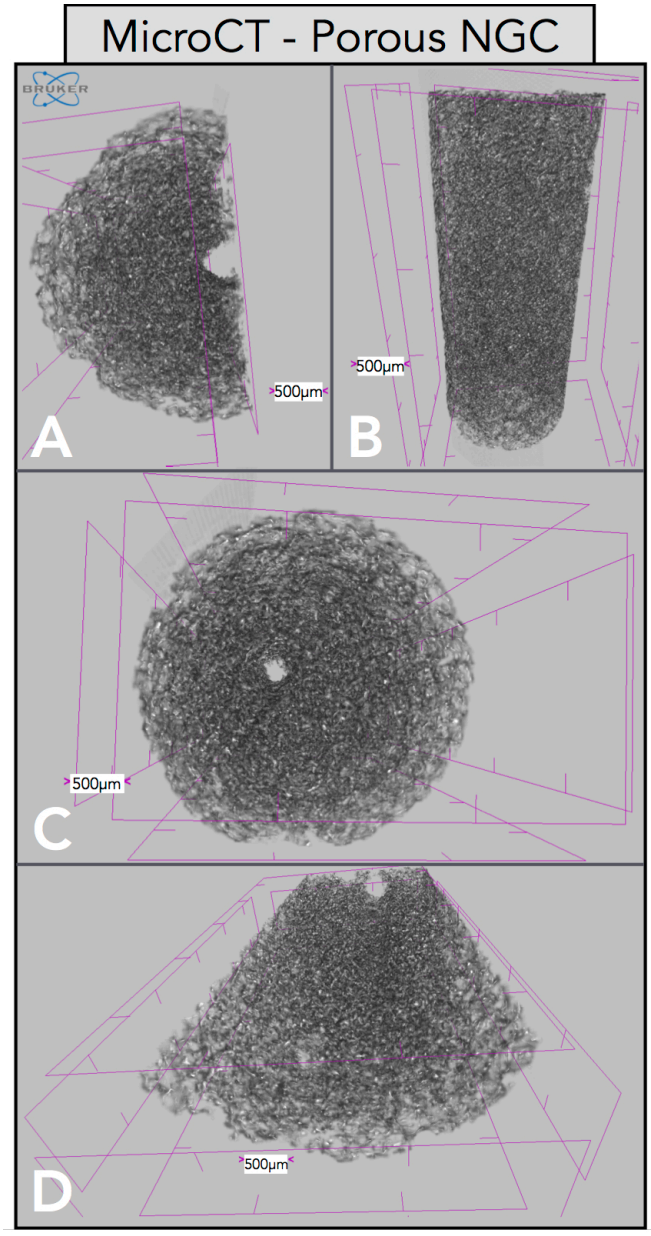

Figure 54: MicroCT model, of a uniform NGC which maintained porosity throughout and the conduit had a uniform internal lumen, produced using suture tube casting techniques. Scale bar 500 µm.

With lower outer porosity a simple test was performed to ensure the conduits retained sufficient porosity for the diffusion of liquids/nutrients. Conduits were

gripped from above and the bottom slowly lowered into a blue dye. The blue dye quickly moved into the pores, confirming the open and interconnected porosity of the conduits (Fig 55).

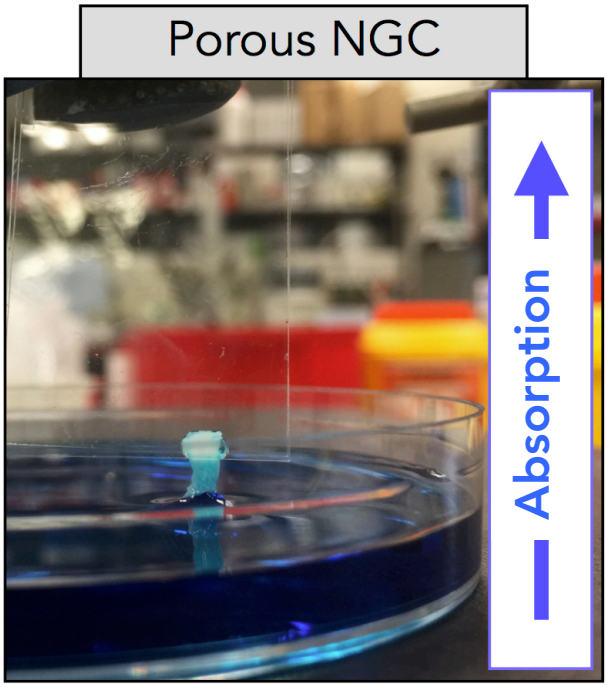

Figure 55: Digital photograph showing PGSm polyHIPE conduit, dipped into blue dye. Dye diffuses into conduit pores, highlighting NGC porosity.

Schwann cells were seeded onto PGSm polyHIPE disks and cultured for 3 weeks. Confocal images (Fig 56) were taken of a z-stack from the polyHIPE disks. Schwann cells are seen throughout the polyHIPE and have migrated into the porous material, outlined in the individual slices (Fig 56, B).

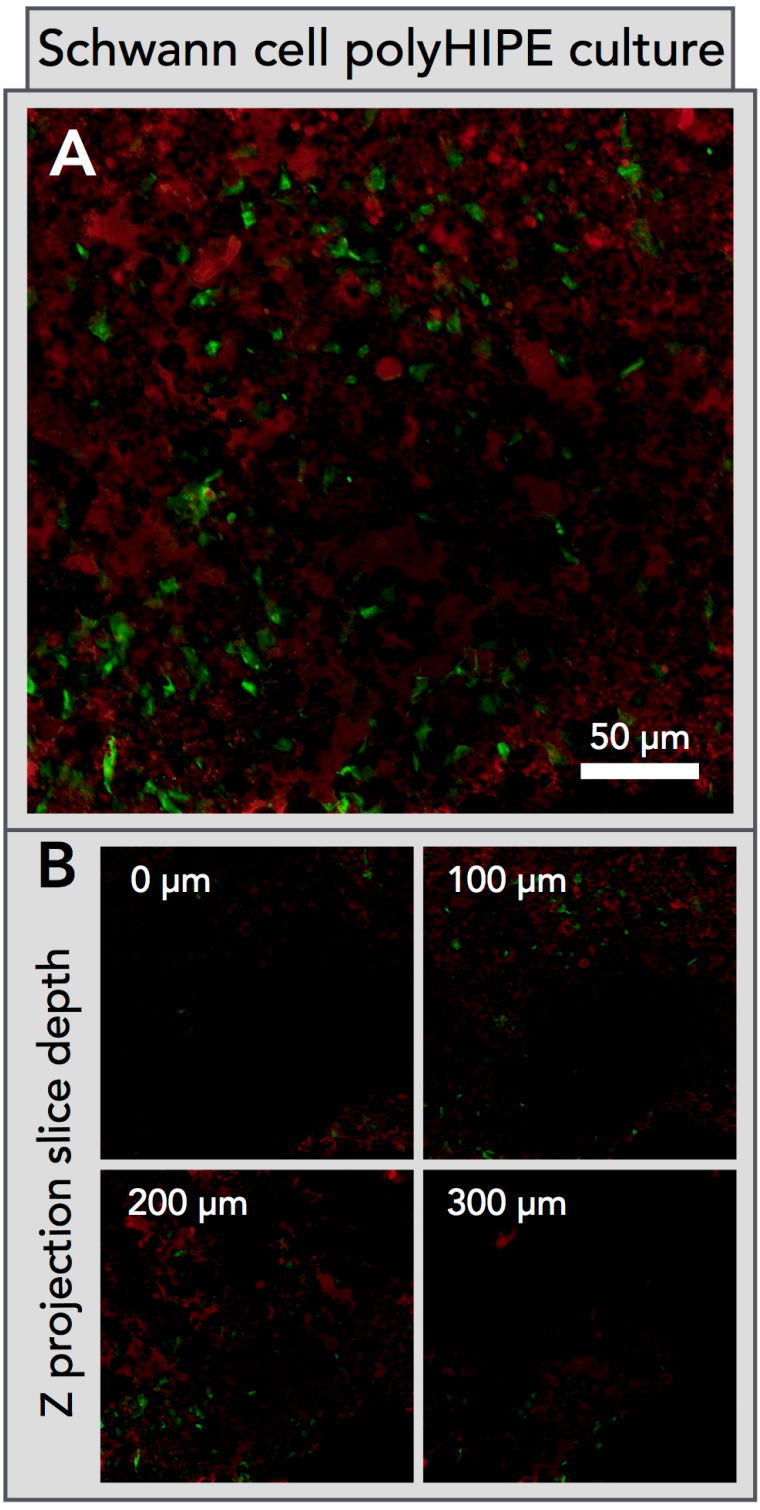

Figure 56: Confocal micrograph - z-stack image of PGSm polyHIPE seeded with Schwann cells and cultured for three weeks (A). PolyHIPE autofluoresces (red) and schwann cells are visualized using antibody S100-beta (green). Individual slices from three stages of the Z-stack show cells throughout the polyHIPE (B).

DRGs were seeded into the end of PGSm polyHIPE NGCs and confocal z-stack micrographs taken (Fig 57) through the outer conduit surface and into the porous wall. The images show neurites (green), Schwann cells (red) and the porous polyHIPE conduit (blue). The porous conduit was visualized as the PGSm polymer autofluoresces. Schwann cells can be seen to have migrated from the cell body, into the polyHIPE conduit, through the porous network and have travelled up to 700 μm.

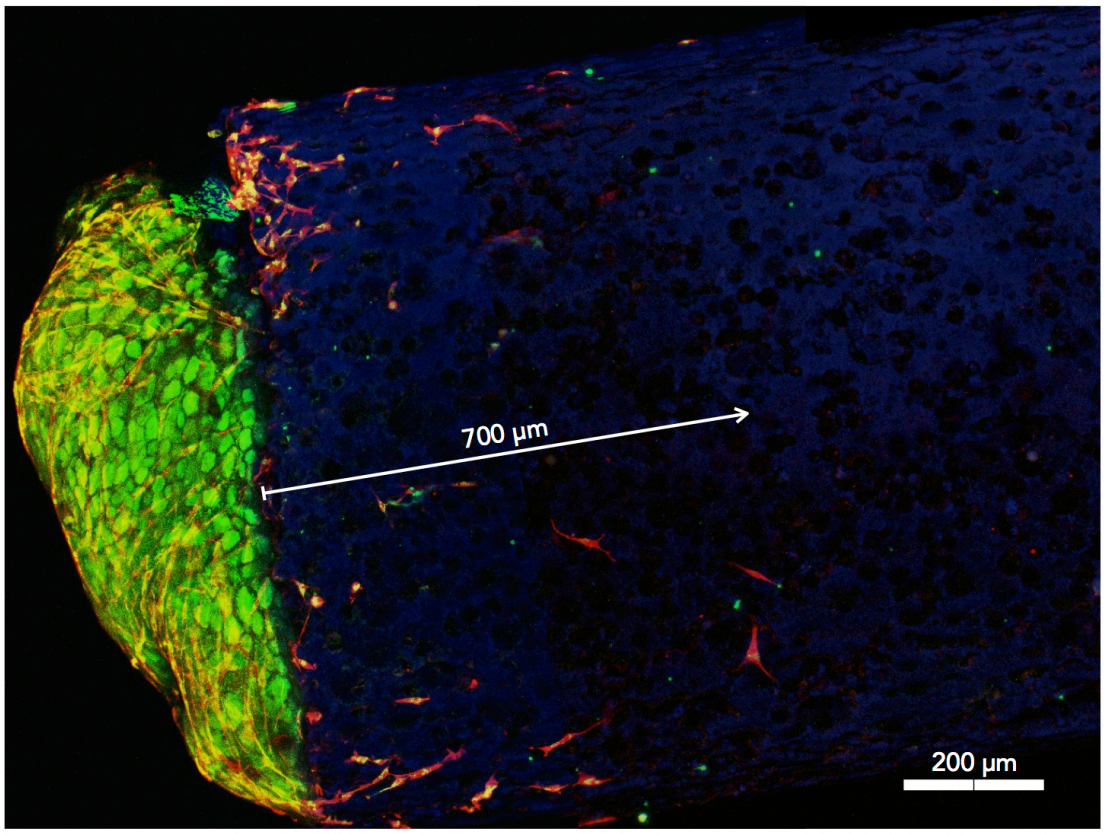

Figure 57: Confocal Z-stack image of porous NGC (blue), seeded with ex vivo DRG. Neurites (green) and Schwann cells (red).

When compared with previously studied non porous conduits (chapter 3.3), Schwann cells appeared to migrate a shorter distance from the DRG body, in the three week culture (Fig 58.)

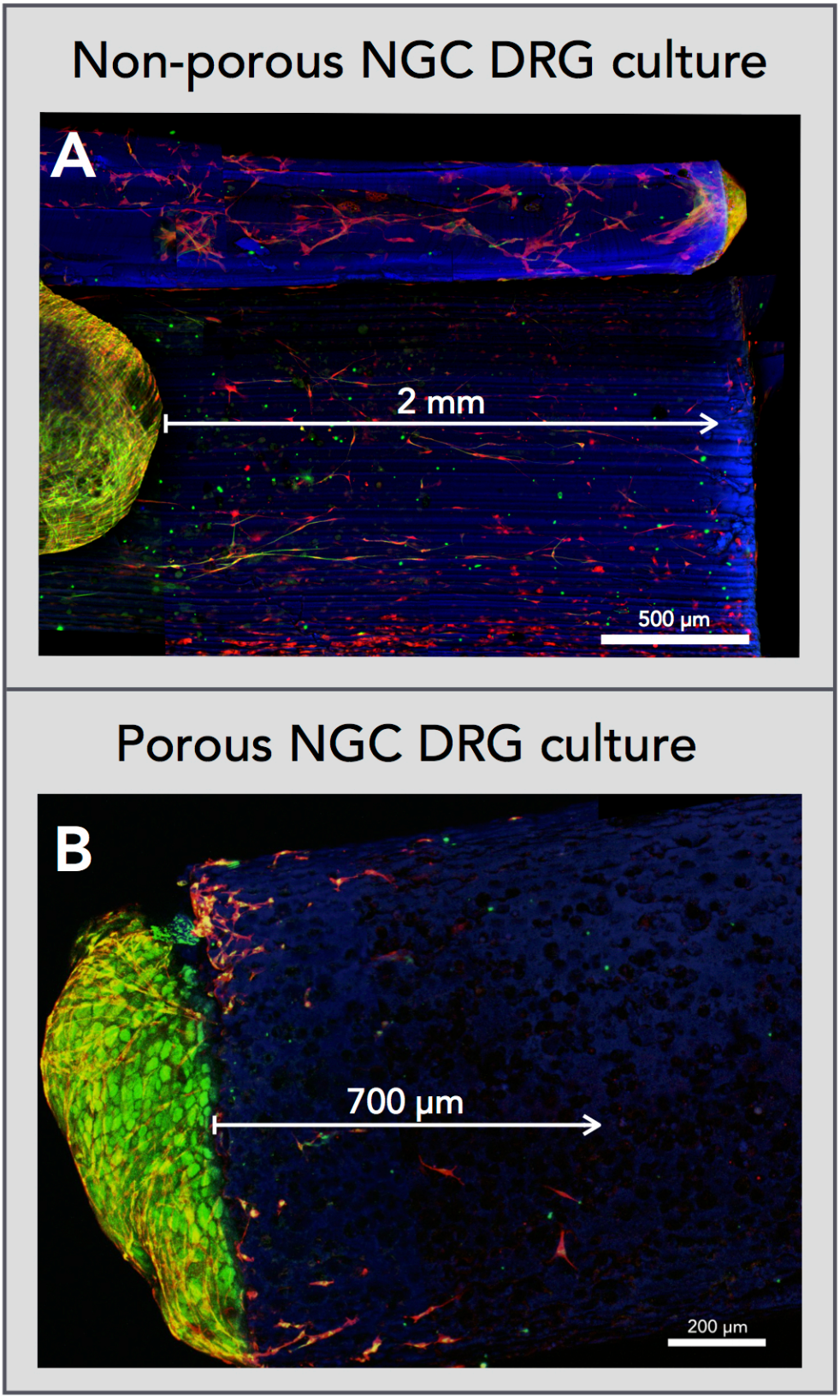

Figure 58: Confocal z-stack micrographs comparing the Schwann cell migration from a DRG body in non porous (A) and porous (B) PGSm conduits. Figure 57: Confocal Z-stack image of porous NGC (blue), seeded with ex vivo DRG. Neurites (green) and Schwann cells (red).

4. Discussion

To our knowledge there are no examples in the literature of polyHIPE PGS/PGSm. There are also no examples of polyHIPE nerve guide conduits of any material in literature to the best of our knowledge. Therefore the aim of the study was to produce uniform, replicable PGSm polyHIPE NGCs, to be used *in vivo*. Emulsions were successfully produced in methods previously explored (chapter 3.2). Conduits were successfully produced via stereolithography and needle tube casting. Conduits could be produced via stereolithography. For this to be possible the laser power required was high and the print speed was low, these variables were necessary to overcome the significant light scattering delivered from the water droplets within the emulsion. Due to the high power of laser, low print speed, and variable light scattering it became extremely difficult to produce uniform and reproducible conduits via stereolithography. Casting techniques using a needle and glass tube were far more effective in producing uniform, reproducible conduits, with porosity on both the internal and external surfaces of the conduit. This technique however was time consuming and there was difficulty aligning the needle centrally.

A suture tube casting technique was developed which successfully overcame the problems of being time consuming and difficulty in centralizing the internal lumen. The conduits were created in batches, drastically minimizing production time. The internal lumen was centralized by threading the suture through the centre of pre-made PDMS molds, which held the tube in place. This established an effective method in creating highly reproducible polyHIPE PGSm conduits in a timely manner. A short amount of time was taken while the emulsion was within the tube and the suture was being secured into the PDMS top. During this time the emulsion began to spread across the internal

hydrophilic glass surface, creating a slightly less porous outer surface (Fig 53, C). Interestingly this may be a benefit for nerve guidance conduits, with a porous conduit allowing nutrient exchange and cell integration, but also a slightly diminished surface porosity helping to direct neurites efficiently. For future experiments it can be postulated that if it was required to provide a more open surface porosity the internal glass surface could be treated or a more hydrophobic material could be used.

SEM images indicate a porous conduit surface, however it was also necessary to determine the internal 3D porosity of the conduits. MicroCT models allowed the visualization of the porosity throughout the 3D construct. MicroCT models identified that conduits were uniform in shape and maintained a high levels of porosity throughout. There was also a clear lumen maintained across the length of the conduit. This is important, as any occlusions within the lumen would hinder regeneration of a nerve.

Previous studies (chapter 3.3) have shown PGSm to be a highly biocompatible material, ideal for use in peripheral nerve research. However, questions were raised whether the open porous network would provide domains for Schwann cells to migrate within and an appropriate substrate for Schwann cell growth. Results from primary Schwann cell studies show that the porous PGSm polyHIPE was a permissive network for Schwann cell growth, with cells surviving over three weeks within the porous network. The use of Live/Dead studies and quantitative assays was complicated due to the 3D nature of the polyHIPE, and so studies were developed using *ex vivo* analysis.

Ex vivo studies performed using DRGs showed that the PGSm polyHIPE conduits supported Schwann cell migration and neurite outgrowth from the cell body. Imaging the conduit using a confocal z-stack only allowed for the

visualization of a small depth into the porous conduit however, it was clear that Schwann cells had migrated through the porous network and along the conduit (Fig 57). Over the three weeks cells were able to migrate further in the previously studied non-porous conduits, than the porous polyHIPE conduits (fig 58.) This is thought to be because cells have migrated within the porous conduit and are moving between the pores at a slower rate. Whereas cells on the non-porous conduit were attached to a flat surface (with topographical grooves), allowing a more efficient route along the conduit.

A compromise arises between enhancing direct axonal regeneration and porosity allowing nutrient exchange, raising the question, what degree of porosity is necessary for nerve regeneration? Porous conduits have the potential of being seeded with cells prior to implantation, increasing the effectiveness of conduits. Porous polyHIPE conduits could provide sites internally for cells to attach and providing protection to cells during implantation. It is already determined that Schwann cells are able to survive many weeks within the porous PGSm network, highlighting the cell seeding capabilities of these polyHIPE conduits. There are currently no examples of polyHIPEs for use in peripheral nerve repair in literature, which suggests further studies would be useful. Particularly as it is understood that permeability allows for nutrient exchange within the conduit and this may be one of the limiting factors of the efficacy of conduits in large gaps[116].

5. Conclusion

The overall findings from this chapter confirm that it is possible to produce polyHIPE PGSm porous conduits via a number of different methods. Stereolithography produced irregular conduits due to light scattering, needle tube casting was too time consuming and complicated, whereas suture tube

casting provided a method to produce uniform conduits in a timely manner. SEM images from suture tube casting showed a lower surface porosity than the others, however microCT imaging confirmed total porosity and uniformity throughout the conduit. The polyHIPE was permissive for Schwann cell culture and Schwann cells had migrated deep (over 300 μm) within the PGSm polyHIPE network. The porous polymer also provided a good substrate for *ex vivo* DRG neurite outgrowth and Schwann cell migration within the polyHIPE network. The question over the efficacy of the porous conduits to provide regeneration across the large injury gaps remains and further *in vivo* studies should be performed to determine this.

3.5 POROUS PGSM MICROPARTICLES FOR CARTILAGE REPAIR

Aim: The aim of this chapter was to develop and explore novel porous PGSm HIPE particles as scaffolds for cartilage tissue engineering through mechanical and in vitro *analysis*

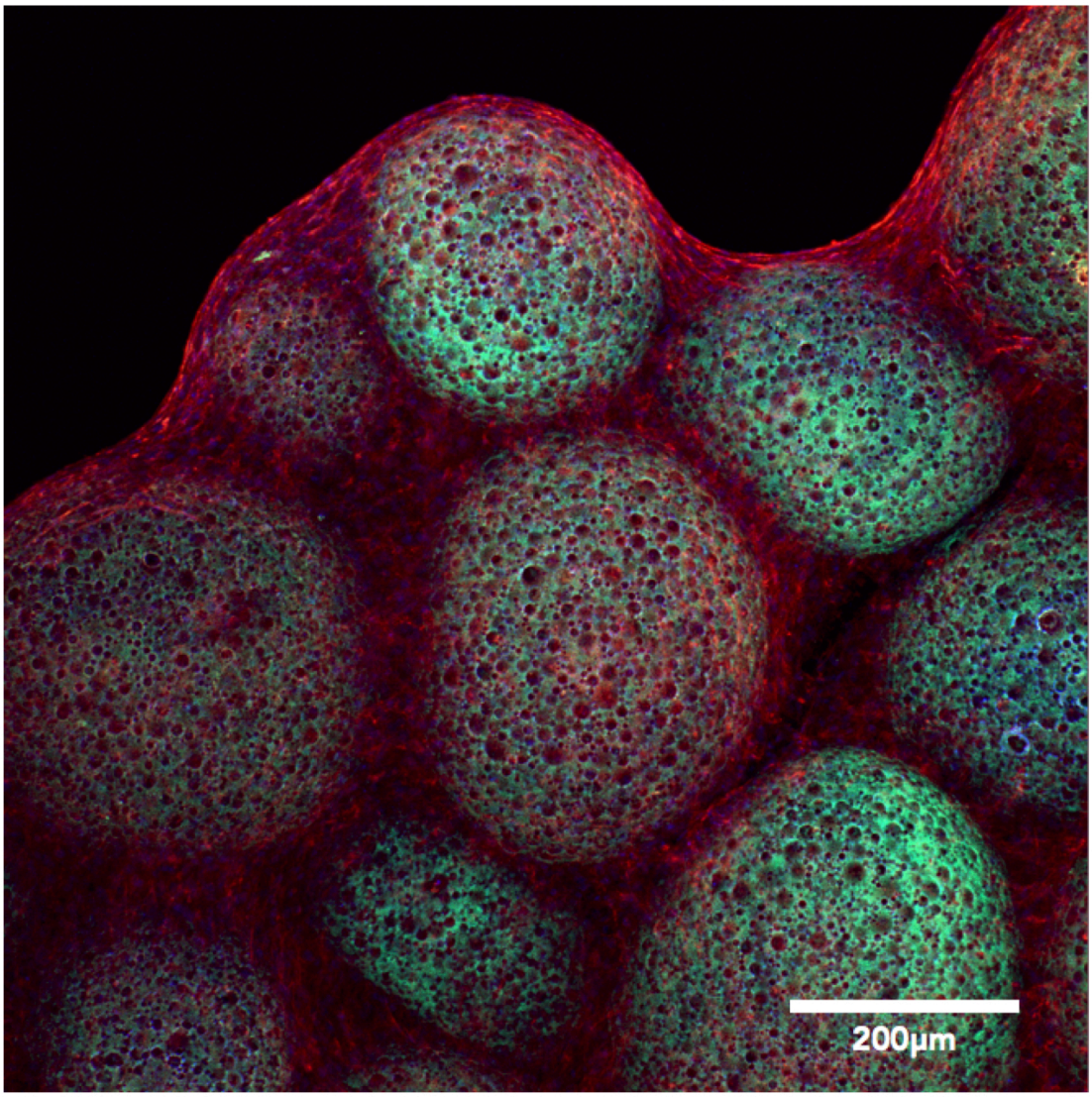

Chondrocytes seeded onto microparticles with collagen fibrils and ECM tissue. Image taken from Fig 69.

1. Introduction

Cartilage is a highly specialized dense connective tissue serving to support and give shape to softer tissues, provide a low friction area for free articulation at joints and provide a model for bone formation[119]. There are three types of cartilage, fibrocartilage, elastic cartilage and hyaline cartilage. Hyaline is the most common type of cartilage often found as articular cartilage at the ends of diarthrodial joints. Fibrocartilage is present in tendon insertions and intervertebral disks, while elastic cartilage can be found in the ear and epiglottis. Cartilage is comprised of chondrocytes populated within a dense extra cellular matrix (ECM). The ECM is made predominantly of water, collagen, chondrocytes and proteoglycans. Collagen makes up the 60% of the dry weight of cartilage, with 90-95% of collagen being collagen type II, and minor proportions of collagen types I, IV, V, VI, IX and XI[119]. The presence of glycosaminoglycans (GaGs) creates a high affinity for water and leads to the high water content of cartilage.

Articular cartilage is a type of hyaline cartilage present in joints[119]. Damage to the articular cartilage caused by injury or pathology often leads to osteoarthritis, causing joint pain and a deterioration in the joint leading to a loss in function. This deterioration often requires surgical intervention such as arthroplasty, osteochondral grafts, arthrodesis, and ultimately total joint replacement. While total joint replacement should remain a last resort, all other surgical techniques currently do not stop the long term destruction of the joint, which is why innovative tissue engineered approaches to developing and regenerating articular cartilage is a highly active research field[120,121]. Articular cartilage is avascular, with a lack of nerves and lymphatic system, limiting it's capacity for repair[120]. Cartilage regeneration techniques currently being explored/in use can be split into three categories:

microfracture and bone marrow stimulation, autologous chondrocyte implantation, and matrix induced autologous chondrocyte implantation (MACI)[121]. Tissue engineered cartilage is a widely researched area for the repair of joint damage and also the repair of nasal and auricular cartilage[122,123].

1.1 Microfracture

Briefly, microfracture utilizes the body's ability to repair itself; by creating a wound site, allowing, MSC's to migrate from the bone marrow and initiate wound repair[124–126]. Commonly the damaged tissue is cleared, allowing healthy repair of new tissue. Small holes are created by a 45° awl, into the subchondral plate creating the stress necessary to initiate wound repair and the growth of healthy cartilage. This relatively inexpensive technique is often the first repair technique used by surgeons, however, results from this type of surgery must be improved. Whilst fresh cartilage formulation is stimulated by microfracture, it is often inferior fibrocartilage that is stimulated to regrow, as opposed to the preferred hyaline cartilage. Studies have shown this mechanically inferior cartilage does not perform long term, and begins to break down at 18 months[121,125,127,128].

1.2 Autologous chondrocyte implantation

Autologous chondrocyte implantation utilizes an *in vitro* culture of the patients' own autologous chondrocytes to help regenerate fresh cartilage. Briefly, this is done through two surgical operations; the first is to take a full thickness biopsy from a low weight bearing area of the joint. This biopsy is used to isolate, culture and expand autologous chondrocytes *in vitro*. These cells are then implanted into the damaged cartilage area and covered by a membrane. Results from ACI studies have been positive; with one study

stating that 10-20 years after surgery 74% of patients reporting their status as better or the same as previous years[129]. There are drawbacks to this procedure, mainly the recovery time for tissue maturation, the requirement of multiple surgeries, the complexity of procedures and related costs. The membrane used to cover the autologous chondrocytes has also been hotly debated – the traditional method involves the use of a periosteal patch, with an alternative method using a bovine collagen type I/III patch. Problems have been commonly reported with the use of the periosteal patch, with regards to hypertrophy of the patch, this can lead to mechanical problems within the joint and revision surgeries[130]. The FDA also limits the use of the collagen patch. Cell distribution irregularities and the potential for cell leakage has led to studies incorporating 3D scaffolds and matrixes[130,131].

1.3 Scaffolds and MACI

The use of scaffolds as cell carriers with tissue engineered cartilage can have many benefits; including the better distribution of cells and filling of cartilage defects, quicker recovery due to scaffold stability, fewer donor site complications and the benefit of a simpler surgical procedure[121]. It is known that the 2D monolayer culture of chondrocytes often leads to dedifferentiation towards a fibroblast phenotype/fibrocartilage. Whereas studies have shown that 3D cultures have a more potent chondrogenic potential[132]. This suggests that by implementing a 3D environment it is possible to limit the dedifferentiation of the chondrocytes and stimulate more hyaline-like cartilage. MACI uses a bilayer scaffold from porcine type I/III collagen which is made up of a smooth highly dense side composed of collagen fibers and a rough side with wide spaced fibers for chondrocyte culture. An initial surgery is needed to collect autologous tissue, from which chondrocytes are isolated, expanded and then seeded onto the scaffold. The

scaffold can be attached to the chondral base with fibrin glue, negating the need for a membrane cover. The rough cell laden side is implanted adjacent the bone and the smooth low friction side toward the joint[130]. Results from MACI are largely positive, with studies reporting similar and perhaps even better results when compared with ACI. Lower incidences of hypertrophy are reported, and it was also noted that MACI is quicker to perform surgically, which was advantageous[130]. Whilst MACI offers many benefits, its superiority over other techniques remains unclear, with the related costs and furthering functional improvement driving the research of alternative 3D scaffolds for tissue engineered cartilage. For example, hyaluronic acid and fibrin based scaffolds have been explored in a similar MACI manner, with similar results[121].

1.4 Tissue engineered cartilage

Research into tissue-engineered cartilage involves the isolation of cells, the culture of these cells seeded onto a biomaterial scaffold, or within a liquid precursor, and the eventual implantation of the scaffold into an injury site. Chondrocytes and MSCs can be isolated from patient biopsies, cultured and seeded onto 3D scaffolds. Chondrocyte cultures remain the obvious choice of cell to use in cartilage tissue engineering, with chondrocytes producing cartilage ECM. However chondrocytes are known to have instability and a loss of phenotype in monolayer cultures, which is why the use of MSCs are also explored[132]. The chondrogenic potential of MSCs however is often largely determined by additional growth factors and mechanical stimuli and material stiffness[133,134]. Also a full cartilage biopsy for the isolation of MSCs may have further complications related to future instances of arthritis.

The scaffolds used for cartilage tissue engineering can either be made from natural biomaterials, which are often protein or polysaccharide based; or

synthetic biomaterials often synthesized from soft polymers. Natural biomaterials offer the benefit of increased biocompatibility with the cells, however synthetic biomaterials allow for more versatility and reproducibility in scaffold design. Example natural biomaterials used for cartilage tissue engineering include silk, collagen, fibrin, chitosan and hyaluronic acid. Examples of synthetic polymers include poly(glycolic acid) (PGA), poly(lactic acid) PLA, poly(ethylene glycol) PEG and polyurethanes[135]. BioSeed, a company from BioTissue Technologies (Freiburg, Germany), have designed a synthetic polymer graft seeded with autologous chondrocytes. This has shown some success, reporting improved clinical scores in humans; however there were also reports of cytotoxic degradation products and poor tissue integration[136,137]. To further enhance and stimulate growth of a cartilage like tissue, a series of factors could help with chondrocyte cultures on the scaffold, including the use of bioreactors, mechanical stimuli and bioactive molecules. However, these techniques can also complicate cultures and increase cost. It is also understood that an ideal 3D microenvironment for cell culture can result in cells with increased chondrogenic potential. It is clear that scaffolds must help mimic and work alongside native tissue – highlighting the need for innovative 3D designed scaffolds using appropriate biomaterials.

1.5 PGS and Cartilage tissue engineering

An ideal scaffold for tissue engineered cartilage would be biocompatible, have good cell interaction including adhesion, growth and differentiation, have a limited tissue response, a complete 3D microenvironment, allow for diffusion, controlled degradation and have similar mechanical properties to the native tissue.

There has been limited research into the use of PGS for cartilage tissue engineering and no research into photocurable or methacrylated PGS for cartilage tissue engineering. As PGS is a versatile, soft and extremely biocompatible polymer, it is a clear candidate material for cartilage tissue engineering. One of the major drawbacks to traditional PGS is the long curing times requiring high temperatures and pressures and limiting the structural capacity of the polymer. The novel PGSm overcomes this drawback, allowing for instantaneous curing; which opens up the polymer for use in far more intricate and complex scaffold designs. Furthermore, the ability to photocure, print and the advantages of the novel PGSm HIPE (explained in chapter 3.2) has lead the research in this study into the development of PGSm HIPE particles.

Scott Hollister's research group from the University of Michigan, explored the use of PGS for cartilage repair. The initial study in 2010 varied the mechanical properties of PGS, tailoring for cartilage repair. The study concluded that PGS is a good candidate material for cartilage tissue engineering largely due to its appropriate mechanical properties. A further study from the group in 2015 compared the material with other polymers. It was concluded from both studies through *in* vitro experiments using chondrocytes, that the material may be suitable for cartilage tissue engineering[138,139]. The studies however used one simple scaffold design, created using a solid freeform-fabricated technique (i.e. wax molding). Also the studies did not use a photocurable version of PGS or the unexplored methacrylated PGSm used in this study.

1.6 PGSm HIPE microparticles

PGSm HIPE's have already been introduced and discussed in chapter 3.2. Briefly a HIPE is an emulsion, created of a mix of immiscible continuous and

dispersed phase materials. Here this is a water-in-oil HIPE, whereby the oil is the polymer, which is spread around individual water droplets. The photocurable nature of the material, PGSm, enables it to be instantly crosslinked in the presence of UV light. Once fully crosslinked and dried a highly porous polymer network is created. This highly porous network can create intricate 3D microenvironments. This has been shown to be extremely important in tissue engineering of cartilage, where dedifferentiation can occur in 2D cultures[136]. One drawback of a polyHIPE and other porous scaffolds, can be the slow speed at which the cells migrate and ingress into the scaffold, if at all. This can be overcome through the use of alternative cell seeding techniques such as injection cell seeding, however, these techniques can also introduce unwanted complications and shear stresses to the cells. Other common limitations of large bulk porous scaffolds, are the difficulty in tailoring the shape of the scaffold and often complicated implantation techniques.

One method to overcome these problems is to develop HIPE microparticles. These are microparticles of a designed size, with interconnected pores; which are used together to create a larger scaffold. The use of porous microparticles can provide more versatility; as many particles used in conjunction can shape the required larger scaffold, allow for quicker implantation techniques and reduce the time for cell ingress into the scaffold. Cell ingress time into the scaffold is reduced due to cells being interspersed with the particles and thus having to travel shorter distances in the many smaller particle scaffolds. Particles can be seeded with cells, allowed to mature in culture and then implanted; or particles can be seeded with cells and then implanted immediately through simple injection. Porous microparticles have been synthesized as reported in the literature using a variety of techniques,

including a recently explored water-in-oil-in-water system[140,141]. The size of the particles, level of porosity and pore size can be tuned using this water-in-oil-in-water system. Porous microparticles have been researched recently for a multitude of applications including drug carriers, cell delivery, chromatography and as biomaterial scaffolds[141].

1.7 Packing density of porous particles

The use of particles to make up a larger scaffold does however add an extra variable, with regards to the packing density of the scaffold. If the packing density is low then the scaffold porosity would be largely determined from the spaces between the particles, however, with a high packing density the porosity of the material would be better related to the scaffold design. It is postulated that a higher packing density would be beneficial for porous particles as scaffolds for cartilage repair.

The literature reports that with spheres of a homogenous size, the maximum packing density is 74%; with the remaining 26% being space surrounding the spheres[142]. The packing density has however been reported to increase with the use of bimodal and heterogeneously sized spheres[143,144]. This is simply down to spheres of differing sizes finding the vacant spaces between the homogenously sized particles, as shown below in (Fig 59). It can be concluded that many heterogenous porous particles, for use collectively as a cartilage tissue engineering scaffold, would have the added advantage of a higher packing density.

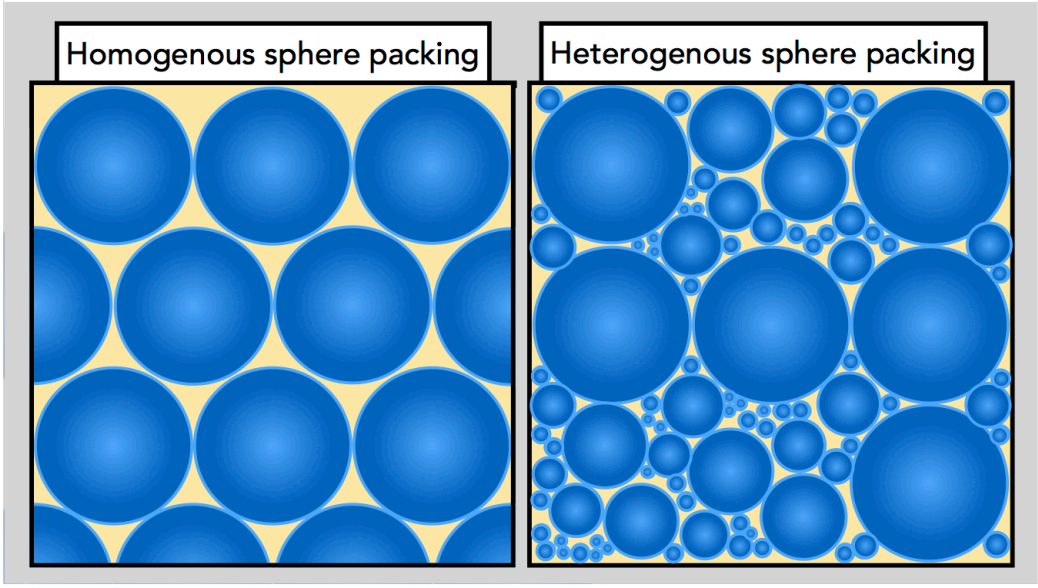

Figure 59: Computer designed image showing the packing density of homogenous and heterogenous spheres (Keynote, Apple)

1.8 Summary of introduction

The literature reports on positive results when comparing ACI to microfracture, highlighting the usefulness of chondrocyte seeding techniques. MACI and the use of 3D scaffolds have had equally positive results, while overcoming some of the limitations such as hypertrophy and the potential dedifferentiation of chondrocytes with 2D culture. Alternative 3D scaffold designs with innovative seeding techniques may yet further improve the efficacy of these tissue-engineered approaches to cartilage repair. Some research has focused on PGS, with indications that it may be a good candidate for cartilage tissue engineering. However, photocurable PGSm has not been researched for cartilage repair. This photocurable polymer can allow for more complex designs such as HIPE particles, with greater control of scaffold size and porosity. Also the use of small polymer particles may allow for injectable scaffolds. This chapter explores the use of 3D porous PGSm HIPE particles as a scaffold for tissue engineered cartilage repair.

2. Methods

The Methods section of this chapter outlines the methodologies related solely to this chapter. Comprehensive methods, including PGSm and HIPE synthesis and characterization can be found in chapters 3.1 and 3.2.

2.1 Particle production

A close circuit system comprising of a peristaltic pump, syringe pump, UV curing chamber, collector and H_2O reservoir was used to produce the particles. A 10 mL syringe, attached to a syringe pump, contained the PGSm emulsion. The needle of the syringe was inserted into the polymer tubing with a peristaltic pump flowing water across the tip of the syringe. As the syringe pump expels the emulsion into the tubing droplets of the emulsion are carried by the water flow, creating a water-in-oil-in-water system. The emulsion is passed through a curing chamber and irradiated with UV light to crosslink the porous polymer particles. The particles are then collected into a cell strainer, with excess water falling through the strainer and into a reservoir completing the setup. Properties of the microparticles could be varied by adjusting the needle size, flow rate and the syringe pump rate. Needle diameters explored were 0.33 mm, 0.61 mm and 1.91 mm, syringe flow rates explored were between 0.1 mL /min and 0.7 mL /min and the peristaltic pump kept was maintained at 450 rpm for water flow. After initial tests, particles were produced with a needle diameter of 0.61 mm and a syringe flow rate of 0.4 mL/min for all further experimentation.

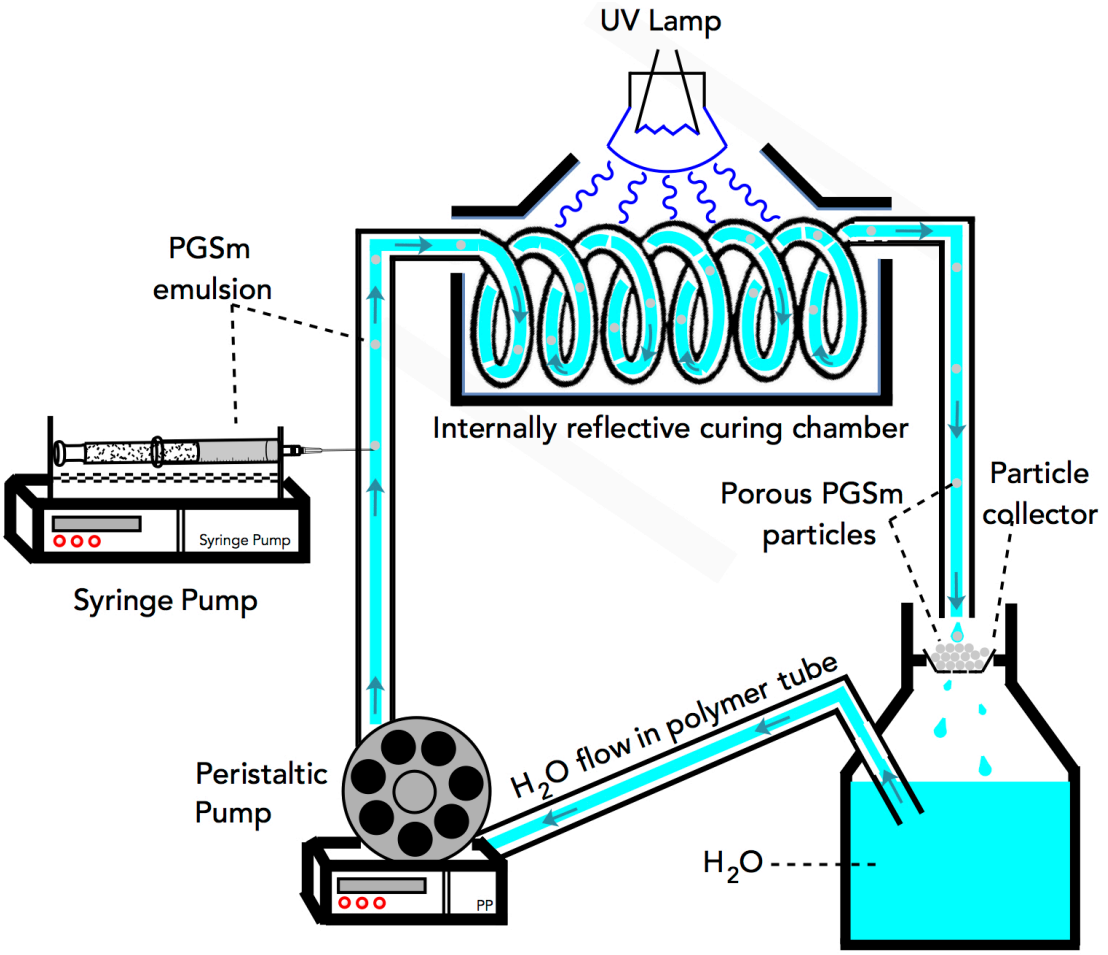

Figure 60: Diagram describing the microparticle synthesis setup developed, showing the flow of water through the system and the injection of HIPE through the syringe pump (Chemdraw)

2.2 Chondrocyte cell Isolation and Culture

Chondrocyte cells were kindly donated by Sarah Lindsay, (PhD student for Dr. Aileen Crawford, Dental School, University of Sheffield), who performed the chondrocyte isolation. Subsequent cultures, cell expansion and experimentation was performed by myself.

Metacarpophalangeal joints were obtained from a local abattoir from skeletally mature, beef cattle (18-24 months) within six hours of slaughter. Joints were sprayed with 70% IMS and 10% Trigene. To further minimize infection risks, all areas of the joint that were not being worked on were

wrapped in foil. A post mortem blade was used to remove the skin from the joints. Bovine metacarpophalangeal joints (the third metacarpal on the hoof) were used, and the skinned joints were moved to a class-2 laminar air cabinet, where all following procedures were performed aseptically. A sterile scalpel was used to pry open and extract synovial fluid from the joint. The scalpel was used to pry the joint apart further and using a scalpel and tweezers articular cartilage was removed from the surface of the joints, and placed into Ca^{2+}/Mg^{2+}-free PBS (phosphate buffer solution).

Articular cartilage pieces were removed from PBS, incubated in 2.5% (w/v) trypsin at 37°C for 30 minutes, and then washed in fresh PBS. High glucose DMEM (Dulbecco's Modified Eagle Medium), containing 1000 units/mL penicillin, 1000 µg/mL streptomycin, 10% FCS (fetal calf serum) and 2 mg/mL bacterial collagenase, was incubated with the cartilage pieces on an orbital shaker within a 37°C incubator and shaken at 30 rotations per minute for 18 hours. After tissue digestion, the cell-containing medium was transferred into centrifuge tubes and centrifuged at 1,000 rpm, 192g for ten minutes. The centrifugation resulted in a pellet of chondrocytes; the supernatant was removed and the pellet resuspended in PBS. The cells then underwent centrifugation again, the pellet resuspended in PBS and the cells pelleted via centrifugation once more. The resultant cell pellet was then resuspended in high glucose DMEM and a haemocytometer was used to calculate cell numbers. A monolayer culture of chondrocytes was then set up in T75 flasks, with basic medium (high glucose DMEM containing 1000 units/mL penicillin, 1000 µg/mL streptomycin, non-essential amino acids, and 10 mM HEPES buffer pH 7.4 and 10% v/v FCS). All cell cultures were incubated at 37°C in a humidified atmosphere of 95% air and 5% CO_2. All experiments were performed using passage one or two cells. Cells were passaged in a standard manner using 0.05% trypsin and 0.02% EDTA at 37°C for 5 minutes.

2.3 Chondrocyte culture and seeding

All porous PGSm particles were centrifuged and redispersed in 70% ethanol for sterilization. PBS and media washes followed in a similar manner, centrifugation allowed for liquids to be quickly exchanged throughout the porous material. A 96 well plate was prepared by adding 15 µL of warm agarose solution (2%) to each well. As the agarose cooled it solidified, creating a flat coating to the bottom of the wells; this ensured that the chondrocytes would not adhere to the bottom of the well. Particles were dispersed in medium and 200µl of particle containing medium (between 25-50 particles) were added to wells in a 96 well plate.

Chondrocytes were used for experimentation at passage 1. The cryovial was warmed at 37°C, and the cell suspension was dispersed in 10mL of PBS and centrifuged at 192 g for 5 minutes. Cells were then dispersed in chondrocyte medium (high glucose DMEM containing 100 units/mL penicillin, 100 µg/mL streptomycin, 10% FCS, and FGF 10 ng/mL), counted and plated in T75 flasks for culture. Cells were used at passage 1. 50,000 cells were added to each of the wells containing the particles (or controls), medium added and the plate placed on an orbital shaker inside of an incubator for a period of 48 hours to allow the cells to evenly attach to the particles. After 48 hours differentiation medium was added to the wells (chondrocyte medium with 50 µg/mL L-ascorbic acid, 1µg/mL insulin), this medium was refreshed twice a week.

After 48 hours cells began to produce ECM between adjoining particles. This linked particles together creating a particle tissue disk.

2.4 Resazurin assay

A cell viability assay using resazurin was conducted at days 2, 7, 14 and 21. Particles seeded with cells, cell free particles and cells cultured on agarose were analysed. The full resazurin methodology can be found in the Methods (chapter 2).

2.5 GaG Assay

After 3 weeks of culture a DMB assay was performed to quantify the presence of sulfated GaGs, the DMB assay was based on Farndale et al method[145]. Papain digestion solution 150µL (200 mM PBS containing 1 mM EDTA, 0.05% w/v papain, 0.96% w/v n-acetyl cysteine, pH 6.8) was added to particles, particle-tissue disks, and medium in 0.5 mL Eppendorf tubes. Samples were incubated at 60°C for 24 hrs. DMB (dimethylmethylene blue) stock solution (0.008 g DMB, 1.52 g glycine, 1.185 g NaCl, 500 mL H_2O) was made, covered with foil and stirred for 2 hours. DMB stock solution pH was adjusted to 3.0 with hydrochloric acid. Chondroitin sulphate stock, used for a standard curve, was diluted 50 µg/mL in distilled water. Chondroitin sulfate calibrations (50 µL) were then added from chondroitin sulfate stock and distilled water in dilutions from 0-50 µg/mL, and added to a 96 well plate to create a calibration curve. A water blank was added to the 96 well plate. 50 µL digestion solution from the samples and the media were added to the well plate also. Using a multichannel pipette 250 µL DMB solution was added to all columns of the samples, calibrations and a reagent blank. The plate was then immediately measured in a plate reader at an optical density (OD) of 525 nm.

2.6 Cryosectioning

Particle tissue disks were fixed in 3.7% formaldehyde for 25 minutes and washed twice in PBS. The disks were placed into a square plastic cryo-molds and OCT medium (Agar Scientific) was poured both under and over the disk. The disk was properly aligned within the cryo-mold and the mold gently introduced to a small pool of liquid nitrogen for periods of 1-2 seconds. This was enough time to freeze the sample in OCT medium, without producing cracks. Once frozen the block was attached to the cryotome and sliced. Slices between 6-15 μm were attached to Superfrost microscope slides (ThermoFisher Scientific), as slides were brought to room temperature the OCT medium melted, leaving the sample on the microscope slide. Staining solutions and procedures are described below. Labels were written on glass slides in pencil. This is standard histological practice as pen ink can be washed away with staining solutions/solvents.

2.7 Histochemical staining – Haematoxylin and Eosin

Samples were immersed in xylene for 30 seconds, then into 100% EtOH for 30 seconds, 70% EtOH for 30 seconds and distilled water for 30 seconds. Sample slides were then immersed in haematoxylin for 3 minutes, washed in running tap water for 5 minutes and then immersed in eosin solution for 1 minute. Slides were then washed in 100% EtOH for 5 minutes, DPX mountant added and a cover slip secured covering the sample.

2.8 Histochemical staining – Picrosirius Red

Samples were dipped in 70% EtOH, rinsed in distilled water and placed in Picrosirius red solution (0.5 g Sirius red/Direct red 80, in 500 mL of saturated aqueous picric acid) for 60 minutes. Slides were then placed in acidified water

for 5 minutes (5 mL acetic acid in 1 L distilled water). Slides were then placed in 100% EtOH for 5 minutes, DPX mountant added and a cover slip secured covering the sample.

2.9 Histochemical staining – Toluidine Blue

Toluidine blue working solution was made from 5 mL of toluidine blue stock solution (1 g Toluidine blue O (Sigma-Aldrich) in 100 mL of 70% EtOH), and 45 mL of 1% Sodium chloride, pH 2.3. Samples were dipped in 70% EtOH, then distilled water, and were placed in toluidine blue working solution for 6 minutes. Slides were then washed in distilled water for 3 minutes, dried, DPX mountant added and a cover slip secured covering the sample.

2.10 Immunofluorescence – Collagen II Antibody

Samples were fixed for 25 minutes and washed in accordance with the immunofluorescence methodology (chapter 2). Primary antibody anti-collagen-II antibody (Abcam) was used at a titre of 1:100 in ICC buffer and left refrigerated overnight. Secondary antibody Alexa 546 goat anti-rabbit IgG ($\lambda_{Ex}/\lambda_{Em}$, 556 nm / 573 nm max; ThermoFisher Scientific) at a titre 1:100 in ICC buffer was added at room temperature for 2 hours. The sample was then washed and submerged in PBS for imaging.

2.11 DAPI and Phalloidin

Once fixed and washed phalloidin-TRITC (tetramethylrhodamine) was added at a titre of 1:1000 in PBS ($\lambda_{Ex}/\lambda_{Em}$, 540 nm / 565 nm max, ThermoFisher Scientific) for 30 minutes at room temperature. The solution was removed and the sample rinsed twice with PBS. DAPI (4',6-diamidino-2-phenylindole) was added at a titre of 1:1000 in PBS for 10 minutes ($\lambda_{Ex}/\lambda_{Em}$, 350 nm / 470 nm

max; ThermoFisher Scientific); the sample was then washed and submerged in PBS for imaging.

2.12 SEM and Micro CT preparation

Samples for SEM imaging not containing cells were dried and gold coated using a gold sputter coater and imaged using a Phillips XL-20 SEM.

Unless otherwise stated, samples containing cells were rinsed in PBS and then fixed in glutaraldehyde (2.5% in PBS buffer) for 1 hour. Samples were then washed in PBS for 15 minutes, then in distilled water for 5 minutes. The samples were introduced to increasing concentrations of EtOH in distilled water (35%, 60%, 80%, 90%, 100%) for 15 minutes each. A 1:1 solution of EtOH and HMDS was introduced to the samples for 1 hour inside a fume cupboard. Samples were then introduced to two 100% HMDS washes for 5 minutes each. HMDS was removed and samples air dried and gold coated as above.

Samples to be analysed with Micro-CT were rinsed in PBS and fixed in glutaraldehyde as above. The samples underwent a second fix and were rinsed in PBS and introduced to an aqueous solution of 2% osmium tetroxide 2 hours. The samples are then analysed using a Skyscan 1272 high resolution microCT.

2.13 Compressive mechanical analysis of chondrocyte disks

After 3 weeks culture, particle tissue disks were removed from culture and excess medium shaken off. Disks were then photographed from above beside a scale to calculate the area of the disks area using ImageJ (National Institutes

of Health, USA). The area and depth of the disks was used to calculate a compressive modulus value of the tissue disks. The disks were placed between the two high-density polymer supports of the compression testing machine (Zwick, zwicki line z 0.5 to), which was loaded with a 500 N load cell and the disks compressed at a rate of 0.1 mm/s. The particle chondrocyte disks remained intact throughout the experiment.

3. Results

3.1 Particle synthesis - SEM image analysis

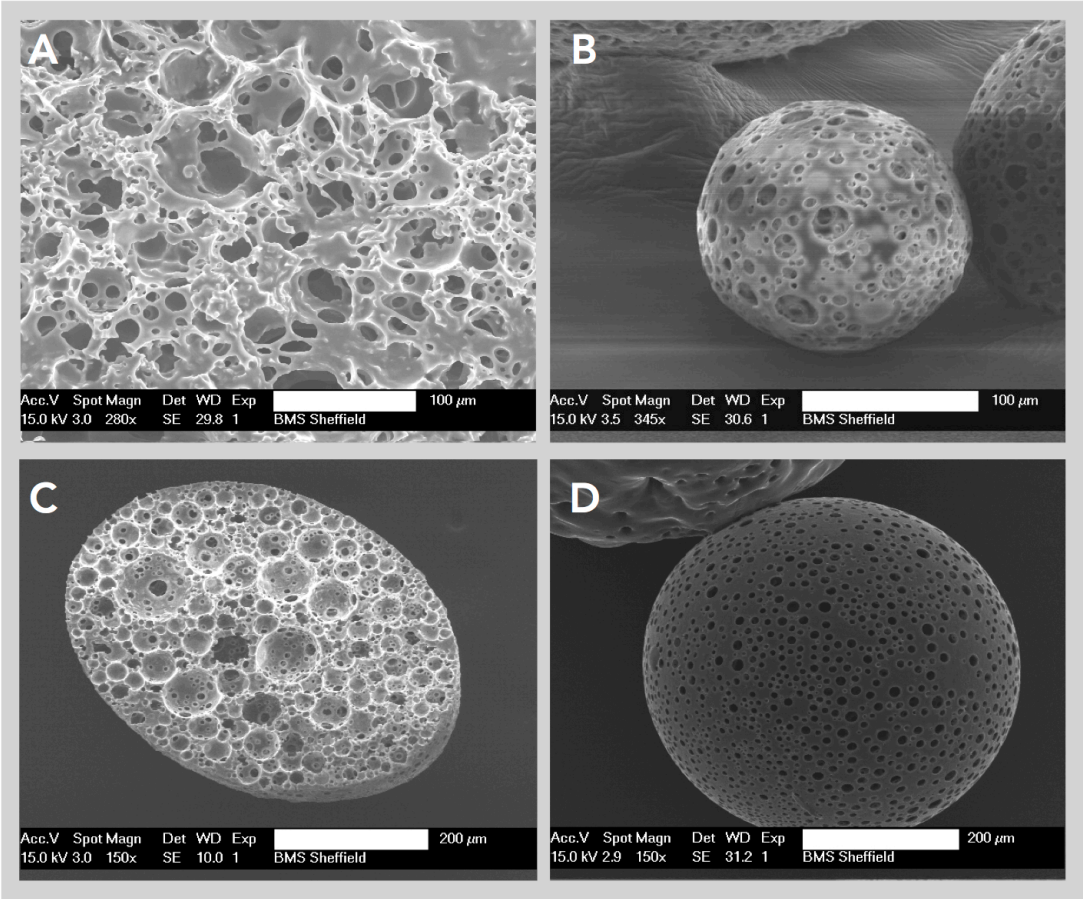

Figure 61: SEM images of the crosslinked emulsion and particles. (A) the bulk emulsion when fully crosslinked and dried, with a scale bar of 100 µm. (B) and (D) are single close ups of a particle synthesized, a scale bar of 100 µm and 200 µm respectively. (C) a particle cut open in two, showing a highly porous interior, scale bar 200 µm.

PGSm and PGSm emulsions were synthesized as discussed in the relevant chapters, (chapter 3.1 and chapter 3.2). The emulsion was then put through the particle synthesis setup to create porous microparticles. (Fig 61, A) illustrates the bulk HIPE when fully crosslinked and dried. A highly porous network is witnessed with interconnected pores between the voids where water droplets have been removed upon drying. SEM images (Fig 61, B and D) show a porous particle produced from the emulsion by the particle synthesis setup, with a porous exterior and interior. The porous interior of the particles is confirmed from a particle that has been cut open. These images show that porous PGSm particles could be produced readily, with porosity throughout and experimentation proved this could be done in a reproducible manner.

3.2 Particle size distribution and synthesis variables

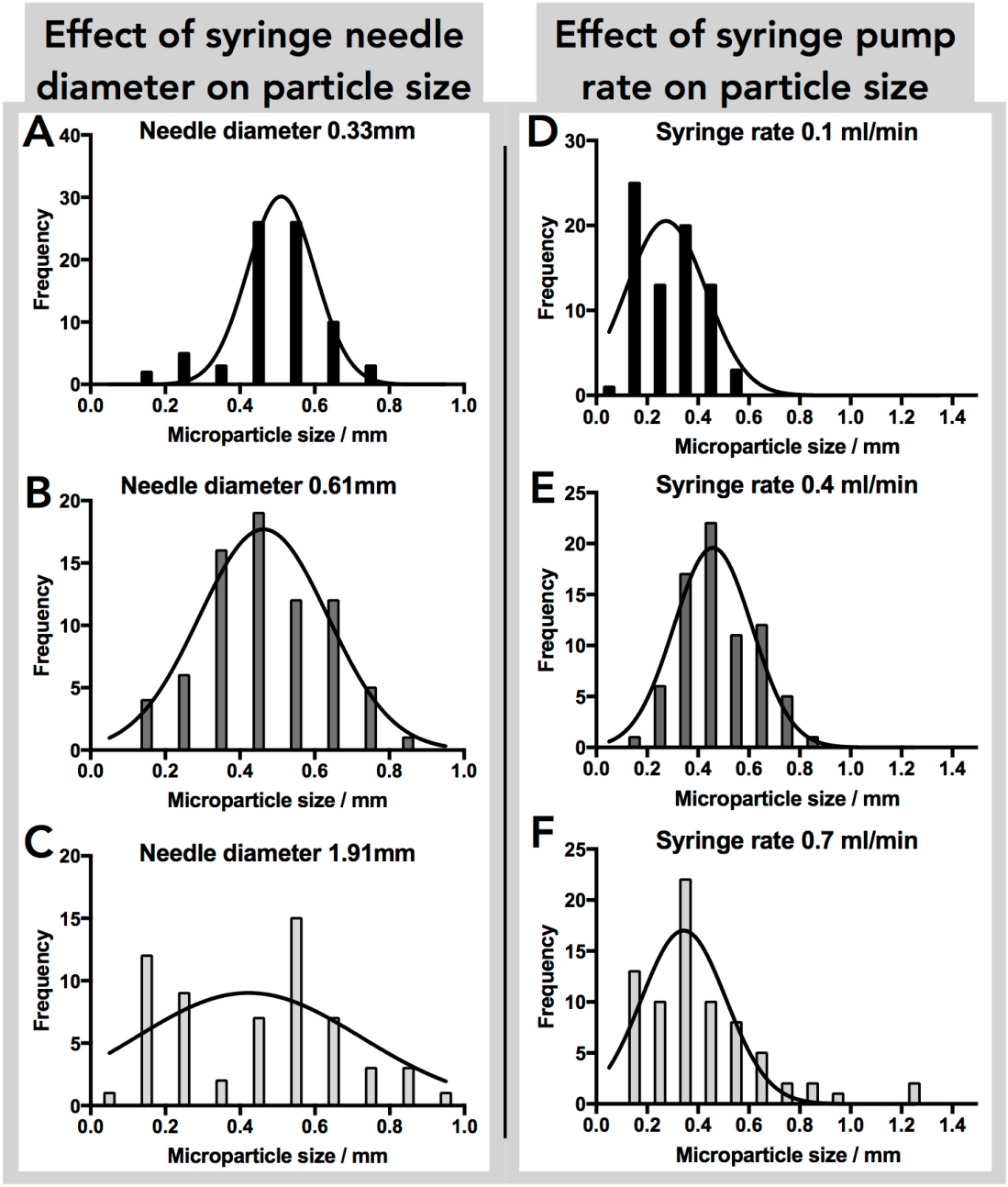

Figure 62: Histograms showing the affects of two experimental variables on the produced microparticle size. Histograms (A)-(C) the effect of changing the syringe needle diameter (0.33 mm, 0.61 mm, 1.91 mm) on particle size. (D)-(F) the effect of changing the syringe pump rate (0.1 mL/min, 0.4 mL/min, 0.7 mL/min) on microparticle size. All histograms were produced using SEM image analysis, whereby 75 individual microparticle diameters were measured using imageJ (NIH). All histograms were also fitted with a Gaussian distribution curve.

Increasing the syringe needle size when synthesizing the microparticles had a direct effect on microparticle size (Fig 62, A-C). It can be seen that with an increase in needle diameter, there was also the evidence of larger particles being synthesized. This can be seen when comparing the largest group of microparticles in (A), (B) and (C) whereby the largest particles measured increase in size with needle diameter. However, when looking at the Gaussian distributions of the three histograms (A)-(C) it is evident that the bell curve peaks are at a similar value in all three, suggesting that the average particle size does not change drastically. Instead the spread of particle size changes with needle diameter, with the largest spread of particle sizes at the highest needle diameter. It can be therefore noted that a small needle diameter may be more appropriate for synthesis of microparticles of a homogenous size; as can be seen in (A), whereby particle size frequency at 0.45 mm and 0.55 mm is higher. (C), shows a range of particle sizes from small, to the larger 1 mm particles, the distribution is wider than can be seen in (A) or (B). The distribution of particles in B shows a far more evenly distributed spread of particle sizes, with the graph conforming to a recognizable bell curve. It can therefore be noted that if particles are required from a more even spread of particle sizes, then the 0.61 mm syringe needle may be most appropriate. For all experiments in this study, a range of particle sizes from 0.2 - 0.8 mm was wanted to optimize the packing of particles (Fig 62); therefore the syringe needle size 0.61 mm was used throughout. Average particle size for parameters used was, 465 μm ±SD 158 μm (standard deviation error used, *n=75*).

Histograms (Fig 62 (D)-(F)) show the effect of altering the syringe pump rate on particle size. It is clear in these histograms that with increasing syringe pump speed from (D) to (F) the size of the particles increases. This can be

seen by the largest group of particles in each, clearly increasing in size from 0.6 mm in (D) to 1.2 mm in (F). Also the average of the Gaussian distribution curve shifts towards the right from (D) to (E) and (F); suggesting the average microparticle size also increases with syringe dispense rate.

3.3 Particle synthesis – Problems encountered

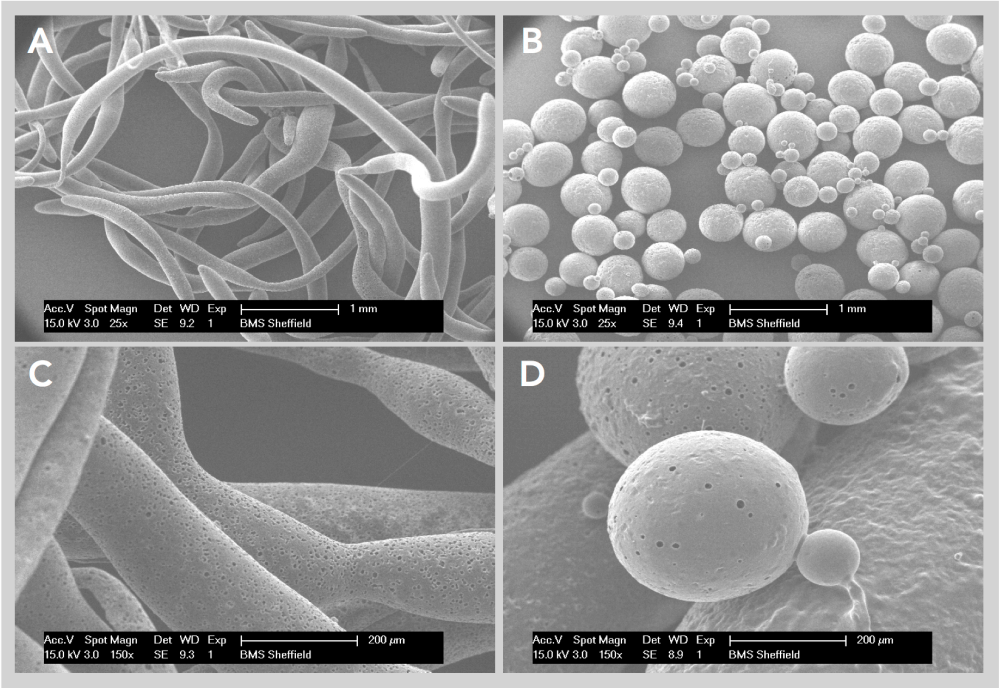

Figure 63: SEM micrographs from particle synthesis process and some of the problems encountered. Lower water flow rates (peristaltic pump speeds) created particles, which had elongated into strands (A) – (scale bar 1 mm). (B) indicate well-formed spherical particles of different sizes, for this experiment a size range could be quite useful for efficient packing; scale bar 1 mm. (C) is an SEM image of the strands at a higher magnification, the image shows that the strands maintain their outer surface porosity, (scale bar 200 µm). With higher water flow rates a diminished porosity was witnessed (D), (scale bar 200 µm).

SEM images illustrate some of the outcomes encountered when exploring a change in variables. SEM micrograph results (Fig 63, A) highlight how variations in the synthesis setup (lower water flow rate) can lead to the production of microstrands as opposed to microparticles; higher magnification images of these strands (C), suggests that the strands still

maintain their outer porosity. (B) indicates the heterogenous nature of the particle sizes which could be synthesized, it also highlighted the ability of smaller particles to surround spaces between the larger particles allowing for better packing density of the particles. (D) indicates that changes in synthesis parameters (higher water flow rates) in particle synthesis lead to the production of semi/non porous particles. The peristaltic pump was therefore set at 450 RPM for experimentations, maintaining a suitable flow rate for porous microparticle production.

3.4 Particle synthesis – Surface skin

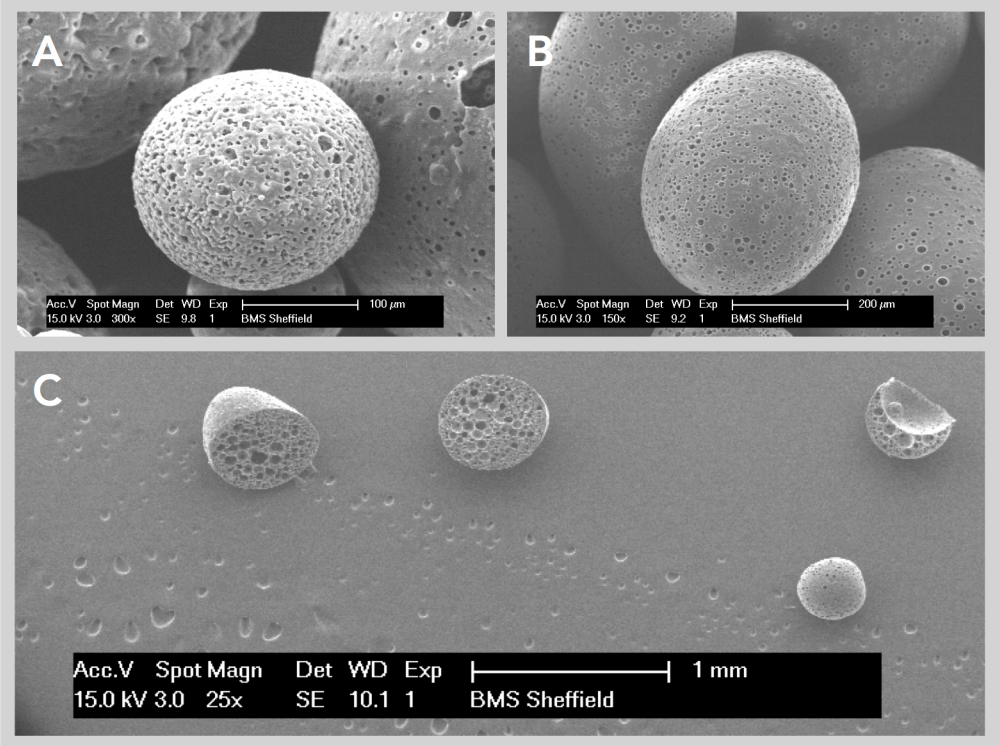

Figure 64: SEM images of non/less porous particles. (A) represents a particle demonstrating some irregular porosity (scale bar 100 µm), (B) is a particle demonstrating less porosity (scale bar 200 µm). (C) shows 3 half particles which had been cut open, and one non/less porous particle (scale bar 1mm).

It had been noted above that changing the parameters could affect the porosity of the particles (Fig 63). This was also noted in SEM images (Fig 64, A and B), these non/less porous particles were cut open and the interior was

found to be highly porous (Fig 64, C). (A) illustrates a somewhat porous particle that has very irregular shaped pores, suggesting that the emulsion may be beginning to collapse at the surface before they are fully crosslinked. This highly porous interior, coupled with the transitional collapse seen in (A) suggests that a change in synthesis parameters can cause the outer layer of emulsion within some particles to collapse, creating a less porous surface skin. To avoid this surface skin, parameters were maintained throughout experimentation.

3.5 Chondrocyte porous particle cell culture

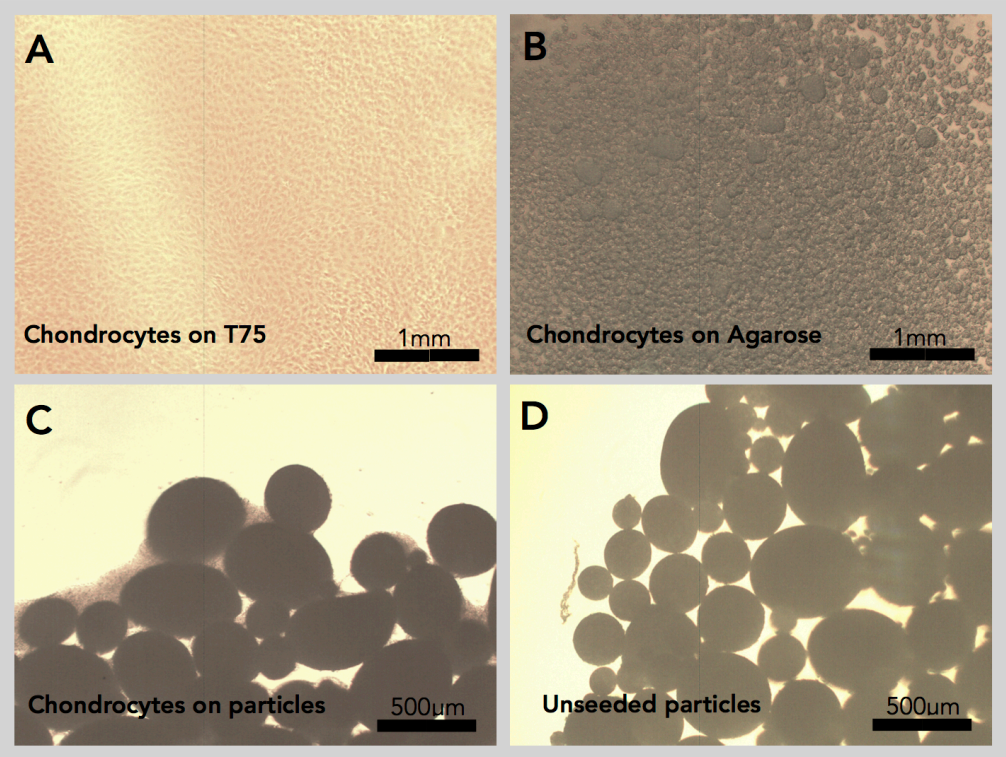

Figure 65: Light microscope images of chondrocytes seeded, after 24 hours, onto a T75 flask (A) onto an agarose coated well plate (B), onto porous PGSm particles (C) and a light microscope image of cell free porous PGSm particles (D), (scale bar 1mm, 1mm, 500µm, 500µm respectively).

After 24 hours chondrocyte cells had begun to attach to the PGSm particles. From microscope images (Fig 65), it was clear chondrocytes had attached to

the T75 flask (A) and cells can be seen attached to the particles seeded with chondrocytes (C). Particles not seeded with chondrocytes clearly have no cells surrounding them (D). Further microscope images (B), illustrates chondrocytes seeded onto a well plate coated in agarose. From the image it was inconclusive whether cells had attached to the surface of the agarose, and further studies were required to determine this.

3.6 Chondrocyte porous particle cell culture results

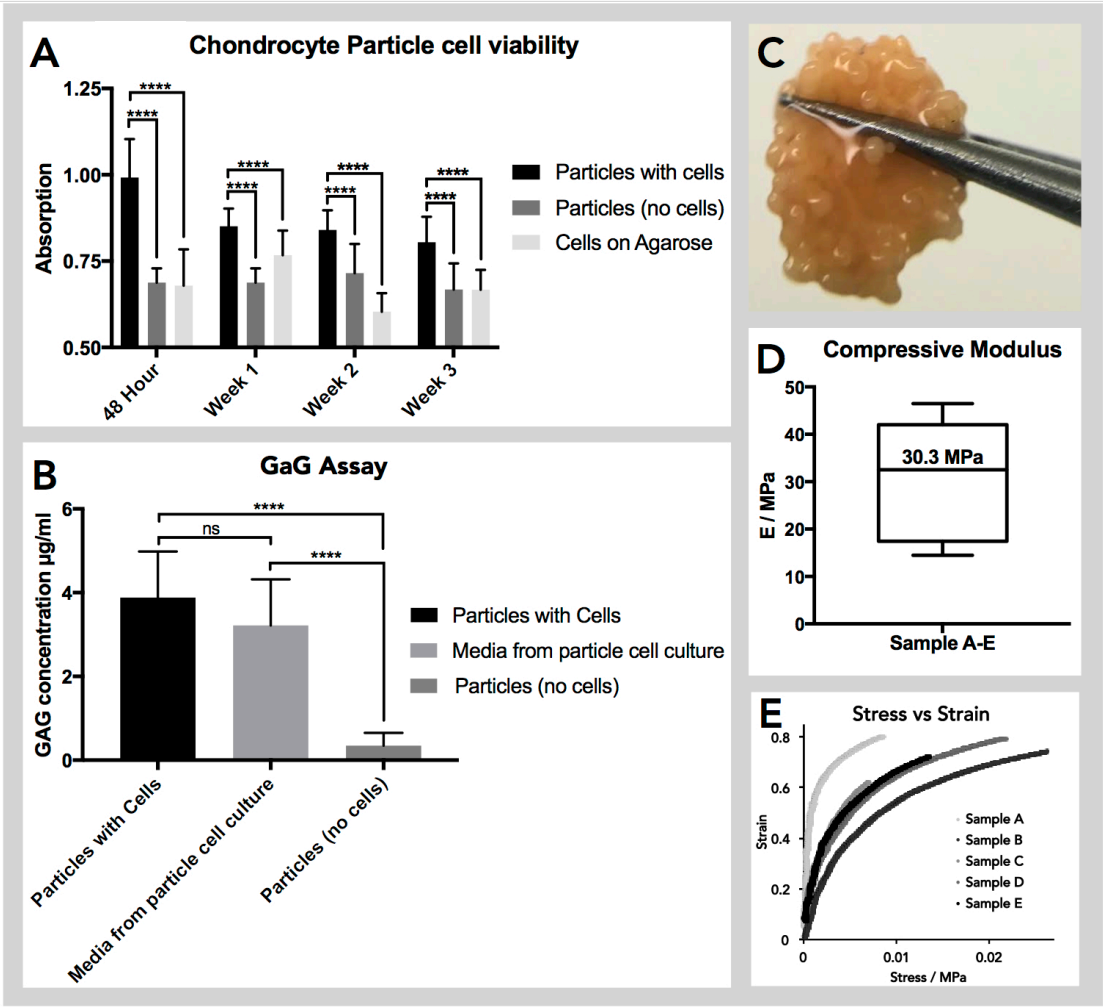

Figure 66: (A) Resazurin cell viability study of the particles seeded with cells, cell free particles and the cells seeded onto agarose. This study was performed at 48 hrs, week one, two and three. A two way Tukey ANOVA shows a statistically higher difference between the seeded particles and other variables at each time point ($p \leq 0.0001$, n=3). (B) A DMB assay for GaGs

after three weeks. This was performed on particles seeded with cells, medium from particles and cell free particles. A one-way Tukey ANOVA shows statistical difference between both particles with cells and medium from the particles with cells when compared with particles without cells ($p \leq 0.0001$). There is no statistical difference between the particles with cells and media from the particles with cells. (C) is a digital photograph of the particles after 3 weeks. Collagen had grown across and through the particles creating a strong disk, seen held between tweezers in (C) (approximate disk diameter 5 mm). (D) compressive modulus of the particles/particle disk after 3 weeks culture, with a mean compressive modulus of 30.3 MPa (n=5). (E) example stress/strain curves obtained from the mechanical testing in (D).

Chondrocyte cells were seeded onto the particles and cultured for a period of three weeks. Experiments were conducted with the use of agarose coated wells containing; (1) porous PGSm particles seeded with chondrocytes, (2) plain agarose coated wells seeded with chondrocytes, and (3) porous PGSm particles without cells (cell free particles). Wells of plain agarose and the cell free particles were used as controls to compare against the particles seeded with cells. Cell viability studies were performed to determine how well the cells survived in each of the three environments. Well plates were placed on an orbital shaker for a 48-hour seeding period, creating maximum attachment opportunities for the chondrocytes to attach to the particles. Following the cell-seeding period, cell attachment was visible on the light microscope (Fig 65). A Resazurin cell viability assay was performed to obtain quantitative data at 48 hours, week 1, week 2 and week 3 (Fig 66, A). As early as the 48-hour time point, there is a clear difference between the particles with cells and the two controls; the particles seeded with cells have a significantly higher absorption result. This suggests that there are a higher number of cells present within these particles, reducing the dye. This pattern occurs over each of the time points across the 3 weeks indicating cell survival on the microparticles for the duration of the experiment.

A DMB assay was performed, to determine the presence of GaGs, suggesting a maturity of the chondrocyte culture (Fig 66, B). Results of the DMB assay at week 3 show a significant presence of GaGs in both the chondrocyte seeded particles and the media from the chondrocyte seeded particles, when compared with the particles without cells. This is a clear indication that the chondrocytes are secreting components required for the ECM.

The digital photograph (figure 66) shows that the particles have joined together and formed a strong particle tissue disk, able to be picked up between tweezers, as demonstrated in the image. The particles without cells seeded, remain independent over the three weeks. This is clear evidence of ECM produced by the chondrocytes.

The chondrocyte particle disk, formed was compressed to provide mechanical compressive data and a Young's modulus value. The graph at (Fig 66, D) shows the average compressive modulus value of tissue particle disks, as 30.3 MPa. (E) provides example stress strain curves obtained.

3.7 Compressive testing of chondrocyte particle disks

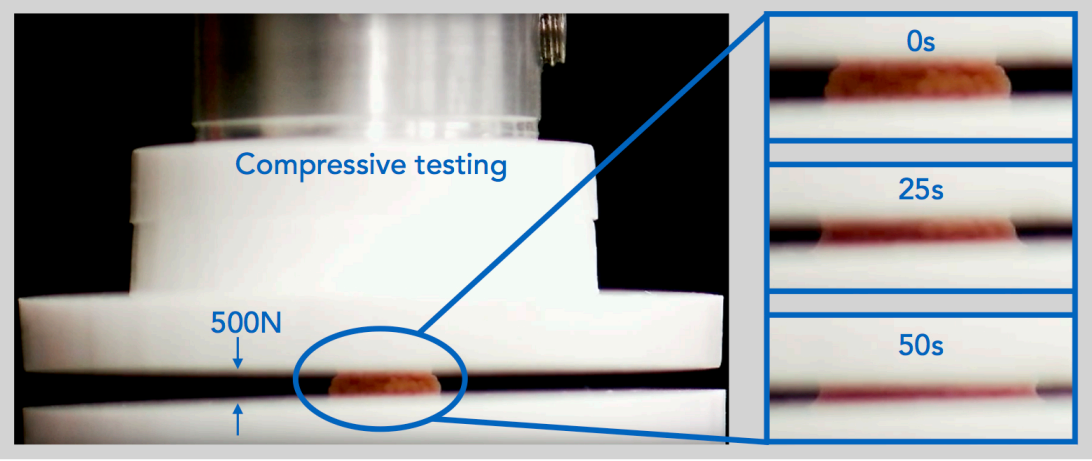

Figure 67: Snapshots from a video showing the compression of the particle chondrocyte disks at 0 s, 25 s and 50 s. Results the compression testing above (Fig 66).

Results from the particle tissue disk compressive testing have been expressed (Fig 66). The particle tissue disk was compressed in an unconfined manner, this can be seen in the image above (Fig 67) whereby the particle tissue disk was observed to spread out laterally during compression. Another observation was that the particle tissue disks remained intact throughout the compression, highlighting the strength of the newly formed tissue disk.

3.8 Histology results from particle disk

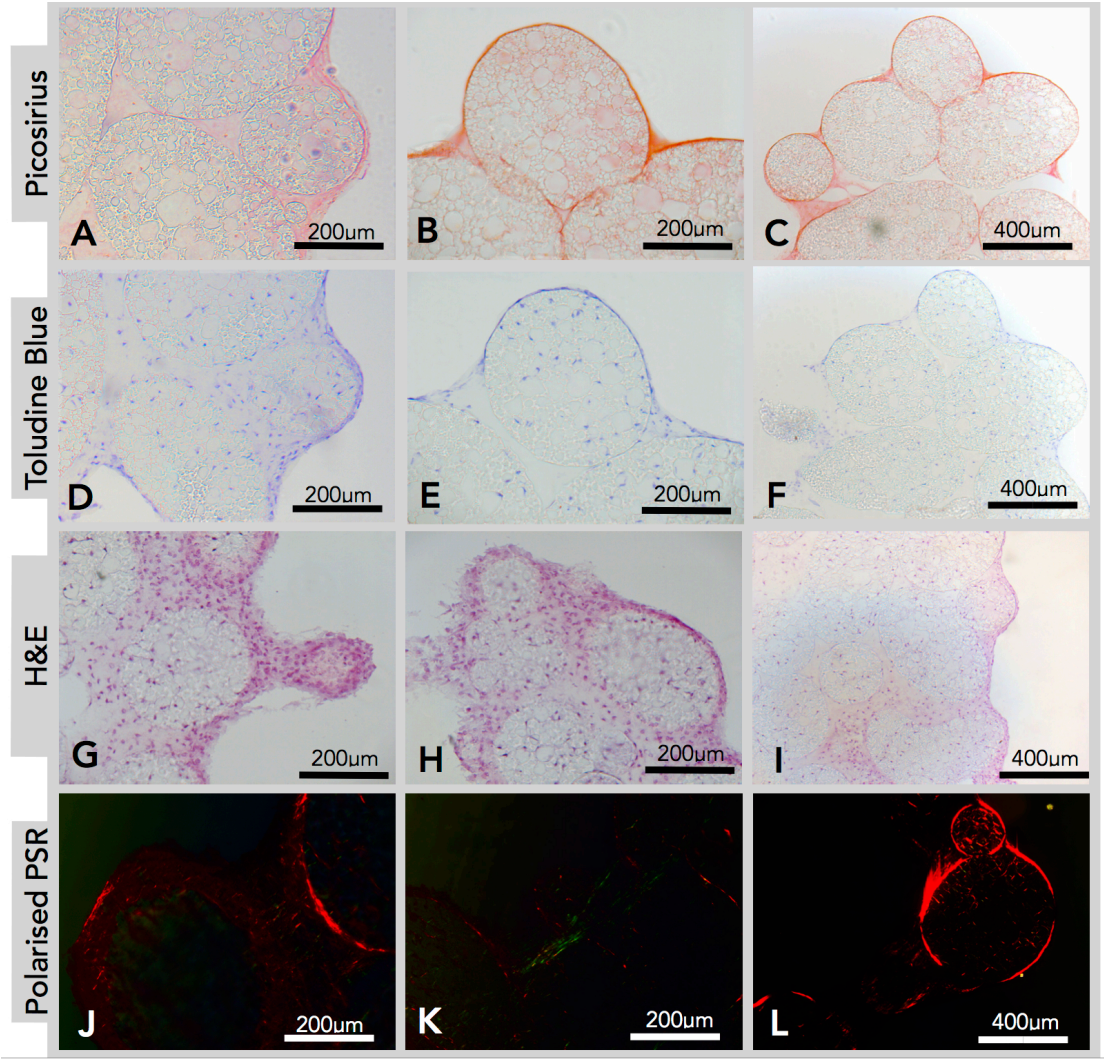

Figure 68: Histological results from particles seeded with chondrocytes after 3 weeks. The first two columns have 200 µm scale bars and the end column has a 400 µm scale bar. The first row (A-C) results from a Picrosirius red stain. The second row (D-F) are results of the toluidine blue stain, with the stain showing as deep blue and purple. The third row (G-I) is results from a H&E stain, these three rows were imaged using an upright light microscope.

The final row (J-L) represents the Picrosirius red stain, imaged using an Olympus BX61 upright microscope, setup using a rotatable polarizer under the condenser.

After a period of three weeks particle tissue disks were histologically analysed. Initially the Picrosirius red stained tissue scaffolds were visualized using an upright light microscope. The Picrosirius red images obtained, (Fig 68, A-C), show red stain surrounding and throughout the centre of the sliced particle tissue disks. This illustrates a presence of red collagen fibrils surrounding the particles and growing right through the porous interior of the particles. As can be seen (Fig 68, A), where an outer layer of collagen surrounds and encapsulates the particles, with a dense network of fibrils inside also.

The toluidine blue images (Fig 68 D-F) have stained the nucleic acid from chondrocyte cells blue; cells can be seen throughout the porous interior network of the particles and within the surrounding ECM. This is further evidence that cells had migrated throughout the porous microparticles. There is also clear evidence of the stain showing areas of deep purple, as seen in (Fig 68, image D). This purple suggests a presence of GaGs, a major component of cartilage.

Haematoxylin and eosin histology results (Fig 68, G-I) again confirm the presence of cells and ECM completely surrounding the particles and cells can be seen to have migrated throughout the inside of the porous particles. There is also clearly visible collagen/ECM forming the particle tissue disk.

The bottom row of images in (Fig 68, J-L), illustrate tissue-engineered scaffolds stained with Picrosirius red and visualised using a polarized light microscope. Images (Fig 68, J-L) show fibers of both red and green,

throughout and surrounding the porous PGSm particles. It is understood by some literature that the colour of collagen fibrils may be related to the maturity and/or type of collagen fibers. This is discussed in more detail in the discussion. Histological results overall show particles have been agglomerated together with fibers of collagen and show major components found within cartilage ECM.

3.9 Collagen II, DAPI & Phalloidin

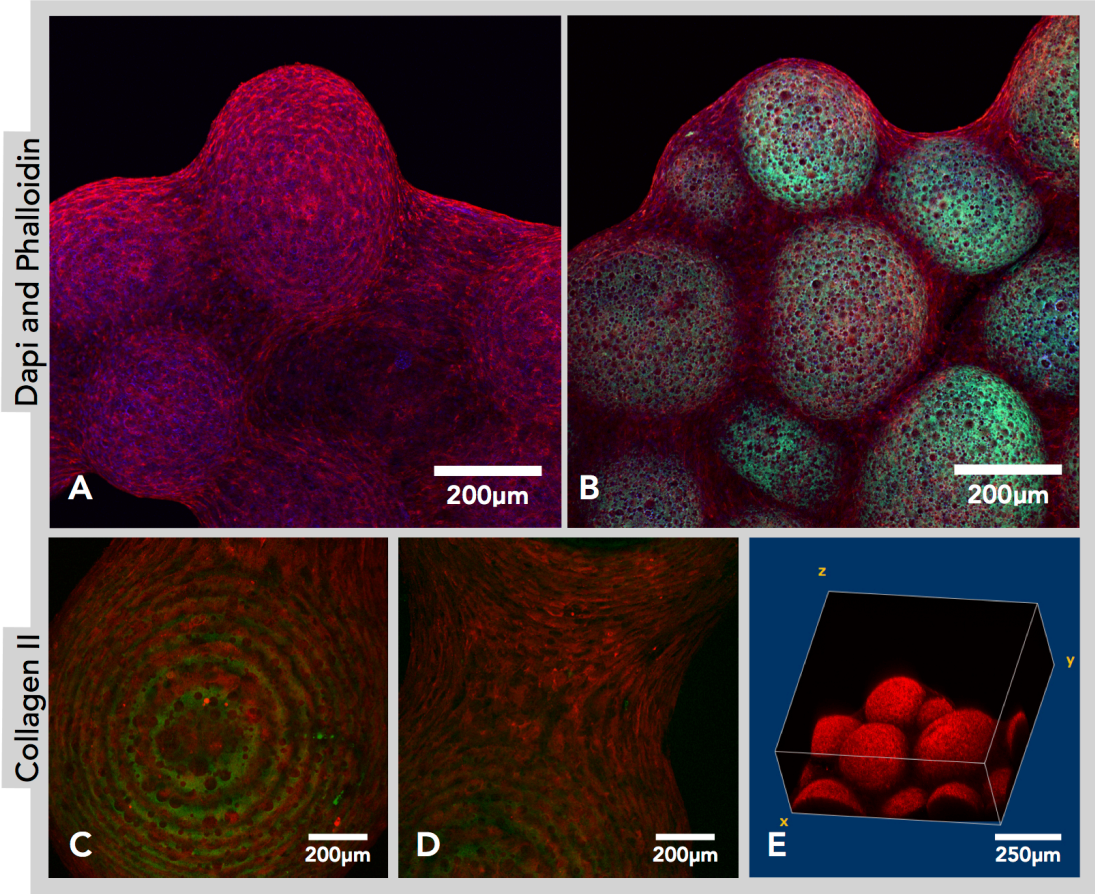

Figure 69: Confocal image results composed of Z-stacks taken of particle tissue disks labeled with either DAPI and Phalloidin or a Collagen-II antibody after three weeks culture with chondrocytes. (A) + (B) particle disk labeled with TRITC phalloidin (red) and DAPI (blue); the porous polymer particles also autofluoresce (green). (C), (D), (E), confocal images of the particle tissue disks IHC labeled with anti-collagen II antibody, and secondary antibody Alexa 546 (red). (E) slices from the z-stack compiled into a 3D image.

After 3 weeks the tissue engineered scaffolds were immunohistochemically labeled and imaged on a confocal microscope. As the scaffolds were 3-dimensional it was important to use a z-stack of images to collect data from several z-slices of the confocal micrograph. (Fig 69, A and B) show the tissue scaffold labeled with DAPI and phalloidin TRITC for nucleic acid and F-actin (which represents cell nuclei and cell cytoskeleton). Cells are seen to cover the surface of the particles and join the particles together. Image (B) is similarly labeled, however the autofluorescence of the polymer is also visualized in the image; allowing a clearer picture of cells covering the particles. From (A) and (B) it is clear there is ECM joining the particles together.

Tissue-engineered scaffolds were labeled with anti-collagen-II antibody, a relevant secondary antibody and then imaged using the confocal microscope to see if there was a presence of collagen-II. As can be seen in (Fig 69, C-E), there is clear evidence of collagen-II being expressed throughout. (C) and (D) show clear evidence of collagen-II (red) fibers covering the particle and in (D) fibres can be seen connecting the gap between two particles. (Fig 69, E) is a 3D representation of collagen-II interspersed within and surrounding the particles.

3.10 MicroCT and SEM results of chondrocyte particle disks

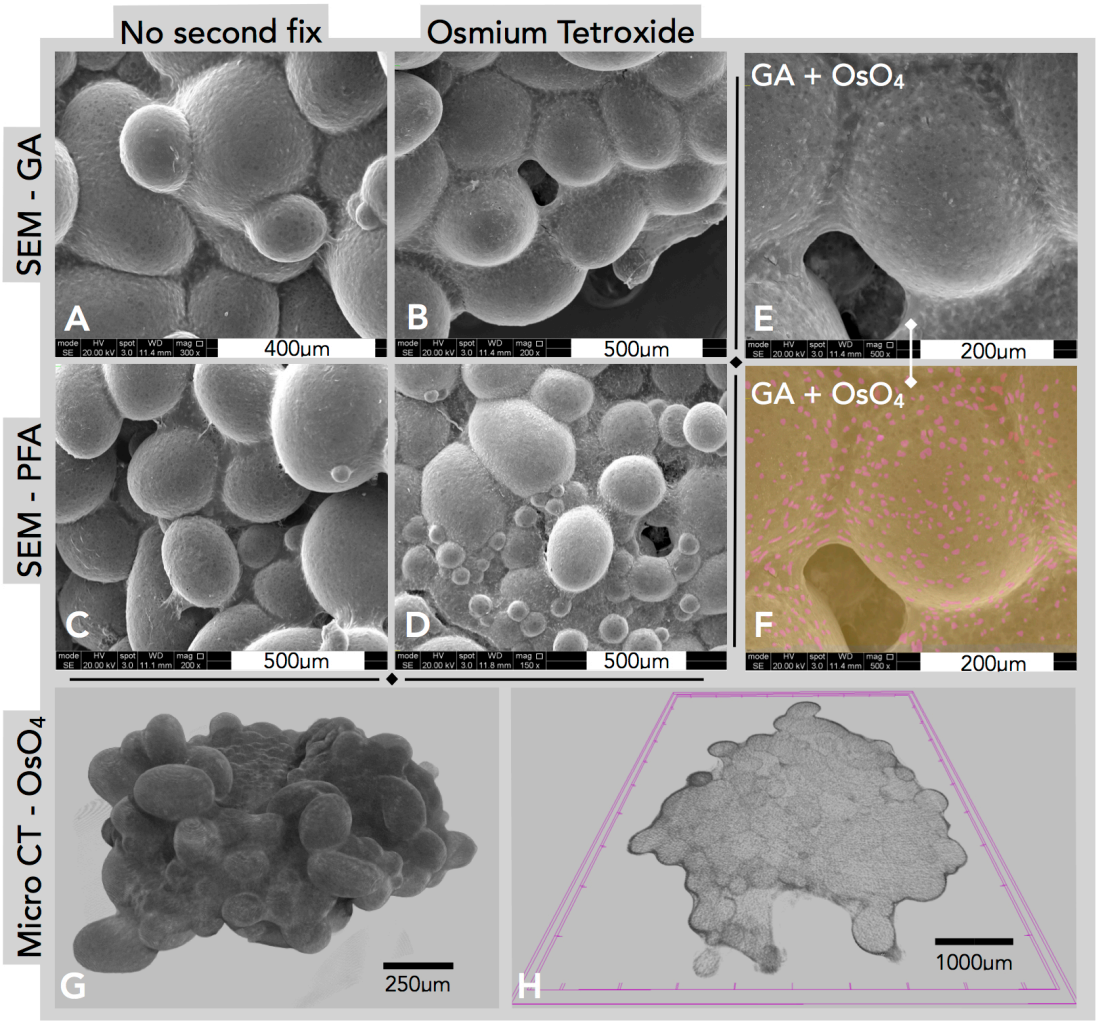

Figure 70: (A)-(D) represents SEM images of particle tissue disks prepared with different techniques. (G) and (H) are microCT models of the particle tissue disk. Images (A) and (B) were fixed in glutaraldehyde, (C) and (D) were fixed in paraformaldehyde. (A) and (C) had no secondary fix, whereas (B) and (D) had a secondary fix in 2% aqueous osmium tetroxide for two hours. (E) is a higher magnification SEM image of the particle disk with a glutaraldehyde and osmium fix (same as (D)); (F) is a false coloured representation of (E). (G) and (H) are microCT representations of the particle tissue disks fixed in glutaraldehyde and osmium tetroxide. (G) is a 3-dimensional representation of the disk. (H) shows a slice within this polymer disk.

Several fixation techniques were tested to ascertain the method that provided the best SEM images for this experiment (Fig. 70, A-D). From the four different fixation methods, glutaraldehyde with a secondary osmium tetroxide

fix produced the best SEM results (D, E, F). Cellular tissue can be seen covering and linking the particles; with individual cells seen attached to the particles within layers of ECM (Fig 70, E and F). Individual cells become more visually apparent in the false coloured image (F).

(Fig 70, G) is a 3-dimensional representation of the particle tissue disk from a microCT scan. Collagen can clearly be seen throughout the particles, forming this tissue disk, with a thicker layer of collagen surrounding the particle tissue disk. Interestingly, by taking a thin slice of this model, it is possible to see within the scaffold, (Fig 70, H). (H) illustrates a slice of the model whereby individual PGSm particles can be seen, along with their porous interior, and collagen fibers surrounding and penetrating the particles.

4. Discussion

The purpose of this chapter was to determine whether PGSm HIPE particles would be suitable for use in cartilage tissue engineering. The PGSm HIPE particles underwent tests in three key areas. First, whether these novel PGSm porous microparticles could be made in a reproducible manner with appropriate mechanical properties. Secondly and perhaps most importantly, assessing whether the material and scaffold is a good choice for cartilage tissue engineering through *in vitro* analysis with primary chondrocytes. And finally, finding suitable techniques to assess and image the tissue engineered constructs to determine the suitability of the microparticles.

4.1 Particle Synthesis and mechanical analysis

Developing reproducible synthesis parameters for the water-in-oil-in-water microparticles proved to be a fairly laborious task due to the high number of variables involved. The HIPE emulsion has already been described in detail

(chapter 3.2), therefore the focus here will be on the parameters related to particle synthesis. Briefly, it has been noted that by varying the parameters of the HIPE synthesis it was possible to vary the level of porosity, interconnectivity and the pore size of the HIPE. The HIPE synthesis itself had many parameters that could be adjusted to tune the properties of the HIPE; the introduction of the microparticle synthesis included even more parameters that could be adjusted. Some of the adjustable parameters were:

- Speed of mixing, rpm - (HIPE)
- Water content - (HIPE)
- Temperature - (HIPE)
- Needle size - (porous microparticles)
- Syringe pump speed - (porous microparticles)
- Water flow speed - (porous microparticles)
- Viscosity of flowing water - (porous microparticles)

Small alterations in these parameters, often lead to differences in the final particles synthesized. Logically it may be assumed that an increase needle size leads directly to an increase in the microparticle size, however, that wasn't necessarily shown to be the case (Fig. 62). The average particle size didn't change much with an increase in needle diameter, instead the homogeneity of the particle sizes did. The most homogenously sized microparticles were found in the smaller needle diameter (A), a more evenly distributed spread of heterogeneously sized microparticles in the middle diameter (B) and an uneven spread of heterogenous microparticles in the larger (C). This may be due to the syringe needle size changing the rate at which the HIPE is injected into the system. A smaller needle may lead to the HIPE being forced into the system faster, whereas a larger needle may lead to

a slower injection of HIPE and therefore uneven particle size. More intrinsic physical occurrences may also be taking place, such as the level of turbulence exhibited by the material through the syringe needle. Also the extremes of the variables have not been explored, with high pressures in the needle perhaps affecting the stability of the HIPE also. Further experimentation could lead into computer modeling/finite element analysis allowing for better knowledge and predictions of synthesized HIPE microparticles. It was also seen however that the microparticle size increased with increasing syringe rate/speeds at which the HIPE was injected into the microparticle synthesis setup. This is understood to be simply down to the higher volume of HIPE being injected as a particle, before the water flow in the system has a chance to break the particle away from the needle. By using the needle size 0.61 mm and the syringe speed 0.4 mL/min with a constant water flow rate, particles were synthesized of a more even spread of sizes, allowing for better packing of the microparticles.

It was seen visually throughout experiments that changes in synthesis parameters would directly affect the particles. With an increase in the peristaltic pump speed (the water flow rate), the particles would begin to decrease in size. If the speed was increased drastically, particles became less/non porous. This may be due to the effect of increasing shear forces created by the water flow, causing the outer surface of the uncrosslinked HIPE particles to collapse (Fig 63). This collapse created an outer skin surrounding some particles. With very low water flow rates however, the particles became elongated and turned into microstrands rather than the preferred microparticles. In a similar, yet converse manner, increasing the syringe rate drastically created microstrands and low syringe rate speeds affected the surface porosity of the particles (Fig 63). Adequate parameters were

determined for these experiments. Should problems persist in future studies, there are some further alterations that could be explored. Using a more stable HIPE, often achievable through the use of stiffer polymers, would decrease the likelihood of the HIPE surface to collapse, forming the surface skin. Another area that could be explored is the use of an alternative to water, with regards to the flow rate. A more viscous liquid such as an aqueous glycerol, would allow for microparticles to be pulled away from the syringe needle at lower flow rates (whilst maintaining particle surface porosity).

It became apparent that by altering many of these parameters it was possible to alter the particle size, level of porosity, interconnectivity and size of pores within the microparticles. This experiment required a spread of differently sized highly porous microparticles; once achieved parameters were kept constant throughout the experiments. Porosity was confirmed throughout the microparticles used for experimentation, from SEM image analysis. The potential for variability achievable with the particles does however highlight the high levels of tunability possible with these microparticles as scaffolds.

The bulk HIPE material underwent compression testing to determine the compressive modulus of the material. Whilst the material is biodegradable and will be used as a carrier scaffold for cells; it is still important to have a similar modulus to that of the native tissue, as it has been well documented that substrate mechanical stimuli can directly affect chondrocyte cultures[146]. The bulk modulus of the HIPE material was found to be between 3 – 5 MPa (as discussed in chapter 3.2, Fig 24,). Dynamic compressive testing results of human articular cartilage at 20 ms after loading in literature report modulus values of 4.4 - 27.2 MPa[147]. Whilst this dynamic test isn't directly comparable, it does provide an understanding of appropriate modulus values; with the

bulk material having a similar modulus value to that of the lower value stated in the literature. Mechanical testing of individual porous PGSm microparticles proved more problematic due to the size and complexity of the small particles. These problems were overcome once the particles had been cultured with chondrocytes for three weeks; wherein collagen fibres joined individual particles together forming a strong disk of particles and chondrocyte ECM (particle tissue disk). Compressive mechanical tests were therefore performed on the particle tissue disks. The particle tissue disk was compressed in an unconfined manner, whilst wet. This allowed for similar compression to what would occur in native cartilage. The culture of chondrocytes was only for a short period of 3 weeks, not a long enough period for fully mature tissue cultures; however the particle tissue disks showed considerable strength in maintaining their collective disk shape throughout the compression testing. The particle tissue disk had a modulus value of 30.3 MPa, a value which whilst it lies outside of the 4.4 - 27 MPa found for native tissue in literature, it is in a similar range[147]. This shows that after 3 weeks culture, particles were joined together and covered in chondrocyte derived ECM to create a tissue with modulus values almost comparable to that of native cartilage. Whilst the compressive testing techniques executed here were simple, they provide a useful understanding of the stiffness of the particle tissue disk. It is also evident that the compressive modulus of the particle tissue disk was calculated to be higher than that of the bulk HIPE PGSm stated above. This interesting result showed that the cells had created ECM and collagen fibers, which had contributed to strengthening and stiffening the particle tissue disks. As the disk was compressed a notable amount of liquid was forced out of the disk, highlighting the scaffolds ability to store water. This is a feature present in articular cartilage, which consists of up to 80% water[119]. Further compressive

studies would be useful in producing dynamic data, directly comparable with that of the native tissue; and accounting for any viscoelastic or creep properties exhibited by the cartilage like - particle tissue disk.

Once adequate particle synthesis parameters were found, the microparticles were synthesized in a very reproducible manner. It was therefore clear that the reproducibility of the particles, coupled with the appropriate mechanical properties; made PGSm porous HIPE microparticles a good candidate scaffold for cartilage tissue engineering and repair. In-depth analysis was then performed to analyze the ability of the particles to culture chondrocytes and cartilage like tissue, *in-vitro.* Assessing whether the scaffold was appropriate for cartilage repair *in-vitro* broadly covered five areas:

- Chondrocyte attachment and survival
- Chondrocyte migration and ingress into scaffolds
- Chondrocyte ability produce ECM
- Presence of GaG's
- Collagen II confirmation

4.2 Chondrocyte studies: *PGSm particle tissue disk*

Agarose coating of wells is a technique well characterized in literature which provides a non-adhesive 2D coating for cell attachment; this was used to coat all wells for experimentation[148]. Chondrocytes therefore did not attach to the bottom of wells, allowing for a greater opportunity for chondrocytes to attach to the particle scaffolds. Immediately following chondrocyte cultures there were clear differences noted macroscopically between wells containing particles seeded with chondrocytes and wells containing cell free particles. Interestingly the individual particles seeded with chondrocytes had joined together to make one collective particle tissue disk, which was surrounded by

dense ECM. Cell viability results showed significantly higher levels of cell viability in wells of the chondrocyte seeded particles, when compared to wells of both the agarose and cell free particles (Fig 66). The viability of the chondrocyte seeded particles was higher at each time point, suggesting cells attached to and survived within the PGSm porous particles throughout the experiment. The viability level of the chondrocyte seeded particles did decrease marginally at each time point. It is thought that this may be because chondrocytes are differentiating and therefore less likely to proliferate, this coupled with natural cell death would produce slightly lower results. Furthermore, whilst the resazurin assay is a gentle non-destructive procedure there will always be a small amount of cell death related to procedural stresses added from the viability study. The conclusive result of the cell viability assay suggested that PGSm porous particles are permissive for use with chondrocyte culture. One area of concern was whether the chondrocytes would be able to penetrate the pores and ingress into the 3-dimensional particles. Good ingress of chondrocytes into the particles requires a complex internal microstructure with appropriate pore sizes and interconnectivity. If the internal microstructure has limited interconnectivity / porosity then the chondrocytes may be starved of nutrients and not survive; however, it is also important that there is adequate 3-dimensional microstructure for the adhesion of the chondrocytes. Histology is one effective method of visualizing the internal components of 3-dimensional tissues.

Histology was performed to analyse the chondrocyte cultures seeded onto the particles. Haematoxylin and eosin stains were used. Haematoxylin has a deep blue / purple colour and stains nucleic acids, whereas eosin is pink and non-specifically stains proteins. Allowing for the visualization of both the nucleus (haematoxylin) and the extra cellular matrix and cytoplasm (eosin)[149].

From the results of the H&E stains (Figure 68) it was clear that the chondrocyte cells had attached to the porous particles and were able to migrate into the particles completely. Specific staining of the ECM using Picrosirius red was useful in appraising collagen fibrils. It was clear from images (Fig 68), that collagen fibrils had been formed in the short three week period. Collagen fibers were present, surrounding the particles, penetrating throughout the porous interior and binding individual particles together creating the particle tissue disk.

Toluidine blue stains were also performed. Toluidine blue is a cationic dye that stains proteoglycans and GaGs[150]. When sulfated GaGs are present several dye molecules are brought close together and the metachromatic nature of the dye causes it to appear purple[151,152]. This "purpling" caused by the presence of GaGs can be seen (Fig. 68, images D-E). Particularly in (Fig 68 image D), a clear purple band can be seen surrounding and throughout the particles, this is evidence of the presence of GaGs within the tissue-engineered scaffolds.

Studies have shown that collagen-II fibers make up most of cartilage ECM, however other collagen types are also present, including collagen-I and collagen-III[153]. Initially some studies indicated that using polarized light microscopy and a PicroSirius red stain, the hue of the imaged fibers may be related to the type of collagen fiber present; with thin green fibers being labeled collagen-III and thicker red fibers being collagen-I.[154] This initial idea has since been revisited, and more recently studies show a relationship between the hue of the fibers and maturity; with juvenile thin fibers being expressed as green, and more mature fibers red.[155,156] (Figure. 68, J-L) show polarized light images of the PicroSirius red stained particle tissue disks, with

collagen fibers of both red and green seen. This may suggest the presence of both mature collagen fibers and more juvenile fibers. This indicates that mature collagen fibers were produced by the chondrocytes, and that fibers were still being produced at time of fixation.

To summarize, histological results clearly show the presence of chondrocytes throughout the microparticles. The presence of chondrocytes within the microparticles was also confirmed using IHC labeling with confocal microscopy, and microCT; wherein the presence of cells can be seen throughout (Figures 69 and 70). Histological results also showed the presence of vast amounts of ECM created by the chondrocytes, with PicroSirius red stains confirming the presence vast network of mature and juvenile collagen fibers. The dense network of collagen fibers created a solid particle tissue disk; seen macroscopically in the digital photograph (Fig 66). Histological results also showed the ECM to contain GaG's.

Glycosaminoglycans (GaG's) are a major component of cartilage ECM, secreted out by hypertrophic chondrocytes[157]. The presence of GaG's are an indication of a more mature cartilage-like chondrocyte culture. GaG's were found to be present in the chondrocyte seeded particles discussed above, from the metachromic nature of toluidine blue (Fig 68). The presence of GaGs was further confirmed; through the use of a DMB assay (Fig 66). The DMB assay clearly showed a presence of GaG's within the chondrocyte seeded particles and secreted into the chondrocyte seeded particle medium. The presence of GaG's is one indicator that the particle tissue disks have formed a cartilage-like tissue, another indicator is the presence of collagen, primarily collagen-II.

Collagen-II is the principle component of and predominantly found in articular and hyaline cartilage. It was therefore of interest to see if these chondrocytes had mimicked behavior of chondrocytes within native cartilage by secreting collagen-II[158]. This was done by IHC labeling of particle tissue disks, with anti-collagen-II antibodies. Results clearly show collagen-II fibers completely covering and connecting individual particles (Fig 69). The presence of collagen II, which is predominant in cartilage, is a good indicator for the formation of cartilage tissue.

4.3 Imaging techniques: *2D, internal and 3D representations*

The tissue engineered particle-disk's irregular 3-dimensional shape, and macro size, proved difficult to be imaged for microscopic analysis. Traditional histological techniques did work, however slicing with the microtome often lead to damage of the intricate porous microparticles. Distortion of the particles and histology did not allow for a good representation of the 3D tissue. The particle tissue disk was also IHC labeled and imaged with a confocal microscope. In image (Fig 69 A) cell nuclei are stained by DAPI (blue) and the F-actin stained by phalloidin (red). Taking a z-stack of the particle tissue disk, enabled a non-destructive representation of the 3D scaffold. This allowed for the determination of individual cells and collagen fibers throughout the tissue disk. Using the autofluorescence of the polymer (green) allowed for high-resolution images showing the interaction of the chondrocytes and matrix to the porous particles (Fig 69). One limitation, however, was depth of penetration achieved through confocal microscopy. Even with the additional benefit of using 2-photon microscopy for deeper tissue penetration, confocal microscopy was limited in the depths achievable and complete 3D constructs were not possible.

One method used to visualize the complete 3-dimensional particle tissue disk was through SEM. Several fixation techniques were explored. It was found that glutaraldehyde fixation with an osmium tetroxide second fix provided the best SEM results. Individual chondrocytes were visible amongst the collagen surrounding the particles. Greater visualization and contrast of cells embedded within ECM was possible with the use of false colouring (Fig 70). The chondrocytes interspersed within dense ECM, seen in the SEM images (Fig 70), is similar in structure and comparable to that of hyaline cartilage. Although SEM provided a representation of the complete 3-dimensional model it only allowed for the visualization of the surface of the particle tissue disk. MicroCT was therefore explored to create a complete 3-dimensional reconstruction of the particle tissue disk, which could be sectioned to visualize the internal components of the particle tissue disk.

MicroCT is a technique more often implemented for use with harder bone. Traditionally the imaging of cartilage/tissue engineered cartilage using micro-CT had been difficult due to the weak signal from cartilage[159]. An osmium tetroxide fix was used in this study to provide better contrast from the soft tissue. Micro-CT scans were able to accurately represent this osmium tetroxide coated soft particle tissue disk and allowed for the complete 3D modeling of the entire construct. Individual slices/sections could also be viewed from the models created, providing an insight into both the complete model and the internal structures of these particle tissue disks. Interestingly the contrast was high enough that collagen fibers could be seen surrounding and penetrating individual polymer particles. The models created (Fig 70) provided further evidence of cartilage like tissue being formed and highlights how useful microCT can be in representing 3-dimensional tissue engineered cartilage, through fixation with osmium tetroxide. This versatile 3D model

could be manipulated, sliced and imaged in many ways, providing a great deal of information regarding the internal structures of the particle tissue disk in a highly representative technique. Unlike confocal microscopy MicroCT allows for complete penetration throughout the entire scaffold, however confocal microscopy offers a far higher resolution representation of the data, with the benefit of specific IHC staining also. MicroCT may offer a less distorted internal view of the particle tissue disk, however, histology provides higher resolution and contrast, with specific staining. SEM can also show high resolution images with false colours highlighting individual cells; however only the surface is visible. By using a combination of these techniques it has been possible to build a more complete picture of this particle tissue disk, with high-resolution 2D and 3D imaging, specific staining and internal components visualized.

5. Conclusion

The overall aim was to assess novel porous PGSm HIPE microparticles for use in cartilage tissue engineering. Particle synthesis techniques were created and successfully adjusted to create reproducible novel PGSm porous microparticles. The bulk material and the particle tissue disk, both had compressive modulus values in a similar area (albeit slightly different to literature) to that of native tissue. Over three weeks culture with primary chondrocytes it was evident that the material and microparticles were a highly effective 3-dimensional scaffold for chondrocyte culture. The particles attached to the scaffold and survived throughout; producing a vast network of dense ECM, creating a strong particle tissue disk, with high water content. Various image analysis show the tissue-engineered particle tissue disk, with chondrocytes interspersed within a dense network of ECM, having a similar structure to that of cartilage. Collagen fibers completely covered the samples,

with the presence of GaGs and collagen II confirmed; both of which are major components of cartilage ECM. This showed that the porous PGSm particles provided a good 3-dimensional microenvironment for chondrocyte culture, leading to the formation of cartilage-like tissue. The tissue particle disks were also imaged using a variety of different techniques, allowing for an accurate visualization of the 3-dimensional tissue. Osmium tetroxide was used to enhance attenuation of X-rays in microCT, to produce complete 3-dimensional models of the particle tissue disk with increased contrast.

Overall it is suggested that the novel PGSm porous microparticles studied provide an effective scaffold to support the growth of cultured chondrocytes. The microparticles allowed and perhaps enhanced the chondrocytes in creating cartilage like tissue. Microparticle size and versatility may also be advantageous, with potentially simple microparticle injections as implantation techniques, a credible option. Further studies should now be considered, with a focus on confirming the redifferentiation of chondrocytes to a cartilage lineage and more informative long term *in vivo* studies.

3.6 IN VITRO PGSM POLYHIPE NEUROBLASTOMA 3D MODEL

Aim: The aim of this shorter chapter was to determine whether PGSm polyHIPE would be useful as a scaffold for 3D tissue engineering neuronal models. The scaffold was be explored for use in two areas, 3D neuroprogenitor models and 3D neuroblastoma models.

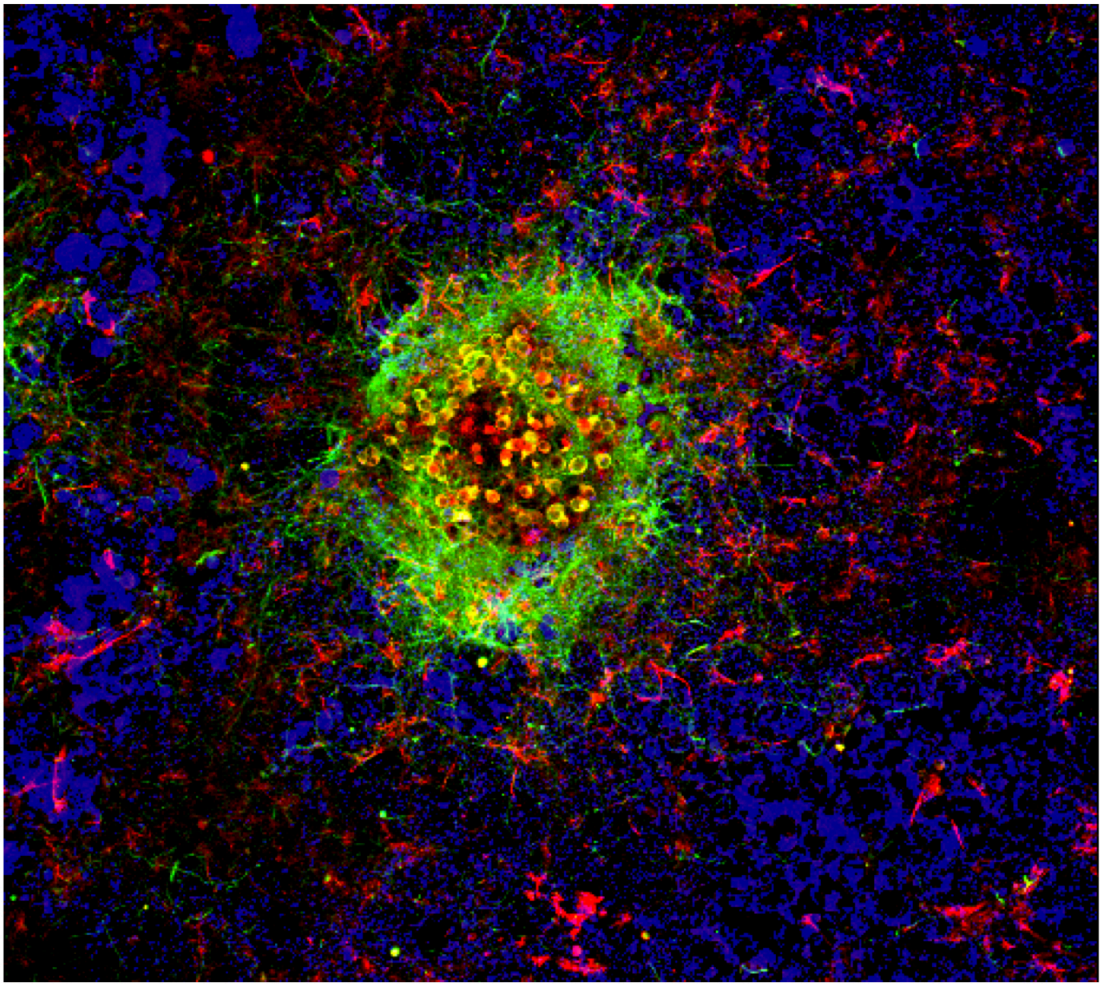

Neuroprogenitor cells cultured in 3D polyHIPE foam. Image taken from Fig 73.

1. Introduction

1.1 Computer models in tissue engineering

Computer models are seen as an alternative research method in modeling the basic principles of biology, without the use of animals or cell cultures and helping with the development of repair techniques. The idea of computer modeling offers many advantages over more traditional animal models, largely in ethics, cost and time. One recent study explored how through the use of computer models, researchers were able to predict the side effects of drugs. This was done by comparing the drugs to information from other molecules with a similar chemical structure, known to give side effects[160]. This highlights useful possibilities for the future, whereby an online database could provide the information required for computer modeling the outcomes from many different compounds. The complexities involved in modeling whole tissues, however, are many and the level of information required to result in accurate models of these are far greater than currently achievable. Computer modeling is often used instead as a preliminary method to *in vivo* testing, choosing the most likely compounds to be successful[161].

1.2 Animal models

Animal models have been used for many years to model the response of drugs and compounds within the human body. Whilst modeling using animals doesn't offer a perfect representation for humans, many of the complex biological responses can be assessed, which is why animal modeling remains the primary research method prior to human trials.

It has been seen in literature that less than 50% of experiments performed on animals accurately predict results in a human[162]. It therefore begs the question why animal testing is used and are there better models for testing? The

ethical use of animal models has been a widely debated topic for many years, yet with advances in research the number of animals being used is still increasing. Home office figures in the UK show a rise in the number of scientific procedures using animals from 4.12 million in 2013, to 4.14 million in 2015, only two years later[163]. The ethical debate remains whether the pain, stress and potential death of an animal is always necessary in furthering scientific research. The time required caring for the animals and high costs involved, outline further drawbacks to the use of scientific research animals. Researchers would suggest that these tests are often regulatory and a necessary precursor for new drugs and methodologies used on humans. To address the ethical issues behind animal testing, a set of guidelines were proposed to help regulate the use of animals in scientific research, known as the three **R**s.

1.3 The three **R**s

The 3**R**s were first described in 1959 by W. M. S. Russell and R. L. Burch[164] and is an ideology appreciated the world over. The principle message of the framework is to ensure humane animal research through the **R**eplacement of animal models, **R**eduction to methods used, allowing for only an essential number of animal models and the **R**efinement of the techniques to allow for the minimum pain to the animals. The overall premise of the 3**R**s is addressed in UK law under the Animals (Scientific Procedures) Act 1986 and directly addressed in the EU Directive, 2010/63/EU.

Replacing animal models where possible negates the need for a **R**eduction of animal numbers or the **R**efinement of the techniques. Scientists have therefore strived to find alternative experimental methods to eradicate the need for animal models. Advances in tissue engineering have helped in the

move away from using animal models, with *in vitro* models being developed to **R**eplace animal models

1.4 In vitro models

In vitro models offer a different approach to research and often act as an in-between to computer and animal models. Cell cultures and tissues can be grown in the lab to be used in testing as an *in vitro* model. This has been done with some success and *in vitro* techniques are now used, particularly in the early stages of research, to screen out undesirable compounds[165]. Research has also been developed for in vitro models of the liver, whereby *in vitro* testing now offers the pharmaceutical industry testing systems with reduced complexity[166,167]. Cosmetic and drug industries now widely use *in vitro* testing for toxicity and efficacy studies. One example of this is the Draize irritancy test of chemicals on the eye, which was once a painful test involving animals, however now an *in vitro* alternative has now been developed through the use of a tissue engineered corneal organ culture model[168].

Often *in vitro* models are used for very simple tests and act only as a precursor to *in vivo* testing. Also, it is understood that simple 2D cultures of cells can lack the complexity of 3D tissues and therefore do not act as an accurate model mimicking the native tissue. It is postulated that 3D *in vitro* cultures and models could offer a more analogous representation of the 3D tissue which it models, leading to more accurate testing[169].

1.5 Neuroprogenitor Cells

Neuroprogenitor cells are self-renewing cells which are responsible for the generation of both neuronal and glial cells within the body. These cells and tissues are of much importance in the research of many neurodegenerative diseases, such as Alzheimers disease[170]. Neuroprogenitor models are

therefore being explored to provide understanding of these disorders, and to develop further treatment methods.

1.6 Neuroprogenitor models

Traditional neural models were focused around transformed human or animal cell lines (SH-SY5Y, PC12), primary rodent CNS cultures or tissue from aborted fetuses. Tumorogenic transformed cell lines often do not represent accurately native neural cells; primary cultures are often of more mature neural cells restricting their use to understand earlier processes, fresh dissections are required for new cultures; and fetal tissue can be difficult to obtained also[171]. It is important that toxicity studies are able to use neural cells from all developmental stages to accurately understand processes from all stages including proliferation, migration, differentiation and synaptogenesis; Neuroprogenitors are therefore increasingly researched as developmental neural models for screening drugs and toxicity studies[171].

There are a number of different neuroprogenitor models researched in literature, these are used to screen drugs and for toxicity studies. Commonly there are rodent cell models, human cell models and the development of neurospheres. Most of these models are monolayer cultures of progenitor cells, with the development of 3D neurospheres is an exception to that[171]. Neurospheres however are only approximately ~200 μm in size and may not well represent the bulk native tissue[172]. 3 dimensional cultures of neuroprogenitor cells may provide more accurate representation of the cells processes in native tissue.

1.7 Neuroblastoma

Neuroblastoma (NB) is a rare form of cancer which is most commonly found in infants under the age of 5 and is known to affect around 100 children

annually[173]. It is however the most common form of cancer diagnosed in children under 1 and accounts for 15% of child cancer deaths[174,175]. The cancer affects neuronal cells derived from neural crest tissues (neuroblasts) found most commonly in the adrenal glands, but can also be found in the neck, pelvis, abdomen and chest[176]. Neuroblasts are un-differentiated neuronal cells which mature and differentiate into neuronal cells or adrenal medulla cells[177]. When these neuroblasts differentiate incorrectly neuroblastoma cells and tumors can form.

1.8 Neuroblastoma treatment

Commonly used treatment methods for neuroblastoma include surgery, chemotherapy and radiotherapy[178]. The technique used is case dependent and in some cases all techniques are required. The development of a drug, the drug's interaction with radiation and its effect on the surrounding tumors are important. This is why NB models are being developed. These models would allow for drug and radiation testing to provide a useful understanding of how the techniques would work clinically to break down tumours.

1.9 Neuroblastoma models

In vivo models, such as TH-MYCN mice, are used for NB modeling[174]. Currently these *in vivo* models provide a good representation of NB biology, however, they have their limitations also, including the need for a high number of experimental animals. To overcome the need for animals, cell lines are being explored as an *in vitro* alternative to animal models. Two cell lines which are used to develop NB models are IMR-32 cells and SHEP1 cells. IMR-32 cells were established in 1967 from a NB tumor of a 13 month old, male human[179]. SHEP1 cells are a twice cloned subline of the NB cell line SK-N-SH from a 1970 metastatic bone tumor[180]. 2D monolayer cultures of these cell lines provide traditional *in vitro* tissue culture NB models and has led to a

deeper understanding of NB biology. Literature concludes however that these monolayers do not adequately represent the NB behavior in 3D. Therefore the development of 3D NB models are required to provide a more accurate model of NB tissue. There is limited literature currently available regarding 3D *in vitro* models of NB, one study however has developed multicellular tumor spheroids. It was concluded that these spheroids may provide a better *in vitro* model for NB, offering a link between using monolayers and *in vivo* models. These spheroids however were only approximately 500 μm in size and may not represent larger NB tissue[181].

1.10 Introduction summary

The main purpose of this shorter chapter is to understand and demonstrate the ability to use PGSm polyHIPE scaffolds in developing 3D tissue models. This 3D tissue model assessment was split in two, using two types of cells, neuroprogenitor and neuroblastoma cells.

It was hypothesized that 3D scaffolds could be used to create a more representative 3D culture of NB cell lines, allowing for a better representation of NB behavior in 3D. Initial experimentation focused on neuroprogenitor models. Primary neuroprogenitors were cultured onto 3D PGSm polyHIPE scaffolds, and cell viability studies performed in order to understand the ability to create 3D neuroprogenitor models.

This chapter then explored the ability to culture NB cell lines on 3D scaffolds, for use as NB models. The NB models were tested using the drug Olaparib and 5G radiation.

2. Methods

2.1 PGSm polyHIPE scaffolds

PGSm synthesis and PGSm polyHIPE synthesis metholodogies have been discussed (chapters 3.1 and 3.2). PGSm polyHIPE disks were produced at 13 mm diameter and approximately 3 mm depth.

2.2 Neuroprogenitor isolation and culture

Neuroprogenitor cells were isolated from embryonic day 18 Sprague Dawley Rat combined cortex and hippocampus with subventricular zone purchased from BrainBits LLC UK. Brain tissue was delivered in HEB solution (Hibernate E, B27, GlutaMAX). The HEB solution from the brain tissue was removed and put to one side, using a silanized pasteur pipette. A silanized pasteur pipette is used to ensure minimal cell attachment onto the pipette. Cell dissociation solution was added to the brain tissue and incubated at 30°C for 10 minutes, brain tissue was gently agitated every 5 to help dissociate the NSCs (Neuronal Stem Cells). The dissociation solution was removed and the HEB solution from earlier was returned to the brain tissue. Using a silanized Pasteur pipette the tissue was titrated until 90% of tissue was dispersed (approx. 1 min). Remaining undispersed tissue was allowed to settle, and the supernatant containing dispersed NSC's was centrifuged at 200g for 1 min. The supernatant was discarded, leaving behind the cell pellet. The cell pellet was dispersed and resuspended in 4 mL of Neurosphere Growth Medium (97% Neurobasal (Life technologies), 2% B27 (Life technologies), 1% Glutamax (Life technologies), 20 µL EGF solution (Sigma Aldrich), 20ul FGF-basic solution (Life technologies), 500 µL Pen/Strep.) 20 µL of cell solution was mixed with 20 µL of Trypan Blue, the resulting Trypan Blue cell solution was then counted using a Neubauer haemocytometer. One hundred and twenty thousand cells were transferred to a T75 flask coated in 2% polyHEMA

(Sigma) and incubated at 37°C, 5% CO_2, for 2-3 days to allow neuroprogenitor neurosphere formation. After 2-3 days neurospheres (floating in medium) were centrifuged at 100g for 2 mins. The supernatant was removed and the remaining cell pellet was redispersed in PBS. The PBS cell solution was centrifuged at 100g for 2 mins. The supernatant was removed and the pellet was resuspended in 1-2 mL StemPro Accutase (Life Technologies) and incubated at room temperature, to dissociate the cells within the neurospheres. The cells were then thoroughly titrated to redisperse the cells. 4 mL of medium was added to the cell suspension for each 1 mL of StemPro Accutase and the solution was centrifuged at 100g for 4 mins, and then centrifuged at 200g for a minute. The supernatant was removed and the cell pellet was redispersed in 1 mL of media. The cell number was counted and cells were seeded onto the surface of the scaffold/glass control at an approximate density of 1500 mm^{-2}. Scaffolds were coated in laminin and cell seeded scaffolds were cultured in 12well plates, incubated at 37°C, 5%, CO_2, with fresh medium changes every 3-4 days. 48 hours after cell seeding, medium was removed and neural differentiation medium was added (97% Neurobasal (Life technologies), 2% B27 with retinyl acetate (Life technologies), 1% Glutamax (Life technologies), 500 µL Pen/Strep.) The addition of retinyl acetate allows for the differentiation of the neuroprogenitor cells.

2.3 Neuroprogenitor cell viability assay

Cell viability studies (MTT assay) were performed on the cell seeded scaffolds on days 4, 7 and 14. Scaffolds used for experimentation were 13 mm glass cover slips, 13 mm flat PGSm disks and 13 mm PGSm polyHIPE disks. For full methodology of MTT assay see Methods (chapter 2).

2.4 Neuroprogenitor immunohistochemical staining

The scaffolds were prepared for immunohistochemical staining on days 4, 7 and 14. IHC staining procedures can be found in the Methods (chapter 2). Briefly, the cell seeded scaffolds were fixed in 3.7% paraformaldehyde in PBS for 15 minutes at room temperature, washed in PBS and then ICC buffer (1%Bovine Serum Albumin, 0.1% Triton X-100 in PBS) was added to each sample and incubated at room temperature for twenty minutes to block and permeabilise the cells. The ICC buffer was removed and primary antibodies Nestin and Beta-III-Tubulin, diluted in 1/100 ICC buffer, were added to the scaffolds. Primary antibodies were left in the refrigerator overnight. Secondary antibodies Alexa Fluor 488 rabbit anti-mouse IgG (λ_{Ex}/ λ_{Em} = 490nm / 525nm, ThermoFisher) and Alexa Fluor 546 goat anti-rabbit (λ_{Ex}/ λ_{Em} = 556nm / 573nm, ThermoFisher) were added at a titre of 1:500 in ICC buffer for two hours at room temperature. Scaffolds were washed in PBS and a DAPI solution (4',6-diamidino-2-phenylindole) dissolved in PBS (1 µg/mL) was added before incubating at room temperature for ten minutes. Scaffolds were rinsed a final time in PBS, before being submerged in PBS in 6 well plates, to allow for confocal imaging with a water dipping objective.

2.5 Neuroblastoma IMR-32 and SHEP-1 cell culture

Cell lines were frozen and thawed as described in the Methods (chapter 2). IMR-32 and SHEP-1 cells were cultured in a similar methods. Cells were incubated at 37°C with 5% CO_2 and passaged when they reached 70-80% confluence, or every four days; whichever occurred first. IMR-32 cells were cultured in DMEM:RPMI 50:50 medium, with 10% (v/v) FCS, 0.25 µg/mL amphotericin B, 100 units/mL penicillin, 100 µg/mL streptomycin and 2 mM L-glutamine. SHEP1 cells were cultured in DMEM:EMEM 50:50 medium, with 10% (v/v) FCS, 0.25 µg/mL amphotericin B, 100 units/mL penicillin, 100

µg/mL streptomycin and 2 mM L-glutamine. 100,000 cells were seeded onto the surface of the polymer disks, glass cover slips and PGSm polyHIPE disks and incubated until treatment.

2.6 Neuroblastoma IMR-32 immunohistochemical staining

Cells were immunolabeled with beta-III-tubulin and DAPI. For full IHC staining see Methods (chapter 2).

2.7 Neuroblastoma drug and radiation testing

Cells were seeded onto PGSm polyHIPE disks and incubated at 37°C, 5% CO_2. After 48 hours scaffolds underwent one of four treatment methods of, no treatment, olaparib drug, 5G radiation and olaparib drug with radiation. Olaparib was introduced to medium to create a 10 mM solution of the drug, this was introduced to scaffolds with the drug treatment. Some scaffolds also underwent radiation for 125 seconds (5G) (IBL 437C, CIS bio international). All scaffolds were then incubated and an alamar blue cell viability assay performed on days 2 and 4 after treatment.

3. Results

PGSm was made into an emulsion and cured into 13 mm disks. These disks were used in experiments assessing the scaffolds for use as a model for neuroprogenitor and neuroblastoma cells. SEM micrographs show a highly interconnected and porous scaffold was used for experimentation.

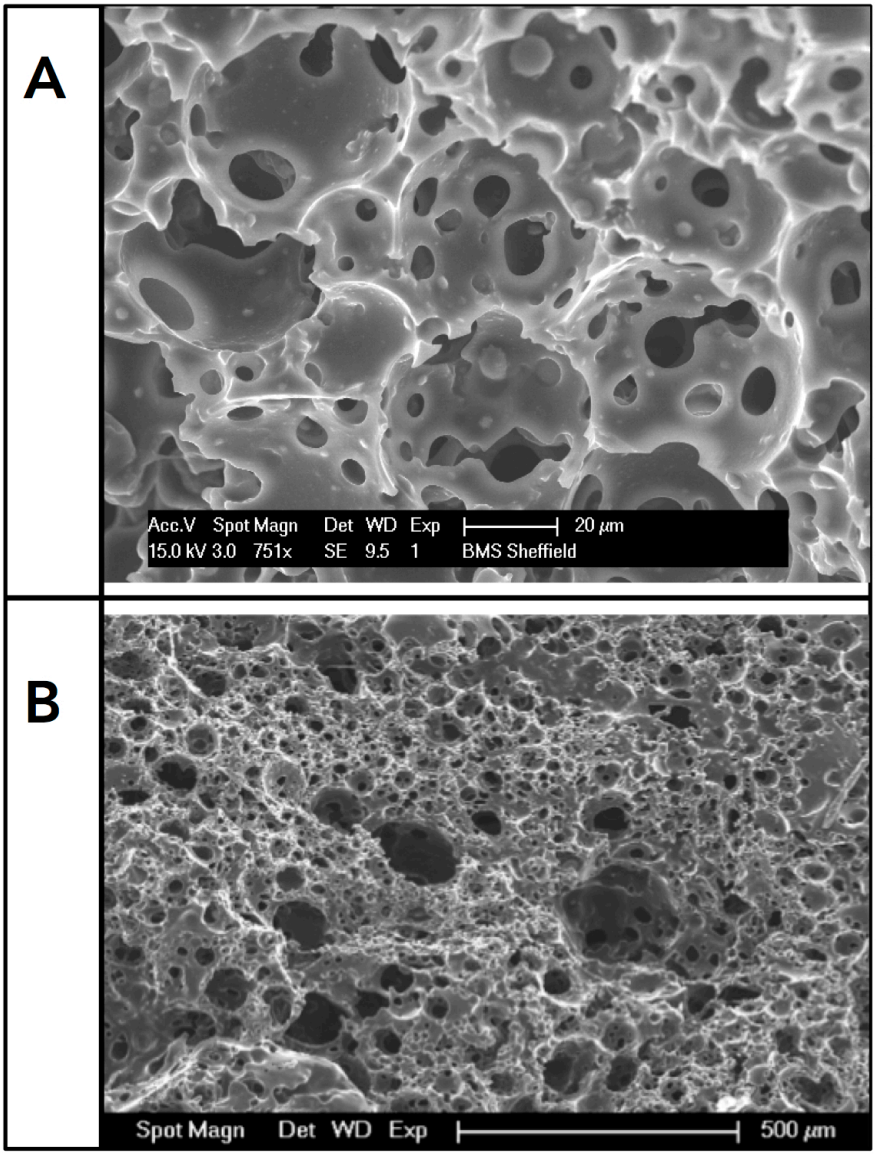

Figure 71: SEM micrographs of PGSm polyHIPE. Images A and B have 20 µm and 500 µm scale bars respectively.

Primary neuroprogenitor cells were cultured onto PGSm disks and glass coverslips. Results (Fig 72) show that a low number of cells are visible on day 4 on both the PGSm disks and the glass cover slips. By day 7 there were more cells visible on both the polymer and the glass, there also appears to be a higher expression of nestin from the PGSm disks, whereas there is a high expression of beta-III-tubulin on the glass coverslips. Day 14 results show a high number of differentiated cells in both (determined by green beta-III-tubulin) glass, however, glass again shows a higher level of differentiated cells

with high levels of nestin still expressed on the PGSm. This suggests that more cells remain as neuroprogenitors on PGSm than glass, or that differentiation is slower on PGSm.

Porous PGSm polyHIPE scaffolds were seeded with the primary neuroprogenitors. Confocal Z-stacks of the neuroprogenitor cells after 14 days (Fig 73) indicate that cells had survived and migrated into the scaffold, with signs of both differentiated and undifferentiated cells being expressed (beta-III-tubulin, green and nestin, red).

Cell viability assays (MTT) were performed on the PGSm disks, the glass coverslips and the PGSm polyHIPE. Results show a graph of all three scaffolds across the 14 days (Fig 74, A). Results indicate an initial statistical difference in cell viability at day 7 between the variables, however, this difference is diminished by day 14 and there is no statistical difference between any of the variables. PGSm HIPE results indicate it is the only scaffold not to have a statistically lower cell viability on day 14 than on day 7, suggesting that the polyHIPE may be an appropriate substrate for 3D cultures of neuroprogenitor cells.

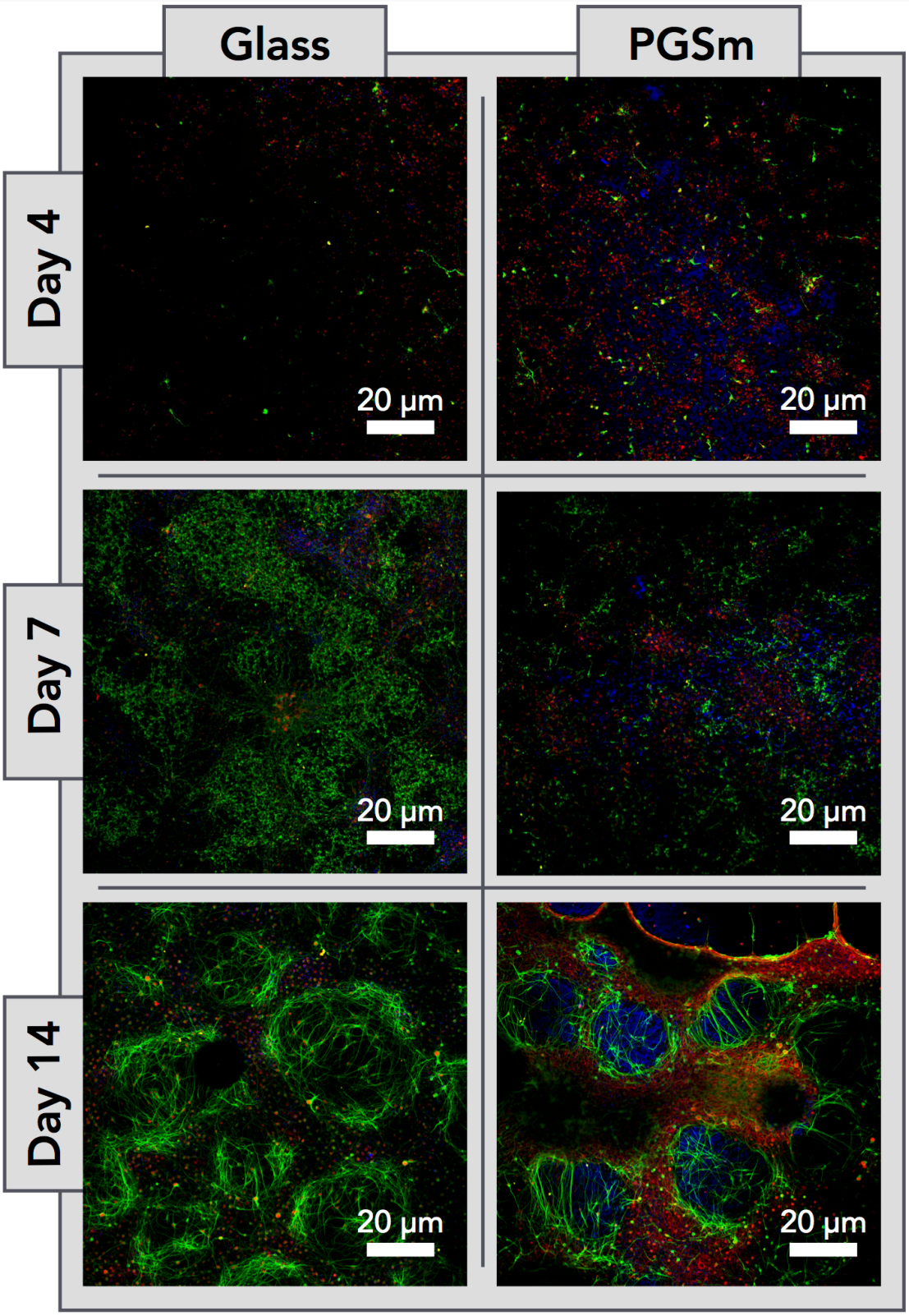

Figure 72: Primary neuroprogenitor cells cultured onto disks of PGSm and glass cover slips for 14 days. IHC labeled with nestin (red) beta-III-tubulin (green) and DAPI (blue). 20 µm scale bar.

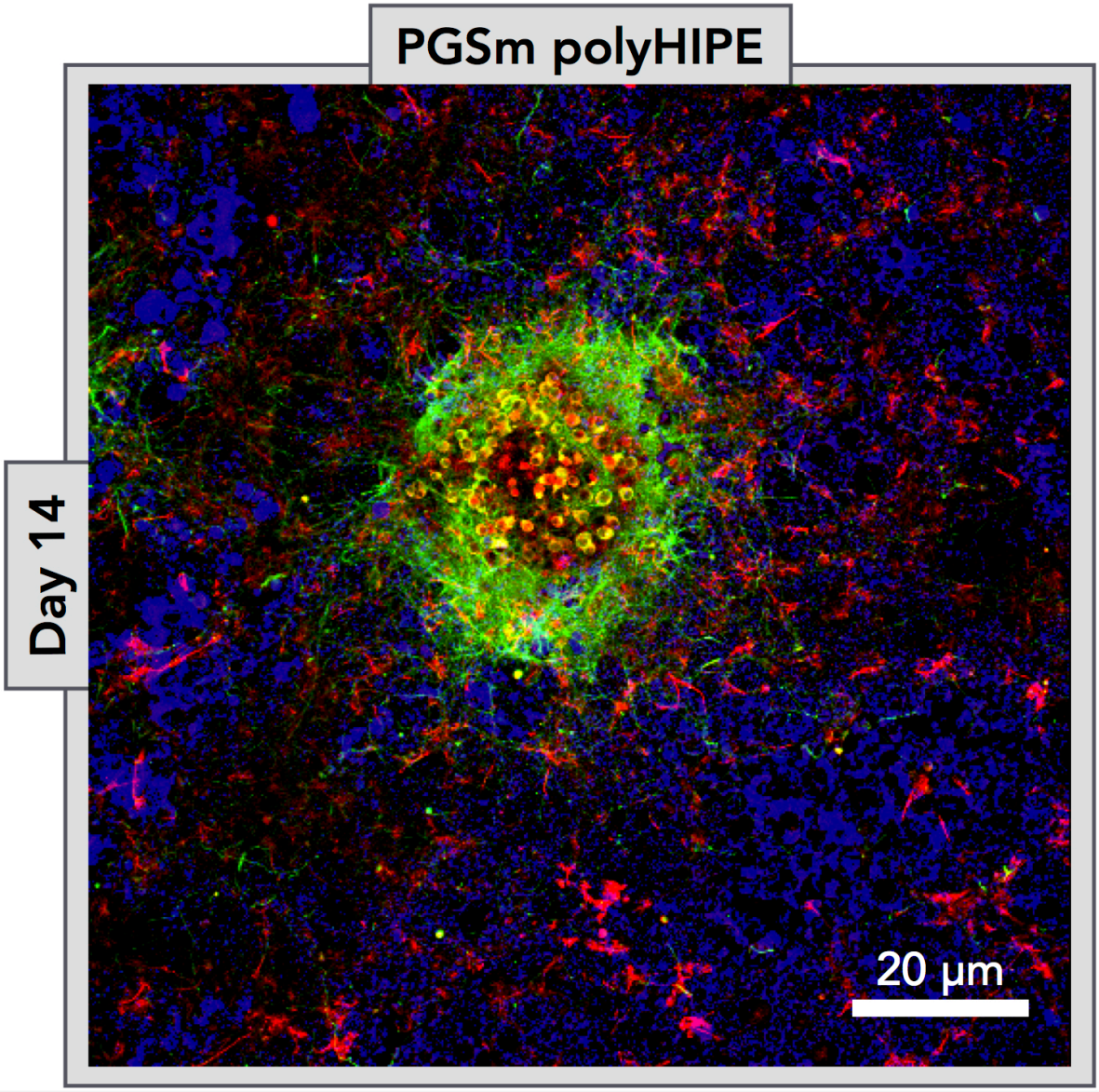

Figure 73: Z-stack confocal image of neuroprogenitor cells cultured within a PGSm polyHIPE scaffold after 14 days. Image acquired from 20 slices across a depth of 225 µm. IHC labeled cells with nestin (red), beta-III-tubulin (green) and DAPI (blue).

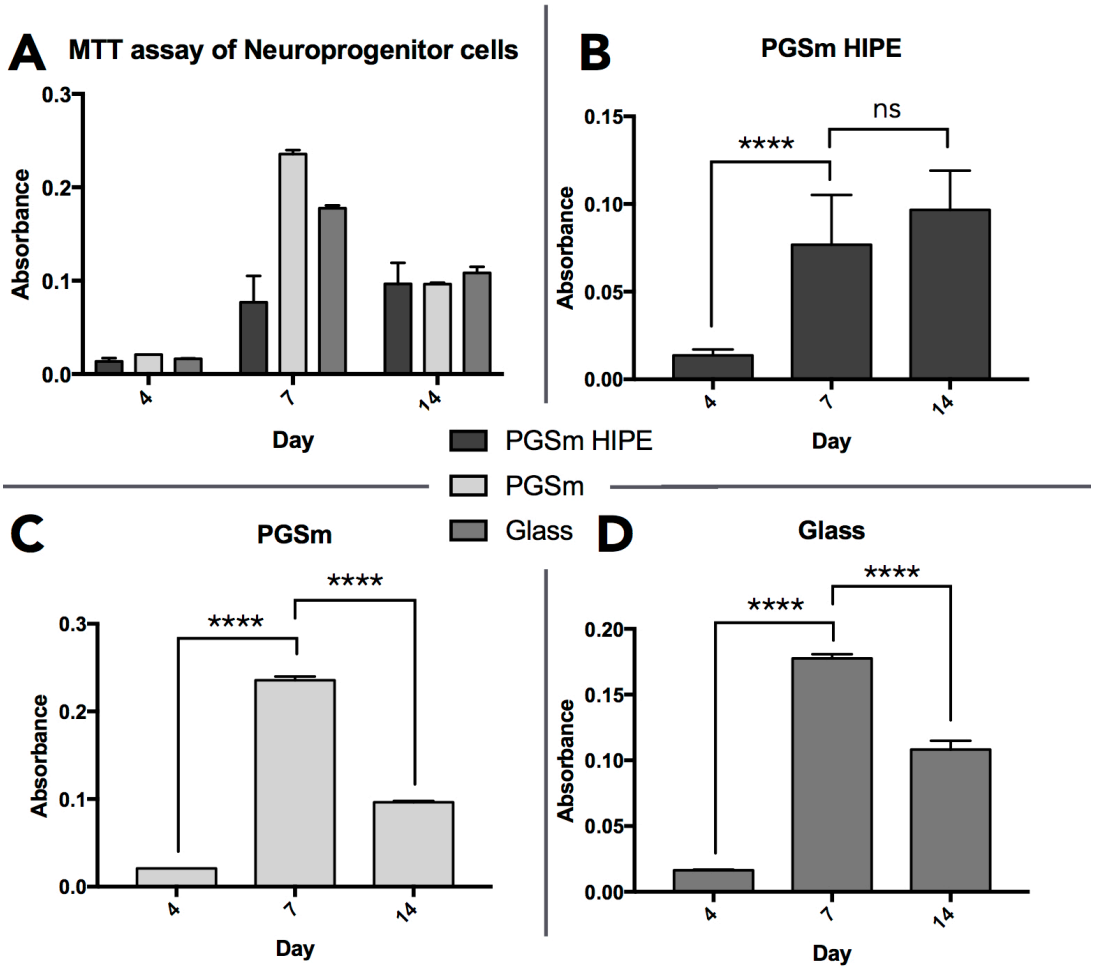

Figure 74: MTT assay of neuroprogenitor cells on HIPE disks (B), PGSm disks (C) and glass cover slips (D). Graph A represents a graph of neuroprogenitor cells cultured on all three substrates for 4, 7 and 14 days. Two way ANOVA, Tukey with multiple comparisons was used for statistical significance (standard deviation error bars, n=2).

IMR-32 cells were cultured onto flat disks of PGSm to test the initial biocompatibility of PGSm with neuroblastoma cells. An example confocal micrograph (Fig 75) shows the neuroblastoma cells cultured onto flat PGSm disks. IMR-32 and SHEP-1 cells were cultured onto flat disks of PGSm, at days 4 and 7 (Fig 76). It is clear from light microscope images that cells were able to attach and proliferate on the surface of the PGSm. Suggesting the material is appropriate for NB culture.

IMR-32 cells were then cultured on PGSm polyHIPE for 7 days. Confocal micrograph z-stacks were taken across 60 μm, with results showing how cells had migrated into the porous network of the scaffold (Fig 77).

Neuroblastoma models were created using both IMR-32 and SHEP-1 cells. Cells were seeded onto scaffolds and incubated for 48 hours, scaffolds then underwent a series of treatments including the drug Olaparib and 5G radiation. The scaffolds were then incubated and cell viability (Alamar blue) studies performed on days 2 and 4. Results (Fig 78) show that all treatment methods resulted in an increase in cell viability. There was no significant difference between any of the treatment methods. Olaparib appears from the graph (Figure 78, B) to lower the cell viability in SHEP-1 cells, however this was not statistically significant.

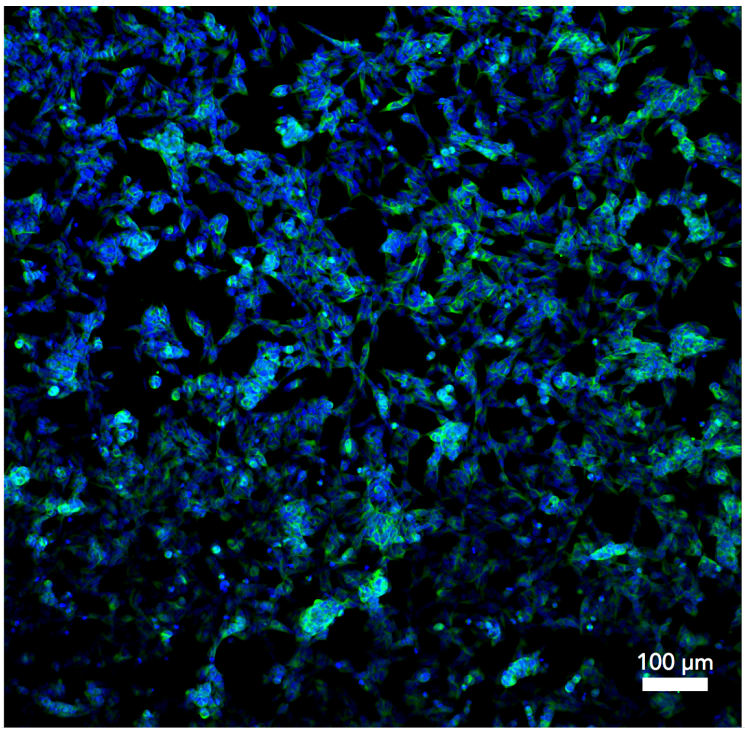

Figure 75: Confocal micrograph image of IMR-32 cells cultured onto flat disks of PGSm. Immunolabeled with anti-beta-III tubulin (green) and DAPI (blue.)

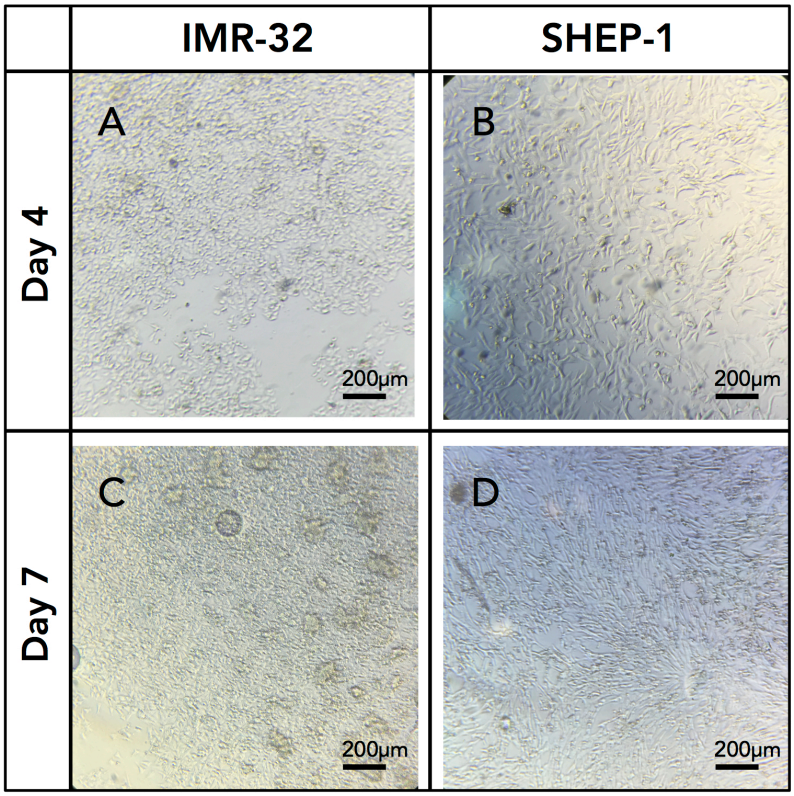

Figure 76: Optical microscope images of cells seeded onto PGSm disks and cultured for days 4 (A + B) and days 7 (C + D). IMR-32 (A + C) and SHEP-1 (B + D) cell lines used. 200µm scale bars.

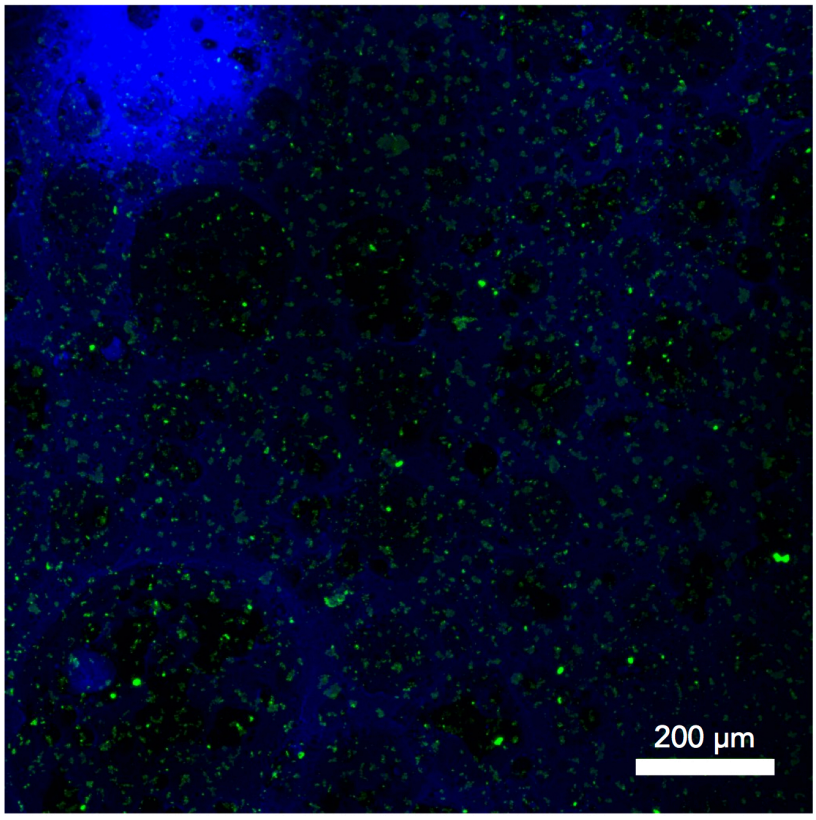

Figure 77: Confocal Z-stack micrograph across a 60µm depth, of IMR-32 cells seeded within PGSm HIPE foam disks, After 4 days of culture cells had migrated into the scaffold. Cells were IHC labeled with beta-III-tubulin (green) and the scaffold autofluoresces (blue).

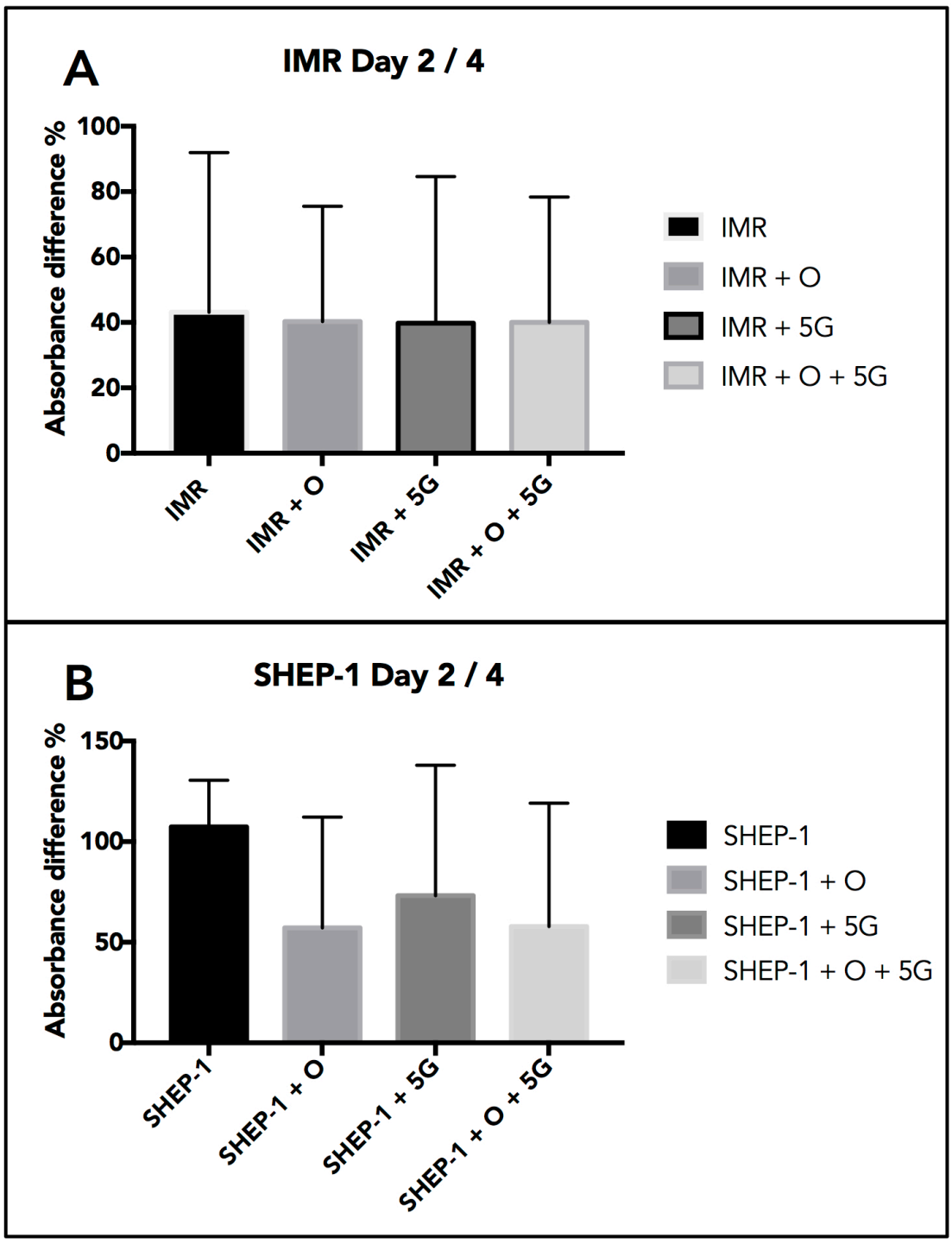

Figure 78: Graphs showing the percentage difference of alamar blue absorbance from days 2 to 4, of IMR-32 cells (A) and SHEP-1 cells (B), seeded onto PGSm polyHIPE disks. Disks underwent treatments of: no treatment, Olaparib drug treatment, 5G radiation treatment and both Olaparib and 5G radiation treatment. No significant difference.

4. Discussion

The main aim of this chapter was to understand whether PGSm polyHIPE scaffolds could be used as a 3D tissue model using both neuroprogenitor and neuroblastoma cells. 3D PGSm polyHIPE scaffolds were made in accordance to previous chapters (chapter 3.2), and cut into 13 mm disks for experimentation.

Nestin is an intermediate filament protein expressed in the development of the eye and brain and is downregulated in terminally differentiated cells, which is why it is understood to be a marker for neuroprogenitors[182,183]. Beta-III-tubulin is a marker for neurons[184]. Results from confocal images show that primary neuroprogenitors were able to attach and proliferate on flat PGSm surfaces over a 14 day period (Fig 72). The expression of beta-III-tubulin (neurites) and the expression of nestin (neuroprogenitor), suggests that the neuroprogenitor cells seeded onto the scaffolds were able to both differentiate and remain as progenitor cells. After 14 days there appears to be a higher ratio of progenitor cells (nestin, red, Fig 72) in the PGSm disk than the glass cover slip. From these results it is clear that the PGSm polymer is a viable substrate for neuroprogenitor cells, with results also indicating PGSm slowing progenitor differentiation. Neuroprogenitor cells seeded onto 3D PGSm polyHIPE scaffolds for 14 days were difficult to be imaged via confocal microscopy due to the 3D nature of the scaffolds. However, results show (Fig 73) that neuroprogenitors were able to differentiate, extend neurites (beta-III-tubulin), and remain as progenitor cells (nestin). Interestingly undifferentiated cells were spread across the scaffold whereas differentiated cells with neurites appear more localized, this may be an example of the progenitor cells behaving as they do within neural stem cell niches[185]. Results from the cell viability study indicate that on flat surfaces of PGSm and glass control,

neuroprogenitor cells undergo an initial significant increase in cell viability at day 7 and then a significant decrease by day 14. Whereas neuroprogenitor cells on the 3D PGSm polyHIPE scaffolds show a significant increase in cell viability up to day 7 and then what appears to be a slight increase (although the increase is not significant) in cell viability up to day 14. This suggests that the cells are either better protected or are within a microenvironment which better mimics the native tissue. Overall the confocal images show that neuroprogenitors attach, differentiate and proliferate within the 3D PGSm polyHIPE scaffolds and cell viability studies suggest that the 3D scaffold may provide a better representation of the native microenvironment.

Neuroblastoma cell lines IMR-32 and SHEP1 were seeded onto flat PGSm disks and glass controls. Confocal and light microscope images show that cells were able to attach to and proliferate on flat PGSm disks. Neuroblastoma cells seeded onto 3D polyHIPE scaffolds were able to migrate and attach throughout the porous network (Fig 77). PolyHIPE scaffolds were seeded for 48 hours and used as NB models for both drug and radiation treatments. Alamar blue cell viability results show that IMR-32 cells appear to be unchanged by the Olaparib drug, radiation, or both and show no significant difference. Whereas SHEP-1 cells appear to have a lower viability when treated with radiation, and even lower when treated with Olaparib/Olaparib and radiation, these results however were slight and showed no statistical significance. The lack of significant findings may be due to the 3D nature of the model, requiring higher doses of radiation and/or Olaparib drug. This may suggest that the model is behaving more representatively to that of the 3D native tissue, although, further studies are necessary.

5. Conclusion

The purpose of this chapter was to assess the capability of PGSm polyHIPE scaffolds as a tissue engineering model for both neuroprogenitors and neuroblastoma. Neuroprogenitors attached and proliferated readily in 3D, with signs indicating a more adherent/viable culture than the monolayer cell study. Neuroblastoma cells were able to migrate within the porous network and radiation and drugs testing performed. Whilst the results of the radiation and drugs testing remain inconclusive, the ability to test these techniques using a 3D PGSm polyHIPE model looks positive. Overall it can therefore be concluded that PGSm polyHIPE scaffolds create an appropriate microenvironment to allow the 3D culture of cells, and may help develop 3D tissue engineering *in vitro* NB models.

3.7 2D PATTERNING AND 3D CULTURE OF EMBRYONIC STEM CELLS

Aim: The main aims of this chapter were to assess the use of 2D patterned PGSm scaffolds and 3D PGSm polyHIPE foams for use as scaffolds for embryonic stem cells.

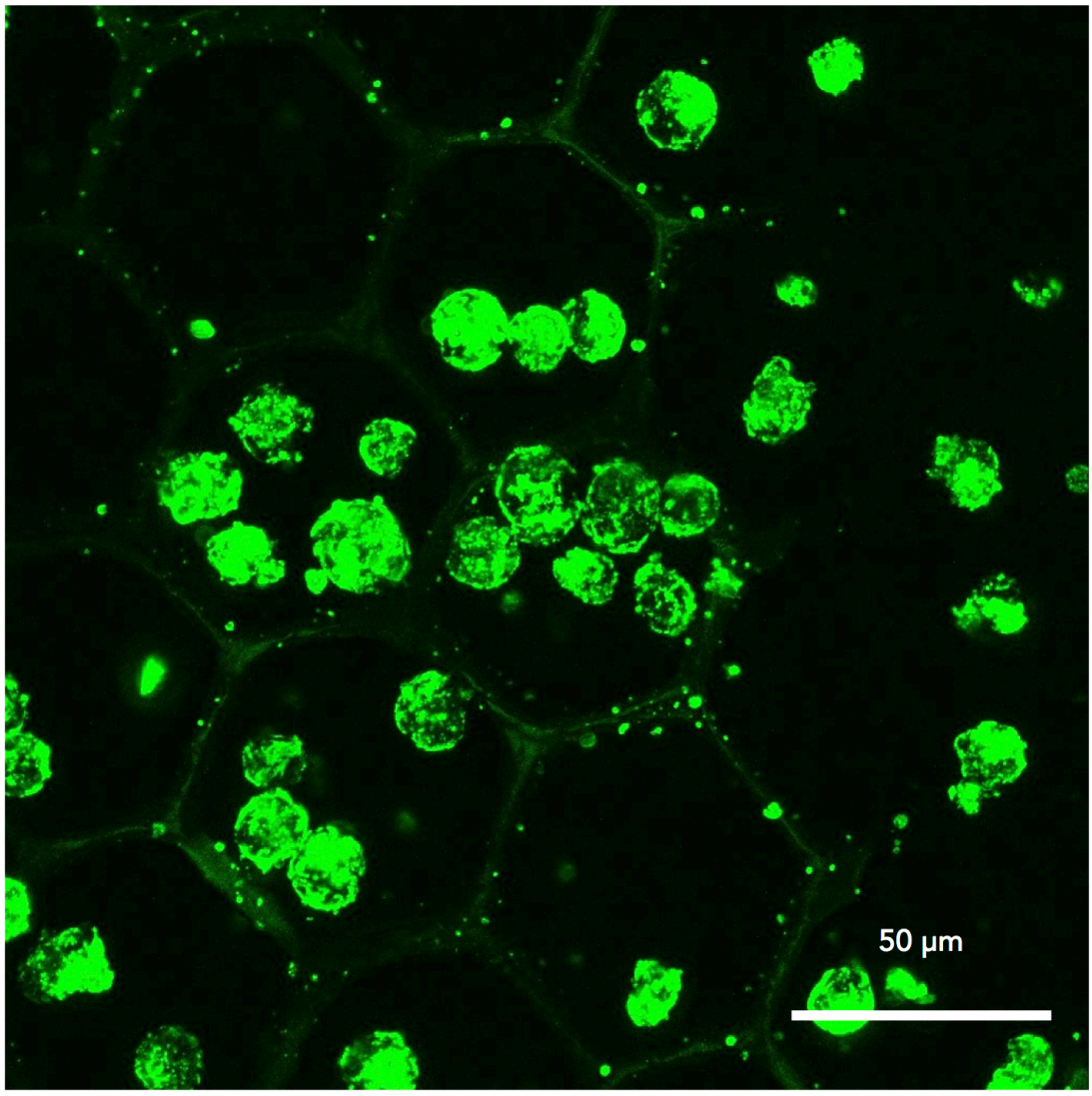

ESCs within a 2D patterned PGSm grid of hexagons. For complete image see Fig.94

1. Introduction

1.1 Pluripotency

The life of a mammalian animal begins with a totipotent zygote, capable of differentiating into all of the specialized cells within the adult animal. The first differentiation event directs cells down two lineages, either the inner pluripotent cell mass (ICM) or the trophectoderm (TE). The TE interacts with the mother's uterus enabling the development of tissues within the placenta[186]. Embryonic stem cells can be isolated from within the ICM and propagated in vitro, whilst retaining their pluripotent ability to differentiate into each of the three germ layers (endoderm, mesoderm, ectoderm)[187].

1.2 ESCs

Human embryonic stem cells (hESC's/ESC's) derived from the ICM of the human blastocyst (see Fig 79) maintain most of their totipotency. These ESCs can be cultured *in vitro* and hold the ability for self renewal and differentiation into all somatic cells[188]. Some adult stem cells reside within the body throughout life within microenvironment pockets, protecting the cells known as niches. These cells are able to be a resource to replenish nearby damaged tissues/dying cells[189]. The capabilities of stem cells within niches to repair damaged tissues has driven the advancement of research into modeling these stem cell niche microenvironments *in vitro*, with 2D and 3D strategies. 2D stem cell niches are simpler to model and dominate the research in this area, however 2D models often lack the complexity of the 3D microenvironments formed physiologically often leading to unexpected spontaneous differentiation[190]. Research has begun to move toward 3D modeling of stem cell niches and 3D cultures of stem cells *in vitro*, however research in this area is still limited.

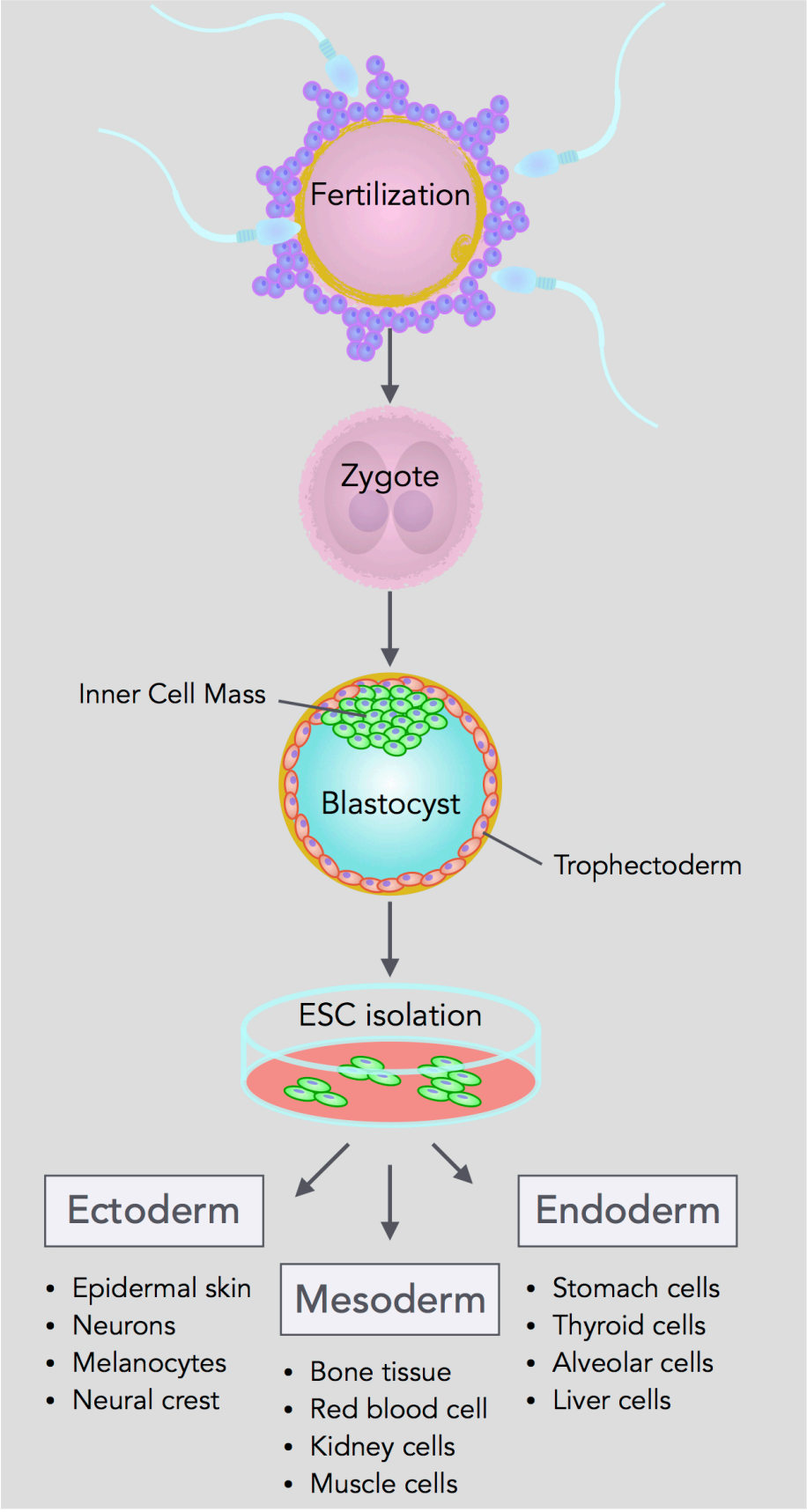

Figure 79: Computer designed image showing the development from fertilization to ESC isolation. ESCs isolated from ICM. (Keynote, Apple)

1.3 IPSCs

Terminal differentiation of pluripotent cells was once believed to be final, however more recent developments over the past decade have shown that adult cells can be reprogrammed and are able return to their pluripotent state, these are known as induced pluripotent stem cells (hIPSCs/IPSCs)[191]. The exact mechanisms which drive the reprogramming of cells into IPSCs are still not fully identified and methods to reprogram cells are often inefficient with low yields[192]. Similarly to ESCs 2D IPSC cultures often lack the required microenvironment with 3D cultures/models being far closer physiologically. The development of research into 3D cultures is at it's early stages and current models have their own limitations[193]. The term human pluripotent stem cells (hPSCs/PSCs) is used to define both ESCs and IPSCs.

1.4 Stem cell niches

Stem cell niches describe a microenvironment containing stem cells often in a state of quiescence, allowing for their self-renewal and differentiation when needed. Stem cell niches have been known for some time, with the term niche first appearing in 1978[194]. Since 1978 when hematopoetic stem cells were found in the bone marrow, niches have been identified in the skin, nervous system, and intestines. It is commonly believed that the microenvironment/niche is greatly important to the maintenance and function of these stem cells through soluble signals, structural cues, and the interactions between the cells and between the cells and the matrix[195]. Research into modeling these niches has therefore heavily focused on scaffold and materials design to mimic the native niches/develop 3D stem cell cultures.

1.5 Stem cell models - moving towards 3D

Through the use of human pluripotent stem cells it is now possible to model human disorders *in vitro*, with aims to overcome some of the ethical, cost and time constraints of animal models. The stem cell models may provide information more translatable to humans, they may allow for a higher throughput of drug/dosing experiments and may also work well as a preliminary to animal models. These models can be developed using either ESCs or IPSCs, IPSCs models were developed with the idea to overcome some of the immunological concerns surrounding ESCs and the potential implantation. 3D organoids derived from PSCs have been developed in literature for modeling various tissues/disorders including structures related to the eye, pituitary, cerebral and intestinal organoids[192]. The inclusion of complex scaffold designs may further 3D stem cell research into other areas and help develop those already modeled in literature. It has been concluded in literature that the structure of scaffolds is of extreme importance in determining stem cell differentiation lineage, with different scaffold structures shown to induce different gene expression within stem cells[196].

1.6 Porous polyHIPE foams as stem cell scaffolds

There is limited research into the use of 3D porous materials for stem cell culture, some research has been performed using the commercially available polyHIPE polystyrene foam Alvetex (Reinnervate, Durham UK)[197]. Research in literature has found that with the use of this commercially available polyHIPE scaffold and a co-culture of adipose derived stem cells and endothelial cells it was possible to create 3D tissue engineered constructs. The use of this commercially available product, however, limits adaptability of scaffold designs to those that are commercially available. Further research has been performed using non-commercial, "in-house" polyHIPE foams, which have successfully demonstrated the ability to culture human embryonic stem cell

derived mesenchymal progenitors (HESMPs) on 3D foams and have evaluated the differentiation toward an osteogenic lineage[198,199]. These foams are non-degradable, which limit their potential in any implantation. Degradable polyurethane HIPEs have also been explored for 3D culture of human mesenchymal stem cells (HMSCs) toward a osteogenic lineage, however research here is in the early stages and only the limited cytotoxic response was assessed[200]. The ability to develop in house polyHIPE foams vastly increases the range of possibilities for scaffold designs. The materials chosen for the foam may also increase the effectiveness of the scaffolds.

1.7 Introduction summary

It can be understood from the developments within literature[196] that with complex scaffold designs, developments can be made in modeling stem cells in 3D – with a focus on determining cell fate through structural designs and material selection. It may therefore be possible to use scaffold design to develop models for disorders, or to maintain cells within a quiescent state (as in stem cell niches).

This chapter explored the use of the novel formulation PGSm as a scaffold material for stem cell culture. This was done through the use of flat disks, 2D patterned scaffolds and 3D porous polyHIPE foams.

2. Methods

2.1 Scaffold production

Scaffolds were produced from PGSm using methodologies previously discussed. For flat PGSm disk methodology see Method (chapter 2), for 2D patterned grids see Method (chapter 2) and for 3D polyHIPE production see methods (chapter 3.2).

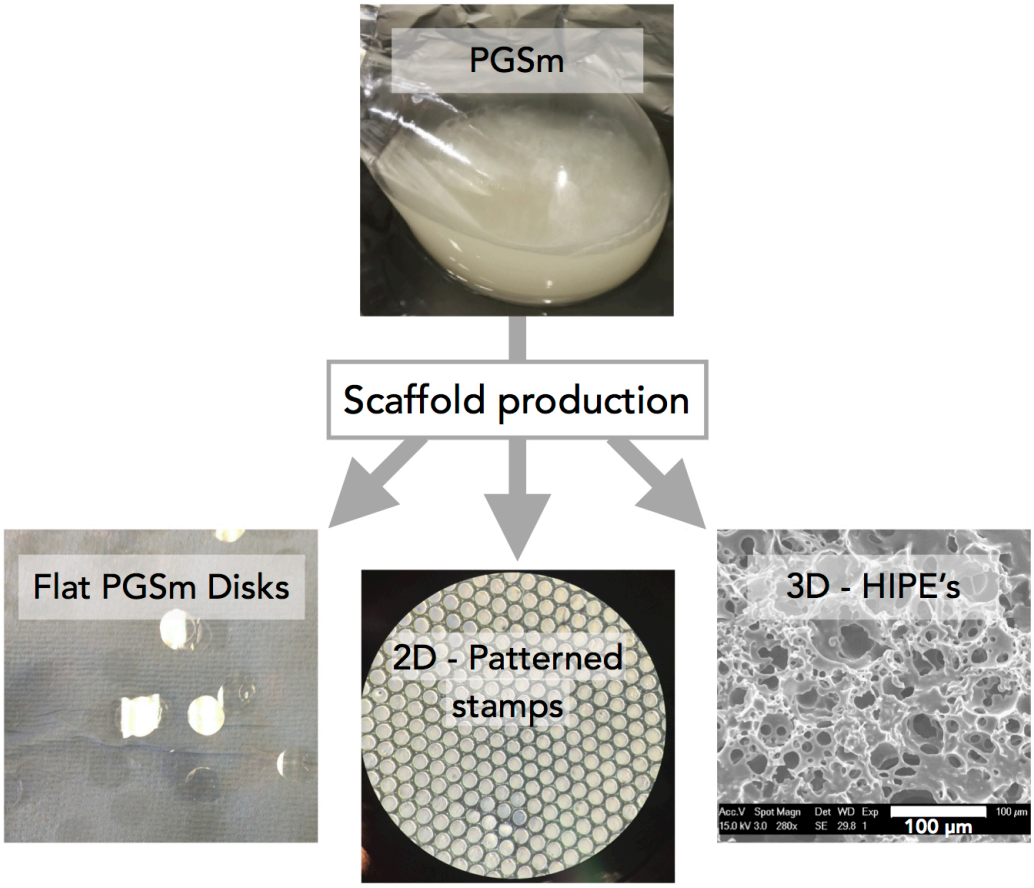

Figure 80: Figure showing the polymer synthesis and scaffold production techniques. PGSm solvent evaporation in first image, with flat PGSm disk production via UV photocuring, 2D patterned stamps via 2-photon polymerization and stamp methodologies, and 3D foams via polyHIPE production. (Keynote, Apple)

Briefly, flat disks were produced by photocuring PGSm onto 13mm glass cover slips. 2D patterned grids were produced using 2-photon polymerization, see Method (chapter 2). Patterned grids were then placed onto disks of uncured PDMS, which were then thermally cured, creating a negative stamp of the patterned grid (Fig 81). A drop of PGSm was placed onto the surface of the negative PDMS stamp and a glass cover slip secured on top. The construct was photocured, and the glass cover slip with PGSm pattern attached was removed. The PDMS stamp allowed for rapid and highly accurate reproduction of the patterned grid. PolyHIPE emulsions were

produced as previously discussed, polyHIPE were photocured into disks with a 13 mm diameter and a 3-5 mm depth.

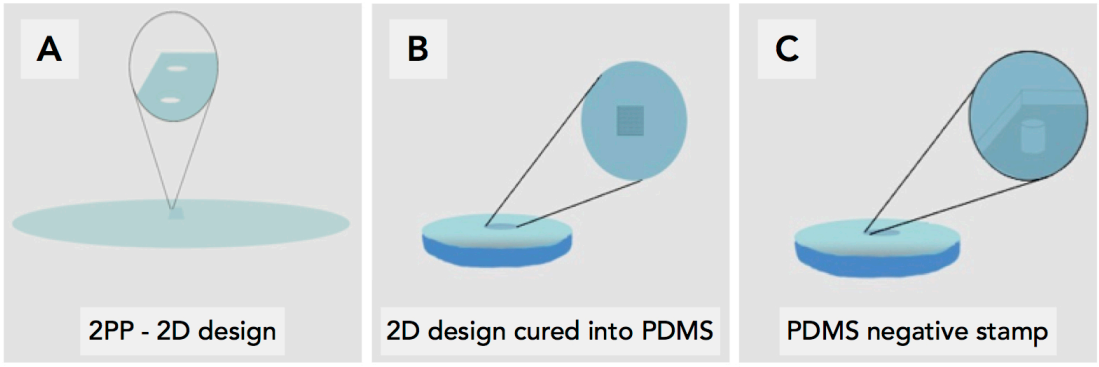

Figure 81: Computer designed model of PDMS stamp creation. (Keynote, Apple)

2.2 ESC *in vitro* cell culture

Cells used for this study were donated by Harry Moore and Andy Wood (Centre for Stem Cell Biology, University of Sheffield.) MShef4, a human embryonic stem cell line (also known as MasterShef4, MstrShef4) was used for all ESC studies. Culture conditions were similar to previously discussed cell culture conditions, briefly cells were incubated at 37°C, 5% CO_2. Traditionally, and for cell cultures prior to experimentation, ESCs and MShef4 cultures are seeded onto TCP coated with human recombinant laminin 521 in Nutristem medium.

Cultures were passaged between 60-90 % confluency. EDTA solution, 0.5 mM, was warmed to 37°C. Medium was removed from the culture vessel and gently washed twice with PBS -/-. EDTA solution, 1.5 mL, was then added to the culture vessel and incubated for 5 minutes. After 5 minutes, cells begun to round up together, the culture flask was then gently tapped on the side to detach the cells from the surface. Nutristem medium, 3.5 mL, was then added to dilute the EDTA solution. The cells were resuspended by mixing in a pipette three times, allowing for the larger clumps of cells to break down.

Cells were counted and then either reseeded onto laminin coated TCP or seeded onto scaffolds for experimentation. 1 million cells were suspended into a small volume of medium and the cell suspension seeded onto scaffolds as a single drop, after allowing 15 minutes for cell attachment Nutristem medium filled the surrounding well.

2.3 ESC immunohistochemical labeling and image acquisition

ESCs and scaffolds were fixed and immunolabeled as discussed previously, for full IHC methodologies see Method (chapter 2). Briefly, samples were fixed with 3.7% paraformaldehyde at room temperature for 15 minutes (3D polyHIPE samples were fixed for 30 minutes.) Primary monoclonal mouse antibodies Tra-1-85 and Tra-1-60 (Centre for Stem Cell Biology, University of Sheffield) were used for experimentation to visualize human cells and human cells expressing pluripotency respectively. Samples were incubated with primary antibodies at a 1:50 titre and refrigerated at 4°C overnight. Unlike previous immunohistochemistry methodologies, PBS was used in place of ICC buffer (without Triton X-100 permeabilization), to ensure primary antibodies attach to surface antigens. The scaffolds were then washed in PBS and secondary rabbit anti-mouse antibody IgG Alexa Fluor 488 (λ_{Ex}/ λ_{Em} = 490nm / 525nm, ThermoFisher) was added at a 1:200 titre for two hours at room temperature. Samples were then washed three times in PBS. Images were acquired as discussed previously using an upright Zeiss LSM 510 confocal microscope with a water-dipping objective (EC Plan-Neofluar 40x/1.30).

2.4 ESC polyHIPE freezing

ESCs were seeded onto PGSm polyHIPE disks and cultured for 10 days. The polyHIPE ESC cell construct was then frozen as discussed previously at a rate of 1°C per minute up to -80°C. Cells were then stored in liquid nitrogen for 7 days. After 7 days the construct was rapidly thawed and warmed to 37°C in a

water bath and cultured for 7 days. 24 hours and 7 days after thawing cells were IHC labeled with Tra-1-60 to understand whether the ESCs survive being frozen and maintain pluripotency.

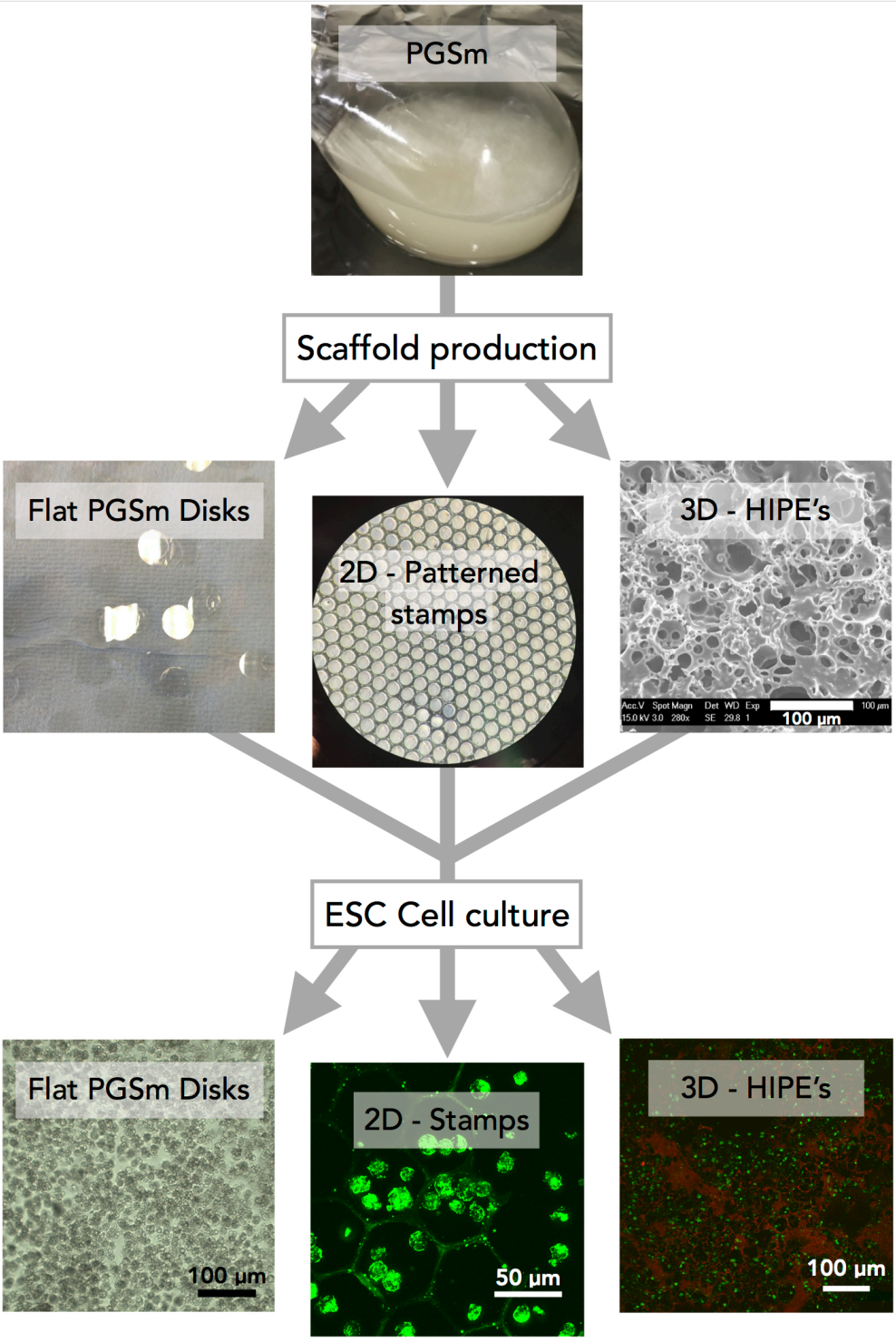

Figure 82: Diagram showing overall methodologies from scaffold production to cell culture. (Keynote, Apple)

3. Results

Using the techniques described above PDMS stamps and PGSm patterned grids were produced (see Figs 83, 84). The produced grids were highly reproducible (as seen throughout experimentation) and accurate with a pore diameter of 50 µm, and a height of 10-20 µm.

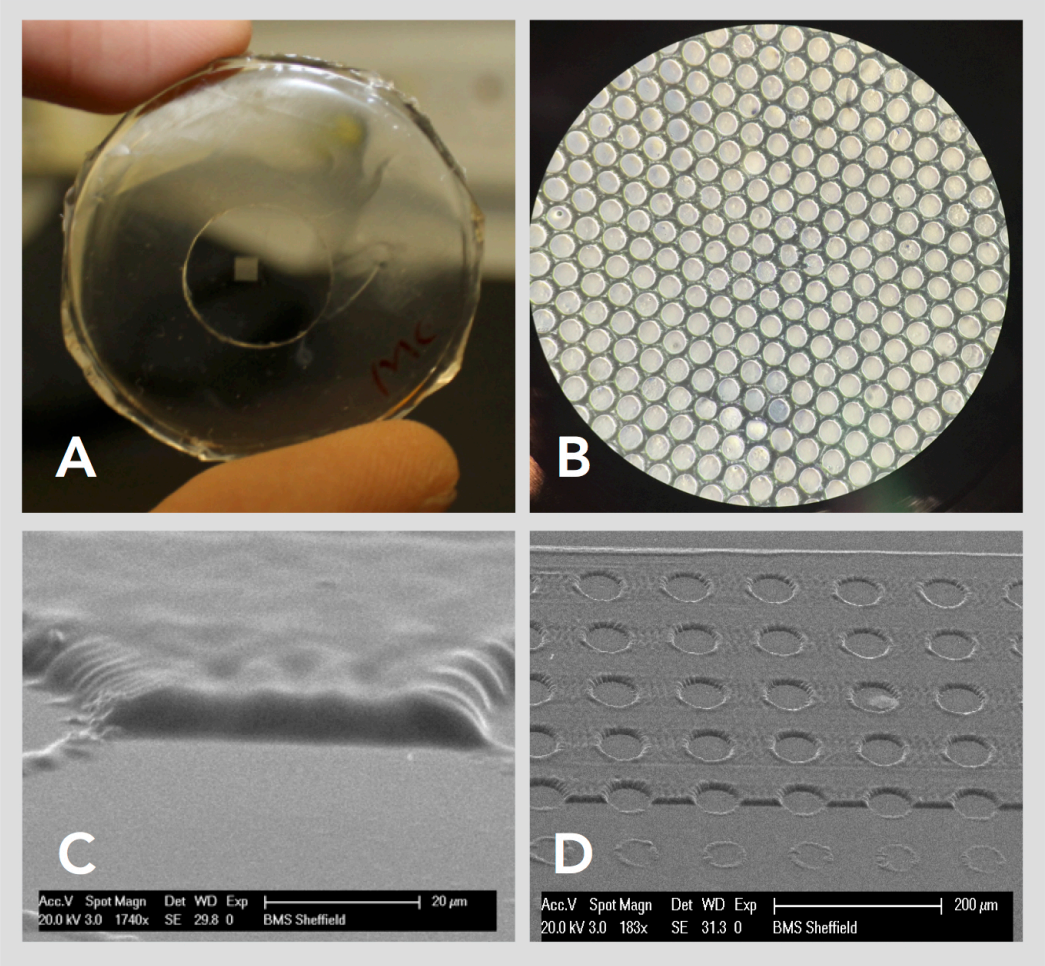

Figure 83: Digital image of PDMS stamp (A), light microscope image of PGSm circle patterned grid (B), SEM images of the grids (C, D).

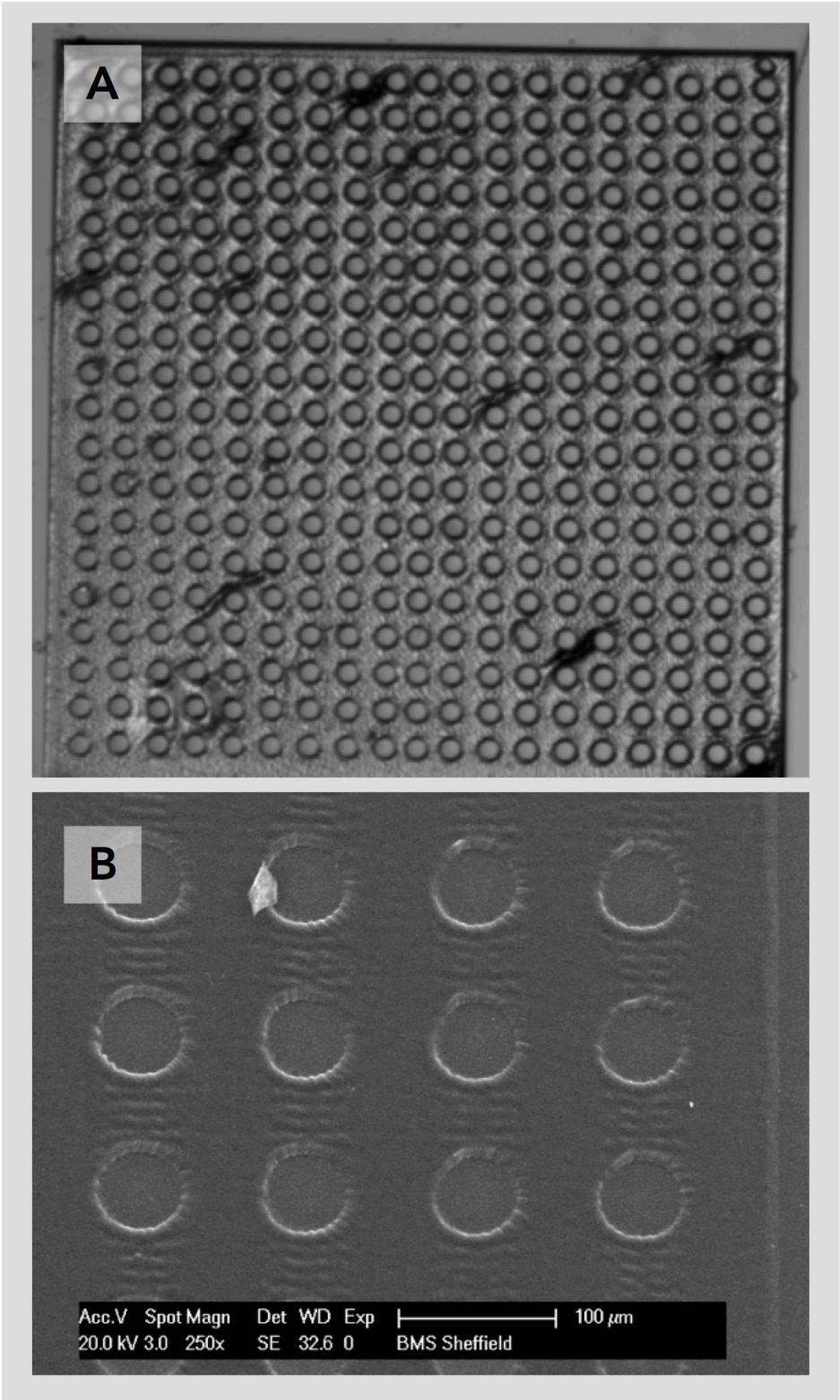

Figure 84: Light microscope image of complete PGSm 2D patterned grid (A) and SEM micrograph of the PGSm grid showing pore diameter (B.)

Three patterns were designed with an increasing packing density of, circles, closed packed circles and hexagons. The circles grid is structurally the strongest and has the lowest packing density. Whereas the packing density of the hexagons is the highest and there is the minimum amount of polymer for the size of the scaffold.

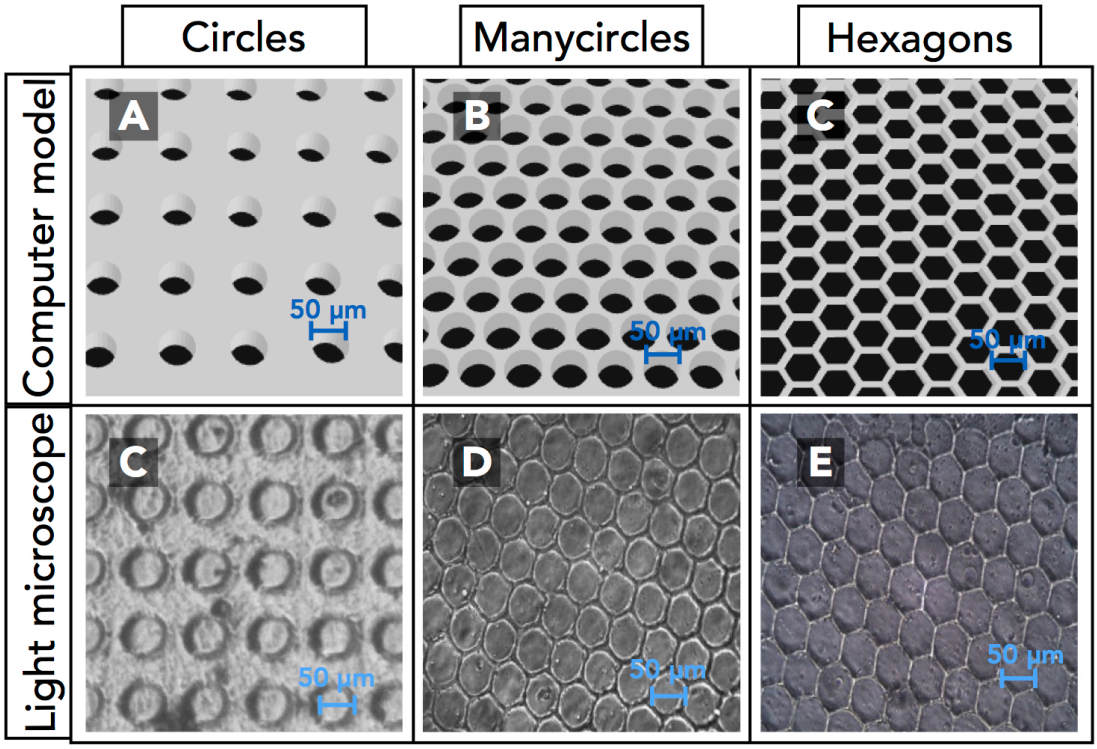

Figure 85: Digital models (A-C) and bright field light microscope images (C-E) of the different patterned grids.

An interesting feature of the patterned grids was that they could be peeled off the glass cover slip surface and scrolled, highlighting the potential useful application as a scrollable injectable scaffold (see Fig 86).

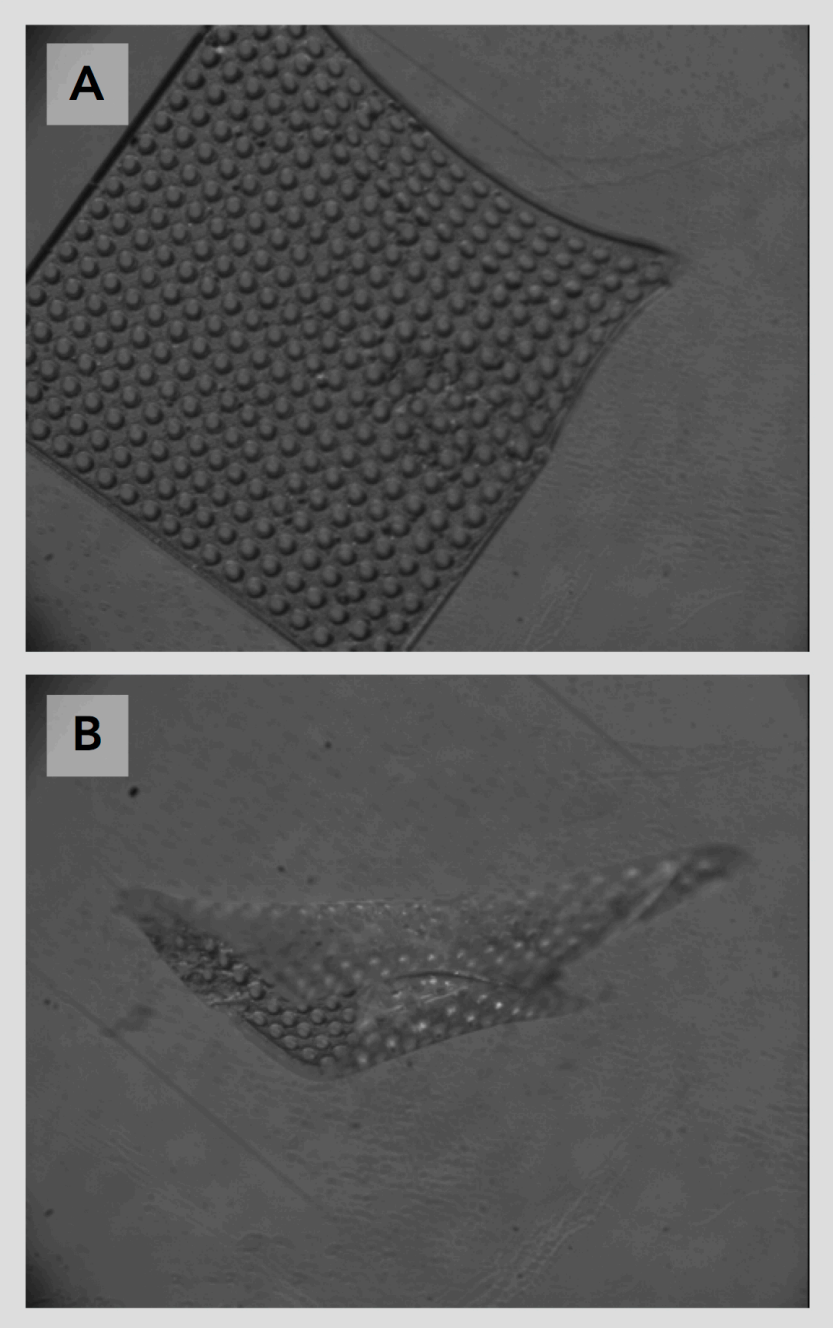

Figure 86: Bright field light microscope images of PGSm grid scaffold being peeled (A) and scrolled (B).

In order to understand the initial biocompatibility of the scaffolds ESC cell viability studies were performed on days 7 and after 1 month of ESC culture on the different scaffolds. Results show that after 7 days of culture there was significantly higher cell viability on the PGSm scaffolds, than on the uncoated glass control (see Fig 87.) After 1 month interestingly results showed

significantly higher viability on the polyHIPE scaffolds (see Fig 88). Overall, viability results showed that cells remained viable on the PGSm scaffolds after one month of culture.

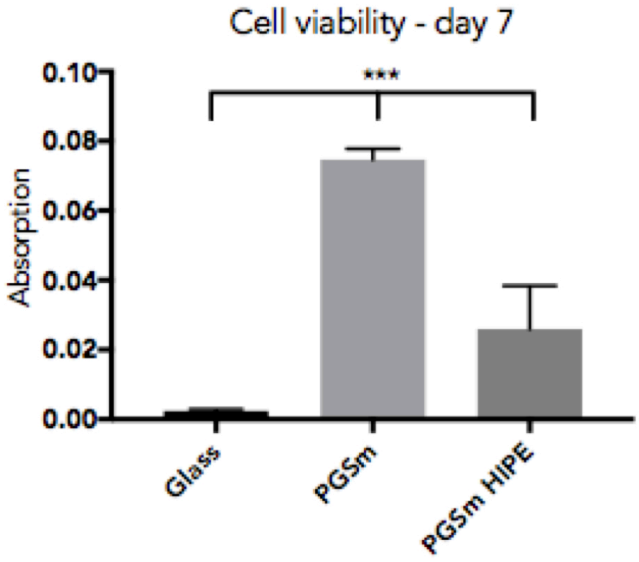

Figure 87: Graph showing cell viability of ESCs cultured onto glass, PGSm flat disks and PGSm polyHIPE after 7 days of culture in nutristem medium. None of the scaffolds were coated with laminin. One-way ANOVA, Tukey was used for statistics. (n=3)

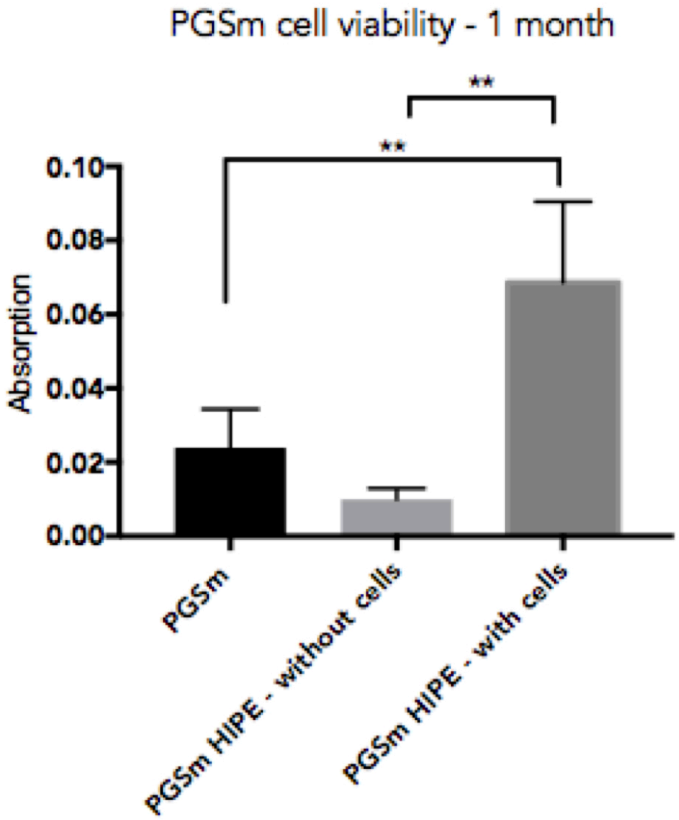

Figure 88: Graph showing cell viability of ESCs after one month of culture on flat PGSm seeded with cells, PGSm polyHIPE without cells and PGSm polyHIPE seeded with cells. One-way ANOVA, Tukey used for statistics (n=2).

ESC morphology was analysed using bright field light microscopy, initially on flat disks of PGSm coated in laminin and then on flat uncoated PGSm. After one week there was no obvious differences in cell morphology (see Fig.89) and therefore all further experiments using PGSm were performed without the use of laminin-521. Using bright field light microscopy the ESCs were visualized migrating to and residing within the pores within the patterned grids (see Fig.90)

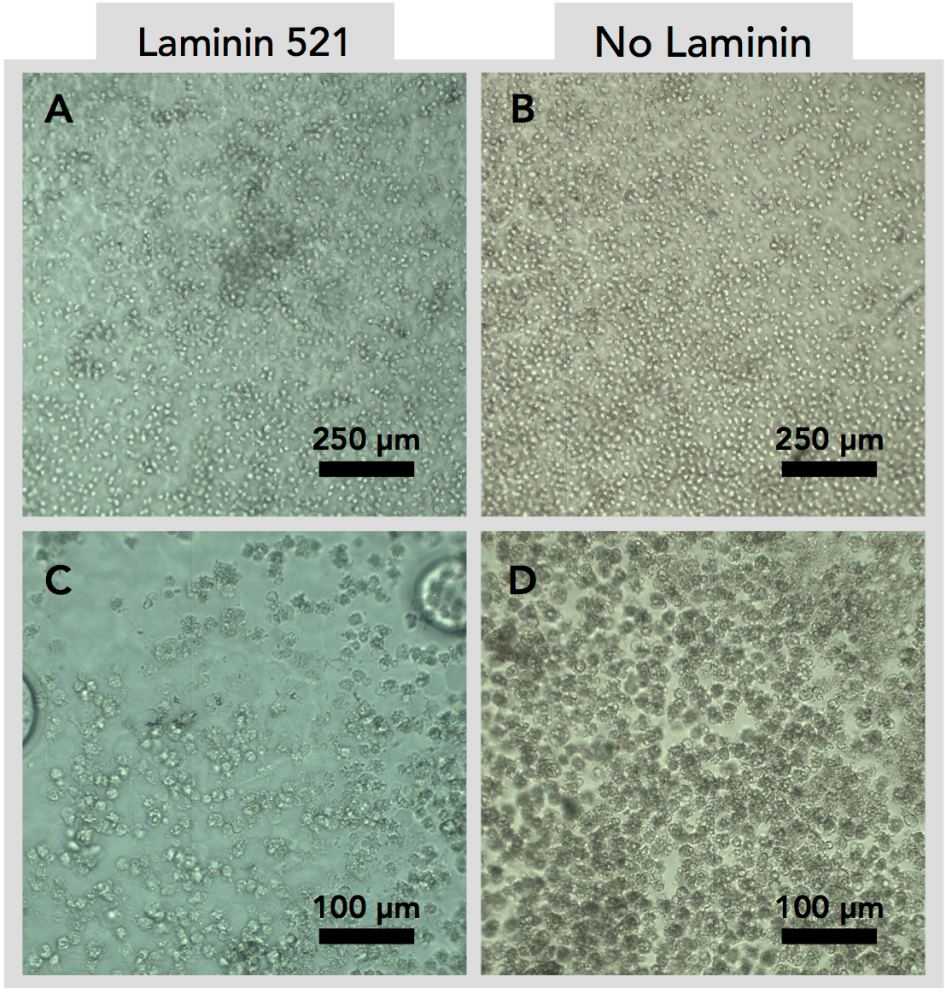

Figure 89: Bright field light microscope images of ESCs cultured onto PGSm flat disks uncoated and coated with laminin.

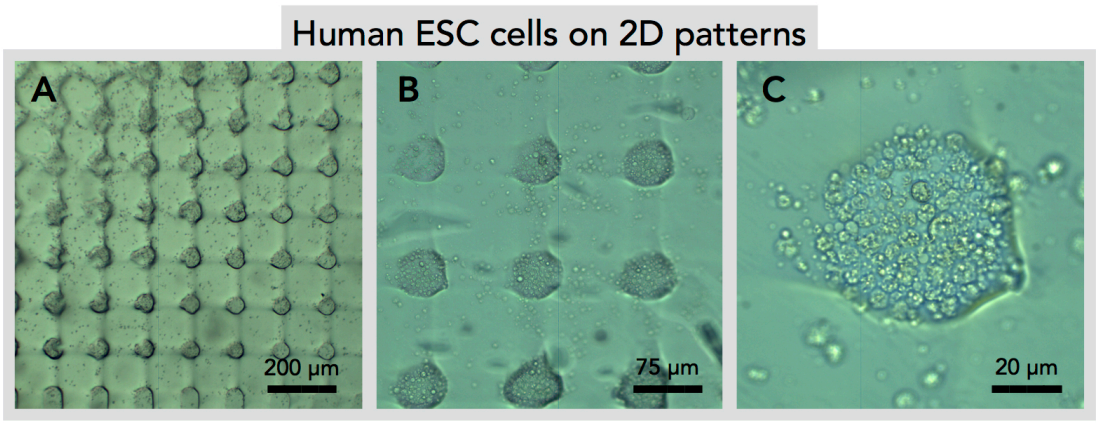

Figure 90: Light microscope image showing ESCs which had migrated within pores within the 2D patterned grid after 7 days of culture

In order to visualize cells within the 3D foam techniques other than bright field light microscopy was required. After 7 days culture, ESCs were labeled with live/dead (Syto-9, propidium iodide) and imaged using an upright confocal microscope. Results revealed few visible dead cells (red), and that it was difficult to differentiate between the polyHIPE foam, which autofluoresced and the live cells. The image was therefore false coloured (cells in blue, PGSm in purple) so ESCs could be easily defined from the PGSm scaffold (see Fig 91). Cells could be seen throughout pores of the porous PGSm polyHIPE.

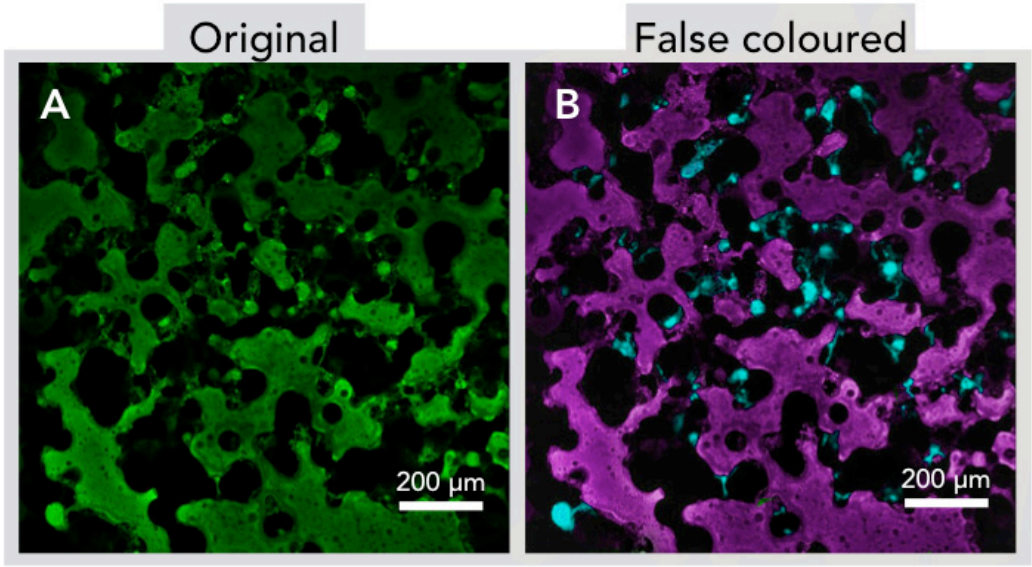

Figure 91: Confocal micrograph, original image, A - false coloured image to highlight cells, B.

ESCs were labeled with antibody Tra-1-85, in order to identify human cells. The results showed that following 7 days culture there were human cells contained within the pores of the polyHIPE. Cells were seen to have a spherical morphology and were witnessed to preferentially reside within the pores, rather than on the surfaces of the PGSm (see Fig 92).

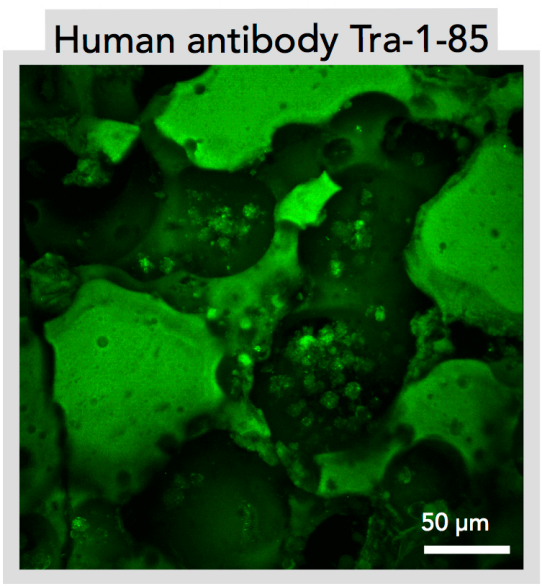

Figure 92: Confocal z-stack micrograph of ESCs labeled with Tra-1-85, within a PGSm polyHIPE foam.

With pluripotency an important consideration for any stem cell scaffold, cells were labeled with the human embryonic pluripotency marker Tra-1-60. Confocal micrographs were then taken of the ESCs following three weeks culture in nutristem, on PGSm without a laminin coating. Cells cultured on flat PGSm disks expressed the pluripotency marker (green) (see Fig 93), with the background showing a flat layer of PGSm (red).

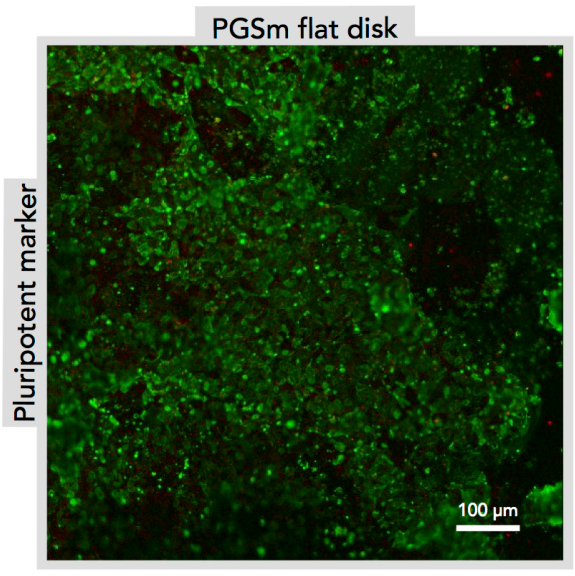

Figure 93: Confocal micrograph of flat PGSm disk seeded with ESCs, cultured for 7 days and labeled with pluripotency marker Tra-1-60 (green), PGSm autofluorescing PGSm (red).

Cells cultured on 2D patterned grids of PGSm were also cultured for three weeks and labeled with the pluripotency marker Tra-1-60. Results show that cells migrated to and preferentially grew within the patterned grids/pockets/niches and that cells expressed the pluripotency marker (green) (see Fig 94).

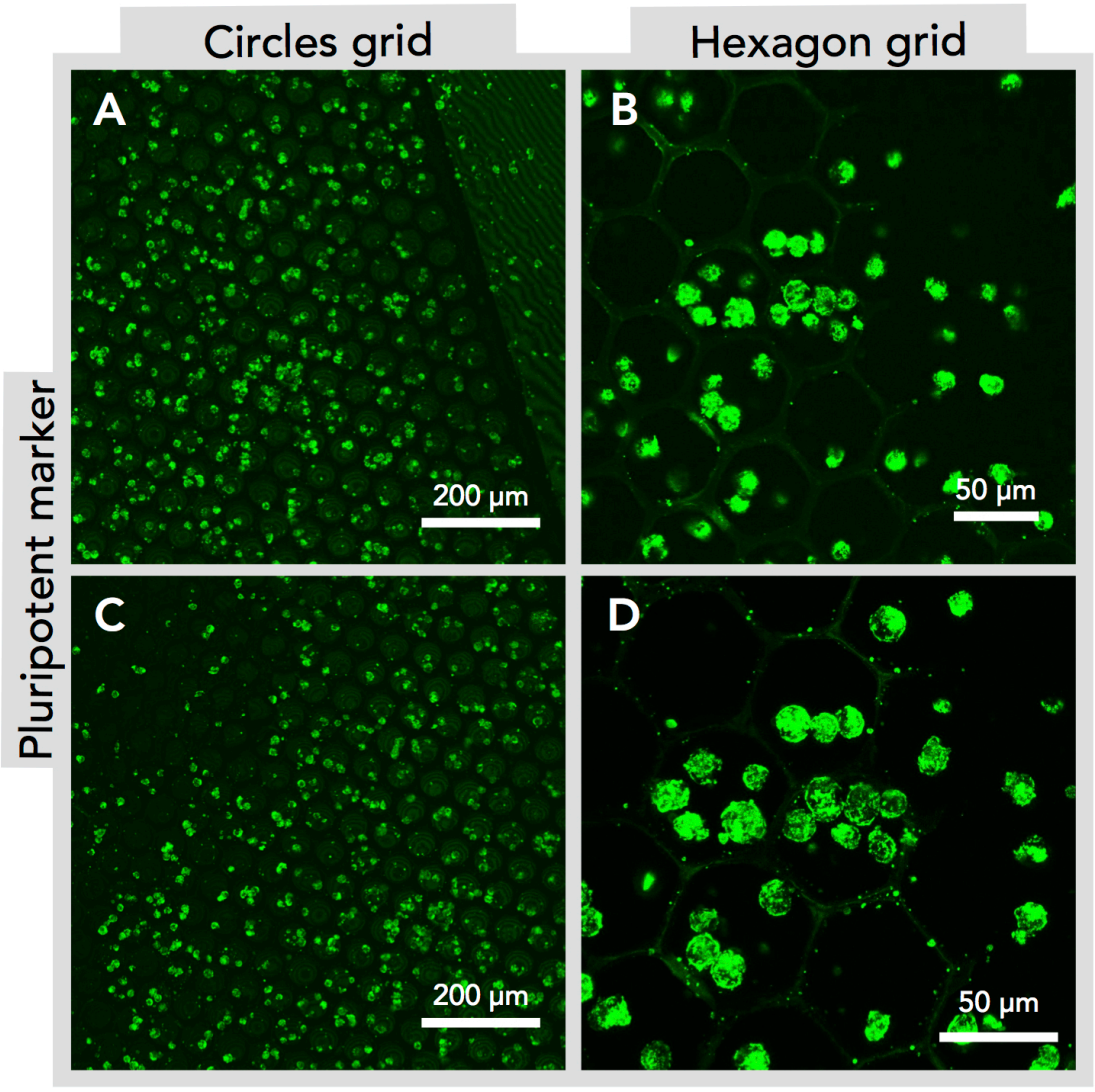

Figure 94: Confocal micrograph of ESCs cultured onto PGSm patterned grids and labeled with pluripotency marker Tra-1-60. A and C are circular pores, whereas B and D are hexagonal.

ESCs were cultured for 3 weeks onto PGSm polyHIPE foam and labeled with the pluripotency marker Tra-1-60. Results from confocal micrograph z-stacks show that ESCs had migrated down into and throughout the pores of the PGSm polyHIPE (red) expressing the pluripotency marker (green) (see Fig 95).

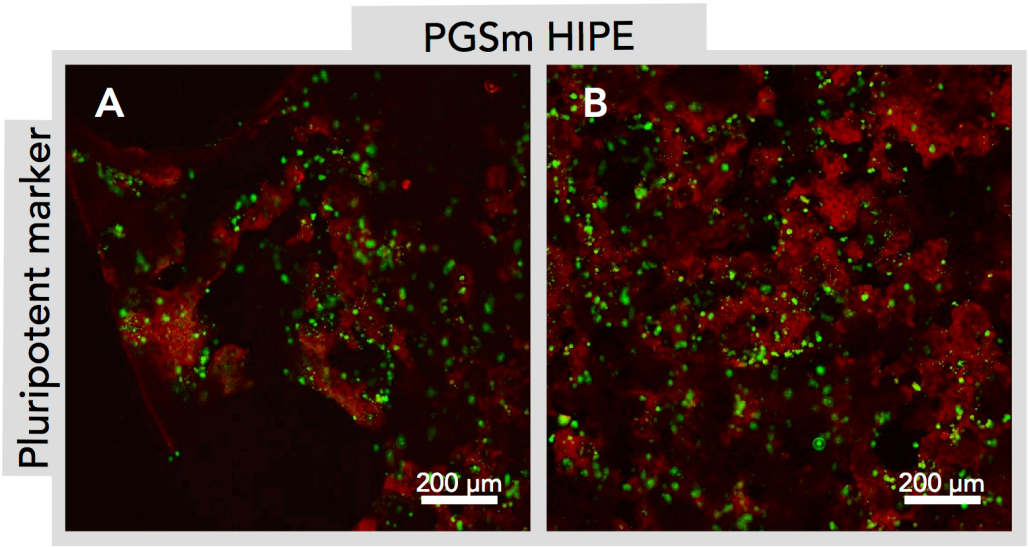

Figure 95: 3D confocal micrograph, showing a z-stack of 3D PGSm polyHIPE cultured for 3 weeks with ESCs and labeled with Tra-1-60 (green)

ESCs were then seeded onto PGSm polyHIPE and cultured, after 10 days the PGSm polyHIPE disk containing cells was frozen. On day 17 the polyHIPE containing cells was thawed and cultured for 24 hours. Cells were labeled with the pluripotency marker tra-1-60, confocal micrograph images show cells after having been frozen, which were contained within PGSm pores (red) expressing the pluripotent marker (green) and maintaining the spherical morphology (see Fig 96.)

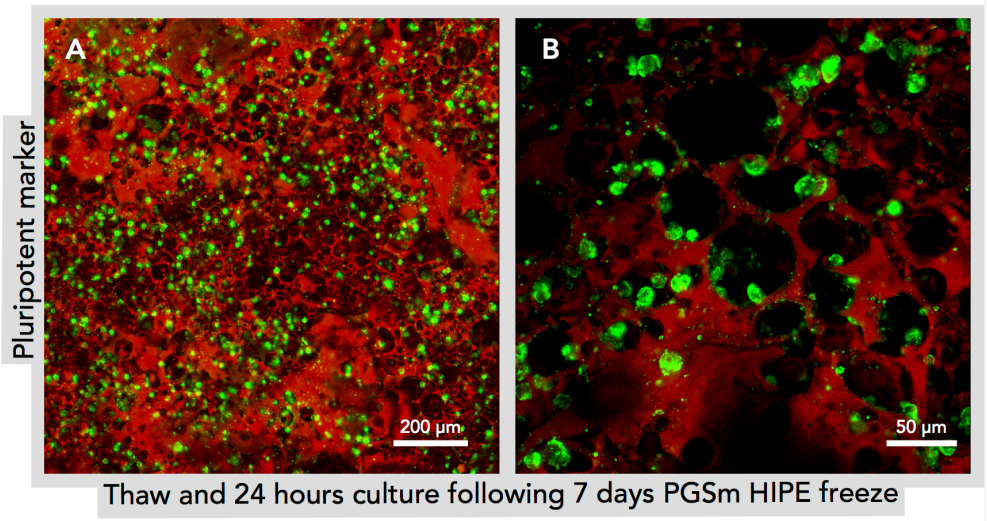

Figure 96: Confocal micrographs showing z-stacks of thawed ESCs expressing the pluripotency marker Tra-1-60, residing within pores of the PGSm polyHIPE (red).

ESCs which were previously cultured, frozen within the polyHIPE and then thawed, were dissociated from within the polyHIPE disk and seeded onto laminin coated TCP, flat PGSm and again onto PGSm polyHIPE. ESCs were cultured for a further 7 days. Cells were labeled once again with the pluripotency marker Tra-1-60, cells expressed the pluripotency marker on all scaffolds/substrates, however on the flat surfaces of TCP and flat PGSm cells had a flattened morphology, whereas on PGSm polyHIPE cells appeared to have a more spherical morphology (see Fig 97.)

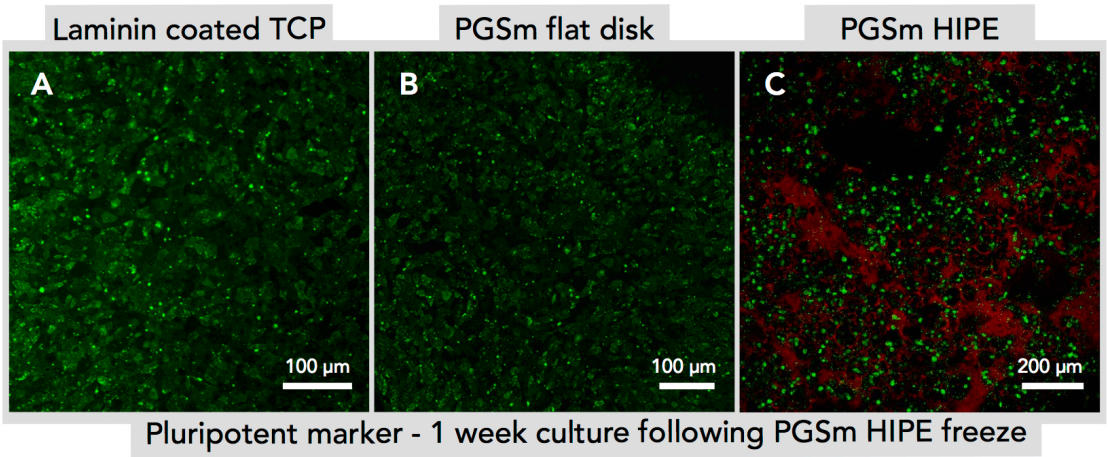

Figure 97: ESCs cultured in PGSm polyHIPE, frozen, thawed, cells dissociated and seeded onto TCP (A), flat PGSm (B) and PGSm polyHIPE (C). Cells labeled with Tra-1-60 (green) and PGSm autofluoresce (red).

Results showed that human ESCs could be cultured onto PGSm whilst maintaining their pluripotency, they preferentially reside within patterned grids/niches and that they could be cultured in 3 dimensions in PGSm polyHIPE (see Fig 98.)

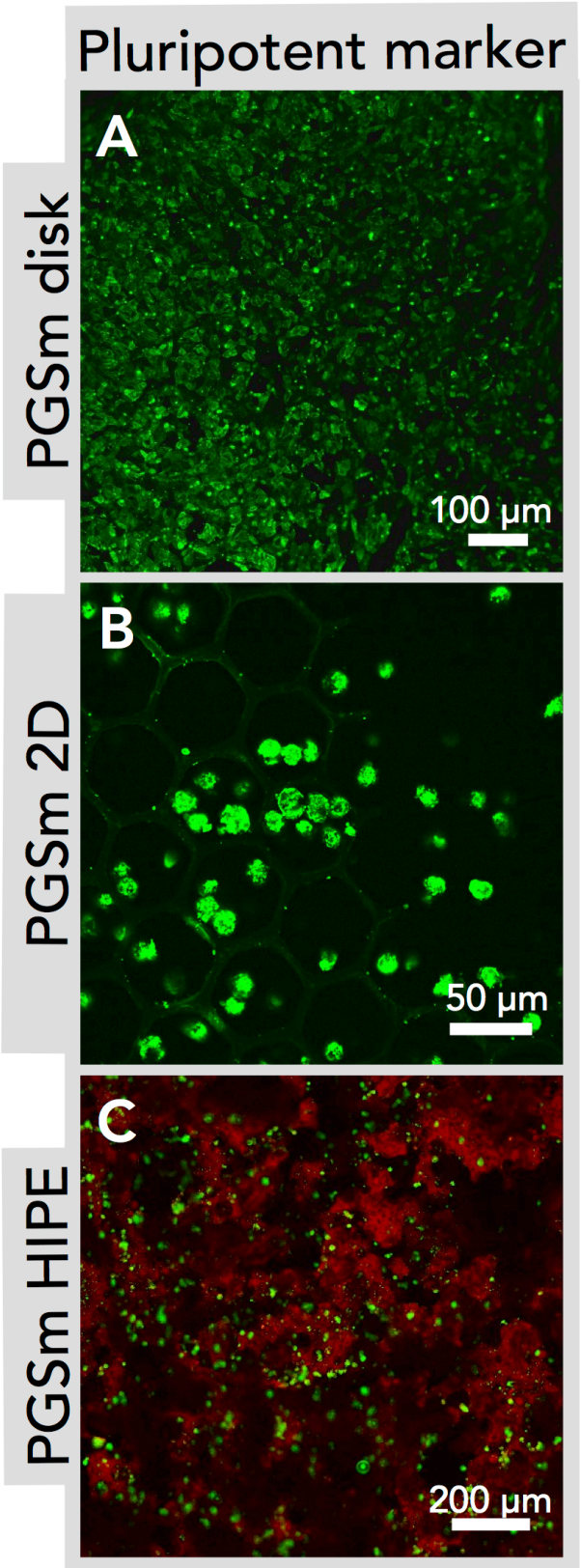

Figure 98: Confocal micrographs of ESCs labeled with Tra-1-60 (green), cultured on flat PGSm (A), patterned PGSm (B), and PGSm polyHIPE foam (C).

4. Discussion

The overall aim of this study chapter was to understand whether PGSm could be a suitable material for use as a scaffold in ESC culture, and to begin to explore the potential applications for the scaffolds, in both 2D and 3D.

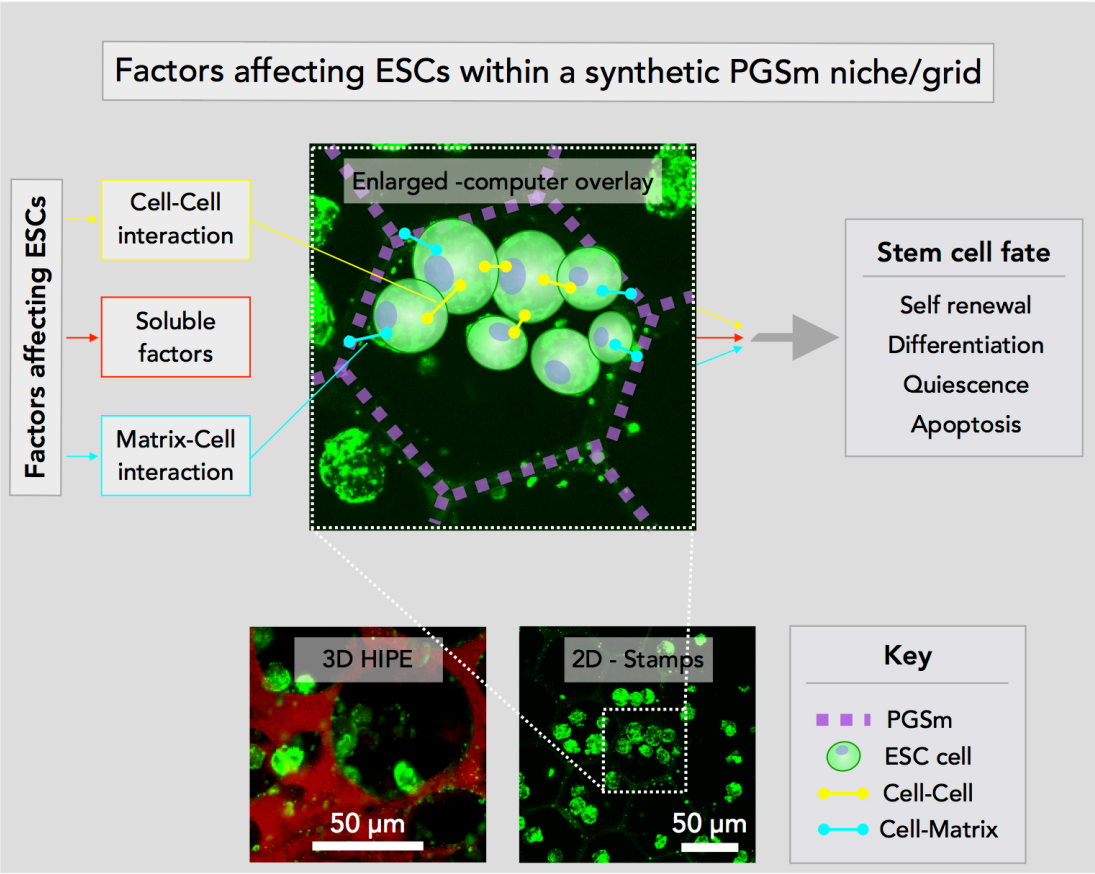

Figure 99: Diagram showing ESCs within pores of 3D HIPE and 2D stamps/grids and describing the factors which affect them and their cell fate. (Keynote, Apple)

There are three main considerations that affect stem cells during *in vitro* and *in vivo* culture, these are cell-cell interactions, soluble factors and matrix-cell interactions (see Fig 99)[201]. In this study soluble factors are kept to a minimum and all experiments were performed using Nutristem medium, which is well known to promote the maintenance of pluripotency. The confinement of cells within pores in both the 2D patterned and 3D HIPE scaffolds may increase cell-cell interactions. The main area of interest for this study was the

interaction between ESCs and PGSm/cell-matrix interactions and how the material can affect the stem cell fate. Two ways the material interacts with the ESCs is through the structure of the PGSm scaffolds and the stiffness of the PGSm. In this study the stiffness of the material is kept constant and therefore will be briefly addressed towards the end of this discussion. The structure of the PGSm had three forms flat disks, 2D patterns and 3D HIPEs.

Initial work started on flat disks of PGSm seeded with ESCs. These initial studies showed that ESCs were readily able to proliferate on the surface of the PGSm, which interestingly wasn't coated in laminin 521. This was an important finding as laminin coating is expensive and time consuming. Further studies compared microscope images of ESCs seeded onto laminin coated and uncoated PGSm, morphological results showed no obvious difference in the cells when coated on either surface (see Fig 89). For this reason all further polymer studies were performed on uncoated PGSm scaffolds.

Cultures of stem cells in 2D have been well documented in literature, however, there has been little research into patterned 2D ESC cultures or cultures of ESCs within a synthetic niche. One study explored confining hESCs within a geometric ring, with results showing hESCs self-organizing into early embryonic spatial patterns[202], indicating that geometrical patterns/structure may have a distinct impact on cell fate. Scaffolds in this chapter/study were patterned into grids/patterns forcing cells into a confined area, similar to what would occur within a stem cell niche. Cells were suspended in medium and seeded onto the patterned grids, ESCs were observed to preferentially migrate within the patterned pores (see Fig 90). After three weeks of culture ESCs were confined within the patterned pores and expressed the

pluripotency marker Tra-1-60. Literature indicates that Tra-1-60 is expressed by all known human pluripotent stem cells[203], this suggested that the ESCs had maintained their pluripotency (see Fig 94). When comparing the 2D patterned scaffolds with the flat PGSm disks it can be seen that after three weeks ESCs within both scaffolds expressed Tra-1-60. The morphology of the cells on the flat disks however was different from the patterned grids. On the flat PGSm disks ESCs had reached far higher levels of confluency and appeared flattened and less spherical, whereas cells within the grids ESCs were sparser and were separated into the pores in small groups of cells (see Figs 93 and 94). It may therefore be postulated that ESCs on the flat PGSm were undergoing a state of self renewal/replication. Whereas pluripotency, distribution of sparse groups of cells and long term survival of ESCs on the patterned grids may suggest ESCs had reached a state of quiescence. ESCs on flat PGSm disks may have had to replicate and become confluent before cell-cell interactions occurred, this may have affected the cells as can be seen by the flattened, less rounded morphology. Whereas cells within the patterned grids preferentially migrated to within the pores where cell-cell interaction was forced by the pore confinement. As quiescence is a common feature of the niche it can be understood that the 2D patterned grids may interact with the ESCs like a synthetic stem cell niche.

Similar findings were observed with ESCs cultured onto 3D polyHIPE scaffolds. Cells were sparsely distributed in groups of cells amongst the 3D pores and after three weeks of culture expressed the pluripotent marker tra-1-60 (see Fig 95). This indicates that the ESCs maintain their pluripotency when cultured in 3D. Also the long term survival, confluency and distribution of cells may again indicate that the cells have reached a state of quiescence. This can be useful as it may now be possible to model ESC cultures and their behavior

in 2D and 3D synthetic PGSm niches. Furthermore, a state of quiescence may be useful for implantation into the body, whereby physiological cues from surrounding tissues once implanted may promote appropriate differentiation.

Implantation studies are possible using PGSm scaffolds seeded with ESCs. 2D patterned scaffolds provide pores within which ESCs can be seeded. The patterned stamps/grids are designed so the whole 2D pattern/grid can be scrolled and injected as a scaffold seeded with stem cells with cells within the pores being protected from some of the shear stresses during implantation (see Fig 86). This unlocks the potential for many different applications where treatment requires stem cells to be implanted locally, such as within the retina[204]. Also stem cells can be implanted seeded within 3D porous polyHIPE foam. This would enable cells to be implanted across a larger volume and the porous nature may help with common problems found in large 3-dimensional scaffolds, such as vascularisation. Whilst these applications are yet to be fully explored with PGSm, the potential uses for the 2D patterned and 3D polyHIPE PGSm scaffolds is clear.

It has been assumed from the ESCs maintaining their pluripotency, the level of confluency and the long term cell survival that the ESCs might have reached a state of quiescence within the 2D patterns and 3D polyHIPE PGSm scaffolds. This may be due to the structural cues from the patterns/polyHIPE however literature has also shown that the material stiffness can often impact the stem cell fate with softer substrates determining self renewal, and pluripotency[205,206], whereas harder materials often determine differentiation and cell growth[207,208]. Studies in bone marrow derived mesenchymal stem cells also showed that soft materials promoted quiscence[209]. The soft nature of PGSm may therefore explain why ESCs on scaffolds expressed pluripotency,

however, the structural cues provided by the 2D patterns and 3D PGSm polyHIPE may have promoted quiescence. It can therefore be concluded that the suspected quiescence exhibited by the ESCs is promoted by a combination of the soft PGSm and the structural cues from the 2D patterns and 3D PGSm polyHIPE.

3D polyHIPE PGSm scaffolds have already shown that they may be useful as a scaffold for cell storage as they don't require laminin coating and promote quiescence in the ESCs. Further experiments showed that ESCs could be seeded within the PGSm polyHIPE foam, the foam and cells frozen and stored in liquid nitrogen. When the foam and cells were thawed confocal images showed that cells had survived, were still evenly distributed within the polyHIPE and ESCs had maintained their pluripotency. The ESCs were then dissociated from the polyHIPE foam, seeded onto flat laminin coated TCP, flat PGSm and PGSm polyHIPE foam and cultured for a further 7 days. Results suggest that cells acted no differently to how they behaved before being frozen, ESCs maintained pluripotency, ESCs on the flat TCP and PGSm surfaces replicated with morphology becoming flattened and cells reaching confluency, and ESCs within the PGSm polyHIPE were well distributed within the 3D pores. This highlights potential use of PGSm polyHIPE as a scaffold for ESC storage. Some of the confocal micrographs obtained in this research included only pluripotent markers, future experiments should also include markers for non-pluripotent cells. This would allow an estimation of the percentage of cells which maintain their pluripotency. Also some experiments in this section only had n=2, for further validity duplicate experiments are required.

5. Conclusion

This chapter explored flat, 2D patterned and 3D polyHIPE PGSm for use as a stem cell scaffold. 2D scaffolds created were highly accurate, reproducible and scrollable for injectable implantation. 3D scaffolds were highly porous and interconnected. ESCs cultured on PGSm maintained pluripotency, this may be due to the soft modulus of PGSm. ESCs preferentially migrated within the 2D patterned pores, allowing for the 2D modeling of stem cell niches or the protected implantation of stem cells to a local tissue. 3D polyHIPE scaffolds enabled a 3D culture of ESCs, distributed well within the foam, allowing for 3D ESC models or further implantation potential. Suspected quiescence observed in 3D scaffolds, and the ability to freeze and thaw cells without damage highlights the potential for polyHIPE PGSm scaffolds to be used for ESC storage.

To conclude, the novel formulation PGSm offers a useful scaffold for stem cell cultures both in 2D and 3D allowing for many application possibilities.

4. CONCLUSIONS AND FUTURE WORK

This project reports upon the findings made from the developments of the novel formulation PGSm and its use in soft tissue applications with a focus on peripheral nerve repair. This conclusion addresses the projct aims and discusses potential future work.

The first aim of the project was to develop the photocurable polymer PGSm, characterizing it chemically and mechanically. Polymer analysis results highlighted the appropriateness of the photocurable material to be used in many soft tissue applications. The polymer maintained many of the beneficial properties of PGS, whilst also possessing the ability to be patterned and structured into highly accurate 2D and 3D scaffolds.

The second aim addressed the ability to structure the polymer into a 3D scaffold/foam appropriate for 3D tissue culture. Techniques were explored to develop PGSm into 3D porous polyHIPEs, which could be rapidly produced with a tunable porosity. The porous nature of the scaffolds, the scaffold biocompatibility and the ability to be 3D printed/photocured into complex scaffolds, make PGSm polyHIPEs a very appropriate scaffold for soft tissue repair.

A further aim set out to analyze the appropriateness of the material for use in nerve guidance conduits. The polymer was therefore explored in detail and performed well *in vitro, ex vivo* and *in vivo.* There was no increased toxicity on the PGSm polymer; *ex vivo* DRG studies highlighted how internal topographical grooves within the lumen beneficially directed aligned neurite

and Schwann cell growth, and *in vivo* studies showed axonal regeneration across the injury gap, through the PGSm NGC and into the distal stump. In this study a mouse model was used, it was hypothesized that within larger models, and looking towards human applications, the diffusion of nutrients within the conduit may become a concern/limiting factor.

As diffusion of nutrients was understood to be a limiting factor, a further aim was to produce porous NGCs using PGSm polyHIPE. 3D printing and casting techniques were explored to develop the reproducible 3D porous PGSm NGCs. *In vitro* studies demonstrated the ability of Schwann cells to migrate throughout the porous polymer network and *ex vivo* studies showed the outgrowth of neurites and Schwann cells from a DRG body and into the porous PGSm NGC. Results indicate that the PGSm polyHIPE conduits may be appropriate in aiding nutrient diffusion in larger gap injuries.

The fifth aim of this project was to develop tunable 3D porous polyHIPE microparticles for the potential use as injectable scaffolds for cartilage repair. Primary bovine chondrocytes were cultured *in vitro* and seeded onto the microparticles. The chondrocytes quickly migrated within the particles and begun to produce large amounts of ECM/collagen which over time aggregated the microparticles into a particle-tissue disk. Compressive mechanical testing was performed on both the bulk porous polymer and the particle-tissue disk following culture, interestingly both had modulus values similar to native cartilage. Histology, IHC labeling and quantitative-GaG assays were performed which showed the presence of GaGs and collagen-II, key components of cartilage ECM. The microparticles provided an appropriate 3D microenvironment for the development of cartilage like tissue,

which was imaged using histology, IHC z-stack confocal imaging, SEM and microCT.

A further aim of the project was to explore the material for use as a 3D tissue-engineered neuronal model. PGSm polyHIPE disks were used as a scaffold for the development of the 3D neuronal model. Initial studies showed the ability of neuroprogenitors to be cultured in 3D within the porous networks. Studies then moved onto neuroblastoma cells, which were cultured in 3D and treated with a drug and/or gamma radiation, to replicate treatment methods used in humans. The results of the drug/radiation study were inconclusive however the study did highlight the potential use of PGSm as a 3D scaffold for the development of a neuronal model.

The final aim of the project was to explore the use of 2D patterned and 3D polyHIPE PGSm scaffolds for ESC culture. Results showed that ESCs migrated preferentially within the 2D patterned pores, which forced cells together similar to within a stem cell niche. ESCs were also cultured onto the 3D polyHIPE and cells were observed to migrate within the polymer network, with long-term cultures being performed in 3D. IHC labeling determined that ESCs maintained their pluripotency throughout 2D and 3D cultures. ESCs were also frozen in polyHIPE scaffolds and stored, thawed and could be dissociated when ready for use. Cells again maintained their pluripotency, highlighting the storage capabilities of ESCs within polyHIPE PGSm.

Future work

The main focus of this project was to develop the 3D printable novel formulation of the soft biomaterial PGSm for peripheral nerve repair. This was done in detail with very promising results. Future studies would focus upon

larger animal models and further developing complex conduit designs. The conduit designs could develop upon the porous conduits produced within this study, could introduce more complex intra-luminal features or a combination of the both to enhance the ability of the conduits to allow regeneration across larger injury gaps.

The development of PGSm into a 3D porous polyHIPE with tunable features and the ability to be 3D printed, opens up the scaffold to may potential applications. The porous scaffolds could be used for a range of soft tissue applications with the porosity being beneficial for potential vascularization within the scaffold. Current studies for cartilage repair show huge promise and the next logical step would be testing with *in vivo* animal models. The injectable porous and degradable microparticles would also be suited for many other soft tissue engineering applications. Studies into the use as a neuronal model highlight the potential for the polymer to be used as a scaffold to help develop 3D models to mimic physiological disorders and treatments. Finally, work into ESC cultures could be developed to understand how biologically the cells interact with the patterned grids, to further understand how they develop in 3D polyHIPE cultures and to explore whether 3D cultures of ESCs could be promoted to differentiate as required.

REFERENCES

1. Parey, Coates, A. *The workes of that famous chirurgion Ambrose Parey by Pare, Ambroise: Th: Cotes and R. Young, London*. (1634).
2. O'Brien, F. J. Biomaterials & scaffolds for tissue engineering. *Mater. Today* **14,** 88–95 (2011).
3. Vacanti, C. A. The history of tissue engineering. *J. Cell. Mol. Med.* **10,** 569–76
4. Maienschein, J. Regenerative medicine's historical roots in regeneration, transplantation, and translation. *Dev. Biol.* **358,** 278–284 (2011).
5. Katari, R., Peloso, A. & Orlando, G. Tissue engineering and regenerative medicine: semantic considerations for an evolving paradigm. *Front. Bioeng. Biotechnol.* **2,** 57 (2014).
6. Wong, J. Y., Bronzino, J. D. & Peterson, D. R. *Biomaterials : principles and practices*. (Taylor & Francis, 2013).
7. Roberts, J. D. & Caserio, M. C. *Basic principles of organic chemistry*. (W.A. Benjamin, 1977).
8. Fried, J. R. *Polymer science and technology*.
9. Sperling, L. H. (Leslie H. *Introduction to physical polymer science*. (Wiley, 2006).
10. Donovan, B. R. & Patton, D. L. in *Encyclopedia of Polymeric Nanomaterials* 1–7 (Springer Berlin Heidelberg, 2014). doi:10.1007/978-3-642-36199-9_412-1
11. Seymour, R. B. (Raymond B., Deanin, R. D. & American Chemical Society. Meeting (192nd : 1986 : Anaheim, C. . *History of polymeric composites*. (VNU Science Press, 1987).
12. Crivello, J. V & Reichmanis, E. Photopolymer Materials and Processes for Advanced Technologies. doi:10.1021/cm402262g
13. O'Toole, M. T. *Mosby's medical dictionary*. (Elsevier/Mosby, 2013).
14. Pagliaro, M., Rossi, M. & Royal Society of Chemistry (Great Britain). *The future of glycerol*. (RSC Pub, 2010).
15. Sebacic Acid -Production Process,Properties, Applications and Uses - CastorOil.in. Available at: http://www.castoroil.in/castor/castor_seed/castor_oil/sebacic_acid/sebacic_acid.html. (Accessed: 28th March 2017)
16. Desai, S. D., Emanuel, A. L. & Sinha, V. K. Biomaterial Based Polyurethane Adhesive

for Bonding Rubber and Wood Joints. *J. Polym. Res.* **10,** 275–281 (2003).

17. Kind, S. *et al.* From zero to hero – Production of bio-based nylon from renewable resources using engineered Corynebacterium glutamicum. *Metab. Eng.* **25,** 113–123 (2014).
18. Wang, Y., Ameer, G. A., Sheppard, B. J. & Langer, R. A tough biodegradable elastomer. *Nat. Biotechnol.* **20,** 602–6 (2002).
19. Nagata, M., Machida, T., Sakai, W. & Tsutsumi, N. Synthesis, characterization, and enzymatic degradation of network aliphatic copolyesters. *J. Polym. Sci. Part A Polym. Chem.* **37,** 2005–2011 (1999).
20. Nagata, M., Kiyotsukuri, T., Ibuki, H., Tsutsumi, N. & Sakai, W. Synthesis and enzymatic degradation of regular network aliphatic polyesters. *React. Funct. Polym.* **30,** 165–171 (1996).
21. Rai, R., Tallawi, M., Grigore, A. & Boccaccini, A. R. Synthesis, properties and biomedical applications of poly(glycerol sebacate) (PGS): A review. *Prog. Polym. Sci.* **37,** 1051–1078 (2012).
22. Legnani, F. G. *et al.* Lactacystin exhibits potent anti-tumor activity in an animal model of malignant glioma when administered via controlled-release polymers. *J. Neurooncol.* **77,** 225–32 (2006).
23. Nijst, C. L. E. *et al.* Synthesis and characterization of photocurable elastomers from poly(glycerol-co-sebacate). *Biomacromolecules* **8,** 3067–73 (2007).
24. Gerecht, S. *et al.* A porous photocurable elastomer for cell encapsulation and culture. *Biomaterials* **28,** 4826–4835 (2007).
25. Zhang, X., Jia, C., Qiao, X., Liu, T. & Sun, K. Porous poly(glycerol sebacate) (PGS) elastomer scaffolds for skin tissue engineering. *Polym. Test.* **54,** 118–125 (2016).
26. Theerathanagorn, T. *et al. In vitro* human chondrocyte culture on plasma-treated poly(glycerol sebacate) scaffolds. *J. Biomater. Sci. Polym. Ed.* **26,** 1386–1401 (2015).
27. Frydrych, M. & Chen, B. Large three-dimensional poly(glycerol sebacate)-based scaffolds – a freeze-drying preparation approach. *J. Mater. Chem. B* **1,** 6650 (2013).
28. Frydrych, M., Román, S., MacNeil, S. & Chen, B. Biomimetic poly(glycerol sebacate)/poly(l-lactic acid) blend scaffolds for adipose tissue engineering. *Acta Biomater.* **18,** 40–49 (2015).
29. Rai, R. *et al.* Biomimetic poly(glycerol sebacate) (PGS) membranes for cardiac patch application. *Mater. Sci. Eng. C. Mater. Biol. Appl.* **33,** 3677–87 (2013).
30. Chen, Q.-Z. *et al.* Characterisation of a soft elastomer poly(glycerol sebacate)

designed to match the mechanical properties of myocardial tissue. *Biomaterials* **29,** 47–57 (2008).

31. Gao, J., Crapo, P. M. & Wang, Y. Macroporous Elastomeric Scaffolds with Extensive Micropores for Soft Tissue Engineering. *Tissue Eng.* **12,** 917–925 (2006).
32. Wang, J., Bettinger, C. J., Langer, R. S. & Borenstein, J. T. Biodegradable microfluidic scaffolds for tissue engineering from amino alcohol-based poly(ester amide) elastomers. *Organogenesis* **6,** 212–6
33. Sundback, C. A. *et al.* Behavior of poly(glycerol sebacate) plugs in chronic tympanic membrane perforations. *J. Biomed. Mater. Res. B. Appl. Biomater.* **100,** 1943–54 (2012).
34. Pritchard, C. D. *et al.* The use of surface modified poly(glycerol-co-sebacic acid) in retinal transplantation. *Biomaterials* **31,** 2153–62 (2010).
35. Sundback, C. A. *et al.* Biocompatibility analysis of poly(glycerol sebacate) as a nerve guide material. *Biomaterials* **26,** 5454–64 (2005).
36. Engelmayr, G. C. *et al.* Accordion-like honeycombs for tissue engineering of cardiac anisotropy. *Nat. Mater.* **7,** 1003–10 (2008).
37. Wu, W., Allen, R. A. & Wang, Y. Fast-degrading elastomer enables rapid remodeling of a cell-free synthetic graft into a neoartery. *Nat. Med.* **18,** 1148–53 (2012).
38. Redenti, S. *et al.* Engineering retinal progenitor cell and scrollable poly(glycerol-sebacate) composites for expansion and subretinal transplantation. *Biomaterials* **30,** 3405–3414 (2009).
39. Marsano, A. *et al.* Scaffold stiffness affects the contractile function of three-dimensional engineered cardiac constructs. *Biotechnol. Prog.* **26,** 1382–90
40. Pomerantseva, I. *et al.* Degradation behavior of poly(glycerol sebacate). *J. Biomed. Mater. Res. A* **91,** 1038–47 (2009).
41. Takemura, R. & Werb, Z. Secretory products of macrophages and their physiological functions. *Am. J. Physiol.* **246,** C1-9 (1984).
42. Seyednejad, H. *et al.* In vivo biocompatibility and biodegradation of 3D-printed porous scaffolds based on a hydroxyl-functionalized poly(ε-caprolactone). *Biomaterials* **33,** 4309–18 (2012).
43. Jeffries, E. M., Allen, R. A., Gao, J., Pesce, M. & Wang, Y. Highly elastic and suturable electrospun poly(glycerol sebacate) fibrous scaffolds. *Acta Biomater.* **18,** 30–39 (2015).
44. Rai, R. *et al.* Bioactive Electrospun Fibers of Poly(glycerol sebacate) and Poly(ε-

caprolactone) for Cardiac Patch Application. *Adv. Healthc. Mater.* **4,** 2012–2025 (2015).

45. Lissant, K. in *Emulsions and emulsion technology. Vol 3* (CRC Press, 1974).
46. Cameron, N. R. & Sherrington, D. C. High Internal Phase Emulsions (HIPEs)- Structure, Properties and Use in Polymer Preparation.
47. Kabalnov, A. S. & Shchukin, E. D. Ostwald ripening theory: applications to fluorocarbon emulsion stability. *Adv. Colloid Interface Sci.* **38,** 69–97 (1992).
48. Pal, R. Techniques for measuring the composition (oil and water content) of emulsions — a state of the art review. *Colloids Surfaces A Physicochem. Eng. Asp.* **84,** 141–193 (1994).
49. Lissant, K. J. The Geometry of High-Internal-Phase-Ratio Emulsions. *J. Colloid Interface Sci.* **22,** 6–2 (1966).
50. Manley, S. S. *et al.* New insights into the relationship between internal phase level of emulsion templates and gas–liquid permeability of interconnected macroporous polymers. *Soft Matter* **5,** 4780 (2009).
51. Silverstein, M. S. Emulsion-templated porous polymers: A retrospective perspective. *Polymer (Guildf).* **55,** 304–320 (2014).
52. Menner, A. & Bismarck, A. New Evidence for the Mechanism of the Pore Formation in Polymerising High Internal Phase Emulsions or Why polyHIPEs Have an Interconnected Pore Network Structure. *Macromol. Symp.* **242,** 19–24 (2006).
53. Lumelsky, Y., Lalush-Michael, I., Levenberg, S. & Silverstein, M. S. A degradable, porous, emulsion-templated polyacrylate. *J. Polym. Sci. Part A Polym. Chem.* **47,** 7043–7053 (2009).
54. Permeable Supports Selection Guide Including Transwell® and Falcon® Cell Culture Inserts About Corning ® Permeable Supports Create a More Natural Environment for Your Cells Transwell® Permeable Supports: a Laboratory Standard.
55. Noble, J., Munro, C. A., Prasad, V. S. & Midha, R. Analysis of upper and lower extremity peripheral nerve injuries in a population of patients with multiple injuries. *J. Trauma* **45,** 116–122 (1998).
56. Mohanna, P. N., Young, R. C., Wiberg, M. & Terenghi, G. A composite pol-hydroxybutyrate-glial growth factor conduit for long nerve gap repairs. *J. Anat.* **203,** 553–565 (2003).
57. Leach, J. B. in *Encyclopedia of Biomedical Engineering* (2006).
58. Clark, W. E. L. G. & Durward, A. *The anatomy of the nervous system: central nervous*

system, peripheral nervous system, autonomic nervous system. (Oxford University Press, 1956).

59. Bobick, J. & Balaban, N. *The Handy Anatomy Answer Book*. (Visible Ink Press, 2008).
60. Madura, T. Pathophysiology of Peripheral Nerve Injury. (1995).
61. Brushart, T. M. & MD. *Nerve Repair (Google eBook)*. (Oxford University Press, 2011).
62. The Myelin Sheath. (1999).
63. Fu, S. Y. & Gordon, T. The cellular and molecular basis of peripheral nerve regeneration. *Mol. Neurobiol.* **14,** 67–116
64. Ichihara, S., Inada, Y. & Nakamura, T. Artificial nerve tubes and their application for repair of peripheral nerve injury: an update of current concepts. *Injury* **39 Suppl 4,** 29–39 (2008).
65. Zochodne, D. W. *Neurobiology of Peripheral Nerve Regeneration*. (Cambridge University Press, 2008). doi:10.1017/CBO9780511541759
66. Schmidt, C. E. & Leach, J. B. Neural tissue engineering: strategies for repair and regeneration. *Annu. Rev. Biomed. Eng.* **5,** 293–347 (2003).
67. Scheib, J. & Höke, A. Advances in peripheral nerve regeneration. *Nat. Rev. Neurol.* **9,** 668–76 (2013).
68. Harrisingh, M. C. *et al.* The Ras/Raf/ERK signalling pathway drives Schwann cell dedifferentiation. *EMBO J.* **23,** 3061–71 (2004).
69. Sousanis, J. World Vehicte Population Tops 1 Billion Units. (2011). Available at: https://secure5.easyasphosting.com/dallasmobility-org/Reports/VehiclePopulation.PDF. (Accessed: 14th June 2014)
70. Woodhall, B. & Beebe, G. W. Peripheral Nerve Regeneration. A Follow-up Study of 3,656 World War II Injuries. (1956).
71. *Textbook of Small Animal Orthopaedics*. (Lippincott, 1985).
72. Joseph. D Bronzino, D. R. P. *The Biomedical Engineering Handbook, Third Edition: Biomedical Engineering Fundamentals*. (CRC Press; 3 edition, 2006).
73. Belkas, J. S., Shoichet, M. S. & Midha, R. Peripheral nerve regeneration through guidance tubes. *Neurol. Res.* **26,** 151–60 (2004).
74. Bellamkonda, R. V. Peripheral nerve regeneration: an opinion on channels, scaffolds and anisotropy. *Biomaterials* **27,** 3515–8 (2006).
75. Bryan, B. M., Lutz, G. E. & O'Brien, S. J. Sural nerve entrapment after injury to the gastrocnemius: a case report. *Arch. Phys. Med. Rehabil.* **80,** 604–6 (1999).
76. Martins, R. S. *et al.* Morbidity following sural nerve harvesting: a prospective study.

Clin. Neurol. Neurosurg. **114,** 1149–52 (2012).

77. Battiston, B., Geuna, S., Ferrero, M. & Tos, P. Nerve repair by means of tubulization: literature review and personal clinical experience comparing biological and synthetic conduits for sensory nerve repair. *Microsurgery* **25,** 258–67 (2005).
78. Taras, J. S., Nanavati, V. & Steelman, P. Nerve conduits. *J. Hand Ther.* **18,** 191–7
79. Gluck, T. *Ueber Neuroplastik auf dem Wege der Transplantation. – gebraucht kaufen bei booklooker – jetzt online bestellen - A01t401B01ZZR*. (1880).
80. Ochs, S. The early history of nerve regeneration beginning with Cruikshank's observations in 1776. *Med. Hist.* **21,** 261–74 (1977).
81. IJpma, F. F. A., Van De Graaf, R. C. & Meek, M. F. The early history of tubulation in nerve repair. *J. Hand Surg. Eur. Vol.* **33,** 581–6 (2008).
82. Gupta, B., Plummer, C., Bisson, I., Frey, P. & Hilborn, J. Plasma-induced graft polymerization of acrylic acid onto poly(ethylene terephthalate) films: Characterization and human smooth muscle cell growth on grafted films. *Biomaterials* **23,** 863–871 (2002).
83. Yao, L. *et al.* The effect of laminin peptide gradient in enzymatically cross-linked collagen scaffolds on neurite growth. *J. Biomed. Mater. Res. - Part A* **92,** 484–492 (2010).
84. Rydevik, B. L. *et al.* An in vitro mechanical and histological study of acute stretching on rabbit tibial nerve. *J. Orthop. Res.* **8,** 694–701 (1990).
85. Merle, M., Dellon, A. L., Campbell, J. N. & Chang, P. S. Complications from silicon-polymer intubulation of nerves. *Microsurgery* **10,** 130–3 (1989).
86. de Ruiter, G. C. W., Malessy, M. J. A., Yaszemski, M. J., Windebank, A. J. & Spinner, R. J. Designing ideal conduits for peripheral nerve repair. *Neurosurg. Focus* **26,** E5 (2009).
87. Mackinnon, S. E., Doolabh, V. B., Novak, C. B. & Trulock, E. P. Clinical outcome following nerve allograft transplantation. *Plast. Reconstr. Surg.* **107,** 1419–29 (2001).
88. Szynkaruk, M., Kemp, S. W. P., Wood, M. D., Gordon, T. & Borschel, G. H. Experimental and clinical evidence for use of decellularized nerve allografts in peripheral nerve gap reconstruction. *Tissue Eng. Part B. Rev.* **19,** 83–96 (2013).
89. Hsueh, Y.-Y. *et al.* Functional recoveries of sciatic nerve regeneration by combining chitosan-coated conduit and neurosphere cells induced from adipose-derived stem cells. *Biomaterials* **35,** 2234–44 (2014).
90. Moore, A. M. *et al.* Limitations of conduits in peripheral nerve repairs. *Hand (N. Y).* **4,**

180–6 (2009).

91. Yang, Y. *et al.* Biocompatibility evaluation of silk fibroin with peripheral nerve tissues and cells in vitro. *Biomaterials* **28,** 1643–52 (2007).

92. Alovskaya, A., Alekseeva, T., Phillips, J., King, V. & Brown, R. Fibronectin, Collagen, Fibrin - Components of Extracellular Matrix for Nerve Regeneration. *Topics in Tissue Engineering* (2007).

93. Hudson, T. W., Evans, G. R. & Schmidt, C. E. Engineering strategies for peripheral nerve repair. *Clin. Plast. Surg.* **26,** 617–28, ix (1999).

94. Verdú, E. *et al.* Alignment of collagen and laminin-containing gels improve nerve regeneration within silicone tubes. *Restor. Neurol. Neurosci.* **20,** 169–79 (2002).

95. LUNDBORG, G., ROSEN, B., ABRAHAMSON, S., DAHLIN, L. & DANIELSEN, N. Tubular repair of the median nerve in the human forearm Preliminary findings. *J. Hand Surg. J. Br. Soc. Surg. Hand* **19,** 273–276 (1994).

96. Geuna, S., Tos, P. & Battiston, B. *Essays on peripheral nerve repair and regeneration*. (Academic Press, 2009).

97. Lee, A. C. *et al.* Controlled release of nerve growth factor enhances sciatic nerve regeneration. *Exp. Neurol.* **184,** 295–303 (2003).

98. Xu, X. *et al.* Peripheral nerve regeneration with sustained release of poly(phosphoester) microencapsulated nerve growth factor within nerve guide conduits. *Biomaterials* **24,** 2405–2412 (2003).

99. Zarbakhsh, S. *et al.* The effects of schwann and bone marrow stromal stem cells on sciatic nerve injury in rat: a comparison of functional recovery. *Cell J.* **14,** 39–46 (2012).

100. Lee, K.-W. *et al.* Fabrication and Characterization of Poly(Propylene Fumarate) Scaffolds with Controlled Pore Structures Using 3-Dimensional Printing and Injection Molding. *Tissue Eng.* **12,** 2801–2811 (2006).

101. Aebischer, P., Valentini, R. F., Dario, P., Domenici, C. & Galletti, P. M. Piezoelectric guidance channels enhance regeneration in the mouse sciatic nerve after axotomy. *Brain Res.* **436,** 165–8 (1987).

102. Karabekmez, F. E., Duymaz, A. & Moran, S. L. Early clinical outcomes with the use of decellularized nerve allograft for repair of sensory defects within the hand. *Hand (N. Y).* **4,** 245–9 (2009).

103. Panseri, S. *et al.* Electrospun micro- and nanofiber tubes for functional nervous regeneration in sciatic nerve transections. *BMC Biotechnol.* **8,** 39 (2008).

104. Rangappa, N., Romero, A., Nelson, K. D., Eberhart, R. C. & Smith, G. M. Laminin-coated poly(L-lactide) filaments induce robust neurite growth while providing directional orientation. *J. Biomed. Mater. Res.* **51,** 625–34 (2000).

105. Jiang, X., Lim, S. H., Mao, H.-Q. & Chew, S. Y. Current applications and future perspectives of artificial nerve conduits. *Exp. Neurol.* **223,** 86–101 (2010).

106. Meek, M. F. & Coert, J. H. US Food and Drug Administration/Conformit Europe-approved absorbable nerve conduits for clinical repair of peripheral and cranial nerves. *Ann. Plast. Surg.* **60,** 110–6 (2008).

107. Kaewkhaw, R., Scutt, A. M. & Haycock, J. W. Integrated culture and purification of rat Schwann cells from freshly isolated adult tissue. *Nat. Protoc.* **7,** 1996–2004 (2012).

108. Hong, Y. *et al.* Mechanical properties and in vivo behavior of a biodegradable synthetic polymer microfiber-extracellular matrix hydrogel biohybrid scaffold. *Biomaterials* **32,** 3387–94 (2011).

109. Owen, D. E. & Egerton, J. Culture of dissociated sensory neurons from dorsal root ganglia of postnatal and adult rats. *Methods Mol. Biol.* **846,** 179–87 (2012).

110. Pateman, C. J. *et al.* Nerve guides manufactured from photocurable polymers to aid peripheral nerve repair. *Biomaterials* **49,** 77–89 (2015).

111. Hong, Y. *et al.* Generating Elastic, Biodegradable Polyurethane/Poly(lactide- *co* -glycolide) Fibrous Sheets with Controlled Antibiotic Release via Two-Stream Electrospinning. *Biomacromolecules* **9,** 1200–1207 (2008).

112. Ji, R.-R., Kawasaki, Y., Zhuang, Z.-Y., Wen, Y.-R. & Decosterd, I. Possible role of spinal astrocytes in maintaining chronic pain sensitization: review of current evidence with focus on bFGF/JNK pathway. *Neuron Glia Biol.* **2,** 259–69 (2006).

113. Wang, W. *et al.* Crosstalk between spinal astrocytes and neurons in nerve injury-induced neuropathic pain. *PLoS One* **4,** e6973 (2009).

114. Beke, S. *et al.* Rapid fabrication of rigid biodegradable scaffolds by excimer laser mask projection technique: a comparison between 248 and 308 nm. *Laser Phys.* **23,** 35602 (2013).

115. Farkas, B., Dante, S. & Brandi, F. Photoinitiator-free 3D scaffolds fabricated by excimer laser photocuring. *Nanotechnology* **28,** 34001 (2017).

116. Oh, S. H. *et al.* Effect of surface pore structure of nerve guide conduit on peripheral nerve regeneration. *Tissue Eng. Part C. Methods* **19,** 233–43 (2013).

117. Kokai, L. E., Lin, Y.-C., Oyster, N. M. & Marra, K. G. Diffusion of soluble factors through degradable polymer nerve guides: Controlling manufacturing parameters.

Acta Biomater. **5,** 2540–2550 (2009).

118. Annabi, N. *et al.* Controlling the porosity and microarchitecture of hydrogels for tissue engineering. *Tissue Eng. Part B. Rev.* **16,** 371–83 (2010).
119. Sophia Fox, A. J., Bedi, A. & Rodeo, S. A. The basic science of articular cartilage: structure, composition, and function. *Sports Health* **1,** 461–8 (2009).
120. Kessler, M. W. & Grande, D. A. Tissue engineering and cartilage. *Organogenesis* **4,** 28–32 (2008).
121. Makris, E. A., Gomoll, A. H., Malizos, K. N., Hu, J. C. & Athanasiou, K. A. Repair and tissue engineering techniques for articular cartilage. *Nat. Rev. Rheumatol.* **11,** 21–34 (2014).
122. Xu, Y. *et al.* Tissue Engineering of Human Nasal Alar Cartilage Precisely by Using Three-Dimensional Printing. *Plast. Reconstr. Surg.* **135,** 451–458 (2015).
123. Liao, H. T. *et al.* Prefabricated, Ear-Shaped Cartilage Tissue Engineering by Scaffold-Free Porcine Chondrocyte Membrane. *Plast. Reconstr. Surg.* **135,** 313e–321e (2015).
124. Steadman, J. R., Rodkey, W. G., Briggs, K. K. & Rodrigo, J. J. [The microfracture technic in the management of complete cartilage defects in the knee joint]. *Orthopade* **28,** 26–32 (1999).
125. Bae, D. K., Yoon, K. H. & Song, S. J. Cartilage Healing After Microfracture in Osteoarthritic Knees. *Arthrosc. J. Arthrosc. Relat. Surg.* **22,** 367–374 (2006).
126. Breinan, H. A., Martin, S. D., Hsu, H.-P. & Spector, M. Healing of canine articular cartilage defects treated with microfracture, a type-II collagen matrix, or cultured autologous chondrocytes. *J. Orthop. Res.* **18,** 781–789 (2000).
127. Kreuz, P. C. *et al.* Results after microfracture of full-thickness chondral defects in different compartments in the knee. *Osteoarthr. Cartil.* **14,** 1119–1125 (2006).
128. Chen, H. *et al.* Drilling and microfracture lead to different bone structure and necrosis during bone-marrow stimulation for cartilage repair. *J. Orthop. Res.* **27,** 1432–1438 (2009).
129. Peterson, L., Vasiliadis, H. S., Brittberg, M. & Lindahl, A. Autologous Chondrocyte Implantation. *Am. J. Sports Med.* **38,** 1117–1124 (2010).
130. Bartlett, W. *et al.* Autologous chondrocyte implantation versus matrix-induced autologous chondrocyte implantation for osteochondral defects of the knee: A PROSPECTIVE, RANDOMISED STUDY. *J. Bone Jt. Surg. - Br. Vol.* **87–B,** 640–645 (2005).
131. Foldager, C. B., Gomoll, A. H., Lind, M. & Spector, M. Cell Seeding Densities in

Autologous Chondrocyte Implantation Techniques for Cartilage Repair. *Cartilage* **3,** 108–17 (2012).

132. Caron, M. M. J. *et al.* Redifferentiation of dedifferentiated human articular chondrocytes: comparison of 2D and 3D cultures. *Osteoarthr. Cartil.* **20,** 1170–1178 (2012).

133. Chatterjee, K. *et al.* The effect of 3D hydrogel scaffold modulus on osteoblast differentiation and mineralization revealed by combinatorial screening. *Biomaterials* **31,** 5051–5062 (2010).

134. Phillips, J. E., Burns, K. L., Le Doux, J. M., Guldberg, R. E. & García, A. J. Engineering graded tissue interfaces. *Proc. Natl. Acad. Sci. U. S. A.* **105,** 12170–5 (2008).

135. Bhardwaj, N., Devi, D. & Mandal, B. B. Tissue-Engineered Cartilage: The Crossroads of Biomaterials, Cells and Stimulating Factors. *Macromol. Biosci.* **15,** 153–182 (2015).

136. Ossendorf, C. *et al.* Treatment of posttraumatic and focal osteoarthritic cartilage defects of the knee with autologous polymer-based three-dimensional chondrocyte grafts: 2-year clinical results. *Arthritis Res. Ther.* **9,** R41 (2007).

137. NESIC, D. *et al.* Cartilage tissue engineering for degenerative joint disease☆. *Adv. Drug Deliv. Rev.* **58,** 300–322 (2006).

138. Kemppainen, J. M. & Hollister, S. J. Tailoring the mechanical properties of 3D-designed poly(glycerol sebacate) scaffolds for cartilage applications. *J. Biomed. Mater. Res. Part A* **94A,** 9–18 (2010).

139. Jeong, C. G. & Hollister, S. J. A comparison of the influence of material on in vitro cartilage tissue engineering with PCL, PGS, and POC 3D scaffold architecture seeded with chondrocytes. *Biomaterials* **31,** 4304–12 (2010).

140. Mandal, T. K., Bostanian, L. A., Graves, R. A., Chapman, S. R. & Idodo, T. U. Porous biodegradable microparticles for delivery of pentamidine. *Eur. J. Pharm. Biopharm.* **52,** 91–96 (2001).

141. Cai, Y., Chen, Y., Hong, X., Liu, Z. & Yuan, W. Porous microsphere and its applications. *Int. J. Nanomedicine* **8,** 1111–20 (2013).

142. Scott, G. D. & Kilgour, D. M. The density of random close packing of spheres. *J. Phys. D. Appl. Phys.* **2,** 311 (1969).

143. Fundamentals of Refractory Technology: Proceedings of the Lecture Series ... - Google Books. Available at: https://books.google.co.uk/books?id=Hn6XJifYzAcC&pg=PA7&lpg=PA7&dq=higher+packing+density+inhomogeneous+particles&source=bl&ots=dwvi-

1EvKQ&sig=9OzVXiuThr1f9xlbm-_pij6SsBY&hl=en&sa=X&ved=0ahUKEwjOiqm39pfSAhXKPpAKHcUgCzQQ6AEIRzAF#v=onepage&q=higher packin. (Accessed: 17th February 2017)

144. Knott, G. M., Jackson, T. L. & Buckmaster, J. Random Packing of Heterogeneous Propellants. *AIAA J.* **39,** 678–686 (2001).

145. Farndale, R. W., Sayers, C. A. & Barrett, A. J. A direct spectrophotometric microassay for sulfated glycosaminoglycans in cartilage cultures. *Connect. Tissue Res.* **9,** 247–8 (1982).

146. Chen, C., Xie, J., Deng, L. & Yang, L. Substrate Stiffness Together with Soluble Factors Affects Chondrocyte Mechanoresponses. *ACS Appl. Mater. Interfaces* **6,** 16106–16116 (2014).

147. Shepherd, D. E. T. & Seedhom, B. B. A technique for measuring the compressive modulus of articular cartilage under physiological loading rates with preliminary results.

148. Svoronos, A. A., Tejavibulya, N., Schell, J. Y., Shenoy, V. B. & Morgan, J. R. Micro-mold design controls the 3D morphological evolution of self-assembling multicellular microtissues. *Tissue Eng. Part A* **20,** 1134–44 (2014).

149. Fischer, A. H., Jacobson, K. A., Rose, J. & Zeller, R. Hematoxylin and eosin staining of tissue and cell sections. *CSH Protoc.* **2008,** pdb.prot4986 (2008).

150. Schmitz, N., Laverty, S., Kraus, V. B. & Aigner, T. Basic methods in histopathology of joint tissues. *Osteoarthr. Cartil.* **18,** S113–S116 (2010).

151. Sridharan, G. & Shankar, A. A. Toluidine blue: A review of its chemistry and clinical utility. *J. Oral Maxillofac. Pathol.* **16,** 251–5 (2012).

152. Kyriacos A. Athanasiou, Eric M. Darling, Jerry C. Hu, Grayson D. DuRaine, A. H. R. Articular Cartilage. Available at: https://books.google.co.uk/books?id=rPktCmxCmiQC&pg=PA256&lpg=PA256&dq=toluidine+blue+glycosaminoglycans+purple&source=bl&ots=hMkvNsEszz&sig=lj0PieG1WmXvkrd_ezZJpjjsHHk&hl=en&sa=X&ved=0ahUKEwjFgYTHqODRAhXlK8AKHdqxBCUQ6AEITjAJ#v=onepage&q=toluidine%2520blue%25. (Accessed: 26th January 2017)

153. Ricard-Blum, S. & Herbage, D. in *Biology of Invertebrate and Lower Vertebrate Collagens* 53–64 (Springer US, 1985). doi:10.1007/978-1-4684-7636-1_4

154. Junqueira, L. C. U., Cossermelli, W. & Brentani, R. Differential Staining of Collagens Type I, II and III by Sirius Red and Polarization Microscopy. *Arch. histol. jap* **41,** 267–

274 (1978).

155. Yassin, F. E.-Z. E.-D., El-Dawela, R. & Kerim, M. Picrosirius red staining assessment of collagen after dermal roller application: A minimally invasive percutaneous collagen induction therapy. *Indian J. Dermatopathol. Diagnostic Dermatology* **1,** 68 (2014).

156. Rich, L. & Whittaker, P. COLLAGEN AND PICROSIRIUS RED STAINING: A POLARIZED LIGHT ASSESSMENT OF FIBRILLAR HUE AND SPATIAL DISTRIBUTION. *Braz. J. morphol. Sci* **22,** 97–104 (2005).

157. Jouls, V. *et al.* Effect of asorbic acid on secreted proteoglycans from rabbit articular chondrocytes. **186,** (1985).

158. Eyre, D. Collagen of articular cartilage. *Arthritis Res.* **4,** 30 (2002).

159. Mansour, J. M. & Welter, J. F. Multimodal evaluation of tissue-engineered cartilage. *J. Med. Biol. Eng.* **33,** 1–16 (2013).

160. Lounkine, E. *et al.* Large-scale prediction and testing of drug activity on side-effect targets. *Nature* **486,** 361–7 (2012).

161. Doke, S. K. & Dhawale, S. C. Alternatives to animal testing: A review. *Saudi Pharm. J.* **23,** 223–229 (2015).

162. Arora, T. *et al.* Substitute of Animals in Drug Research: An Approach Towards Fulfillment of 4R's. *Indian J. Pharm. Sci.* **73,** 1–6 (2011).

163. Annual Statistics of Scientific Procedures on Living Animals Great Britain 2015.

164. RUSSELL, W. M. S. & BURCH, R. L. The principles of humane experimental technique. *Princ. Hum. Exp. Tech.* (1959).

165. Kimber, I. *et al.* Alternative approaches to the identification and characterization of chemical allergens. *Toxicol. Vitr.* **15,** 307–312 (2001).

166. Brandon, E. F. ., Raap, C. D., Meijerman, I., Beijnen, J. H. & Schellens, J. H. . An update on in vitro test methods in human hepatic drug biotransformation research: pros and cons. *Toxicol. Appl. Pharmacol.* **189,** 233–246 (2003).

167. Godoy, P. *et al.* Recent advances in 2D and 3D in vitro systems using primary hepatocytes, alternative hepatocyte sources and non-parenchymal liver cells and their use in investigating mechanisms of hepatotoxicity, cell signaling and ADME. *Arch. Toxicol.* **87,** 1315–1530 (2013).

168. Xu, K., Li, X. & Fu-Shin, X. Corneal organ culture model for assessing epithelial responses to surfactants. *Toxicol. Sci.* (2000).

169. Breslin, S. & O'Driscoll, L. Three-dimensional cell culture: the missing link in drug discovery. *Drug Discov. Today* **18,** 240–249 (2013).

170. Tincer, G., Mashkaryan, V., Bhattarai, P. & Kizil, C. Neural stem/progenitor cells in Alzheimer's disease. *Yale J. Biol. Med.* **89,** 23–35 (2016).

171. Breier, J. M. *et al.* Neural progenitor cells as models for high-throughput screens of developmental neurotoxicity: State of the science. *Neurotoxicol. Teratol.* **32,** 4–15 (2010).

172. Brewer, G. J. & Torricelli, J. R. Isolation and culture of adult neurons and neurospheres. *Nat. Protoc.* **2,** 1490–1498 (2007).

173. About neuroblastoma | Children's cancers | Cancer Research UK. Available at: http://www.cancerresearchuk.org/about-cancer/childrens-cancer/neuroblastoma/about. (Accessed: 12th June 2017)

174. Teitz, T. *et al.* Preclinical Models for Neuroblastoma: Establishing a Baseline for Treatment. *PLoS One* **6,** e19133 (2011).

175. Maris, J. M. Recent Advances in Neuroblastoma. *N. Engl. J. Med.* **362,** 2202–2211 (2010).

176. Hoehner, J. C. *et al.* A developmental model of neuroblastoma: differentiating stroma-poor tumors' progress along an extra-adrenal chromaffin lineage. *Lab. Invest.* **75,** 659–75 (1996).

177. Neuroblastoma - Childhood: Introduction | Cancer.Net. Available at: http://www.cancer.net/cancer-types/neuroblastoma-childhood/introduction. (Accessed: 12th June 2017)

178. Choices, N. Neuroblastoma - NHS Choices.

179. IMR-32 ATCC ® CCL-127™ Homo sapiens brain; derived from meta. Available at: https://www.lgcstandards-atcc.org/products/all/CCL-127.aspx?geo_country=gb#characteristics. (Accessed: 12th June 2017)

180. SK-N-SH ATCC ® HTB-11™ Homo sapiens brain; derived from meta. Available at: https://www.lgcstandards-atcc.org/Products/All/HTB-11.aspx#generalinformation. (Accessed: 12th June 2017)

181. Kumar, H. R. *et al.* Three-dimensional neuroblastoma cell culture: proteomic analysis between monolayer and multicellular tumor spheroids. *Pediatr. Surg. Int.* **24,** 1229–34 (2008).

182. Duval, M. *et al.* Purification of developmentally regulated avian 400-kDa intermediate filament associated protein. Molecular interactions with intermediate filament proteins and other cytoskeleton components. *Biochem. Cell Biol.* **73,** 651–657 (1995).

183. Anti-Nestin antibody [Rat 401] (ab6142) | Abcam. Available at:

http://www.abcam.com/nestin-antibody-rat-401-ab6142.html. (Accessed: 16th June 2017)

184. Liu, C., Zhong, Y., Apostolou, A. & Fang, S. Neural differentiation of human embryonic stem cells as an in vitro tool for the study of the expression patterns of the neuronal cytoskeleton during neurogenesis. *Biochem. Biophys. Res. Commun.* **439,** 154–159 (2013).

185. Fuentealba, L. C., Obernier, K. & Alvarez-Buylla, A. Adult neural stem cells bridge their niche. *Cell Stem Cell* **10,** 698–708 (2012).

186. Marikawa, Y. & Alarcón, V. B. Establishment of trophectoderm and inner cell mass lineages in the mouse embryo. *Mol. Reprod. Dev.* **76,** 1019–32 (2009).

187. Mitalipov, S. & Wolf, D. in *Engineering of Stem Cells* **114,** 185–199 (Springer Berlin Heidelberg, 2009).

188. Thomson, J. A. *et al.* Embryonic stem cell lines derived from human blastocysts. *Science* **282,** 1145–7 (1998).

189. Young, H. E. & Black, A. C. Adult stem cells. *Anat. Rec.* **276A,** 75–102 (2004).

190. Lewis, E. E. L. Modelling the mesenchymal stem cell niche in vitro using magnetic nanoparticles. (2016).

191. Takahashi, K. & Yamanaka, S. Induction of Pluripotent Stem Cells from Mouse Embryonic and Adult Fibroblast Cultures by Defined Factors. *Cell* **126,** 663–676 (2006).

192. Avior, Y., Sagi, I. & Benvenisty, N. Pluripotent stem cells in disease modelling and drug discovery. *Nat. Rev. Mol. Cell Biol.* **17,** 170–182 (2016).

193. Shi, Y., Inoue, H., Wu, J. C. & Yamanaka, S. Induced pluripotent stem cell technology: a decade of progress. *Nat. Rev. Drug Discov.* **16,** 115–130 (2016).

194. Schofield, R. The relationship between the spleen colony-forming cell and the haemopoietic stem cell. *Blood Cells* **4,** 7–25 (1978).

195. Di Maggio, N. *et al.* Toward modeling the bone marrow niche using scaffold-based 3D culture systems. *Biomaterials* **32,** 321–329 (2011).

196. Kumar, G. *et al.* The determination of stem cell fate by 3D scaffold structures through the control of cell shape. *Biomaterials* **32,** 9188–9196 (2011).

197. Neofytou, E. A. *et al.* Adipose tissue-derived stem cells display a proangiogenic phenotype on 3D scaffolds. *J. Biomed. Mater. Res. Part A* **98A,** 383–393 (2011).

198. Viswanathan, P. *et al.* 3D surface topology guides stem cell adhesion and differentiation. *Biomaterials* **52,** 140–7 (2015).

199. Owen, R. *et al.* Emulsion templated scaffolds with tunable mechanical properties for bone tissue engineering. *J. Mech. Behav. Biomed. Mater.* **54,** 159–172 (2016).

200. Changotade, S. *et al.* Preliminary In Vitro Assessment of Stem Cell Compatibility with Cross-Linked Poly(ε-caprolactone urethane) Scaffolds Designed through High Internal Phase Emulsions. *Stem Cells Int.* **2015,** 283796 (2015).

201. Kolind, K., Leong, K. W., Besenbacher, F. & Foss, M. Guidance of stem cell fate on 2D patterned surfaces. *Biomaterials* **33,** 6626–6633 (2012).

202. Warmflash, A., Sorre, B., Etoc, F., Siggia, E. D. & Brivanlou, A. H. A method to recapitulate early embryonic spatial patterning in human embryonic stem cells. *Nat. Methods* **11,** 847–854 (2014).

203. Schopperle, W. M. & DeWolf, W. C. The TRA-1-60 and TRA-1-81 Human Pluripotent Stem Cell Markers Are Expressed on Podocalyxin in Embryonal Carcinoma. *Stem Cells* **25,** 723–730 (2006).

204. Kador, K. E. & Goldberg, J. L. Scaffolds and stem cells: delivery of cell transplants for retinal degenerations. *Expert Rev. Ophthalmol.* **7,** 459–470 (2012).

205. Chowdhury, F. *et al.* Soft Substrates Promote Homogeneous Self-Renewal of Embryonic Stem Cells via Downregulating Cell-Matrix Tractions. *PLoS One* **5,** e15655 (2010).

206. Lü, D., Luo, C., Zhang, C., Li, Z. & Long, M. Differential regulation of morphology and stemness of mouse embryonic stem cells by substrate stiffness and topography. *Biomaterials* **35,** 3945–3955 (2014).

207. Evans, N. D. *et al.* Substrate stiffness affects early differentiation events in embryonic stem cells. *Eur. Cell. Mater.* **18,** 1-13–4 (2009).

208. Eroshenko, N., Ramachandran, R., Yadavalli, V. K. & Rao, R. R. Effect of substrate stiffness on early human embryonic stem cell differentiation. *J. Biol. Eng.* **7,** 7 (2013).

209. Winer, J. P., Janmey, P. A., McCormick, M. E. & Funaki, M. Bone Marrow-Derived Human Mesenchymal Stem Cells Become Quiescent on Soft Substrates but Remain Responsive to Chemical or Mechanical Stimuli. *Tissue Eng. Part A* **15,** 147–154 (2009).